



School of Natural Sciences

S $\pi$ RALS – SOUTHERN HEMISPHERE PARALLAX INTERFEROMETRIC  
RADIO ASTROMETRY LEGACY SURVEY

by

Lucas Jordan Hyland, B.Sc. (Hons)

November 2020

Supervisors:  
Prof Simon P. Ellingsen  
Dr James A. Green

Submitted in fulfilment of the requirements  
for the Degree of Doctor of Philosophy



I declare that this thesis contains no material which has been accepted for a degree or diploma by the University or any other institution, except by way of background information and duly acknowledged in the thesis, and that, to the best of my knowledge and belief, this thesis contains no material previously published or written by another person, except where due acknowledgement is made in the text of the thesis.

Signed: \_\_\_\_\_  
Lucas Jordan Hyland

Date: \_\_\_\_\_



This thesis may be made available for loan and limited copying in accordance with  
the *Copyright Act 1968*

Signed: \_\_\_\_\_  
Lucas Jordan Hyland

Date: \_\_\_\_\_



# ABSTRACT

The exact structure of the spiral arms of our home Galaxy, the Milky Way, is an unknown that can be primarily resolved by a higher sampling of parallaxes to high mass star forming regions from both the Northern and Southern Hemispheres. The Northern Hemisphere has been very well sampled by surveys like BeSSeL and the VERA key project, yet they are unable to observe sources in the southern sky and complete the picture of the Milky Way.

An upcoming large maser astrometry project the Southern Hemisphere Parallax Interferometric Radio Astrometry Legacy Survey or S $\pi$ RALS is commenced mid–2020 will measure the parallaxes to Southern Hemisphere high mass star formation regions. Using three 12 m and one 30 m radio telescopes spread over Australia, S $\pi$ RALS will measure parallaxes for dozens of High Mass Star Formation Regions in the 3rd and 4th Galactic Quadrant and thereby determine spiral arm properties and Galactic kinematics inaccessible to Northern Hemisphere instruments. However, as hardware and accessibility is different between BeSSeL and S $\pi$ RALS , effort is required to develop observing method and calibration techniques to account for this difference and even improve on it.

The aims of this thesis are as follows:

Firstly, to analyse BeSSeL VLBA data and measure parallaxes for three 22 GHz water masers and one 6.7 GHz methanol maser located in the First Galactic Quadrant. This increases the understanding of Galactic structure and establishes a benchmark for VLBI astrometry for S $\pi$ RALS to aspire to. I have been able to successfully measure the parallax and proper motion of the methanol maser and 2 of the water masers, and measure proper motions for the last water maser. I then use these results to determine the locations of these all masers in the Galaxy and final all four are in the Perseus spiral arm.

Secondly, to determine a target list for S $\pi$ RALS by conducting a targeted survey of known Southern Hemisphere 6.7 GHz methanol masers. Significant effort is required to measure a parallax and therefore identification of the best targets for each Galactic region is important for time and data quality. I find that there are 53 suitable first targets for S $\pi$ RALS and a further 29 likely appropriate for future VLBI astrometry. I am able to determine the compactness of 103 methanol masers, equivalent to a 55% detection rate; the remaining 45% of surveyed masers are too weak or diffuse.

Thirdly, to develop and test inverse MultiView, a phase calibration technique nominally designed for ionospheric calibration. I find that inverse MultiView can be used to model and subtract residual delay errors due to additional effects like residual troposphere and interferometer baseline offsets. I also find that inverse MultiView is able to out–perform traditional techniques and enable target–calibrator separations of at least 8° at 8.2 GHz. With inverse MultiView I am able to achieve microsecond astrometry on a relatively new interferometric array which will be used for S $\pi$ RALS , thereby paving the way for future high accuracy Southern Hemisphere maser parallaxes.

# TABLE OF CONTENTS

<b>TABLE OF CONTENTS</b>	i
<b>LIST OF TABLES</b>	vii
<b>LIST OF FIGURES</b>	ix
<b>1 Introduction</b>	1
1.1 Structure of the Milky Way . . . . .	2
1.2 Astrophysical Distances . . . . .	2
1.2.1 Kinematic Distance . . . . .	3
1.2.2 Trigonometric Parallax . . . . .	3
1.3 Masers . . . . .	5
1.3.1 Theory . . . . .	5
1.3.2 Water . . . . .	6
1.3.3 Methanol . . . . .	7
1.4 S $\pi$ RALS . . . . .	8
1.4.1 Mapping the Milky Way . . . . .	8
1.4.2 BeSSeL and VERA . . . . .	11
1.4.3 Southern Hemisphere – S $\pi$ RALS . . . . .	12
<b>2 VLBI Astrometry and Calibration</b>	17

## TABLE OF CONTENTS

2.1	Introduction . . . . .	18
2.2	Distance and Astrometric Uncertainty . . . . .	18
2.2.1	Determination of distance . . . . .	18
2.3	Delay Calibration . . . . .	20
2.3.1	Correlation . . . . .	20
2.3.2	Geodetic and Source Position Delay . . . . .	21
2.3.3	Electronic and Clock Offset Delays . . . . .	22
2.3.4	Additional Delays . . . . .	23
2.4	Calibrating for the Atmosphere . . . . .	24
2.4.1	Phase Referencing . . . . .	24
2.4.2	Dry Tropospheric Delay . . . . .	26
2.4.3	Wet Tropospheric Delay . . . . .	27
2.4.4	Ionospheric Delay . . . . .	28
2.5	Amplitude Calibration . . . . .	29
2.5.1	Alternative maser calibration . . . . .	30
2.5.2	Alternate quasar calibration . . . . .	30
2.6	Additional Considerations . . . . .	32
2.6.1	Annual Parallax Sampling . . . . .	32
2.6.2	Proper motion . . . . .	33
2.7	Summary – Standard Astrometric VLBI Calibration . . . . .	34
<b>3</b>	<b>Parallax and Proper Motions of First Galactic Quadrant Star Forming Regions</b>	<b>39</b>
3.1	Introduction . . . . .	40
3.2	Observations and Reduction . . . . .	41
3.2.1	K-band: BR210A to E . . . . .	41
3.2.2	Wide C-band: BR210F . . . . .	42
3.2.3	Sources . . . . .	42
3.2.4	Calibration . . . . .	42
3.3	Results and Discussion . . . . .	44
3.3.1	Astrometry and Parallax Fitting . . . . .	44
3.3.2	G021.87+0.01 . . . . .	44
3.3.3	G037.81+0.41 . . . . .	47
3.3.4	G060.58–0.18 . . . . .	50

## TABLE OF CONTENTS

3.3.5 G070.29+1.60 . . . . .	53
3.3.6 Kinematics and Spiral Arm Modelling . . . . .	57
3.4 Concluding Remarks . . . . .	59
<b>4 Southern Hemisphere 6.7 GHz methanol maser compactness catalogue</b>	<b>61</b>
4.1 Introduction . . . . .	62
4.2 Source Selection and Observations . . . . .	62
4.3 Data Reduction . . . . .	66
4.3.1 <i>AIPS</i> reduction . . . . .	66
4.3.2 Notes on external ParselTongue scripts . . . . .	67
4.3.3 Maser Visibility Fitting . . . . .	70
4.4 Categorisation . . . . .	72
4.4.1 Fitting Results . . . . .	72
4.4.2 Visibility Amplitude vs. <i>uv</i> –distance . . . . .	72
4.4.3 Emission density/compactness index $\xi$ . . . . .	73
4.4.4 Constraints and grades . . . . .	75
4.4.5 Summary . . . . .	75
4.5 Discussion . . . . .	78
4.5.1 Non-detections . . . . .	78
4.5.2 Interstellar scattering . . . . .	79
4.5.3 Class II Methanol Variability and Flaring . . . . .	80
4.5.4 Variation from Model . . . . .	81
4.6 Conclusion - First Targets . . . . .	83
<b>5 MultiView</b>	<b>85</b>
5.1 Background . . . . .	86
5.2 Inverse MultiView Theory . . . . .	87
5.2.1 Baseline delay differential $\Delta\tau_{bl}$ . . . . .	87
5.2.2 Dry Tropospheric delay differential $\Delta\tau_{dtr}$ . . . . .	89
5.2.3 Positional delay difference . . . . .	91
5.2.4 Final delays . . . . .	93
5.2.5 Total delay/phase solution . . . . .	93
5.3 Observing Method and Phase-Fitting . . . . .	94

## TABLE OF CONTENTS

<b>6 MultiView–Ring Calibration</b>	<b>99</b>
6.1 Introduction . . . . .	100
6.2 Source Selection . . . . .	101
6.2.1 Quasar benefits and Quality $Q$ . . . . .	101
6.2.2 Sensitivity Limitations . . . . .	102
6.2.3 Quasar Arrangement . . . . .	103
6.3 Method and Observations . . . . .	106
6.3.1 Array and Frequency . . . . .	106
6.3.2 Observing Structure . . . . .	106
6.4 Reduction Processes . . . . .	110
6.4.1 Correlation . . . . .	110
6.4.2 Antenna Position Corrections . . . . .	110
6.4.3 Antenna Amplitude Calibration . . . . .	114
6.4.4 Initial Phase Referencing and Orbit Source Position Corrections . . . . .	115
6.4.5 MultiView Fitting . . . . .	116
6.4.6 Inverse Phase Referencing and Self-Calibrating . . . . .	117
6.5 Results and Discussion . . . . .	119
6.5.1 Astrometry . . . . .	119
6.5.2 Phase Slopes . . . . .	121
6.5.3 Astrometric Uncertainty . . . . .	127
6.6 Final comments . . . . .	131
<b>7 Conclusion</b>	<b>133</b>
7.1 Summary of Results . . . . .	133
7.2 Current and Future work . . . . .	134
<b>BIBLIOGRAPHY</b>	<b>137</b>
<b>A ADDITIONAL TABLES AND FIGURES 1</b>	<b>147</b>
A.1 Additional Figures . . . . .	147
A.1.1 Maser and Calibrator Synthesised Maps . . . . .	147
A.1.2 G021.87+0.01 Time-Series Spectra and Maps . . . . .	151
A.2 Additional Tables . . . . .	153
A.2.1 BR210 Epochs . . . . .	153

## TABLE OF CONTENTS

A.2.2 Astrometric Products . . . . .	154
<b>B ADDITIONAL TABLES AND FIGURES 2</b>	<b>159</b>
B.1 Maser Compactness Tables . . . . .	159
B.2 Maser Compactness Statistics . . . . .	166
B.3 All Maser Spot Compactness . . . . .	168
<b>C MultiView Additional</b>	<b>203</b>
C.1 Additional Equations . . . . .	203
C.1.1 Delay Plane Derivations . . . . .	203
C.1.2 Finite Sum of Angles . . . . .	207
C.2 Additional Figures . . . . .	210
C.2.1 Raw Phases . . . . .	210
C.2.2 Phase and Phase Slopes measured by MultiView . . . . .	222
C.3 Additional Tables . . . . .	226
C.3.1 Inverse Phase Referencing Astrometry . . . . .	226
C.3.2 Inverse MultiView Astrometry . . . . .	229
C.3.3 Self-Calibration Astrometry . . . . .	230

TABLE OF CONTENTS

# LIST OF TABLES

3.1	Observed BeSSeL masers . . . . .	43
3.2	Parallax and Proper Motions . . . . .	44
3.3	Masers in Galactocentric coordinates . . . . .	58
4.1	V534 LBA telescopes . . . . .	63
4.2	V534 LBA baselines . . . . .	63
4.3	Compact maser catagorisation descriptions . . . . .	78
6.1	ACSI baselines . . . . .	106
6.2	MV observational epochs . . . . .	109
6.3	MV02* antenna positions and velocities . . . . .	111
6.4	Ceduna position offsets . . . . .	112
6.5	Quasar shifts . . . . .	117
A.1	BR210 Epochs . . . . .	153
A.2	Final astrometric values for G021.87+0.02. . . . .	154
A.3	Final astrometric values for G037.81+0.41 . . . . .	155
A.4	Final astrometric values for G060.57–0.18 . . . . .	156
A.5	Final astrometric values for G070.29+1.60 . . . . .	157
B.1	Best 6.7 GHz Maser . . . . .	159

## LIST OF TABLES

B.2 Maser Parameters . . . . .	162
B.3 Non-detections . . . . .	165

# LIST OF FIGURES

1.2	Schematic of Galactic rotation . . . . .	4
1.3	Schematic of Trigonometric Parallax . . . . .	5
1.4	Masering . . . . .	5
1.5	Microwave spectroscopy . . . . .	6
1.6	Water energy levels . . . . .	7
1.7	Methanol energy levels . . . . .	8
1.8	Galaxy as seen from Earth . . . . .	9
1.9	Oort et al. 1958, Figure 4 . . . . .	10
1.10	Georgelin and Georgelin 1976, Figure 11 . . . . .	10
1.11	Caswell & Haynes (1987) Figure 5. . . . .	11
1.12	Reid et al. (2019) Figure 1. . . . .	12
1.13	ASCI Array . . . . .	14
2.1	Parallax to distance asymmetry . . . . .	19
2.2	Geodetic Effect . . . . .	21
2.3	VLBI Atmosphere . . . . .	25
2.4	Mapping Functions . . . . .	27
2.5	Ionospheric Delay vs. Observing Frequency . . . . .	29
2.6	Model parallax . . . . .	33

## LIST OF FIGURES

3.1	First quadrant $l - v$ diagram . . . . .	41
3.2	G021.87+0.01 Parallax Fit . . . . .	45
3.3	Proper motion distance G021.87+0.01 . . . . .	46
3.4	G021.87+0.01 Sky position . . . . .	46
3.5	G037.82+0.41 Parallax Fit . . . . .	48
3.6	G037.82+0.41 Sky position . . . . .	49
3.7	G037.81+0.41 Spectrum and Spotmap . . . . .	49
3.8	G060.57-0.18 Parallax Fit . . . . .	51
3.9	G060.58-0.18 Sky position . . . . .	52
3.10	G060.57-0.18 quasar distribution . . . . .	52
3.13	G070 region bayesian distance estimator . . . . .	54
3.11	G070.29+1.60 Parallax Fit . . . . .	55
3.12	K3-50A/W58a GMC and Masers . . . . .	56
3.14	Galactic and Galactocentric Coordinates . . . . .	57
3.15	Spiral Arm Fit . . . . .	58
4.1	Southern Hemisphere Methanol Masers . . . . .	64
4.2	All masers $l - v$ diagram . . . . .	65
4.3	Example visibility fitting . . . . .	68
4.4	G192.600-0.048 spectrum . . . . .	68
4.5	Data Reduction Process for V534 . . . . .	69
4.6	Global distributions of $S_C$ , $\theta_C$ , $S_H$ and $\theta_H$ . . . . .	71
4.8	Global distributions of $\xi$ , $S_{B_\lambda}$ and $R_{B_\lambda}$ . . . . .	74
4.11	Maser catagory populations . . . . .	79
4.12	Size distribution in $l$ and $b$ . . . . .	80
4.13	Maser Plot . . . . .	82
4.14	Best masers $l - v$ diagram . . . . .	83
5.1	Figure 1. Rioja et al. (2017) . . . . .	86
5.2	Positional Tropospheric Error . . . . .	91
6.1	Quasar Quality Histogram . . . . .	102
6.2	Good quasars . . . . .	103
6.3	G0634-2335 Ring Plot . . . . .	104

## LIST OF FIGURES

6.4	G1336-0829 Ring Plot . . . . .	105
6.5	G1901-2121 Ring Plot . . . . .	105
6.6	Block Diagram for the MV02* observing structure. . . . .	107
6.7	Bayesian clock-fitting . . . . .	111
6.8	AstroGeo vs. SCHED Ceduna Position . . . . .	112
6.9	Before/After position correction . . . . .	113
6.10	Calibrating Ceduna IFs with 3C279 . . . . .	114
6.11	G0634-2335 Radplot . . . . .	115
6.12	SN1 MV026 G0634-2335 . . . . .	116
6.13	G1901 on baseline Cd-Ho . . . . .	118
6.14	Positional Uncertainty vs. Radius Centre . . . . .	119
6.15	Fractional Flux Recovery vs. Radius Orbit . . . . .	120
6.16	Offset quasars . . . . .	120
6.17	MV026 Slopes . . . . .	122
6.19	Measured slopes vs. model troposphere slopes . . . . .	126
6.20	Random Slope Uncertainty vs. Metrics . . . . .	129
6.21	X-band MultiView Errors . . . . .	130
A.1	G021.87+0.01 maps . . . . .	147
A.2	G037.82+0.41 maps . . . . .	148
A.3	G060.58-0.18 maps . . . . .	148
A.4	G070.29+1.60 maps . . . . .	149
A.5	G021.87+0.01 spectra . . . . .	151
A.6	G021.88+0.01 spotmaps . . . . .	152
B.1	Spot Compactness 1 . . . . .	166
B.2	Spot Compactness 2 . . . . .	167
B.3	All maser and spot compactness . . . . .	168
C.1	G0634-2335 MV025 Phases . . . . .	210
C.2	G1901-2112 MV025 Phases . . . . .	211
C.3	G1336-0829 MV025 Phases . . . . .	212
C.4	G0634-2335 MV026 Phases . . . . .	213
C.5	G1901-2112 MV026 Phases . . . . .	214

## LIST OF FIGURES

C.6 G1336–0829 MV026 Phases . . . . .	215
C.7 G0634–2335 MV027 Phases . . . . .	216
C.8 G1901–2112 MV027 Phases . . . . .	217
C.9 G1336–0829 MV027 Phases . . . . .	218
C.10 G0634–2335 MV028 Phases . . . . .	219
C.11 G1901–2112 MV028 Phases . . . . .	220
C.12 G1336–0829 MV028 Phases . . . . .	221



# 1

## INTRODUCTION

The exact structure, number of spiral arms and size of our home galaxy, the Milky Way is still largely shrouded in mystery. While numerous optical and radio surveys have determined distances to stars, molecular clouds or even whole regions, the day is not yet here where we may see the Milky Way in its entirety.

This thesis stands to introduce and discuss a new contender in the pursuit of mapping the Milky Way— the Southern Hemisphere Parallax Interferometric Radio Astrometry Legacy Survey or S $\pi$ RALS . S $\pi$ RALS intends to use Very Long Baseline Interferometry to measure trigonometric parallaxes of High Mass Star Forming Regions traced by class II methanol masers. The distances will then be used to infer the otherwise ambiguous spiral structure in the Southern Hemisphere and combine the results those from Bar and Spiral Structure Legacy and VLBI Explorer Radio Astronomy projects, which use the same technique from the Northern Hemisphere. Together, the results can produce the most accurate representation of the structure, size and kinematics of the Galaxy.

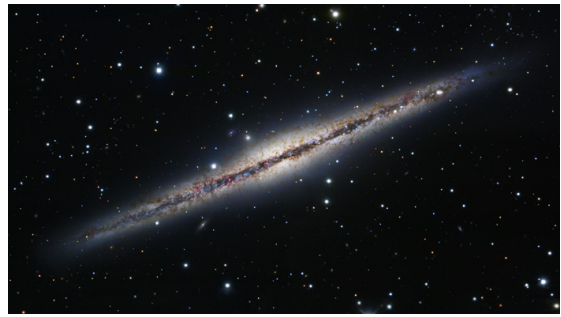
In the next few sections I will discuss the origins of the mystery of Galactic structure and the ongoing resolutions to it, specifically those relevant to the field of astrometry, radio astronomy and Very Long Baseline Interferometry.

## 1.1 Structure of the Milky Way

Galaxies are broadly divided into three categories: elliptical, spiral and irregular. Elliptical galaxies are considered to be ‘old’, characterised by a low surface brightness, a featureless circular/oblong shape and mostly population II stars in a hot dynamic environment (dominated by random radial motion; Hubble, 1936). Spiral galaxies are characterised by an overall flat disk-like structure containing many population I stars and a rigid density pattern etched into the face. Spirals also generally contain a central bulge that possesses very similar properties to an elliptical galaxy (Merritt, 1999). Lastly, irregulars are the remaining 2–3% of galaxies which ‘lack both rotational symmetry and, in general, dominating nuclei’ (Hubble, 1936). Figure 1.1a below is a Hubble telescope image of M51a, the ‘Whirlpool Galaxy’ and it’s near companion NGC5194b. This image shows an example of what a spiral galaxy looks like ‘face-on’ as seen in visible light. This identification comes from the ability to directly observe the density pattern



(a) Pictured here is the typical spiral galaxy: M51 aka the Whirlpool Galaxy and its interacting companion NGC5194b. M51 is approximately 9.5 million parsecs away and is only brought into such clarity by high-resolution Hubble Space Telescope images, which clearly show the fine-detail spiral structure and more importantly, the red hydrogen- $\alpha$  emission in the arms tracing the High Mass Star Formation Regions.



(b) Pictured here is the almost directly edge-on galaxy NGC891 as by the Hubble space telescope. Although NGC891 is very obviously a spiral galaxy due to its flat shape, dust lanes and blue colour, any spiral pattern that it may possess is indiscernible. *Image Credit: Robert Gendler, NAOJ, HST/NASA, BYU, <http://www.robgendlerastropics.com/NGC891-Subaru-HST.html>.*

and the relative intragalactic distances. All face-on or partially face-on resolved galaxies in the near universe can be easily classified as such. However due to our location inside the disc of the Milky Way, our view of the Galaxy is much more similar to that of an edge-on galaxy (much like Figure 1.1b).

## 1.2 Astrophysical Distances

Distance remains to be one of the most elusive properties for astrophysicists and astronomers to measure. Many distance measurements rely on indirect techniques, such as standard candles – where an object with an approximately known luminosity is measured at a certain intensity at Earth, thus giving the distance by the  $1/d^2$  dependence. Examples of this are photometric or spectroscopic distances, where the observed intensity of stellar radiation in particular bands or the absorption/emission lines observed in the spectrum infer stellar classification and therefore

## 1.2. ASTROPHYSICAL DISTANCES

absolute luminosity. The accuracy of these techniques suffer primarily from dust extinction effects in the line-of-sight reddening of photometric data or insufficient photon counts for spectroscopic data.

Another technique worthy of mention is the method of dispersion measure— where you observe an amount of dispersion in the (normally low-frequency  $\nu < 2$  GHz) radio emission along a line-of-sight. Combining this with a modelled or known electron column density causing the dispersion implies a likely distance (e.g. Cordes, 2004; Yao et al., 2017). Again, modelled techniques suffer from model inaccuracies and ionised regions can additionally corrupt the electron content assumptions (e.g. Sagittarius A\*; Reid et al., 1988).

### 1.2.1 Kinematic Distance

In radio astronomy, kinematic distance estimates are a widely-used and easy method for estimating astrophysical distance, although still plagued by potential systematic uncertainty (Gómez, 2006).

The methodology for kinematic distances is fairly simple: assuming that all matter in the Galaxy rotates in strictly circular paths of the same direction and assuming that the rotational speed is only dependant on the Galactic radius, observed Doppler velocities can be used to infer the Galactic radius. By accounting for projection effects, assuming an *a priori* radius  $R_0$  and rotational velocity  $\Theta_0$  of the solar system, distance to objects can be calculated.

Figure 1.2 shows a diagram of kinematic distance estimation: objects rotate clockwise around the Galactic centre with velocity  $\Theta$  ( $\text{km s}^{-1}$ ) given by the rotation curve  $\Omega$  (in  $\text{km s}^{-1} \text{ pc}^{-1}$ ). The observed velocity  $v$  ( $\text{km s}^{-1}$ ) of an object will be the relative velocity along the line-of-sight:

$$v = (\Omega(R)R - \Theta(R_0)) \sin l \cos b \quad (1.1)$$

where  $l, b$  are the target source's Galactic coordinates and  $R_0$  is the Sun's Galactic radius.

While simple, kinematic distances suffer from a few downsides. Firstly inside the solar circle, two distances (labelled ‘near’ and ‘far’; Figure 1.2) will give the same projected line-of-sight velocity and make the distance ambiguous without further information. In addition, the rotation curve of the Galaxy ( $\Omega(R)$ ) needs to be modelled from distance–velocity data to accurately reflect the Galaxy and therefore needs to be based off another distance estimate.

Finally, any non-circular motion of a gas clump, star etc. around the Galaxy or internal motions (like water masers with a large velocity spread; Titmarsh et al., 2013) will skew the only measurable quantity. As with any methodology, modelling requires confirmation based on real and direct measurable quantities, which is where the next technique comes in.

### 1.2.2 Trigonometric Parallax

Trigonometric parallax is known as the ‘gold standard’ of astronomical distances determinations as it serves as the method by which other distance techniques and standard candles can be calibrated. The technique is geometric, direct and requires no assumptions about luminosities, temperatures or intermediate environments (like dust extinction, electron content).

As the Earth orbits around the Sun, it sweeps out a well-defined ellipse with semi-major axis (aphelion) and semi-minor axis (perihelion). The distance of 1 astronomical unit (AU) was

## 1.2. ASTROPHYSICAL DISTANCES

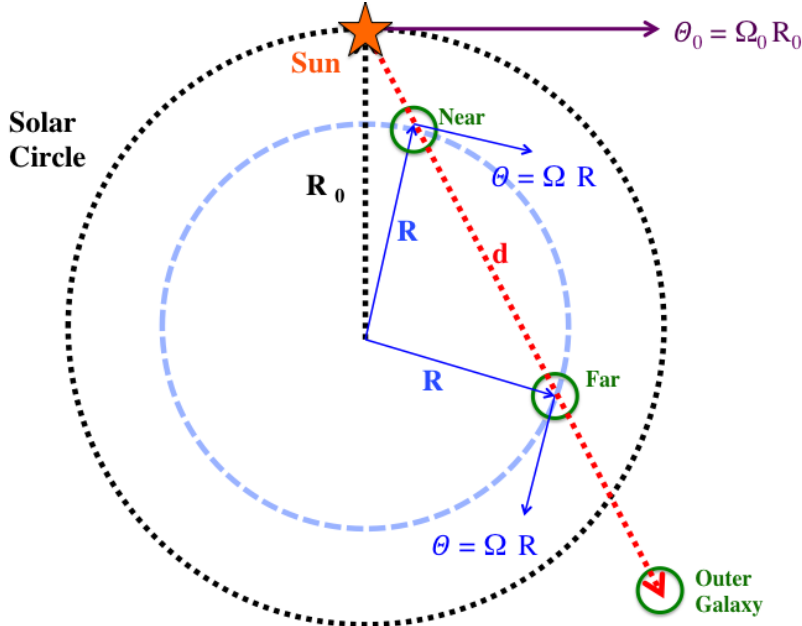


**Figure 1.2:** Top-down schematic of Galactic rotation.

initially conceived as the average between these two, thus being the year-average distance between the Sun and the Earth. However in 2012 it was redefined as exactly 1 AU =  $1.49597870700 \times 10^{11}$  m (Capitaine et al., 2012). A parallax is the change in relative angular displacement of any object due to this motion measured with respect to a fixed reference point (Figure 1.3). If the object is  $d$  parsecs (pc) away from the Sun, then the parallax  $\varpi$  it exhibits will be:

$$\varpi = \frac{1}{d} \quad (1.2)$$

in units of arcsecond (as). The definition is actually the reverse— an object that exhibits a PARallax of 1 arcSECond

Friedrich Wilhelm Bessel measured the first parallax to the star 61 Cygni in 1838 of  $\varpi = 313.6 \pm 20.2$  mas, which implies a distance of  $3.19_{-0.36}^{+0.47}$  pc and within error of the more recent values from *Gaia* of  $\varpi = 286.1457 \pm 0.059$  mas (Gaia Collaboration et al., 2018). Not only does this illustrate the accuracy of the parallax technique, but also the large increase in precision that has been achieved over the previous 1.5 centuries ( $\sim 2.5$  orders of magnitude). For reasons that I will explain soon, trigonometric parallax techniques have an upper limit on the error that allows distance determination so this increase in precision is very important for distant targets. The parallax precision is very much linked to how accurately the position of an object can be determined at each epoch and for an unresolved object this is proportional to the observing instrumentation resolution. The highest angular resolution and therefore positional accuracy that can be regularly achieved is with Very Long Baseline Interferometry (VLBI), however, for reasons I will discuss in Chapter §2 this can typically only be realised when the target is unresolved. For this reason and others, many of the best targets for VLBI astrometry are masers.

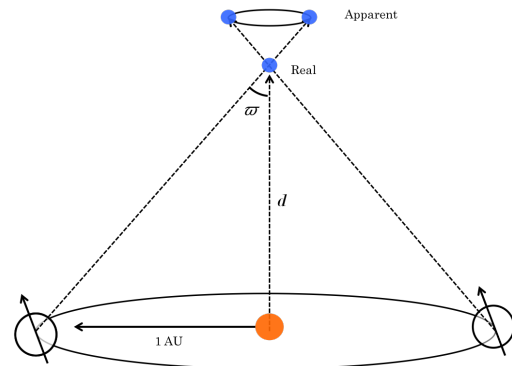


**Figure 1.3:** Simplified schematic of trigonometric parallax for a target source very close to the North Ecliptic Pole. The parallax  $\varpi$  is half the total angle subtended by the Earth as it orbits the Sun when  $d \gg 1$  AU relative to some stationary background.

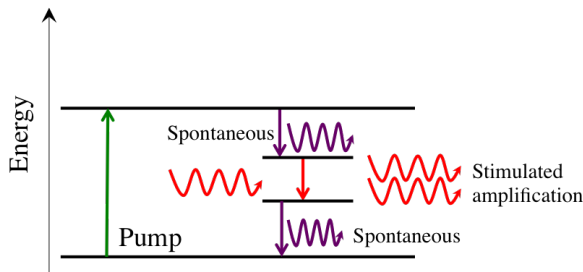


**Figure 1.4:** Simplified schematic of maser action. Molecule is excited by some pumping mechanism (green) to a higher energy state. Spontaneous de-excitation can occur at some transitions (purple), but at some energy level spontaneous emission is unfavourable and the molecule remains in a meta-stable state. Background radiation can stimulate de-excitation, resulting in amplification (red).

## 1.3 Masers

Astronomical masers (originally Maser: Microwave Amplification by Stimulated Emission of Radiation; colloquially *noun*: maser(s), *verb*: masing, to mase, *adjective*: masable) are a physical phenomena that occur in specific conditions in the interstellar medium. While masers predate lasers in laboratory conditions (1953; Gordon et al., 1955, vs. 1960 by T. H., Maiman), they both predate observations of astrophysical masers. The first astrophysical maser discovery did not occur until the 60's, with the OH species around 1.6 GHz. This discovery can be best attributed to Weaver et al. (1965) whom was the first to spectrally resolve the emission and noted the clear departure from local thermodynamic equilibrium (LTE) and now characteristically small line-widths.

In modern astrophysics and astronomy, masers predominantly fall into two areas; analysing maser spectra and multiple transitions infer environmental conditions like magnetic fields, local thermodynamics, stellar environments or star forming regions; and using masers to determine kinematics including outflows, proper motions, Galactic rotation and trigonometric parallax.

### 1.3.1 Theory

Whereas much emission at radio-frequencies for many molecules occurs via spontaneous transitions and can be related to the statistical thermal temperature of the environment, maser emission is due to unmitigated stimulated emission along the line of sight and are therefore very luminous and highly beamed compared to the latter. The initial trigger for masing is some mechanism that excites a molecular species, called the ‘pump’. The nature of the pumping can be anything that can provide adequate energy to excite the molecule into a transitional path con-

### 1.3. MASERS

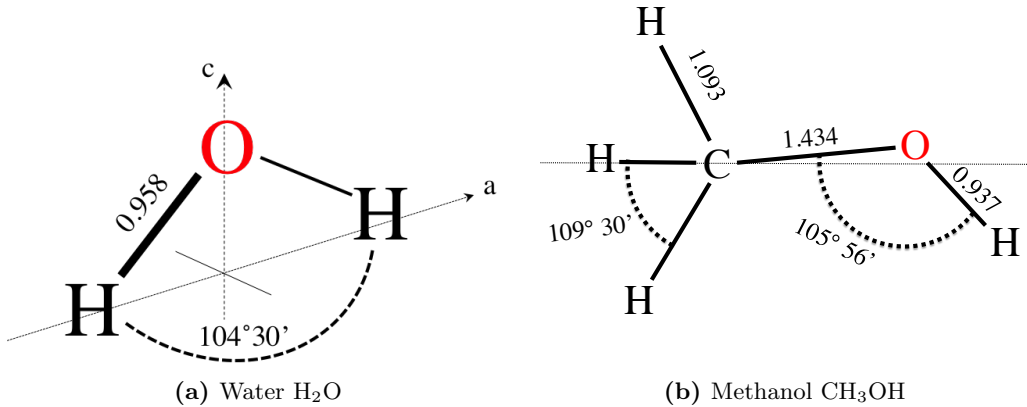


**Figure 1.5:** Molecular structure as obtained from microwave spectroscopy. Bond lengths are in angstroms ( $\text{\AA}$ ).

taining a maser step. Due to a departure from LTE in the environment, the molecular species is unlikely to undergo damping collisions which might otherwise partition the energy. In addition the masable step normally has some selection rules that make spontaneous emission from the upper level ‘forbidden’. This leads to the molecule having an over-representative population in this higher energy level that is inherently unfavourable – called a population inversion. When a suitable background source is introduced, stimulated emission occurs and all the molecules along the line of sight emit largely coherently – the maser. As long as the rate of pumping is greater than the rate of stimulated emission and much greater than the rate of spontaneous emission, population inversion is maintained and the maser can and will persist.

While the background source can be many different phenomena– spontaneous emission from the molecules themselves, Cosmic Microwave Background radiation or some other source of continuum emission, the primary categorical variable that distinguishes masers from one another is the pumping mechanism. The two types of maser that are typically discussed are collisionally or radiatively pumped – one originating from excitation by molecules in a dense or shocked gas environment, the other from suitably energetic constant sources of radiation.

The masers that will be discussed here originate from rotational transitions, the energy of which are determined by the moment of inertia of the molecule and the various possible modes. While this will be briefly discussed below, both Townes & Schawlow (1955) and Gray (2012) are excellent sources for more theoretical, technical and in-depth further reading.

#### 1.3.2 Water

Water is an asymmetric top and has three axis of rotation. It also has three independent vibrational modes of the hydrogen atoms– two stretches and one bend, where only the bend contributes to the energy structure in space and especially at radio frequencies. Therefore rotational energy levels of water are given as  $J_{K_a} K_c$  where  $J$  is the total angular momentum and  $K$  is the angular momentum component in the  $a$  and  $c$  directions (Figure 1.5a).

Finally, water can come in two sub-species – ortho: where the nuclear spins of the two hydrogens are parallel, or para: where the spins are anti-parallel. Only even-even levels exist in para- $\text{H}_2\text{O}$

### 1.3. MASERS

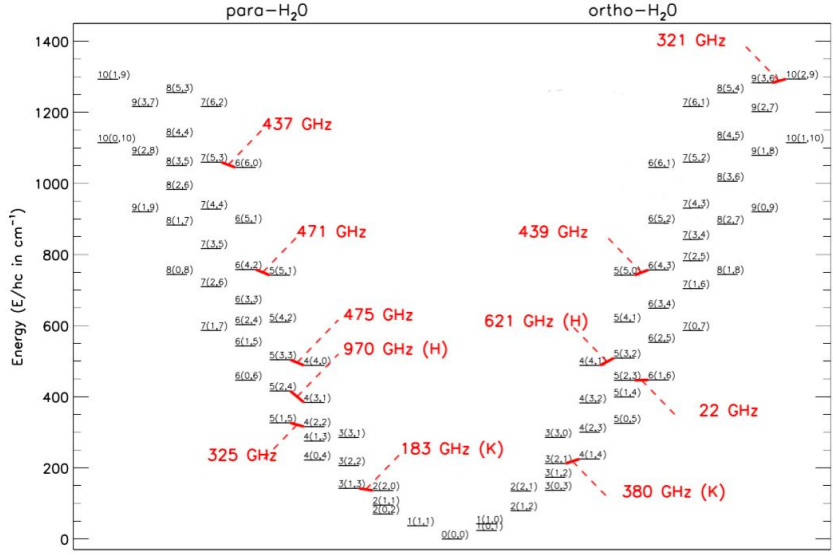


**Figure 1.6:** Lowest rotational energy levels  $J_{K_a K_c}$  for the ground vibrational state of water. **Red:** Common maser transitions and those observed by Kuiper Airborne Observatory (K) and *Herschel* (H) – The most relevant to analysis and discussion in this thesis being the  $J_{K_a K_c} = 6_{16} \rightarrow 5_{23}$  22.2 GHz transition. Adopted from Figure 1. Neufeld et al. (2017).

and even–odd for ortho– $\text{H}_2\text{O}$  (Figure 1.6).

The strongest and most prominent maser transition known is the  $J_{K_a K_c} = 6_{16} \rightarrow 5_{23}$  22.2 GHz transition of ortho– $\text{H}_2\text{O}$ , first detected by Cheung et al. (1969). This transition is well-known for being a shocked gas tracer and is commonly found near High Mass Star Formation Regions (HMSFR) as outflows or water–fountains from late-type stars (e.g. Orosz et al., 2019) and as extremely luminous megamasers in the centre of star forming galaxies (Dos Santos & Lepine, 1979). I discuss and measure trigonometric parallaxes to 22.2 GHz water masers in Chapter §3.

#### 1.3.3 Methanol

The physics of methanol masers is rather complex due to methanol being a 6-atom molecule and it being an asymmetric top with hindered internal rotation. However, due to the energy levels that can be accessed in an interstellar medium only the lowest-energy vibrational-torsional quantum state is typically considered. Within this, the slightly asymmetric nature of methanol leads to the torsion of the –OH tail group about the  $\text{CH}_3$  bond to be split into 2 levels, a non-degenerate  $A$  (+ or – due to parity) and degenerate  $E$ . These two types of methanol have slightly different orientations of the –OH group relative to the  $\text{CH}_3$  group and therefore a different moment of inertia. As such the  $\pm A$  and  $E$  have different rotational energy levels and transitions (Figure 1.7).

The strongest transition for methanol and the second strongest maser transition known is the  $J_K = 5_1 \rightarrow 6_0 A^+$  transition at 6.66851928 GHz (Menten, 1991b). While methanol is divided into two classes based off source of pumping – collisional class I and radiative class II (Menten, 1991a). The 6.7 GHz transition is class II and (to date) unambiguously associated with sites of

## 1.4. S $\pi$ RALS

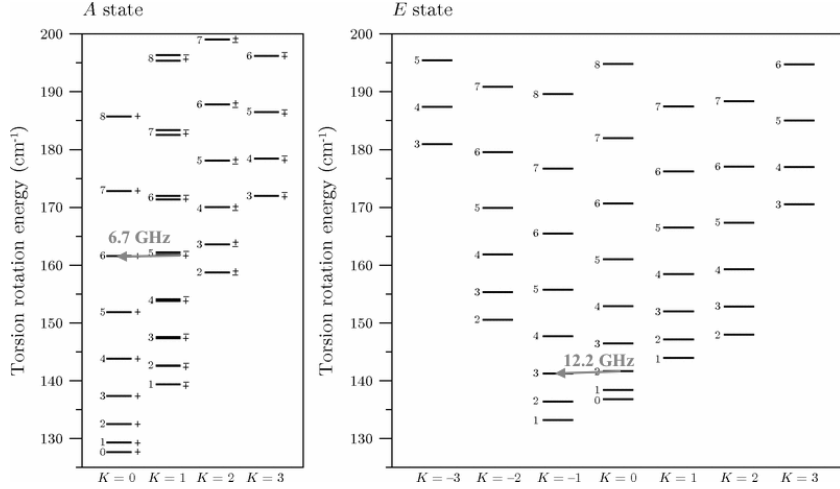


**Figure 1.7:** Lowest rotational energy levels  $J_K$  for the ground vibrational-torsional state ( $v = 0$ ) of  $E$  and  $A$ -type methanol Jansen et al. (2011). Labelled are the  $J_K = 5_1 \rightarrow 6_0 A^+$  6.7 GHz and  $J_K = 2_0 \rightarrow 3_{-1} E$  12.2 GHz transitions relevant to analysis and discussion in this thesis.

HMSF (Ellingsen, 2006; Breen et al., 2013). I discuss and measure a trigonometric parallax to a 6.7 GHz methanol maser in Chapter §3 and model their spatial structure and compactness in Chapter §4.

Other masers, 12.2 GHz class II methanol, OH and SiO masers are mentioned in passing throughout this thesis but are otherwise not relevant for discussion here.

## 1.4 S $\pi$ RALS

### 1.4.1 Mapping the Milky Way

When considering the structure of the Milky Way, one must first consider the primary issue: that we have a limited perspective of its structure from our position inside it. Figure 1.8 is that perspective, the Galaxy as a projection on a sphere, with no immediate way to determine 3D structure.

Although objects can be theoretically resolved into their 2D angular separations and angular sizes with higher resolution telescopes, the absolute sizes or distances of objects along the same line of sight remains impossible to directly observe. In addition, the derived angular sizes and separations are meaningless without a reference scale (standard ruler).

While kinematic distances or dispersion measure techniques add a ‘depth’ axis which can be converted into distance, trigonometric parallax realise the 3D motion and structure of the Galaxy and use that to measure the distance. Therefore trigonometric parallax is the ideal candidate for distance estimates inside the Milky Way, however it was not until the last few decades that optical or VLBI astrometry could achieve the precision necessary to make it an independent mapping tool on the Galactic scale.

Perhaps the earliest quantitative maps of the Milky Way were produced in the mid-50’s, with

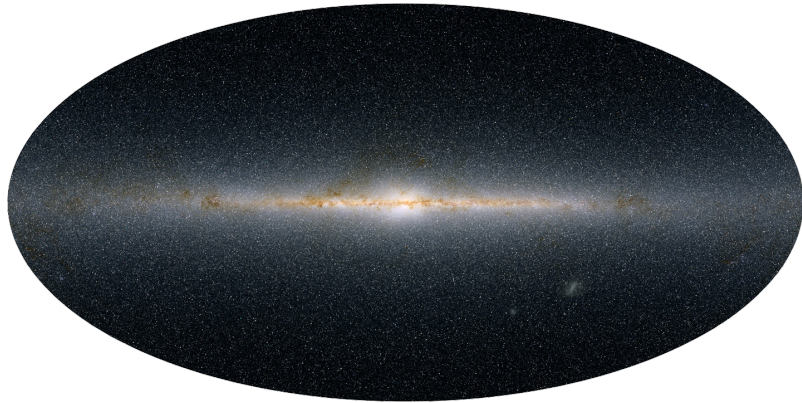


**Figure 1.8:** Mollweide projection of the entire sky as seen by the Two Micron All-Sky Survey (2MASS). The projection is centered on the Galactic Center, taken to be Sagittarius A\*. This point of view represents how the sky appears from the Earth in the Galactic Coordinate system with the centre of the image being  $(l, b) = (0^\circ, 0^\circ)$ . *Atlas image mosaic courtesy of 2MASS/UMass/IPAC-Caltech/NASA/NSF.*

the first complete map by Oort et al. (1958). This work used the emission at 21 cm (due to the spin inversion of neutral hydrogen) to trace out the density distribution of neutral hydrogen throughout the Galactic system. The immediate observation was that the bulk of the neutral medium was confined to a flat disk approximately 220 pc thick. Distances were approximated using kinematic distance techniques and projection of the 21 cm emission/absorption revealed rudimentary spiral structure (see Figure 1.9).

Oort details the nomenclature of some arms: Orion (containing the Sun), Perseus (outside solar circle), and Sagittarius (inside solar circle) and to some extent the 3 kpc arm. Although the names of these arms slightly changed over time, the general locations and associations remained the same. This work stands out as the grounding influence on determinations of Galactic structure, however numerous problems (many outlined by Oort himself) meant that the spiral arms could not be determined with any accuracy using this method.

Following this, perhaps the next notable chapter begins with Georgelin & Georgelin (1976). One of the initial works that outlined a model for the spiral structure of the Milky Way, this work served as a reference for many further works. At the time, radio recombination lines from ionised hydrogen and radio molecular lines had only recently been discovered and extensively observed, in addition to optical data of HII and OB stars in the Southern Hemisphere.

A model of Galactic rotation was initially established by measuring the radial velocities of 151 optical HII regions and spectrophotometric distances to their respective exciting stars. Stellar distances (via spectroscopic parallax) were used wherever they were available, however, when they were unavailable, kinematic distances were calculated using the rotation models derived. Kinematic distance ambiguities were individually removed with reasonable assumptions pertaining to whether the HII region was optically observed (likely near) or not (likely far) in addition to absorption of lines at a higher velocity (far) and vice versa. Combining the optical results with the radio results, a picture of the Galaxy was formed (Figure 1.10). Assuming that the high-excitation HII regions were of higher importance ('brilliant and extended') and hence more readily trace spiral structure (like seen in external galaxies), 80% of the thus-defined HII regions fell along two symmetric pairs of arms with a pitch angle of 12°.

## 1.4. S $\pi$ RALS

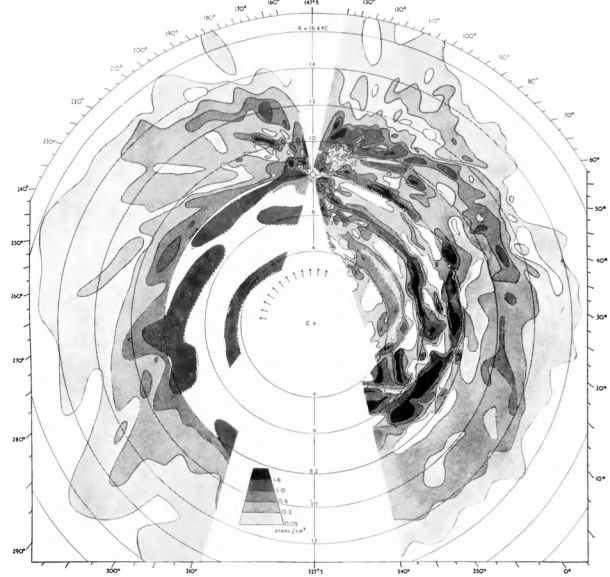


**Figure 1.9:** Figure 4 from Oort et al. (1958). Original caption: *Distribution of neutral hydrogen in the Galactic System. The maximum densities in the z-direction are projected on the galactic plane, and contours are drawn through the points.*

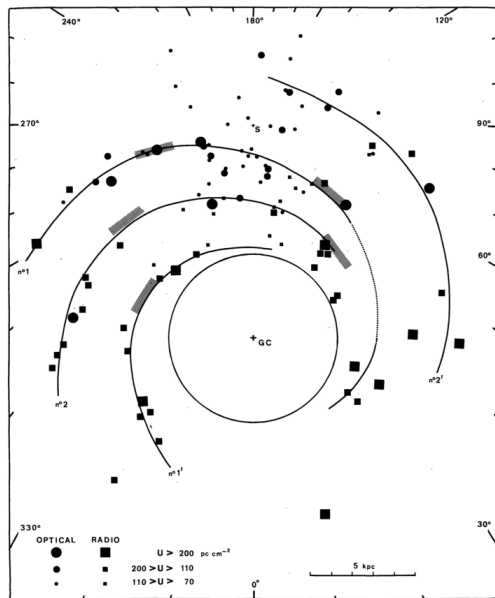


**Figure 1.10:** Figure 11 from Georgelin & Georgelin (1976). Original caption: *Spiral model of our Galaxy obtained from high-excitation-parameter HII regions ( $U > 70 \text{ pc cm}^{-3}$ ); the resulting spiral pattern has two symmetric pairs of arms (i.e for altogether). No. 1 Major arm: Sagittarius-Carina arm; No. 2 Intermediate arm; Scutum-Crux arm; No. 1'. Internal arm: Norma arm; No 2'. External arm: Perseus arm. Hatched areas correspond to intensity maxima in the radio continuum and in neutral hydrogen.*

## 1.4. S $\pi$ RALS

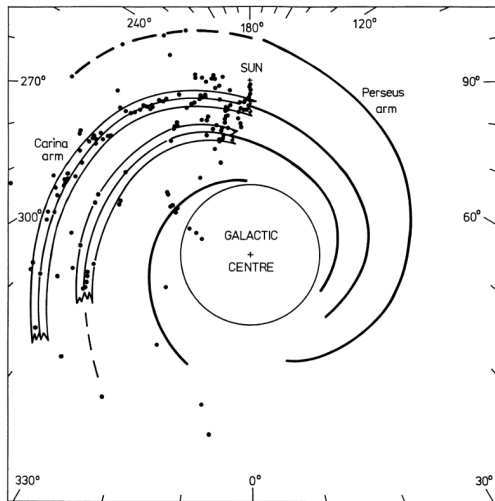


**Figure 1.11:** Figure 5 Caswell & Haynes (1987). Original caption: *Spiral pattern delineated by HII regions in the Galaxy. Individual HII regions from the present work are shown only if there is no distance ambiguity. Two segments of spiral arms derived from the present work are shown with a thickness 1 kpc. ....*

Many works thereafter were based heavily on this work – like Taylor & Cordes (1993), who were able to map the Galactic electron distribution by matching and perturbing arm locations to measurements of dispersion measure. Caswell & Haynes (1987) used HII regions traced by radio recombination lines to map the Southern Hemisphere, calculating kinematic distances and resolving ambiguities with techniques including HI absorption. While they collected independent data they found good agreement with Georgelin & Georgelin (1976) and provided a more refined map of the Southern Hemisphere arm (Figure 1.11).

*Hipparcos* (HIgh Precision PARallax COLlecting Satellite) was an astrometry satellite launched by the European Space Agency (ESA) in 1989 and continued operations until 1993. *Hipparcos* had a median astrometric accuracy of  $\Delta\theta = 0.8$  mas, allowing distances of objects (primarily stars) to be determined up to  $\sim 125$  pc from the Sun (to 10% uncertainty; Perryman et al., 1997). In total, *Hipparcos* reported astrometry for  $\gtrsim 115000$  stars in the local Galaxy.

*Gaia* is ESA’s space astrometry mission – an optical astrometry satellite capable of measuring absolute positions of stars to an accuracy of between  $\gtrsim 4 - 20$   $\mu$ as (depending on magnitude and band; Perryman, 2002). Launched in 2013, *Gaia* is the direct successor to *Hipparcos* and will end its mission sometime after 2022, after which time it is expected to have measured astrometry for over  $\sim 1 \times 10^9$  stars.

### 1.4.2 BeSSeL and VERA

Bar and Spiral Structure Legacy (BeSSeL) survey was an US National Radio Astronomy Organisation (NRAO) Very Long Baseline Array (VLBA) large project. The core aim of BeSSeL was to map the Northern Hemisphere spiral structure of the Milky Way via trigonometric parallaxes of 22.2 GHz water and 6.7 GHz/12.2 GHz class II methanol masers (Brunthaler et al., 2011; Reid et al., 2009a, 2014, 2019). The VLBA consists of  $10 \times 25$  m radio telescopes with a maximum baseline of  $\sim 8600$  km. The long baselines combined with well-calibrated, optimal sampled data allowed an expected astrometric accuracy  $\Delta\theta \sim 10$   $\mu$ as, bringing the distant Galaxy ( $d \gtrsim 10$  kpc) into sharper focus.

VLBI Exploration of Radio Astrometry (VERA) was a Northern Hemisphere VLBI array/project

## 1.4. S $\pi$ RALS

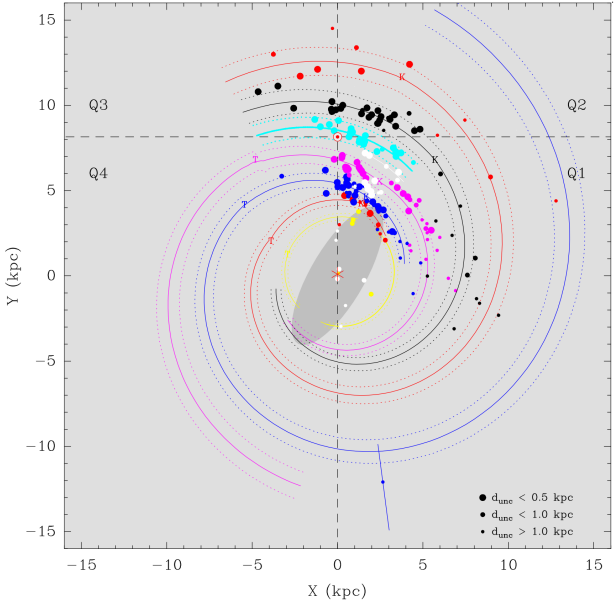


**Figure 1.12:** Figure 1 from Reid et al. (2019) including BeSSeL and published–VERA parallaxes. Plane–view of the Milky Way where Galactic rotation is clockwise. Spiral arms are fit to inverted parallaxes (dots: size inversely proportional to distance uncertainty)– **Cyan**: Local arm; **blue**: Scutum–Centaurus-OSC arm; **black**: Perseus arm; **purple**: Sagittarius–Carina arm; **yellow**: 3 kpc arm(s); **red**: Norma–Outer arm; **white**: unclear/spur.

dedicated to maser astrometry by the National Astronomical Observatory of Japan (NAOJ). VERA (interferometer) is comprised of  $4 \times 22$  m radio telescopes spread over Japan with a maximum baseline of 2300 km. Despite this, it is also the only VLBI array dedicated to phase–reference astrometry. To this effect, they utilise a unique ‘dual–beam’ receiver system where simultaneous observations of target masers and reference quasars can be conducted, which greatly minimises the ambiguity of calibrating tropospheric line–of–sight effects (Honma et al., 2003).

VERA targets water masers tracing star forming regions, but also SiO masers tracing evolved stars. The former boasts results with astrometric accuracy comparable to BeSSeL (Reid et al., 2019; VERA Collaboration et al., 2020).

Combined, the two Northern Hemisphere maser–astrometry surveys have measured over 200 maser parallaxes and mapped the 1st, 2nd and 3rd Galactic quadrants Figure 1.12. It is clear from Figure 1.12, that the 4th Galactic quadrant is heavily under-represented.

### 1.4.3 Southern Hemisphere – S $\pi$ RALS

The Southern Parallax Interferometric Radio Astrometry Legacy Survey (S $\pi$ RALS – pronounced ‘spirals’) in an emerging Australian–led maser astrometry project. While first announced in September 2018 (at the Cagliari Maser IAUS; Hyland et al., 2018), the first iteration of S $\pi$ RALS dates back to pre–2010 – with the first epoch on the then V255 project observed March 30<sup>th</sup> 2008 on the Australian Long Baseline Array (LBA). This project is responsible for the first Southern Hemisphere parallax (Krishnan et al., 2015) and consequent works including Krishnan et al. (2017) and Sanna et al. (2015).

As briefly discussed, parallax inversion requires an astrometric accuracy of  $\frac{\Delta\varpi}{\varpi} < 0.2$  and in the LBA parallax reduction by Krishnan et al. (2015, 2017), authors report an astrometric accuracy of  $80 – 150 \mu\text{as}$ . At this uncertainty, maser distances are required to be  $d < 1.3 – 2.5$  kpc which severely limits the mapping capability of maser astrometry.

#### 1.4. S $\pi$ RALS

The LBA observations of Krishnan et al. (2015, 2017) had a maximum baseline length of approximately  $B = 3500$  km which implies a synthesised beam size of  $\theta_B = 3$  mas at 6.7 GHz. Taking into account the  $\text{SNR} > 100$  detections of relevant quasars and target maser in images, per-epoch thermal astrometric uncertainty ( $\Delta\theta_T \approx \frac{1}{2} \frac{\theta_B}{\text{SNR}}$ ; Reid & Honma, 2014) is around  $\Delta\theta_T = 15\mu$  as. If I assume (incorrectly) optimal parallax sampling over the 5 epochs there should be  $\Delta\theta = 2\Delta\varpi$  as one measures twice the parallax between two maxima. This leaves an apparent  $\Delta\theta \geq 0.3$  mas per-epoch systematic uncertainty.

If I assume that this parallax uncertainty is solely due to residual ionospheric delays between target and calibrator (average separation  $\theta_{sep} = 2.5^\circ$ ;  $\Delta\theta = \theta_{sep} \frac{\Delta\tau}{|B|}$ ;  $\tau_{iono} = 40.3 L_e \nu^{-2}$ ) there would be a minimum of 10 TEC units residual ionosphere per epoch. This is at the upper end of what is expected by Walker & Chatterjee (1999) and likely implies a combination of residual ionosphere and poorly constrained tropospheric and clock delays due to limited available bandwidth in those observations (see Krishnan et al., 2015, for more details).

The final issue is poor parallax sampling. Although I will introduce the relevant equations and theory in Chapter §2 at this point I can say that due to non-preferential scheduling availability on the LBA, astrometric epochs did not necessarily align with peak parallax peaks or sample the parallax curve optimally. This leads to a parallax sensitivity reduction of approximately a factor of 2.

Therefore to measure trigonometric parallaxes in the southern sky it was decided that a Southern Hemisphere trigonometric parallax array was necessary; with appropriate frequency coverage, availability, ionospheric calibration techniques and target pre-selection.

The AuScope array (Lovell et al., 2013) is an existing S/X geodetic array comprised of Hobart 12m, Katherine 12m and Yarragadee 12m. It operates as part of the International VLBI Service (IVS) with a downtime of approximately  $\sim 100$  days/year that is available for parallax observations. Ceduna 30m (McCulloch et al., 2005) operates as part of the LBA with an uptime of only a few weeks/year and therefore the array will be the AuScope–Ceduna Interferometer (ASCI; Figure 1.13) with a maximum baseline of  $B \approx 3500$  km. A possible extension to the array is the Warkworth 30m telescope, owned and operated by the Institute for Radio Astronomy and Space Research (IRASR), which would extend the maximum baseline up to  $B \approx 5500$  km or  $B_\lambda = 120 M\lambda$  at 6.7 GHz.

With Hobart and Katherine upgraded to wide-C band capable receivers (completed in 2017 and 2019 respectively), Yarragadee scheduled for upgrade and Ceduna/Warkworth with pre-existing C-band capabilities but planned wideband upgrades, S $\pi$ RALS aims to measure dozens of trigonometric parallaxes towards High Mass Star Formation regions traced by 6.7 GHz class II methanol masers over the next 3 years.

## 1.4. S $\pi$ RALS

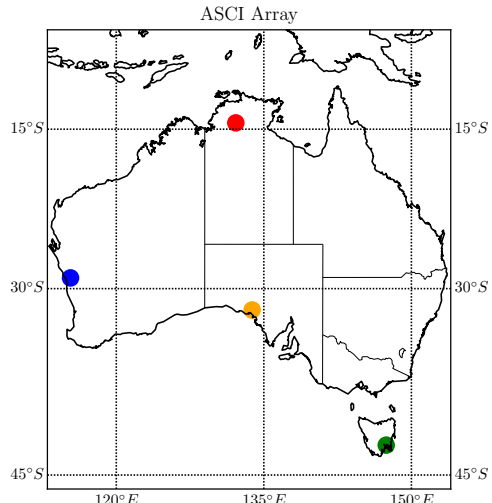


**Figure 1.13:** The AuScope–Ceduna Interferometer formed with telescopes at Ceduna (yellow), Hobart (green), Katherine (red) and Yarragadee (blue). All radio telescopes are owned and operated by the University of Tasmania.

This thesis aims to answer the questions of target selection, ionospheric calibration and methodology relevant to accomplishing this goal: Chapter §2 goes over appropriate theory and methodology of VLBI astrometric calibration; Chapter §3 demonstrates said calibration via the reduction and analysis of recent BeSSeL VLBA data and determination of new distances towards the Perseus spiral arm; in Chapter §4 I reduce and analyse LBA data to determine target selection for the S $\pi$ RALS project and to determine Southern Hemisphere methanol maser compactness properties; Chapter §5 discusses atmospheric calibration techniques and introduces MultiView and in Chapter §6 I observe, calibrate and test inverse MultiView calibration and contrast it against traditional phase referencing.



#### 1.4. S $\pi$ RALS

# 2

## VLBI ASTROMETRY AND CALIBRATION

Astrometry is the science of accurately positioning objects in the sky and Very Long Baseline Interferometry (VLBI) currently boasts the highest regularly achievable angular resolution and therefore the highest possible positional accuracy. In this chapter I will review the calibration techniques necessary to achieve this high positional accuracy, the relevant theory and discuss why the highest precision is required for trigonometric parallax. I will also introduce and justify additional modified calibration techniques used throughout the data analysis presented in Chapter 3 and 4, and finish with a summary of steps needed to calibrate VLBI data for astrometry.

## 2.1 Introduction

This chapter presents specific details about the multiple aspects of VLBI calibration required to obtain high accuracy astrometry necessary for determining Galactic-scale distances. The following topics are discussed:

- Section §2.2 establishes how and why distance determination in the Galaxy via trigonometric parallax is dependent on astrometric uncertainty and delay calibration;
- Section §2.3 begins discussion of the delay calibration process from the correlation stage and as it continues into the data reduction process;
- Section §2.4 introduces phase referencing and discusses atmospheric calibration not included in Section §2.3;
- Section §2.5 defines amplitude calibration techniques that are used in this thesis;
- Section §2.6 discusses parallax determination from astrometry, parallax sampling and proper motions;
- Section §2.7 contains a practical summary of astrometric VLBI calibration that is applied in Chapter 3 and Chapter 6.

## 2.2 Distance and Astrometric Uncertainty

### 2.2.1 Determination of distance

A given parallax,  $\varpi$ , with an uncertainty  $\sigma_\varpi$  yields a distance  $d$  with some upper and a lower bound. Since there are more objects (for a uniform distance distribution) outside than inside the distance range (because of the different sampled volumes) a higher number of objects from outside the distance range will scatter in than the number from inside scattering out. A source can have a measured parallax  $\varpi \pm \sigma_\varpi$  when it has a true parallax  $\varpi_T$  such that the probability distribution of detecting the correct parallax is:

$$P(\varpi) = \frac{1}{\sqrt{2\pi}\sigma_\varpi} \exp\left(-\left(\frac{\varpi - \varpi_T}{2\sigma_\varpi}\right)^2\right)$$

This Gaussian distribution is symmetric in  $\varpi$ , with the  $[0, \varpi_T + \sigma_\varpi]$  and  $[\varpi_T - \sigma_\varpi, 0]$  ranges having equal area and is strongly peaked about the mean/mode  $P(\varpi_T)$ . However using traditional Taylor expansion methods to estimate the error in  $d$  ( $\sigma_d$ ) would yield:

$$\begin{aligned} d &= \frac{1}{\varpi} \\ \implies \sigma_d &= \left| \frac{d(1/\varpi)}{d\varpi} \sigma_\varpi \right| = \frac{\sigma_\varpi}{\varpi^2} \end{aligned}$$

and systematic underestimation in the error for  $d$ . Figure 2.1 shows the effect of increasing  $f$  on the (relative) probability of determining to incorrect distance  $P\left(\frac{1}{\varpi} - \frac{1}{\varpi_T}\right) / \frac{1}{\varpi_T}$ . At  $f \geq 0.2$  is would not be uncommon to determine a distance that was off by a factor of 2.

## 2.2. DISTANCE AND ASTROMETRIC UNCERTAINTY

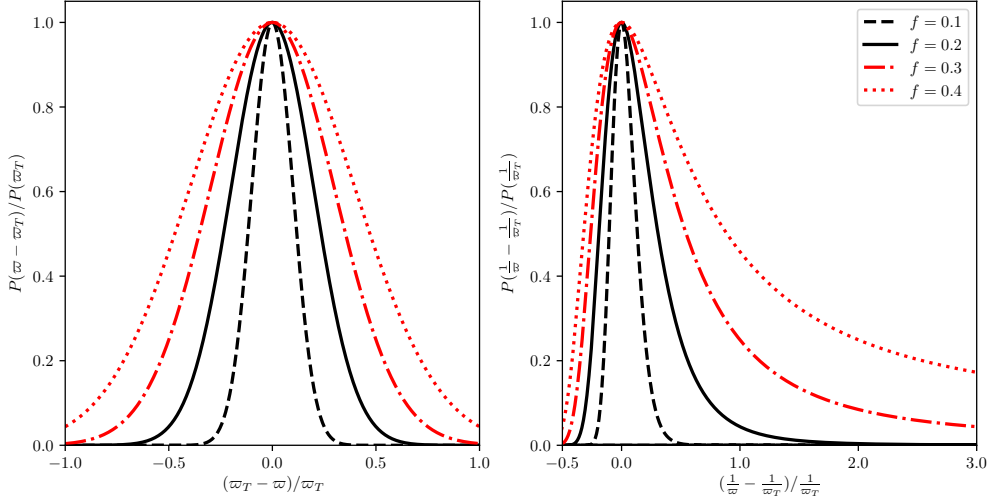


**Figure 2.1:** Parallax to distance asymmetry as a function of fractional uncertainty  $f$ . **Left:** Parallax probability distribution  $P$  against parallax  $\varpi$  as a function of fractional parallax uncertainty  $f$ . X-axis is centred on and normalised by true parallax  $\varpi_T$ , y-axis is similarly centred and scaled by  $P(\varpi_T)$ . **Right:** Distance probability distribution against centred, scaled distance as a function of  $f$ . This effectively demonstrates (unnormalised) probability of fractional distance error given  $f$ .

It is reported that this effect causes a systematic bias where measured parallaxes will on average yield too small distances (Lutz & Kelker, 1973) and this effect is only a function of fractional parallax error  $f = \frac{\sigma_\varpi}{\varpi}$ , not total parallax. However Lutz & Kelker (1973) specifically concerns inverting stellar parallaxes in a magnitude limited sample.

In a more practical vein, Bailer-Jones (2015) determines that the optimal way to determine distance from parallax is to not only consider the non-linearity of the parallax-to-distance conversion but to truncate and modulate the probability distribution to consider realistic Galactic sizes. Nevertheless, at  $f = 0.1$  the effect is negligible, there is a turnover point at  $f = 0.25$  and at  $f = 0.5$  no answer can be reasonably determined. This generally puts an upper limit of  $\sim 10\%$  on fractional uncertainty.

In the Galaxy, we expect masers to be anywhere from 0.4 (e.g. Orion nebula) to 20 kpc away (Sanna et al., 2017) with a reasonable upper-median estimate of 10 kpc. Such a maser will have a trigonometric parallax of 0.1 mas and for a reasonable fractional uncertainty of  $\frac{\sigma_\varpi}{\varpi} = 10\%$  it is required that  $\sigma_\varpi = 10 \mu\text{as}$ . The positional uncertainty required to detect this parallax in multiple epochs is  $\sigma_\theta \lesssim 20 \mu\text{as}$  and the only way to regularly achieve this positional accuracy is with VLBI astrometry.

As I will introduce soon, the path delay between two elements in an interferometer due to a positional offset  $\Delta\theta$  goes as  $\tau_\theta \approx \Delta\theta \frac{|B|}{c}$  where  $|B|$  is the baseline. Therefore in order to detect the delay due to a very small position offset aka a trigonometric parallax, the interferometric delay needs to be calibrated very accurately.

## 2.3 Delay Calibration

### 2.3.1 Correlation

The correlation stage is the first point of reduction and pre-calibration for any VLBI data set. Baseband data is taken from a pair of telescopes and correlated to form a visibility data product:

$$\bar{V}_{jk}(t, \nu) = V_{jk}(t, \nu)e^{-2\pi\phi_{jk}(t, \nu)} \quad (2.1)$$

where  $V_{jk}(t, \nu)$  is the normalised visibility amplitude and  $\phi_{jk}(t, \nu)$  is the phase for baseline  $B_{jk}$  at time  $t$  and frequency  $\nu$ . The visibility  $\bar{V}_{jk}(t, \nu)$  is produced for each baseline, at each time step ( $m$ ) for  $t = t_{int}m$  and each frequency step (channel,  $n$ ) for  $\nu = n\Delta\nu + \nu_{ref}$ . The fundamental relationship between phase  $\phi$ , frequency  $\nu$  and delay  $\tau$  is:

$$\phi = 2\pi\nu\tau \quad (2.2)$$

such that the output phase from the correlator tracking changes will be:

$$\begin{aligned} \phi(t, \nu) &= \frac{\partial\phi}{\partial t}(t - t_0) + \frac{\partial\phi}{\partial\nu}(\nu - \nu_{ref}) \\ &= \dot{\tau}(t - t_0) + \tau(\nu - \nu_{ref}) \end{aligned} \quad (2.3)$$

where I now only have the delay  $\tau$  (units s) and delay-rate/rate  $\dot{\tau}$  (units s/s). Therefore the delay and the instantaneous rate that it changes are the fundamental variables to correct in visibility data.

The measured delay ( $\tau_m$ ) is comprised of many different effects added in series:

$$\tau_m = \tau_{geo} + \tau_{tr} + \tau_{iono} + \tau_{cl} + \tau_e + \tau_\theta + \tau_\sigma + \tau_{th} \quad (2.4)$$

where I have (in order) the delay due to: geometry, troposphere, ionosphere, clock offset, electronics, target position, target structure and thermal uncertainty.

In practice, many of these effects are partially removed in the correlation stage as there is always a delay detection threshold between two adjacent channels. For a correlated frequency step (channel width) of  $\Delta\nu$  and a delay of  $\tau$ , the phase difference between two adjacent channels ( $\delta n = 1$ ) has to be much less than a wrap in phase (aka  $\Delta\phi = 2\pi$ ) otherwise no delay can be determined. As such it has to be the case that:

$$\begin{aligned} \Delta\phi &= 2\pi\tau(n_2\Delta\nu + \nu_0 - n_1\Delta\nu - \nu_0) \ll 2\pi \\ \therefore \tau\Delta\nu &\ll 1 \end{aligned}$$

with  $\tau$  in seconds and  $\Delta\nu$  in cycles/Hertz. Delays of order  $\tau \sim 1$  ms would require extremely high spectral resolution which requires more computational time and storage space for visibility products.

In general the delays corresponding to baseline geometry, troposphere and clock offset have their bulk effects removed in the correlation stage such that the remaining residual delays have magnitude  $|\tau_m| \lesssim 10$  ns.

## 2.3. DELAY CALIBRATION

### 2.3.2 Geodetic and Source Position Delay

The largest source of pre-correction delay in a VLBI array is the geodetic delay due to the baseline geometry. For a baseline  $\mathbf{B}$ , when an observed source has some distance  $d$ , if  $d \gg |\mathbf{B}|$  then the wavefronts approaching the baseline can be considered plane parallel to good approximation. The time delay between the signal arriving at one antenna w.r.t the other will be:

$$\tau_{geo} = \frac{\hat{\mathbf{s}} \cdot \mathbf{B}}{c} \quad (2.5)$$

where  $\hat{\mathbf{s}}$  is the direction of the radiation,  $\mathbf{B}$  is the baseline vector in metres and  $c$  is the speed of light (Figure 2.2).

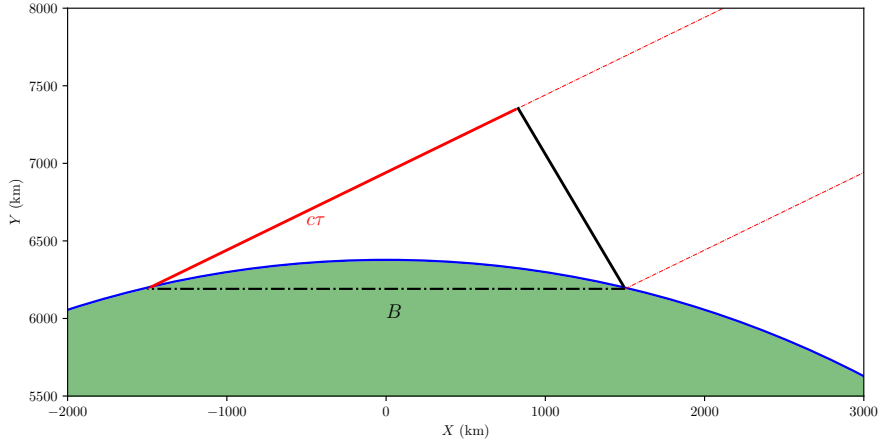


**Figure 2.2:** To-scale diagram of the geometric delay encountered for 2 telescopes separated by  $|\mathbf{B}| = 3000$  km observing a target source at  $\theta = 30^\circ$  to the baseline vector. In this example the measured delay (red) will be  $c\tau \approx 2600$  km or  $\tau = 8.67$  ms.

Antenna positions are defined on a Cartesian grid with the centre of mass of the Earth at  $(X, Y, Z) = (0, 0, 0)$ ,  $XY$ -plane defined by the equator (latitude  $0^\circ$ ) and  $XZ$ -plane defined by the prime meridian at Greenwich (longitude  $0^\circ$ ). Since this is a fixed reference frame and tectonic plate movement is not accounted for, ‘positions’ on the Earth are time variable and are also denoted a velocity  $\dot{X}$  etc. The baseline between antenna 1 and 2 is the instantaneous difference in the positions:

The correlation process is able to use *a priori* antenna positions and velocities to model  $\mathbf{B}$  and to account for the changes. Error in the geodetic delay due to antenna position uncertainty is a function of observed target position  $(\alpha, \delta)$ , observational sidereal time  $(t_{lst})$  and is given by:

$$c\Delta\tau_{bl} = \Delta B_x \cos(t_{lst} - \alpha) \cos \delta - \Delta B_y \sin(t_{lst} - \alpha) \cos \delta + \Delta B_z \sin \delta \quad (2.6)$$

where  $\Delta B_x, \Delta B_y, \Delta B_z$  are the baseline uncertainties in the  $X, Y, Z$  directions and  $c\Delta\tau_{bl}$  is in metres. If the relative magnitudes of the uncertainties are equal then the equation can be reduced to:

$$c\Delta\tau_{bl} \approx |\Delta B|$$

over the whole sky to a good approximation.

### 2.3. DELAY CALIBRATION

Often tied in with the geodetic delay is the delay due to target source positional uncertainty:

$$\begin{aligned} c\tau_\theta &= \sigma_\alpha \cos \delta ( B_x \sin(t_{lst} - \alpha) + B_y \cos(t_{lst} - \alpha) ) \\ &\quad + \sigma_\delta ( -B_x \cos(t_{lst} - \alpha) \sin \delta + B_y \sin(t_{lst} - \alpha) \sin \delta + B_z \cos \delta ) \\ &\leq \sigma_\theta |\mathbf{B}| \end{aligned} \quad (2.7)$$

where  $\sigma_\alpha$  and  $\sigma_\delta$  are the associated errors in the Right Ascension and Declination components of the target source position and  $\sigma_\theta = \sqrt{\sigma_\alpha^2 + \sigma_\delta^2}$ . Unlike the geodetic delay which varies slowly over the day with delay-amplitudes given by the component errors, the rate of change in delay due to a source positional offset is a strong factor of baseline length:

$$\begin{aligned} c\dot{\tau}_\theta &= \sigma_\alpha \cos \delta ( B_x \cos(t_{lst} - \alpha) - B_y \sin(t_{lst} - \alpha) ) \\ &\quad + \sigma_\delta ( B_x \sin(t_{lst} - \alpha) \sin \delta + B_y \cos(t_{lst} - \alpha) \sin \delta ) \end{aligned} \quad (2.8)$$

and longer baselines will have a greater delay and much greater rate.

The science of geodesy is able to solve for source and antenna positions simultaneously using absolute astrometry. Over the past decade the International VLBI Service (IVS) has performed regular observations of quasars and catalogued the International Celestial Reference Frame (ICRF). They are able to measure baseline lengths and quasar positions up to  $\Delta B = 1$  cm and  $\sigma_\theta \geq 0.1 - 0.3$  mas and the Earth Orientation Parameters (EOPs) – a documentation of various irregularities to the Earth's rotation which are applied directly to VLBI data to correct for those effects.

The high precision achieved for quasar positions are due to the regular IVS observations and averaging the results (which is fine for stationary objects like quasars). The positional accuracy at a certain epoch will be dependent on the final residual delay:

$$\sigma_\theta \approx \frac{c\Delta\tau}{|\mathbf{B}|} \geq 0.6 \text{ mas} \quad (2.9)$$

from Equation 2.7 if  $|\mathbf{B}| = 3500$  km and  $c\Delta\tau \geq 1$  cm. As this accuracy is 1–2 orders of magnitude too low for accurate trigonometric parallax estimation, we require relative astrometry which I will cover in Section §2.4.1.

#### 2.3.3 Electronic and Clock Offset Delays

No radio telescope or consequent signal path is identical and differences in propagation time through cables and devices will cause a bulk electronic delay relative to the other telescopes in the array ( $\tau_e$ ). In fact this delay is expected to be slightly different for each recorded intermediate frequency (IF) at a telescope due to small but measurable differences in paths and/or phase offsets in the local oscillators.

Each radio telescope time stamps recorded data using internal clocks phase-locked to a time and frequency standard (usually a hydrogen maser), making them theoretically accurate to the Allen standard deviation of the masers  $\sigma_A \sim 10^{-15}$  s/s. However as each maser is independent they gain and lose time at a constant and measurable rate with respect to each other, equivalent to multiples of  $\sigma_A$  or  $\sim 1$  ns/day. As 1 ns is equivalent to  $\sim 30$  cm or  $\sim 20$  mas, this effect is very important to measure and to take into account.

When all telescopes are referenced to one antenna in the array, all the clocks drift linearly w.r.t

### 2.3. DELAY CALIBRATION

this antenna. Therefore the bulk electronic delay and clock offset rate can be subtracted by fringe searching and linear clock-fitting in the correlation stage. Post-correlation, electronic delay residuals are expected to be  $|\delta\tau_e| \lesssim 100$  ns and the clocks can be estimated and removed to  $|\delta\dot{\tau}_{clock}| < 10^{-15}$  s/s provided that there have been multiple observations of strong ‘fringe finder’ sources over the course of an experiment. While there will always be a measurement residual, theoretically clock electronic delays could be removed to the level of pre-reduction levels ( $c\delta\tau \sim 1$  cm) at the correlation stage, but in practice this is tedious and time-consuming as it would require a high spectral resolution and additional correlator passes. In practice there are post-correlation techniques to subtract residuals for both clock and electronic delays down to the detection limit. Correlator model is moderately accurate such that there is no negative impact on the quality of final data products by using this simple two step process.

During reduction, further electronic delay calibration is performed with what is referred to as a *manual phase calibration*. The antennas are ‘synced-up’ at some point in time to remove their individual electronic delay component (which is expected to be constant over the observational period). For this purpose, delays are solved on a strong quasar target that is observed simultaneously by all telescopes. Application of this solution will remove electronic delays.

All telescopes as part of the ASCI array use Vremya-CH 1005 Hydrogen masers\* as frequency standards.

#### 2.3.4 Additional Delays

The final causes of path delay are attributed to the atmosphere (troposphere and ionosphere), source structure and general thermal uncertainty. I will discuss atmospheric delay and consequent calibration schemes in Section §2.4.

Source structure can also add delay ( $\tau_\sigma$ ). For a point source, where we know the position accurately there will be no contribution from source structure. However, for any non-point like object some of the emission comes from locations away from the phase centre (nominal position of the source) and hence will impact the delay in a way that depends on intensity distribution of the emission from the source.

Delay/phase tied to target structure is the only antenna-independent observable and therefore effectively reduced by self-calibration. This is important as unlike the other delays addressed before and hereafter, delay introduced by resolved target structure cannot be reduced by phase referencing. While delay uncertainty due to structure can be reduced by self-calibration, care must be taken to apply solutions to calibrator and target identically. Therefore to obtain the best astrometry it is always best to carefully select targets or calibrators that do not have significant structure.

Thermal noise ( $\tau_{th}$ ) is unable to be calibrated. This is not typically considered a limiting factor as it due to stochastic processes and in final astrometric products takes the form of a positional accuracy ( $\sigma_{th}$ ):

$$\sigma_{th} = \left( \frac{4}{\pi} \right)^{\frac{1}{4}} \frac{\theta_b}{\sqrt{8 \ln 2}} \frac{1}{SNR} \text{ rads} \quad (2.10)$$

where  $SNR$  is the signal-to-noise for detection and  $\theta_b = \lambda/B$  is the synthesised beam size for the interferometric array (Reid et al., 1988). For small  $\theta_b$  (large arrays) and high  $SNR$  detections,  $\sigma_{th}$  can be reduced far below the expected error introduced by other sources of delay.

---

\*[www.vremya-ch.com/english/product/](http://www.vremya-ch.com/english/product/)

## 2.4. CALIBRATING FOR THE ATMOSPHERE

For the ASCI Array, maximum baseline is  $|\mathbf{B}| \sim 3500$  km and observing frequencies 6.7 and 8.4 GHz give synthesised beam size of  $\theta_b = 2.6$  and 2.0 mas. For detections in final images  $\text{SNR} \geq 100$ ,  $\sigma_{th} \leq 52$  and  $40\mu\text{as}$  respectively.

## 2.4 Calibrating for the Atmosphere

The atmosphere can be broadly divided into three components: the non-dispersive dry/wet troposphere and the dispersive ionosphere. All three components contribute a large, dynamic delay into target visibilities, which can change drastically over various lines-of-sight and rapidly cause large loss of  $SNR$  and astrometric uncertainty.

### 2.4.1 Phase Referencing

Hereafter I will refer to VLBI astrometry with the expectation that phase referencing has/will be performed. Phase referencing astrometry is the narrow-field case of measuring relative position/phase differences between a target and calibrator, separated by some angular distance  $\theta$ . The general idea is that as long as  $\theta$  is kept small, atmospheric contributing effects to the delay along a line-of-sight (LOS) will be identical. If there is a calibrator with a measured delay  $\tau_C$  at time  $t_i$ , this delay can be applied/subtracted from target data/delay  $\tau_T$  at time  $t_{i+1}$ . The delay in target data is present whether detectable or not (e.g in the case of masers there is a delay in data but as a line source delay is impossible to measure) and the various forms of delay subtract:

$$\begin{aligned}\tau_T(t_{i+1}) - \tau_C(t_i) &= (\tau_{bl,T} - \tau_{bl,C}) + (\tau_{tropo,T} - \tau_{tropo,C}) + (\tau_{iono,T} - \tau_{iono,C}) \\ &\quad + \delta\dot{\tau}_{clock}(t_{i+1} - t_i) + (\delta\tau_e - \delta\tau_e) + (\tau_{\theta,T} - \tau_{\theta,C}) + (\tau_{\sigma,T} - \tau_{\sigma,C}) + \tau_{th} \quad (2.11) \\ &= \Delta\tau_{bl} + \Delta\tau_{tropo} + \Delta\tau_{iono} + \tau_{\theta,T} - \tau_{\theta,C} + \tau_{th}\end{aligned}$$

where  $\delta\tau$  signifies an effect that is a residual due to previously being partially accounted for.

The strong assumptions are that: for pre-calibrated effects  $\delta\tau_e, \delta\dot{\tau}_{clock}$ , while there are residuals they will be small and not change by any significant amount between  $\Delta t = t_{i+1} - t_i$ ; the structure of target and calibrator are non-existent or subtracted with self-calibration then  $\tau_{\sigma,1} \approx \tau_{\sigma,2} \approx 0$ ; the positional uncertainty of the calibrator  $\tau_{\theta,C}$  will appear as a small constant offset in consecutive epochs. This can be easily achieved for compact quasar calibrators or compact target masers.

Therefore I am left with only the tropospheric, ionospheric and baseline-based delay differences and the accuracy to which they can be removed. Taking Equation 2.6, phase referencing has the effect to reduce the baseline uncertainty by:

$$\Delta\tau_{bl} = \frac{|\bar{\mathbf{s}}_2 - \bar{\mathbf{s}}_1| |\Delta B|}{c} \approx \theta_{sep} \frac{|\Delta B|}{c} \quad (2.12)$$

which is equivalent to a position error of

$$\Delta\theta \approx \theta_{sep} \frac{|\Delta B|}{|B|} \geq 0.01 \text{ mas}$$

## 2.4. CALIBRATING FOR THE ATMOSPHERE

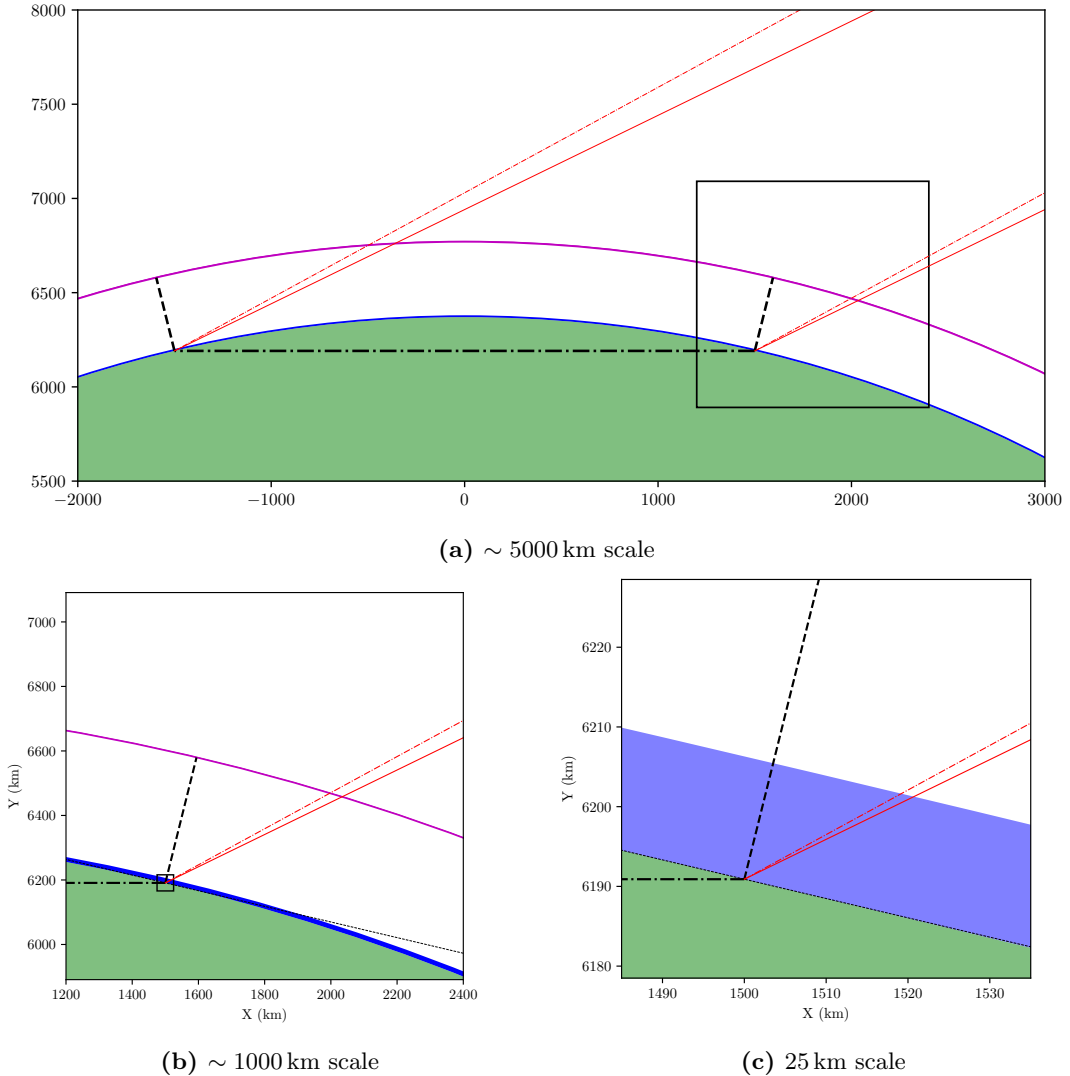


**Figure 2.3:** Diagrammatic representations of the true VLBI and atmospheric scales present for a VLBI baseline. Baseline length is  $B = 3000$  km (black dot-dashed line). Magenta line represents the thin ionosphere ( $\sim 10$  km approximation) at a height of 400 km above the Earth's surface and red lines are lines-of-sight from each element towards the two targets (solid and broken). Black dashed lines are local zenith for respective baseline elements. Respective rays are parallel due to target distance.

if  $\theta_{sep} \geq 1$  deg,  $|\Delta B| = 1$  cm and  $|\mathbf{B}| = 3500$  km. In the next few sections I will discuss the possible ways to use phase referencing observations to reduce the tropospheric and ionospheric errors to a level where the astrometric accuracy required for parallax measurements of objects at distances of up to 10 kpc can be achieved.

## 2.4. CALIBRATING FOR THE ATMOSPHERE

### 2.4.2 Dry Tropospheric Delay

The dry component of the troposphere can contribute 200 cm or more zenith delay (Reid & Honma, 2014). However, the large majority of this effect is removed during the correlation stage using ‘seasonally averaged’ models for temperature, pressure and humidity (Deller et al., 2007). As with every and all modelling techniques this will leave residuals which are expected to be of the order of  $\pm 10$  cm zenith delay (Reid et al., 2014). From the geometry and respective heights in Figure 2.3 I derive that relative path-lengths  $\tau_{tropo}$  as a function of elevation  $\varepsilon$  can be described  $\tau_{tropo} = \tau_z m_i$  by the following mapping function:

$$m_1(\varepsilon) = \frac{\sin(\varepsilon) - \sqrt{\sin(\varepsilon)^2 + \left(\frac{H}{R_\oplus}\right)^2 + \frac{H}{2R_\oplus}}}{1 - \sqrt{1 + \left(\frac{H}{R_\oplus}\right)^2 + \frac{H}{2R_\oplus}}} \quad (2.13)$$

where  $H$  is the height of the troposphere ( $\sim 15$  km),  $R_\oplus = 6370$  km is the radius of Earth and  $\varepsilon$  is the antenna elevation measured from local horizon. I take this to be the correct and full mapping function, however, in this thesis I will use two approximations to this. Firstly the Neill’s mapping function:

$$m_2(\varepsilon) = \sin(\varepsilon) + \frac{a}{\sin(\varepsilon) + \frac{b}{c + \sin(\varepsilon)}} \quad (2.14)$$

where  $a = 5.6795 \times 10^{-4}$ ,  $b = 1.5139 \times 10^{-3}$  and  $c = 4.6730 \times 10^{-2}$ . This function is used extensively during geoblock and baseline fitting programmes (discussed below). Secondly:

$$m_3(\varepsilon) = \sec\left(\frac{\pi}{2} - \varepsilon\right) = \sec(Z) \quad (2.15)$$

as shown in Honma et al. (2008), where  $Z = \frac{\pi}{2} - \varepsilon$  is the zenith angle. Figure 2.4 shows the distribution of these functions and the differences between them.

As is hinted at by the geometry in Figure 2.3 and shown by all the mapping function, the additional path length increases rapidly for decreasing elevations and doubles the zenith delay after  $\varepsilon \lesssim 30^\circ$ . Equation 2.13 reveals that for elevations  $\varepsilon \rightarrow 0$  I approach a maximum additional path of  $\sim \sqrt{\frac{2R_\oplus}{H} \frac{H/R_\oplus + 1}{H/R_\oplus + \frac{1}{2}}} \approx 71.3$ .

In phase referencing observations, delay is relative to a nearby position ( $Z_2 = Z_1 + \delta z$ ):

$$\Delta\tau_{dtropo} = \tau_z(m_3(Z_2) - m_3(Z_1)) \approx \tau_z \sec^2 Z_1 \sin Z_1 \delta z \quad (2.16)$$

where I have used the  $m_3$  mapping function for mathematical simplicity. This function diverges rapidly for values of  $Z_1 \geq 60^\circ$  or  $\varepsilon_1 \leq 30^\circ$ . Therefore, it is generally accepted (despite the existence of calibration methods), that phase referencing observations should be conducted at elevations  $\varepsilon > 30^\circ$  so that delay errors are minimised while getting as much  $uv$ -coverage as possible. For reasonable elevations  $\varepsilon$ , this reduces the tropospheric delay error ( $\Delta\tau_{dtropo}$ ) by a factor of  $\delta z$ .

The current methodology for removing the residual dry tropospheric delay is called *geoblock fitting* (Reid et al., 2009a). This is performed by scheduling ‘geoblocks’ during observations spaced roughly every 2–3 hours. Each geoblock consists of 10–20 quasars at different elevations and generally takes  $\sim 30$  mins per geoblock. For each geoblock  $b$  a zenith delay  $\tau_{z,bi}$  can be

## 2.4. CALIBRATING FOR THE ATMOSPHERE

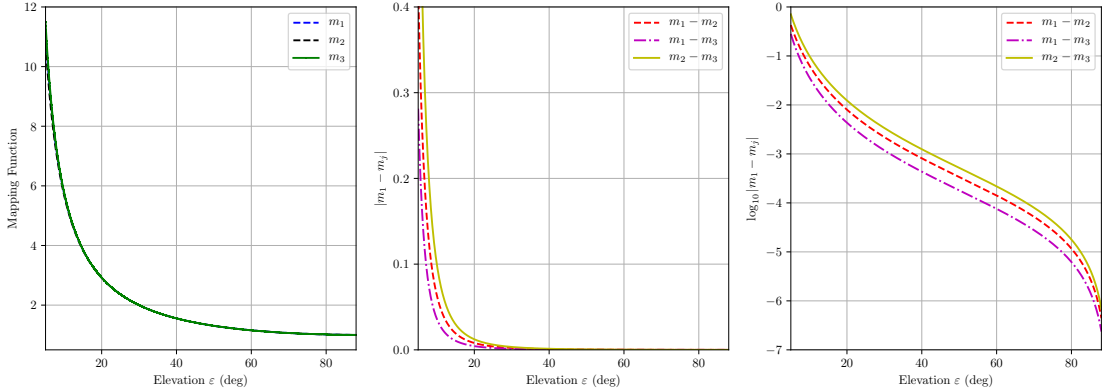


**Figure 2.4:** **Left:** magnitudes and **centre/right** differences between mapping functions  $m_1$ ,  $m_2$  and  $m_3$  given in text against elevation  $\varepsilon$ . Right plot is in log units to highlight differences difficult to see in centre plot.

determined for each antenna  $i$  by fitting the elevations to Equation 2.14. In practice the geoblocks are used to determine the dynamic tropospheric component **and** the residual clock–delay rates  $\delta\dot{\tau}_i$  by fitting Equation 2.17 to antenna elevations  $\varepsilon_{ik}$  observed at time  $t_l$ :

$$\tau(t_l)_{ij} = \tau_{0,ij} + (\delta\dot{\tau}_i - \delta\dot{\tau}_j)(t_l - t_0) + \tau_{z,bi} m_2(\varepsilon_{ik}) - \tau_{z,bj} m_2(\varepsilon_{jk}) \quad (2.17)$$

The tropospheric delay is a non-dispersive delay and as such is the same at all frequencies. Therefore it is not only advantageous to maximise recorded bandwidth to better constrain the delay but it also allows a smaller delay to be detected. In order to minimise delays due to source position offsets, only quasars with catalogued reliable positions should be used for this analysis. Also, each quasar needs to be compact and bright enough to be detected across the whole bandwidth on each baseline to get a reliable multiband delay detection.

### 2.4.3 Wet Tropospheric Delay

The wet atmosphere is characterised by a fast (minute-scale) change in the amount of water vapour present along the LOS. In order to remove these effects, the target and reference calibrator need to be observed near ‘simultaneously’. The tropospheric coherence time ( $T_{coh}$ ) is defined to be the characteristic time-scale that the wet tropospheric component varies enough to cause a phase ambiguity:

$$2\pi\sigma_A T_{coh}\nu \sim 1 \quad (2.18)$$

where  $\sigma_A = 0.7 \times 10^{-13}$  is the Allan standard deviation for the troposphere (Reid & Honma, 2014). For radiation of frequency 6.7 GHz, this leads to a coherence time of  $T_{coh} \sim 5$  mins. Thus, to avoid decorrelation and successfully phase reference the wet-tropospheric phase, the source and reference need to be observed within a time-scale of 5 mins or less.

Due to the wet-troposphere being randomly dynamic, there is no known structural form that can reduce the errors by separation between target and calibrator. As such *as long* as time–phase interpolation can occur the LOS delay is considered identical if the separations are small, subject to the interpolation errors. There are two main schools of wet-tropospheric removal which take advantage of observing techniques to minimise delay errors.

## 2.4. CALIBRATING FOR THE ATMOSPHERE

*In-beam calibration* involves looking at a source and calibrator simultaneously, with both inside the same primary beam. Therefore, there is no specific time-interpolation required which resolves the issue. This technique becomes particularly common for low-frequency observations where beam size becomes appreciably large such that there is a high chance of finding in-beam calibrators. However, it is difficult to find a source and calibrator close enough at mid/high frequencies ( $\nu \gtrsim 4$  GHz).

*Nodding* is perhaps the most commonly-used option for mid/high frequency phase-referencing observations. It involves bracketing target source observations with calibrator source observations well within  $T_{coh}$ . Nodding becomes difficult for high-frequency observations ( $\nu \gtrsim 30$  GHz) and requires either very sensitive and/or fast-slewing telescopes. Nodding is the primary technique used in Chapter §3 to analyse recent BeSSeL VLBA data.

I will introduce and discuss an alternative technique in Chapter §5.

### 2.4.4 Ionospheric Delay

The ionosphere is a layer of ionised plasma with a characteristic height of 400 km. Unlike the troposphere, the ionosphere introduces a *dispersive* delay: one that is frequency-dependant:

$$c\tau_{iono} = 40.3 I_e \nu^{-2} \text{cm} \quad (2.19)$$

with  $\nu$  in GHz (Figure 2.5).  $I_e$  is the total electron content (TEC) along the line of sight measured in units of TECU ( $1 \text{TECU} = 1 \times 10^{16} \text{ electrons m}^{-2}$ ). Typical total zenith values of  $I_e$  are expected to be  $I_e < 50$  TECU excluding major solar events. Due to the characteristic height of the ionosphere, for most elevations the field of view is very large and small differences in the LOS will lead to very different ionospheres (e.g. shown in Figure 2.3). In turn this makes it difficult to characterise the ionosphere or make initial assumptions of local similar delays. The most general method to subtract bulk  $I_e$  contributions is to use TEC maps provided by NASA Jet Propulsion Laboratory (JPL) as well as other groups. These maps are calculated from GPS data (which operate at 1.23 and 1.58 GHz) and can be imported to calculate the expected delay through that region of the ionosphere. Rather than the absolute delay along a line of sight being the same, if the residuals in a region are similar then phase referencing should serve to reduce the error. However Walker & Chatterjee (1999) estimate that the ionospheric residuals in these maps is around 5 – 10 TECU, which is 4.5 – 9 cm at 6.7 GHz, 2.9 – 5.7 cm at 8.4 GHz and 0.4 – 0.8 cm at 22 GHz. In addition the resolution of TEC maps is reduced in the Southern Hemisphere due to the spacing and number of GPS stations compared to the North (4800 vs. 1000 GPS stations).

Dual-frequency observations are without a doubt the best way to remove residual line-of-sight delays due to the ionosphere, as is conducted in geodetic VLBI observations at S (2.3 GHz) and X ( $\sim 8.2$  GHz). This is because they are currently the only way to directly ‘measure’ and therefore accurately remove the ionospheric residual. Given a total (or total-residual) LOS delay  $\tau(t, \nu) = \tau_{nd}(t) + \tau_d(t) \nu^{-2}$  the non-dispersive component will affect all frequencies identically and subtracting the total delay at two frequencies leaves only the dispersive delay:

$$\tau(t, \nu_2) - \tau(t, \nu_1) = \tau_d(t) \left( \frac{1}{\nu_2^2} - \frac{1}{\nu_1^2} \right) \quad (2.20)$$

$\tau_d$  can then be appropriately subtracted from the delays towards both LOS and therefore this

## 2.5. AMPLITUDE CALIBRATION

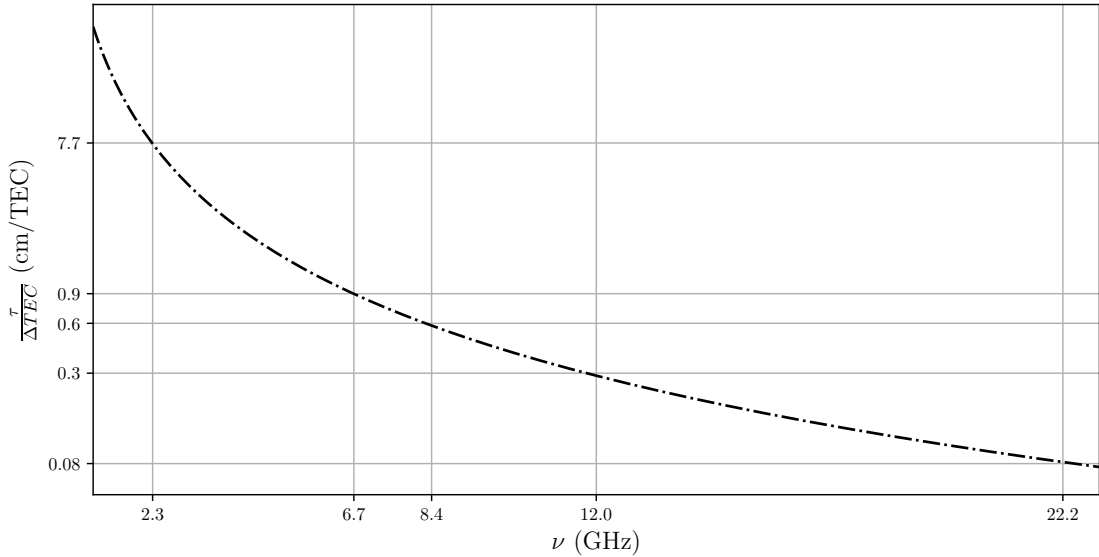


**Figure 2.5:** Dispersive delay causes by ionosphere. **y-axis:** Delay per unit TEC; **x-axis:** frequency in GHz.

still requires the assumption that the delay does not vary much in angular separation. Therefore in traditional nodding-techniques, derived residual delays are believed to be a ‘DC’ effect and the solution directly applied from calibrator to target (either spectra line or too weak to derive delays). In fact, it is very likely that for any degree-scale field of view there is a smooth-gradient of residual delay which most-likely would break down on the 10’s of degree scale (Dodson et al., 2017).

## 2.5 Amplitude Calibration

A distant source of electromagnetic radiation with spectral luminosity  $L_\nu$  ( $\text{W Hz}^{-1}$ ) will illuminate the surface of a radio telescope with flux density

$$S_\nu = \frac{L_\nu}{4\pi d^2}$$

The surface of the telescope will sum the flux density ( $\text{W m}^{-2} \text{Hz}^{-1}$  or  $\text{Jy}$ ) and it will be detected as a voltage at the receiver. However this summation and detection process is not perfect and there will be losses such that the actual power at the receiver will be

$$P \propto \eta A S_\nu$$

where  $\eta$  is the antenna efficiency ( $0 < \eta < 1$ ) and  $A$  is the antenna collecting area. The radio telescope records a normalised response voltage proportional to the power received.

The SEFD (system equivalent flux density) is the system noise (contributions from antenna, receiver, electronics etc) expressed in units of flux density and in practice serves as a conversion

## 2.5. AMPLITUDE CALIBRATION

between normalised voltages/power and flux density. For astrometric VLBI, poor amplitude calibration can lead to incorrectly weighted baselines which can corrupt images and potentially ruin astrometric accuracy. Absolute amplitude calibration requires careful and constant monitoring of the above contributing factors which may be unavailable at some sites. While correct weighting of baselines is important, absolute amplitude determination is not the primary goal, therefore alternative methods to calibrate antenna SEFDs become available.

### 2.5.1 Alternative maser calibration

In the event that traditional methods are either impossible or insufficient and amplitude calibration is required pre-imaging, masers themselves present a possible solution. At any one time, if the angular size of a maser is smaller than the primary beam of all telescopes in an array, then the velocity-corrected bandpass-subtracted autocorrelation spectra should be identical (excluding noise). If at least one telescope in the array has stable and accurate pre-calibration applied, or if the maser has a known spectral flux density this can be used as a reference for the remaining spectra. This technique sacrifices absolute amplitude calibration for relative amplitude calibration under the condition that the above criteria are met.

If a maser has some reference spectral flux density  $S_{\nu_r}$  and some baseline  $B_{ij}$  flux density

$$s_{ij} = |\sqrt{\mathbf{s}_i \mathbf{s}_j}| i = j$$

then the correction factor will be:

$$\Gamma = \frac{S_{\nu_r}}{s_{ij}}$$

As this springs from autocorrelations I need to multiply the antenna-based data by  $\sqrt{\Gamma}$  as I ultimately want to correct the cross-correlations. This can be calculated separately for each telescope in the array over time.

### 2.5.2 Alternate quasar calibration

Unlike masers, quasars are continuum sources that have a relatively low ‘per spectral channel’ flux density ( $\sim 100\text{ mJy}$  level) and as such it is more difficult to detect them in autocorrelation spectra above the system temperature and with the thermal noise. However, they are generally unresolved and have much better detections in cross-correlation spectra across the band where system noise from each telescope is largely absent as they do not correlate.

In order to calibrate quasars over a bandwidth and baseline, I first need to establish that this is appropriate.

#### 2.5.2.1 Calibrating amplitude over frequency

Due to synchrotron emission contributing the majority of flux to the quasars, they are well modelled by a power law spectrum:

$$S_{\nu} = S_0 \nu^{\alpha} \quad (2.21)$$

## 2.5. AMPLITUDE CALIBRATION

Taylor expanding the above equation about some reference frequency  $\nu_0$ , assuming that  $\alpha \neq 0$  I want to know the flux density change over a spanned-bandwidth from  $\nu_0$  to  $\nu_0 + \Delta\nu$ :

$$S_\nu(\nu_0 + \Delta\nu) = S_0 \nu_0^\alpha \sum_{n=0}^{\infty} \frac{\alpha(\alpha-1)\dots(\alpha-n)}{n!} \left( \frac{\Delta\nu}{\nu_0} \right)^n \quad (2.22)$$

For typical frequencies and spanned-bandwidths explored in this thesis (e.g.  $\nu_0 = 6300$  MHz,  $\Delta\nu = 374$  MHz and  $\nu_0 = 8213$  MHz,  $\Delta\nu = 256$  MHz) it is reasonable to assume that  $(\Delta\nu/\nu_0)^n \ll 1, n > 1$ . Now equation Equation 2.22 reduces to:

$$S_\nu(\nu_0 + \Delta\nu) = S_0 \nu_0^\alpha \left( 1 + \alpha \frac{\Delta\nu}{\nu_0} \right) \quad (2.23)$$

Using Kellermann et al. (1969), I take the median spectral index of quasars to be  $\alpha \approx -1.0$  in the neighbourhood of our frequencies of interest. Now I can see the fractional change of the flux density over the bandwidth is:

$$\begin{aligned} \frac{S_\nu(\nu_0 + \Delta\nu) - S_\nu(\nu_0)}{S_\nu(\nu_0)} &\approx -1.0 \frac{\Delta\nu}{\nu_0} \\ &= 6\% \text{ at } 6.3 \text{ GHz} \\ &= 3\% \text{ at } 8.2 \text{ GHz} \end{aligned}$$

Therefore a constant amplitude over a small bandwidth is a reasonable assumption. This allows one to assume a fixed flux density of a quasar over the whole bandwidth, and calibrate the bandwidth compared to this number. In addition I can average a quasar over the spanned bandwidth and ensure the imaged flux density is accurate for each baseline.

### 2.5.2.2 Calibrating amplitude over baseline

Assuming a quasar of known zero-spacing flux density  $S_0$  that has emission resembling a 2D Gaussian with angular size (full width at half maximum)  $\theta$ . Then the visibility amplitude of the quasar can be represented as:

$$S_{uv} = S_0 \exp \left( -\frac{2\pi^2}{8 \ln 2} (\theta B_\lambda)^2 \right) \quad (2.24)$$

where  $B_\lambda = uv/\lambda$  is the projected baseline length  $uv$  expressed in terms of wavelength  $\lambda$ . If the peak flux density of such a source were constant over time and it never underwent evolutionary/structural changes we could use the source as a VLBI flux density calibrator. If the detected flux density on baseline  $B_{ij}$  is

$$s_{ij} = |\sqrt{\bar{s}_i \bar{s}_j}|, i \neq j$$

then the ratio of  $s_{ij}$  to  $S_{uv}(B_{ij})$  serves as a diagnostic for the ‘goodness of calibration’ as a function of baseline pairs. Consider

$$s_{ij} = x_i x_j$$

being the ‘true’ flux density and

$$S_{uv}(B_{ij}) = \delta x_i \delta x_j x_i x_j$$

## 2.6. ADDITIONAL CONSIDERATIONS

being the detected flux density, with  $0 < \delta x \leq 1$ . If the model and source flux are identical for all baseline pairs, then  $\delta x_i = 1 \forall i$  and the data is perfectly calibrated. Elsewise we can simply solve for the antenna-dependent offset between baselines and correct it.

To isolate the parameters we consider that for  $N$  antennas there are  $\frac{N(N-1)}{2}$  independent baselines. While the immediate problem is non-linear:

$$\delta x_i \delta x_j = \frac{S_{uv}(b_{ij})}{s_{ij}}, i \neq j \quad (2.25)$$

we can assume that the required corrections are small  $\delta x_i = 1 + \epsilon_i$  so that we can get:

$$(1 + \epsilon_i)(1 + \epsilon_j) = (1 + \epsilon_i + \epsilon_j + \epsilon_i \epsilon_j) = \frac{S_{uv}(b_{ij})}{s_{ij}} \quad (2.26)$$

and it is likely that  $\epsilon_i \epsilon_j \ll 1$ . We now can convert this to a matrix formula to solve for the offsets.

$$\epsilon_i + \epsilon_j = \frac{S_{uv}(b_{ij})}{s_{ij}} - 1 = d_{ij} \quad (2.27)$$

$$\begin{bmatrix} 1 & 1 & 0 & 0 & \dots & 0 & 0 & 0 \\ 1 & 0 & 1 & 0 & \dots & 0 & 0 & 0 \\ \vdots & \vdots & \vdots & & \ddots & \vdots & \vdots & \vdots \\ 0 & 0 & 0 & \dots & \dots & 0 & 1 & 1 \end{bmatrix} \begin{bmatrix} \epsilon_1 \\ \epsilon_2 \\ \vdots \\ \epsilon_N \end{bmatrix} = \begin{bmatrix} 0 & d_{12} & d_{13} & \dots & d_{1N} \\ d_{21} & 0 & d_{23} & \dots & d_{2N} \\ d_{31} & d_{32} & 0 & \dots & d_{3N} \\ \vdots & \vdots & \vdots & \ddots & \vdots \\ d_{N1} & d_{N2} & d_{N3} & \dots & 0 \end{bmatrix}$$

Where we set  $d_{ii} = 0$  to mask the solution. The above is the matrix equation

$$\mathbb{P}\mathbf{x} = \mathbb{D}$$

where  $\mathbb{P}$  is a  $N \times N(N-1)/2$  matrix,  $\mathbf{x}$  is a  $1 \times N$  vector containing the solutions and  $\mathbb{D}$  is a  $N \times N$  matrix of the observables.  $\mathbb{P}$  is non-singular if  $N \geq 3$  and therefore has an inverse such that we can solve the above for  $\mathbf{x}$ :

$$\mathbf{x} = (\mathbb{P}^T \mathbb{P})^{-1} \mathbb{P}^T \mathbb{D} \quad (2.28)$$

The array  $1 + \mathbf{x}$  contains the correction that needs to be applied to each telescope in the array to match the model and therefore calibrate the telescope SEFDs.

## 2.6 Additional Considerations

### 2.6.1 Annual Parallax Sampling

The first of many pre-data collection considerations is optimal sampling. A parallax is a magnitude and is a constant over all observations, however, it modulated by the Earth's orbit around the Sun and depends on source position. As the parallax magnitude is (in Galactic maser cases) very small and astrometric data contains comparable uncertainty as it is, further measurement uncertainty should be minimised if possible.

To begin with, a source with equatorial position (RA, DEC) =  $(\alpha, \delta)$  and distance  $d = \frac{1}{\omega}$  at any

## 2.6. ADDITIONAL CONSIDERATIONS

given time  $t$  (yrs) will have a parallax of magnitude:

$$x = \varpi T_e (Y \sin \alpha - X \sin \alpha) + \mu_x (t - t_{\text{ref}})$$

$$y = \varpi T_e (Z \cos \delta - X \cos \alpha \sin \delta - Y \sin \alpha \sin \delta) + \mu_y (t - t_{\text{ref}})$$

$$\begin{aligned} X &= \cos 2\pi(t - t_0) \\ Y &= \sin 2\pi(t - t_0) \cos \theta \\ Z &= \sin 2\pi(t - t_0) \sin \theta \\ T_e &= 1.0 + 0.0167 \sin 2\pi(t - 0.257) \end{aligned} \tag{2.29}$$

where  $x, y$  (mas) are the sampled position of the source in the RA, DEC directions,  $\alpha, \delta$  are the nominal source position in RA and DEC at  $t_{\text{ref}}$ ,  $t$  is fractional time of year,  $\theta = 23.4^\circ$  is obliquity of the Earth,  $t_0 = 0.22$  yr is the time of the vernal equinox,  $T_e$  describes the eccentricity of the Earth's orbit,  $\varpi$  is the parallax (mas), and  $\mu_x, \mu_y$  are the proper motions in  $x, y$  (mas/year).

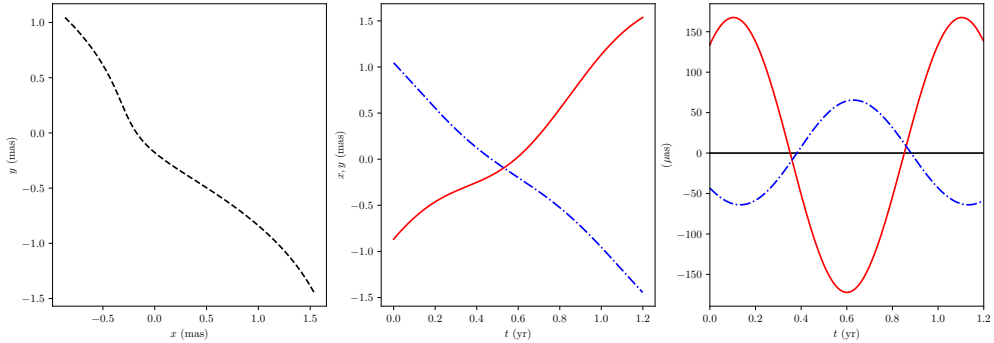


**Figure 2.6:** Simulated parallax for 6.7 GHz maser G329.339+0.148:  $\alpha \sim 16.0$  hr,  $\delta \sim -52.7^\circ$  and kinematic distance  $d \sim 6.0 - 8.5$ . I arbitrarily set  $\mu_x = 2.0$  and  $\mu_y = -2.0$  mas/yr, and set  $\varpi = 0.143$  mas. **Left:** apparent motion of target across sky. **Centre:** respective apparent motions in  $\alpha$  (or  $x$ , red) and  $\delta$  (or  $y$ , blue). **Right:** projected parallax motion (subtracting proper motion) in  $x$  and  $y$ .

Since the change in the measured astrometric position for the target source with time depends on the proper motion of the source in RA and DEC and the parallax, a minimum of 3 observations are required. However, this leaves zero degrees of freedom remaining to calculate residuals and in practice many more epochs of observations are generally conducted to reduce the uncertainty in the measured proper motion and parallax. As such optimal parallax sampling has a weak dependence on target  $\alpha$  and  $\delta$ . Figure 2.6 shows a simulated parallax. In this instance the Right Ascension component is 2.5× more sensitive to the parallax amplitude due to the projection of Earth's orbit and therefore observations made at the times when the RA offset due to parallax will be at a maximum magnitude (in this case early July for the minimum and early February for the maxima) is optimal.

### 2.6.2 Proper motion

A proper motion is defined as the movement of an object tangential to the line of sight. Spectral line Doppler shift can be used to measure relative LOS velocity, a principle kinematic distance

## 2.7. SUMMARY – STANDARD ASTROMETRIC VLBI CALIBRATION

determinations utilise. However proper motions require sufficiently accurate astrometry and/or time.

As demonstrated in Figure 2.6 the proper motion is often much larger in apparent magnitude than the parallax, unless the target is particularly close or the proper motion is extremely large (e.g. Barnards Star;  $\mu_y = 10.3 \times 10^3$  mas/yr Barnard, 1916).

In VLBI astrometry, cardinal directions are always expressed as RA/DEC ( $\alpha, \delta$ ) and hence the measured proper motions are  $\mu_x = \mu_\alpha \cos(\delta), \mu_y = \mu_\delta$ . Poleski (2013) provides a succinct conversion from the measured equatorial coordinate system to a more relevant Galactic coordinate system via introduction of a simple rotation matrix:

$$\begin{bmatrix} \mu_{l*} \\ \mu_b \end{bmatrix} = \frac{1}{\cos b} \begin{bmatrix} C_1 & C_2 \\ -C_2 & C_1 \end{bmatrix} \begin{bmatrix} \mu_{\alpha*} \\ \mu_\delta \end{bmatrix}$$

where

$$\begin{aligned} C_1 &= \sin \delta_G \cos \delta - \cos \delta_G \sin \delta \cos(\alpha - \alpha_G) \\ C_2 &= \cos \delta_G \sin(\alpha - \alpha_G) \\ \cos b &= \sqrt{C_1^2 + C_2^2} \end{aligned}$$

and  $\alpha_G = 192.859^\circ$  and  $\delta_G = 27.128^\circ$ . This method requires no initial conversion into native Galactic coordinates. The ‘\*’ on the proper motions indicate reduced proper motions due to the area inequality at high  $l$  or  $\delta$ :  $\mu_{l*} = \mu_l \cos b$  and  $\mu_{\alpha*} = \mu_\alpha \cos \delta$ . In VLBI astrometry we directly measure  $\mu_{\alpha*}$  and  $\mu_\delta$ .

## 2.7 Summary – Standard Astrometric VLBI Calibration

Throughout this thesis I will refer back to the Standard Astrometric VLBI Calibration scheme outlined in this section. This is a procedure to calibrate VLBI data starting from correlated data product form into a final form - either astrometric images (Chapter §3), *uv*-tracks (Chapter §4) or pre-multiview fitting stage (Chapter §6).

Based heavily on the procedures outlined in Brunthaler et al. (2011); Reid et al. (2009b,c) Standard VLBI Calibration is almost completely performed via *AIPS* (Astronomical Image Processing Software; Greisen, 1990) and the python wrapper software *ParselTongue/Obit* (Kettenis et al., 2006). *ParselTongue* enables access to the *AIPS* data and tables from within a python environment and facilitated examination and manipulation of the data in ways that are not provided by existing *AIPS* tasks. Nevertheless *AIPS* provides the fast calculation and general data visualisation/manipulation via its *tasks*, *tables* and *catalogue* structure.

Here we concisely summarise Standard Astrometric VLBI Calibration procedure:

1. The initial calibration step is to flag data that has been collected outside of mutual onsource time (slewing) or influenced by clock-jumps or strong radio frequency interference;
2. Geoblock analysis:
  - (a) Taking the geoblock data, delays and phase corrections are applied corresponding to known Earth Orientation Parameter (EOP) corrections and feed rotation effects due

## 2.7. SUMMARY – STANDARD ASTROMETRIC VLBI CALIBRATION

to parallactic angles for circular polarised feeds. TEC maps are downloaded and used to estimate ionosphere delays, which are then applied.

- (b) A single scan of source within the geoblock dataset is chosen based off mutual onsource time by all telescopes and SNR. Manual phase calibration is performed on this scan: single-band delays and phases are calculated (rates are specifically zeroed) for each polarisation/IF and applied to the remaining geoblock data;
  - (c) All geoblock scans are fringe-fit for a single multiband delay and rate for each each scan. These solutions are then fed into an external tropospheric zenith delay/residual clock delay fitting programme **fit\_geoblocks\_tropos** which outputs an AIPS-friendly input file containing tropospheric zenith delays vs. time for each antenna;
  - (d) When wide-band observations have also been undertaken, dispersive delay solutions are first taken out of the dispersive geoblock delay inputs before tropospheric zenith delay fitting.
3. The calibrator and maser datasets are calibrated identically and in parallel:
    - (a) TEC maps are applied, EOP and feed rotation effects are corrected, then zenith delay solutions are applied;
    - (b) Telescope gains and system temperatures are applied to correct the raw voltage amplitudes to Jy;
    - (c) If known, target/calibrator positional offsets are applied. This can only be calculated at one epoch and must be applied identically to all epochs thereafter;
    - (d) The manual phase calibrator scan is chosen, delays and phases are calculated and applied;
    - (e) Telescope motion in the source direction due to Earth orbit and rotation at telescope position not included in correlator model is calculated. This Doppler Shift is applied so that for all telescopes the frequencies observed are those that would be observed at the geocentre.
  4. Either a specific channel of the maser or a calibrator is chosen as the phase reference (PR) source. If it is the calibrator it is normal PR and if it is the maser/target it is referred to as reverse-PR;
  5. If the quasar is chosen:
    - (a) The calibrator is averaged in frequency to increase SNR and a fringe-rates/phases are calculated at the correlated+shifted position. This solution is applied to the maser and itself;
    - (b) self-calibration can be performed on the quasar to remove structure phases, solutions are applied to maser and quasar identically;
    - (c) maser scans not observed within the coherence time to the quasar are flagged (if multiple quasars);
    - (d) maser channel(s) are imaged via CLEAN algorithm and emission regions are fitted with Gaussian ellipticals. Centroids positions are recorded for parallax fitting.
  6. If the maser is chosen:
    - (a) A single maser channel is chosen and fringe-rates/phase are calculated at its correlated + shifted position.

## 2.7. SUMMARY – STANDARD ASTROMETRIC VLBI CALIBRATION

- Side note: in the case of low SNR multiple maser channels can be averaged to increase SNR. However, care must be taken to ensure that emission originates from the same maser spot otherwise astrometric accuracy will be significantly decreased.
- (b) fringe solutions can be applied to maser and self-calibration can be performed. Solutions are identically applied to maser and quasar;
- (c) quasar is averaged in frequency and the fringe solution is applied;
- (d) quasar is imaged via CLEAN algorithm and emission region is fit with Gaussian elliptical. Centroid positions have sign reversed and are recorded for parallax fitting.



## 2.7. SUMMARY – STANDARD ASTROMETRIC VLBI CALIBRATION

# 3

## PARALLAX AND PROPER MOTIONS OF FIRST GALACTIC QUADRANT STAR FORMING REGIONS

In this chapter I present measurements of parallaxes towards 4 star forming regions in the First Galactic Quadrant. These parallaxes were observed as part of the Bar and Spiral Structure (BeSSeL) Survey's most recent programme: BR210. I use the measured and previous parallaxes to fit a spiral arm model to the maser distributions in the Perseus arm and use the proper motions to determine local Galactic kinematics. Finally I discuss the applicability of these techniques to S $\pi$ RALS.

### 3.1. INTRODUCTION

## 3.1 Introduction

The BeSSeL Survey has been an ongoing legacy project on the VLBA since 2010 and in that time has collected data on just under 200 masers\* cumulating in the reduction and publication of  $> 90\%$  (Reid et al., 2019, not including parallaxes published as part of the VERA project). These parallaxes, proper motions and resultant distances individually provide important size, luminosity and kinematic information about the specific star forming region, which can be then used in other studies. However when combined in a large collections they are utilized to trace the structure, dynamics and constrain the size and mass of our Galaxy.

Despite the large and sweeping success of BeSSeL and VERA, there have been numerous target masers for which a parallax observation has not resulted in a significantly constrained distance. Most of these can be attributed to water maser variability and eventual spot disappearance over the course of a year. Even in cases where the maser spot persists for a majority of a year, disappearance in final epochs can cause large uncertainties and parallax measurement uncertainty approaching 20% or far exceeding it in terms of parallax fit degeneracy.

Initial BeSSeL observations (made under project codes BR145 and BR198) were limited to targeting 22.2 GHz water and occasional 12.2 GHz class II methanol masers. Upgrades to the VLBA in 2015 allowed observations of 6.7 GHz methanol masers, and in response BeSSeL conducted the BR149 series exclusively dedicated to targeting these masers. At the sacrifice of generally less compact maser spots, 6.7 GHz methanol masers have greatly reduced average variability compared to their 22 GHz counterparts. This means phase reference features persist for periods much longer than a year. In addition at these lower frequencies interferometer coherence times are much longer and it was believed that phase errors resulting from residual tropospheric delays would allow as stable (if not more stable) phase referencing solutions. Therefore BR149 proceeded with the observations of 6.7 GHz methanol masers as 4 epochs per maser spaced out over 12 months.

Regrettably, parallax measurements for the methanol masers in BR149 were significantly noisier than previous water maser measurements and as a result sometimes maser distances were very difficult to constrain. The source of this added uncertainty is attributed to residual ionosphere, which was not initially expected to be a major influence at intermediate frequencies. In some extreme cases, different quasars would even give systematically different parallax measurements, suggesting a parallax ‘gradient’ over the sky (Reid et al., 2017; Zhang et al., 2019). This type of measurement uncertainty is particularly deleterious when there are only a small number of epochs in a parallax measurement, such as for BR149.

Therefore BR210 was introduced to combat these issues. Targeting both 22 GHz water and 6.7 GHz methanol masers, BR210 stands out among BeSSeL projects in observational approach and includes 16 epochs and multiple quasars per maser.

Figure 3.1 shows modelled locations for the Local, Perseus and Outer arms as derived from pitch angles and rotation curves given in Reid et al. (2019) projected on a  $l-v$  diagram with CO emission contours. Included are the locations of many HMSFR as traced by 6.7 GHz methanol masers. Concerning the Perseus arm, there exists a region between  $50 < l < 80^\circ$  with little in the way of dense gas regions or HMSFR, which is commonly referred to as the *Perseus gap*, and is inexplicable by either arm projection or sensitivity.

The aim of the parallax observations described in this chapter is to increase our knowledge of

---

\*<http://bessel.vlbi-astrometry.org/observations>

### 3.2. OBSERVATIONS AND REDUCTION

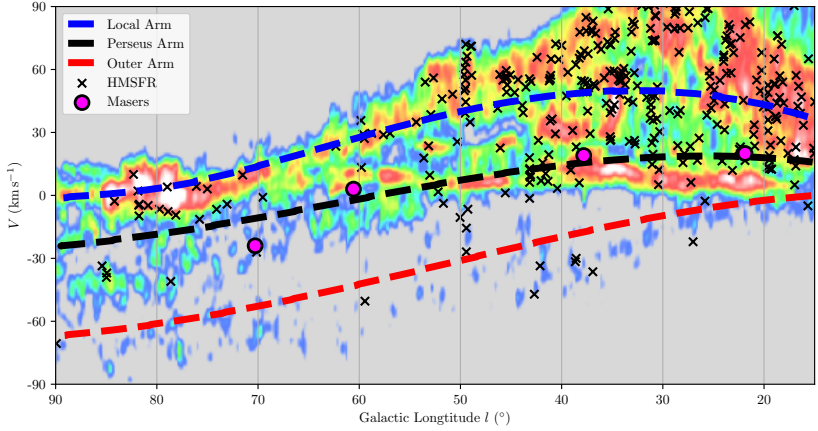


**Figure 3.1:**  $l - v$  diagram of the first Galactic quadrant. **Coloured contours:** Integrated CO emission from Dame et al. (2001); **Blue, black and red dashed lines:** projected arm locations for the Local, Perseus and Outer arms respectively; **Black crosses:** High mass star formation regions as traced by 6.7 GHz methanol masers from Yang et al. (2019); **Pink:** location of masers analysed in this chapter.

the structure of the first Galactic quadrant, particularly concerning the Perseus arm and Perseus gap by analysing BeSSeL VLBA data for three water masers and one methanol maser observed as part of BR210 and discuss the nuances of each parallax and region.

## 3.2 Observations and Reduction

Observational data were collected on the NRAO VLBA: project codes, epochs of observation and fractional year are shown in Table A.1. BR210 observations were split into five separate groupings, labelled A through to F, each containing 4–5 target masers based on sky distribution. BR210A→E comprises 22.2 GHz water masers while BR210F includes only 6.7 GHz methanol masers.

The individual observing sessions were  $\sim 7 - 9$  hours with approximately identical layouts. Each epoch contains 1 shared track for between 4–5 individual maser targets bracketed by geoblocks. In addition there are two geoblocks placed bracketing the transit  $\pm 2$  hours. Geodetic block data was recorded in left circular polarization with  $8 \times 16$  MHz bands, and line data was recorded in dual polarisation with  $4 \times 16$  MHz (8 IFs total and 512 Mbits/s rate in both recording modes). For  $K$ -band and  $C$ -band the modes were slightly different. The data were correlated with the DiFX software correlator (Deller et al., 2011) in Socorro, New Mexico.

### 3.2.1 K-band: BR210A to E

Mode 1, geoblock: These bands were spaced such that the lower edge was

$$\nu_L = 23522 + 14 \times (0, 1, 4, 9, 15, 22, 32, 34) \text{ MHz}$$

### 3.2. OBSERVATIONS AND REDUCTION

for each of the eight 16 MHz bands. This spacing is deliberate as it maximises delay–sensitivity in the synthesised bandwidth by minimising degenerate spacings. Synthesised bandwidth for geoblock data is  $\Delta\nu = 492$  MHz.

Mode 2, line: Masers, associated calibrators and fringe–finder calibrators were observed  $\Delta\nu = 64$  MHz continuous bandwidth centred on  $\nu_0 = 22.235$  GHz.

For both modes all sources and IFs were correlated in 32 spectral channels ( $\delta\nu_{cont} = 0.5$  MHz/chan). Line data processed in an additional pass: a zoom band for one of the IFs (that contained the maser line), correlated 2000 channels giving fine frequency resolution  $\delta\nu_{line} = 8$  kHz/chan or velocity resolution  $\delta v = 0.108$  km s $^{-1}$ .

#### 3.2.2 Wide C-band: BR210F

Mode 1: two frequency groupings of  $4 \times 16$  MHz IFs spaced 2.978 GHz apart. Each grouping was  $\Delta\nu = 496$  MHz synthesised bandwidth with lower band edge frequencies as given below:

$$\begin{aligned}\nu_{L,LO} &= 4112 + 4 \times (1, 20, 80, 120) \text{ MHz} \\ \nu_{L,HI} &= 7090 + 4 \times (1, 20, 80, 120) \text{ MHz}\end{aligned}$$

again spaced to maximise delay–sensitivity in the individual 4.3 and 7.3 GHz groups. Mode 2: Masers and calibrators were observed in 4 adjacent 16 MHz IFs centred on  $\nu_0 = 6.668$  GHz.

All data correlated with 32 channels pass 1. Second pass on mode 2 data: central 8 MHz zoom band of the third IF correlated with 2000 spectral channels  $\delta\nu_{line} = 4$  kHz/chan or velocity resolution  $\delta v = 0.18$  km s $^{-1}$ .

#### 3.2.3 Sources

The targets consisted of three 22.2 GHz water masers and one 6.7 GHz methanol maser believed to be located in the Perseus Arm of the Milky Way based on kinematic distances and known Galactic structure. Maser and reference quasar information is given in Table 3.1.

#### 3.2.4 Calibration

The VLBA data reduction was conducted via the Standard VLBI Calibration procedure (see Section §2.7) as applicable to the observing frequencies and modes listed above. The only difference to the calibration procedure came in the form of various time range flagging: more often than not there was a clock jump directly after the first geoblock compared to the second. This is a known issue and comes about as a consequence of the first (and only the first) frequency change in an experiment. The resolution to this issue is to flag the time range before the jump at offending stations.

### 3.2. OBSERVATIONS AND REDUCTION

**Table 3.1:** Information on observed masers and quasars. Columns: (1) Name in Galactic coordinates for masers and J2000 for quasars, (2) Right Ascension in J2000, (3) Declination in J2000, (4) median self-calibrated image integrated flux density, (5) separation between maser and quasar, (6) mean maser emission velocity, (7) maser type—either 22.2 GHz H<sub>2</sub>O or 6.7 GHz CH<sub>3</sub>OH.

Name	$\alpha_{J2000}$ (hh : mm : ss)	$\delta_{J2000}$ (dd : mm : ss)	S (mJy)	$\Delta\theta$ (deg)	V (km s <sup>-1</sup> )	Type
<b>G021.87+0.01</b>	18 : 31 : 01.7367	-09 : 49 : 01.116	...	...	+19.6	H <sub>2</sub> O
J1825-0737	18 : 25 : 37.6096	-07 : 37 : 30.013	116 <sup>+1</sup> <sub>-1</sub>	2.566	...	
J1835-1115	18 : 35 : 19.5754	-11 : 15 : 59.326	< 10	1.793	...	
<b>G037.81+0.41</b>	18 : 58 : 53.8794	+04 : 32 : 15.004	...	...	+19.0	H <sub>2</sub> O
J1855+0251	18 : 55 : 35.4364	+02 : 51 : 19.563	72 <sup>+16</sup> <sub>-29</sub>	1.874	...	
J1856+0610	18 : 56 : 31.8388	+06 : 10 : 16.765	151 <sup>+19</sup> <sub>-29</sub>	1.738	...	
<b>G060.57-0.18</b>	19 : 45 : 52.5019	+24 : 17 : 42.749	...	...	+3.7	CH <sub>3</sub> OH
J1946+2418	19 : 46 : 19.9607	+24 : 18 : 56.909	24 <sup>+5</sup> <sub>-1</sub>	0.116	...	
J1949+2421	19 : 49 : 33.1420	+24 : 21 : 18.245	124 <sup>+12</sup> <sub>-9</sub>	0.921	...	
<b>G070.29+1.60</b>	20 : 01 : 45.3486	+33 : 32 : 45.711	...	...	-26.7	H <sub>2</sub> O
J1957+3338	19 : 57 : 40.5499	+33 : 38 : 27.943	126 <sup>+6</sup> <sub>-24</sub>	1.024	...	
J2001+3323	20 : 01 : 42.2090	+33 : 23 : 44.765	137 <sup>+13</sup> <sub>-13</sub>	0.151	...	

### 3.3. RESULTS AND DISCUSSION

## 3.3 Results and Discussion

### 3.3.1 Astrometry and Parallax Fitting

The first step after calibration is fitting elliptical Gaussians to maser or quasar emission in phase referenced images. This process was performed manually with *AIPS* task **JMFIT** and option DOPRINT=−4. Tables A.2, A.3, A.4 and A.5 show the measured flux densities and astrometric positions of masers or quasars over time resulting from this fitting.

The parallax  $\varpi$  and proper motions  $\mu_x$ ,  $\mu_y$  are solved from the measured position over time ( $x$ ,  $y$ ) via weighted-least squares on Equation 2.29. This process is undertaken using the FORTRAN programme **fit\_parallax\_multi\_4d** (written and provided by Mark J. Reid). Measured parallax and proper motions are given in Table 3.2 with the parallax and proper motion curves given in Figures 3.2, 3.5, 3.8 and 3.11.

**Table 3.2:** Measured parallax and proper motions of masers. (1) Maser name in Galactic coordinates, (2) quasar name in J2000, (3) measured parallax,

Maser	Reference	$\varpi$ (mas)	$\mu_x$ (mas yr <sup>−1</sup> )	$\mu_y$ (mas yr <sup>−1</sup> )	$D$ (kpc)
<b>G021.88+0.01</b>	J1825 − 0737	$0.014 \pm 0.124$	$-3.60 \pm 0.48$	$-6.35 \pm 0.16$	$\gtrsim 2.5$
Best estimate					$13.7^{+0.9}_{-0.8}$
<b>G037.82+0.41</b>	J1855 + 0251	$0.093 \pm 0.010$	$-2.622 \pm 0.025$	$-5.837 \pm 0.037$	
	J1856 + 0610	$0.074 \pm 0.011$	$-2.660 \pm 0.028$	$-5.514 \pm 0.037$	
Weighted average		$0.084 \pm 0.008$	$-2.64 \pm 0.02$	$-5.68 \pm 0.03$	$11.90^{+0.82}_{-0.72}$
<b>G060.57−0.18</b>	J1946 + 2418	$0.130 \pm 0.011$	$-3.237 \pm 0.028$	$-5.729 \pm 0.040$	
	J1949 + 2421	$0.131 \pm 0.014$	$-3.217 \pm 0.036$	$-5.638 \pm 0.033$	
Weighted average		$0.130 \pm 0.009$	$-3.23 \pm 0.02$	$-5.67 \pm 0.03$	$7.69^{+0.38}_{-0.34}$
<b>G070.29+1.60</b>	J1957 + 3338				
&	J2001 + 3323	$0.097 \pm 0.011$	$-1.46 \pm 0.04$	$-3.69 \pm 0.05$	$11.2^{+1.1}_{-1.2}$

### 3.3.2 G021.87+0.01

G021.87+0.01 is a 22.2 GHz water maser spatially associated with an extended green object (EGO) and HII regions GAL021.87+00.01 and GAL021.88+00.02 (Rodgers et al., 1960; Wink et al., 1982, respectively). I measured a parallax of  $\varpi = 0.014 \pm 0.124$  mas towards G021.88+0.01, which is not statistically significant. Due to the very high fractional uncertainty ( $f \sim 9$ ) no inclusion of priors into the parallax probability can resolve the issue. Parallax inversion suggests the distance estimate is  $D \gtrsim 2.5$  kpc: even with the uncertainty encountered, a maser at this distance would have a measurable parallax and therefore this is the preliminary lower-bound estimate.

Using the measured recession velocity of the maser  $v = 19.6^{+5}_{-2} \text{ km s}^{-1}$ , I calculate a kinematic

### 3.3. RESULTS AND DISCUSSION

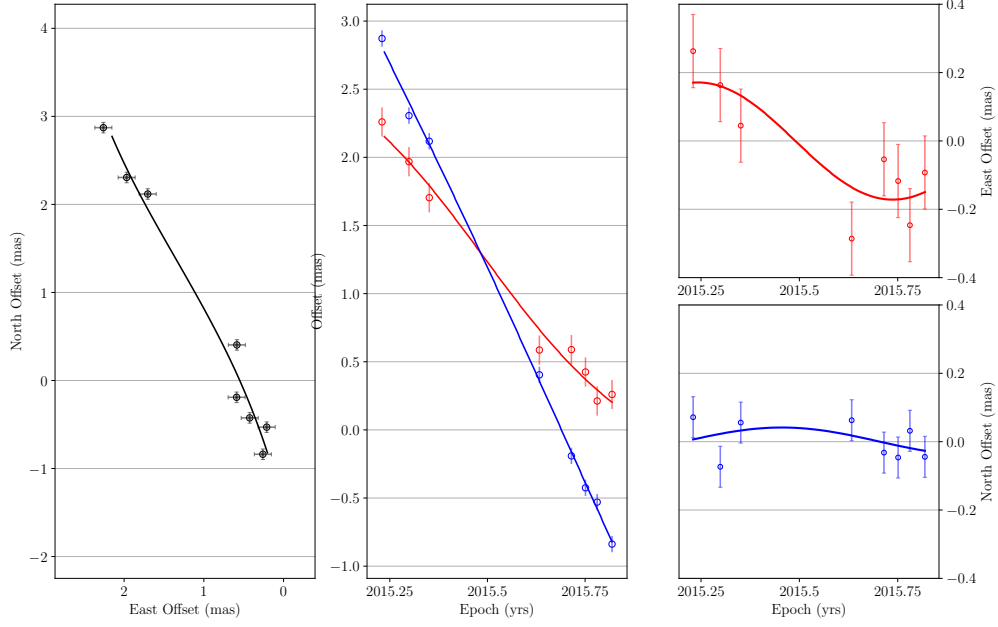


**Figure 3.2:** Parallax of G021.87+0.01 against QSO J1825–0737. Epochs 1, A, B, C, D, E, F, G are excluded from fit due to lack of detectable phase reference feature in either spectrum or map.

distance. Taking an analytic rotation curve:

$$\begin{aligned}\Theta(R) &= \Theta_{\odot}(K_1 + K_2 \frac{R_{\odot}}{R}) & 3 < R < 8 \text{ kpc} \\ &= \Theta_{\odot} & R > 8 \text{ kpc}\end{aligned}$$

with  $K_1 = 0.171$ ,  $K_2 = 0.889$  (McClure-Griffiths & Dickey, 2016a) and  $\Theta_{\odot} = 235 \pm 5 \text{ km s}^{-1}$ ,  $R_{\odot} = 8.35 \pm 0.15$  (Reid et al., 2014). As it has a positive velocity in the first quadrant, it is likely to be inner Galaxy ( $R < R_{\odot}$ ) and therefore gives near/far kinematic distances  $D_n = 1.8^{+0.7}_{-0.9}$  and  $D_f = 13.7^{+0.9}_{-0.7}$  kpc. The lower-bound distance estimate helps to resolve the ambiguity by supporting the far distance.

Although the parallax was not statistically significant, the proper motions were. I measured proper motions of  $\mu_x = -3.60 \pm 0.48$  and  $\mu_y = -6.35 \pm 0.16 \text{ mas/yr}$ . In Galactic coordinates this becomes  $\mu_{l*} = -7.3 \pm 0.3$ ,  $\mu_b = 0.2 \pm 0.3 \text{ mas/yr}$  and signifies almost complete motion in the negative  $l$ -direction (which is towards the Galactic centre). Using the above rotation curve, I calculate the possible velocities tangential to the line of sight with:

$$v_t = \sqrt{\Theta(R)^2 + \Theta_{\odot}^2 - 2\Theta(R)\Theta_{\odot}(R_{\odot} - d \cos l)}$$

where  $R$  is calculated via  $R^2 = d^2 + R_{\odot}^2 - 2R_{\odot}d \cos l$ . The Galactic rotation speed of the maser will be

$$v_{tm} = 4.7 d \mu_{l*} \text{ km s}^{-1}$$

where 4.7 is the approximate conversion between  $\text{km s}^{-1}$  and  $\text{AU/yr}$  if  $d$  is in kpc and  $\mu_{l*}$  is in mas/yr. Figure 3.3 shows the result of this basic modelling. Favourable regions include

### 3.3. RESULTS AND DISCUSSION

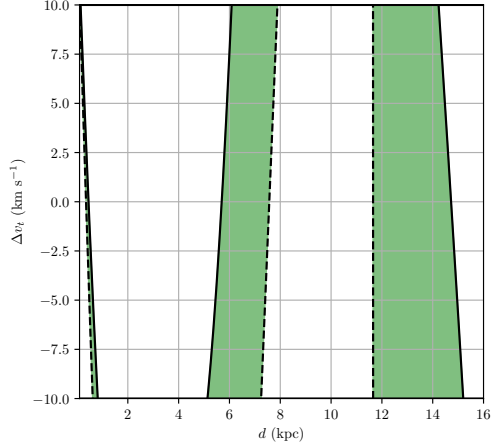


**Figure 3.3:** Modelled proper motion distance for G021.87+0.01 vs. residual velocity. **Solid line:** Upper 95% CI limit with  $\mu_1 = -6.4 \text{ mas/yr}$ ; **Dashed line:** Lower 95% CI with  $\mu_1 = -8.2 \text{ mas/yr}$ . **Green region:** acceptable velocity differences bounded by  $\pm 10 \text{ km s}^{-1}$ .

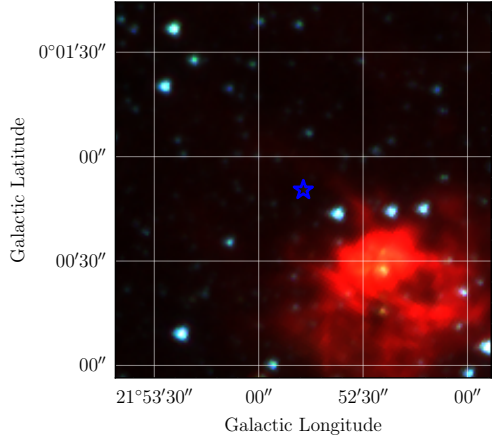


**Figure 3.4:** Astrometric position of H<sub>2</sub>O maser G021.87+0.01 against *Spitzer* GLIMPSE data. **Blue star:** position of G021.87+0.01  $l = 21.87977$ ,  $b = 0.01401$  deg. **RGB image:** 8, 4.5 and 3.6  $\mu\text{m}$  emission.

$0.1 < D < 0.8$ ,  $6.3 < D < 8.5$  and  $11.8 < D < 15.2$  kpc, the largest of these being consistent with the lower distance estimate and far kinematic distance.

It should be noted that the velocity structure of the Galactic centre region ( $4 \lesssim D \lesssim 11.8$  kpc) is more complex and hence poorly modelled. However, this does not disregard the likelihood of finding a target in this region to the random/viralised velocities of gas/stars in this region.

Finally, Figure 3.4 shows the sky position of G021.87+0.01 against photometric *Spitzer* IRAC data. The maser is spatially co-incident with a region of enhanced 4.5  $\mu\text{m}$  emission (aka. an EGO) outside of a larger region of 8  $\mu\text{m}$  emission. The small angular size of the EGO circumstantially supports a large distance.

Looking at additional information that may be relevant to estimating the distance to this source, it is listed as having an ‘Unconstrained’ KDA resolution from either HI self absorption, emission/absorption or 8  $\mu\text{m}$  absorption (Ellsworth-Bowers et al., 2015).

One of the main attributed reasons for the poor parallax constraint are maser morphological changes over the course of the observations. As clearly seen in Figure A.5, the spectrum changes drastically over a period of  $\sim 4$  weeks, before a longer stable period. The spread of the observations regrettably does not allow for careful sampling of the flux density over time, however,

### 3.3. RESULTS AND DISCUSSION

it is clear that the spectrum remained more stable for at least 8 weeks after the 4th epoch. At the date of the 4th epoch the spectrum is very weak and likely dimming below detectable levels. Comparing the calibrator flux density for epoch 4 against previous and future epochs indicates that this dimming is likely intrinsic and not a calibration or onsource-time issue; in fact, the noise level remains similar over the epochs.

Therefore, the spectra for the initial 4 epochs is very likely emanating from a different set of maser spots than the following 7, after which the maser dims below detectable levels. This necessity to ‘change’ phase reference features whether intended or otherwise introduces large systemic uncertainties that likely mask any detectable parallax signature. The spectral feature from latter epochs was from the same region and velocity, but likely a different part of the star formation region. Luckily all features apparently shared the same proper motion and this is why it was clearly detectable despite the feature change.

The phase reference feature (post epoch 7) also had structure. Imaging it with all 9 antennas proved difficult and began to resolve the internal structure which seemingly had varying intensity between the components. Therefore only the inner-five VLBA antennas (FT, KP, LA, OV and PT) were used and this also placed a lower-bound on the astrometric accuracy of any particular epoch at approximately  $\Delta\theta = \theta_{sep} \frac{1\text{cm}}{1508\text{ km}} \sim 60\mu\text{as}$ .

Finally only one of the two calibrators was sufficient intensity to be used as a phase reference calibrator. As the maser was weak and variable, inverse phase referencing was impossible for almost all epochs and normal phase referencing was required. The way the observations were conducted was designed for inverse phase referencing and therefore the sensitivity on the maser was reduced by a factor of  $\sqrt{2}$  as half the data were outside the coherence time.

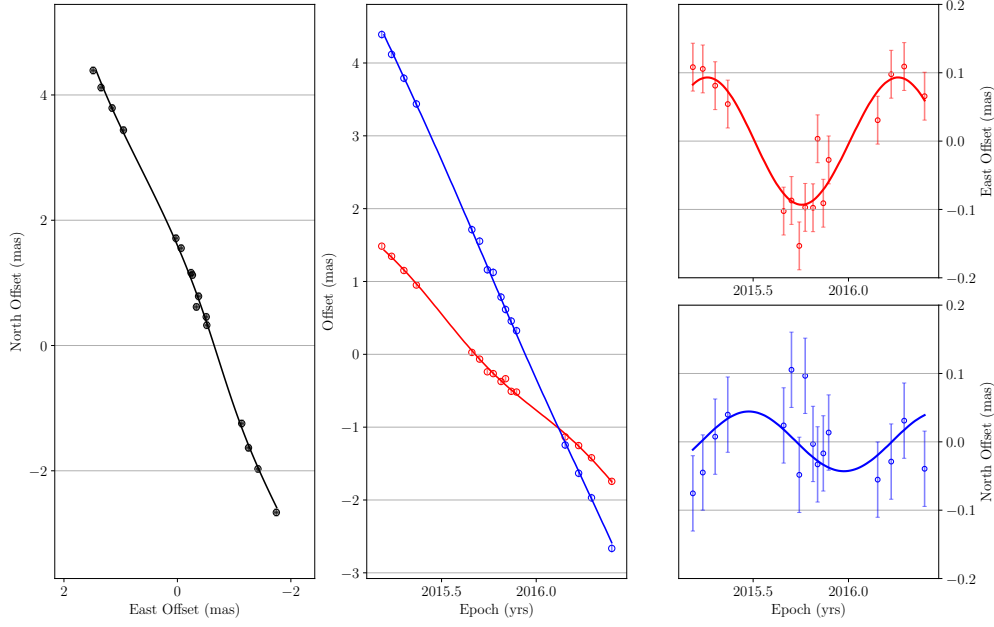
#### 3.3.3 G037.81+0.41

G037.81+0.41 is a 22.2 GHz water maser located towards HII regions and submillimeter sources in the inner Galaxy (Figure 3.6). I measured a parallax of  $\varpi = 0.084 \pm 0.008$  mas towards this star formation region, which implies a distance of  $D = 11.90^{+0.82}_{-0.72}$  kpc. As the parallax has fractional uncertainty  $f \simeq 0.1$ , no inclusion of priors or additional information is required and this is considered a direct measurement of the distance. The proper motions were measured as  $\mu_x = -2.64 \pm 0.02$ ,  $\mu_y = 5.68 \pm 0.03$  mas/yr, which converts to Galactic proper motions of  $\mu_{l*} = -6.27 \pm 0.02$ ,  $\mu_b = -0.266 \pm 0.002$  mas/yr.

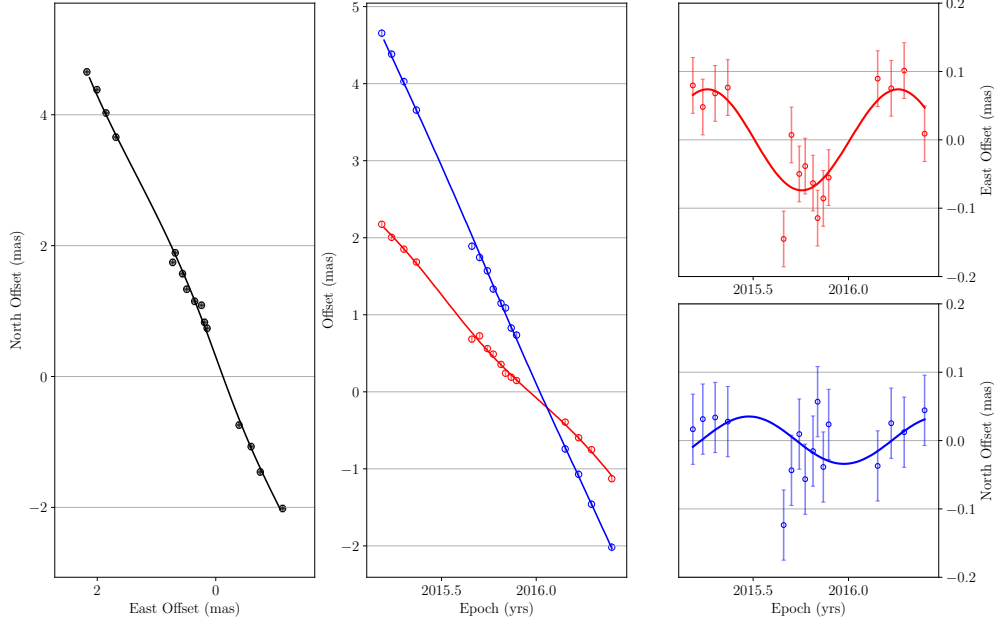
Figure 3.7 shows the spectrum and spatial–velocity distribution of maser spots (spotmap) for G037.82+0.41. The water maser has a spectrum with  $\sim 5$  peaks but a rich spatial distribution of spots. The spatial distribution of spots is reflective of a bipolar outflow as is commonplace in water maser structures.

The parallax measurement of G037.82+0.41 is a prime example of everything going right: compact maser component, compact and bright quasar sources, non-variable reference feature and no external/weather problems impacting observations. As such the astrometry is able to reach the theoretical minimum of  $\sigma_\theta \sim 0.01$  mas and this is reflected in the formal fitting errors for the parallax ( $\sigma_\theta = 2\sigma_\varpi \sim 16\mu\text{as}$ ).

### 3.3. RESULTS AND DISCUSSION



(a) With respect to J1855+0251.



(b) With respect to J1856+0610.

**Figure 3.5:** Parallaxes and proper motions of target G037.82+0.41 referenced to corresponding calibrators.

### 3.3. RESULTS AND DISCUSSION

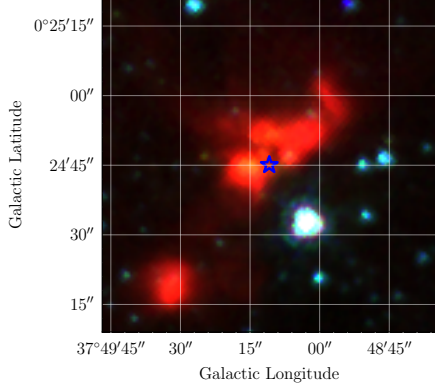


**Figure 3.6:** Astrometric position of H<sub>2</sub>O maser G037.82+0.41 against *Spitzer* GLIMPSE data. **Blue star:** position of G037.82+0.41  $l = 37.81968$ ,  $b = 0.41252$  deg. **RGB image:** 8, 4.5 and 3.6  $\mu$ m emission.

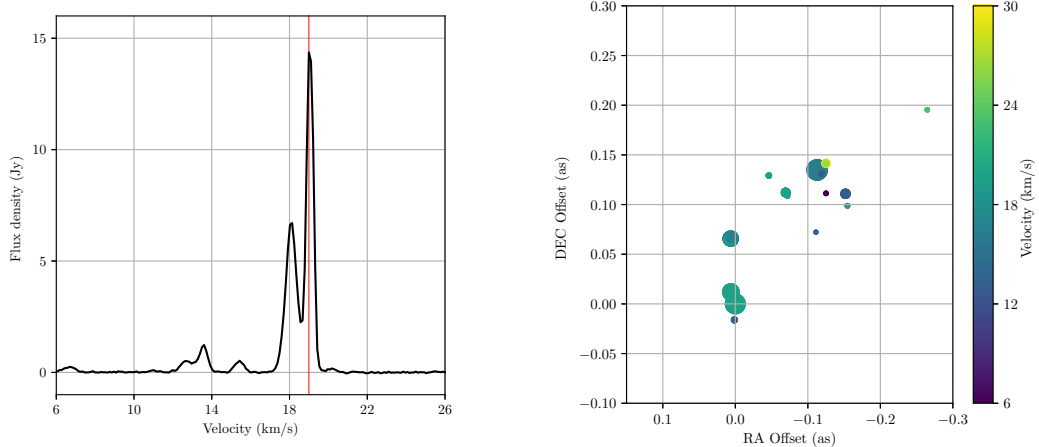


**Figure 3.7:** Spatial-velocity distribution of emission in G037.81+0.41 on epoch BR210C9. **Left:** Spectrum. Vertical red line indicates phase reference velocity. **Right:** Spotmap. Phase reference feature at (0,0). Phase reference velocity does not line up with peak in spectrum as there are two emission regions overlapping in frequency and spatially proximate (North–East of phase reference feature, similar velocity).

### 3.3. RESULTS AND DISCUSSION

#### 3.3.4 G060.58–0.18

G060.58–0.18 is 6.7 GHz class II methanol maser located towards a giant molecular cloud and HII region (Figure 3.9). A simple maser with a single emission region present in the auto- and cross-correlation spectrum, it only had one maser spot visible in the maps over the 16 epochs. This spot was compact and showed very little sign of variation and no signs of evolution.

I measured a parallax of  $\varpi = 0.130 \pm 0.009$  mas for G060.48–0.18 which gives a distance of  $D = 7.69_{-0.34}^{+0.38}$  kpc. The low fractional uncertainty  $f = 0.07$  makes the distance probability distribution near-Gaussian and therefore unambiguous. I also measured a proper motion of  $\mu_x = -3.23 \pm 0.02$  and  $\mu_y = -5.67 \pm 0.03$  mas/yr which become  $\mu_{l*} = -6.52 \pm 0.05$ ,  $\mu_b = -0.09 \pm 0.01$  mas/yr.

These values are statistically identical to the published parallax and proper motion of  $\varpi = 0.121 \pm 0.015$  mas and  $\mu_x = -3.26 \pm 0.15$  and  $\mu_y = -5.66 \pm 0.15$  mas/yr (Reid et al., 2019). These older measurements were attained as part of BR149(R) and used a 4-quasar setup of J1946+2418, J1949+2421 (which were used in BR210), J1946+2300 and J1936+2357 observed in 4 epoch total. Despite the fact that BR210 had 4× as many epochs there was not an assumed 2× decrease in parallax uncertainty (instead  $\frac{9}{15}$ ). Either formal errors in the original observations were underestimated, or there are sources of systematic uncertainty, so increasing the number of epochs does not reduce the uncertainty by  $\sqrt{N}$ . Nevertheless, the systematic errors must be sufficiently small or epoch independent to not skew the result.

The maser feature used for astrometry had a constant unresolved flux density of  $S_\nu \sim 5$  Jy, allowing for inverse PR to both quasars at all epochs with high  $\text{SNR} \geq 150$  (Table A.4). The quasars themselves were of very high quality in terms of flux density, absence of structure (Figure A.3) and perhaps most importantly: angular distance from maser (Figure 3.10).

The two quasars J1946+2421 and J1949+2418 were  $\theta_{sep} = 0.116$  and  $0.921$  deg from the maser respectively. Given the SNR on the detected quasars, the thermal noise is expected to be  $\sigma_{th} \sim 4\mu\text{as}$  and implies that the systematic uncertainty in the per-epoch astrometry is  $\sigma_\theta = 2\sigma_\varpi = 22$  and  $28\mu\text{as}$  for each quasar. Since the quasars are offset from the maser in approximately the same direction I consider the case where measurement uncertainty is modelled as being radially dependent on the separation between the calibrator and target:

$$\begin{aligned}\sigma_\theta^2 &= \sigma_{sys}^2 + \sigma_{cont}^2 \\ &= \theta_{sep}^2 \left( \frac{c\sigma_\tau}{|B_{max}|} \right)^2 + \sigma_{const}^2\end{aligned}$$

and fit the two-point data, I get  $\sigma_{const} = 22\mu\text{as}$  and  $\frac{c\sigma_\tau}{|B_{max}|} = 5.3 \times 10^{-9}$ . Therefore the expected average per-epoch residual delay is  $c\sigma_\tau = 4.5$  cm, which is consistent with that expected from ionosphere even after TEC calibration (Walker & Chatterjee, 1999).

This maser was repeated in BR210 as it is specifically important that the distance estimate is accurate. G060.57–0.18 is one of the few maser located in the Perseus Gap and the distance to this source has now been independently confirmed.

### 3.3. RESULTS AND DISCUSSION

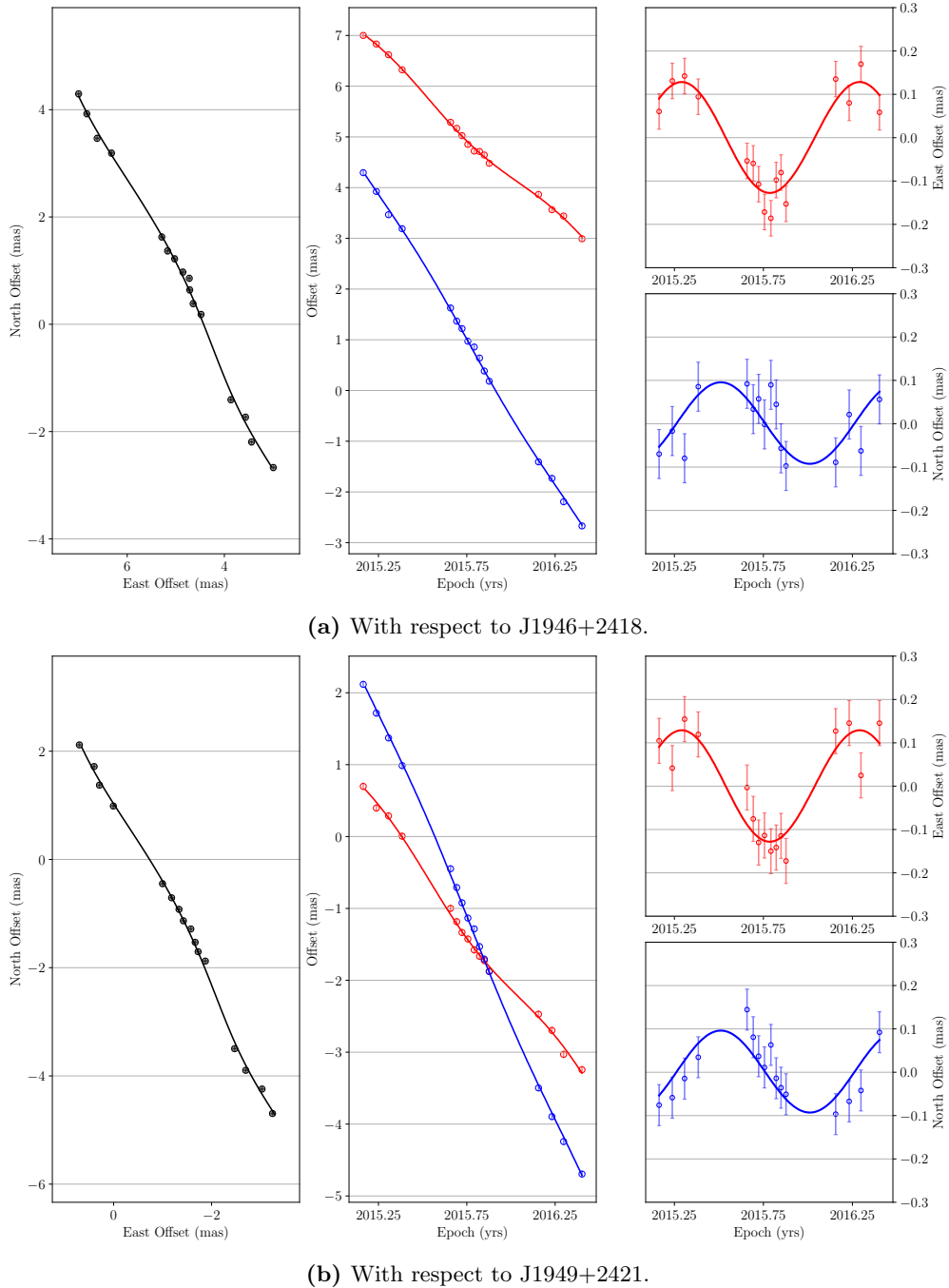


**Figure 3.8:** Parallaxes and proper motions G060.57–0.18 referenced to corresponding calibrators.

### 3.3. RESULTS AND DISCUSSION

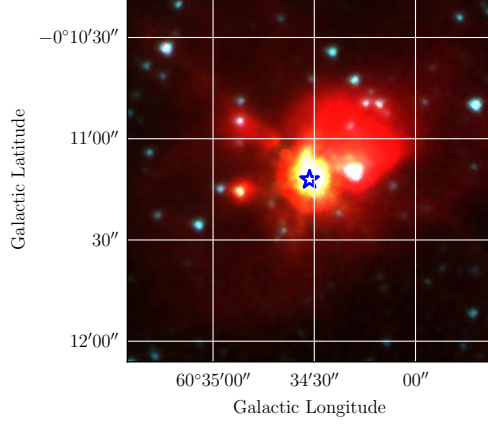


**Figure 3.9:** Astrometric position of  $\text{CH}_3\text{OH}$  maser G060.58–0.18 against *Spitzer* GLIMPSE data. **Blue star:** position of G060.58–0.18. **RGB:** 5  $\mu\text{m}$  emission; **RGB image:** 8, 4.5 and 3.6  $\mu\text{m}$  emission.

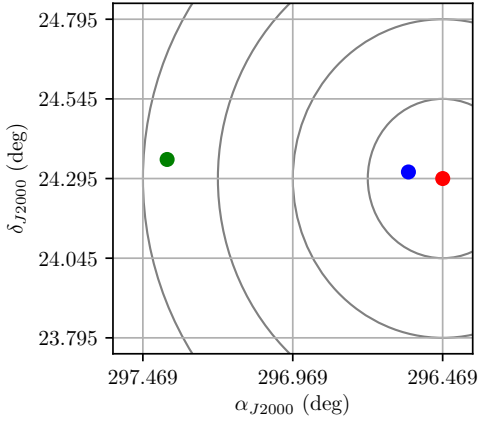


**Figure 3.10:** Quasar distribution for G060.57–0.18. **Red:** Maser position; **Blue:** J1946+2418 position; **Green:** J1949+2421 position. Quasars are aligned radially in the positive  $\alpha$ -direction. Concentric circles emanating from maser position are spaced 0.25 deg.

### 3.3. RESULTS AND DISCUSSION

#### 3.3.5 G070.29+1.60

G070.29+1.60 is a 22 GHz water maser located in the giant molecular cloud K3-50A/W58a (Kohoutek, 1965; Wynn-Williams, 1969). This maser is located near the centre of strong IR emission revealed by WISE data (Figure 3.12) and has an apparent companion 6.7 GHz methanol maser G070.18+1.74. The velocities of the two masers are statistically identical  $v_{\text{H}_2\text{O}} = -26.7 \pm 10$  and  $v_{\text{CH}_2\text{OH}} = -23 \pm 5 \text{ km s}^{-1}$  and appear to be part of the same molecular cloud. G070.18+1.74 is located on an arc offset  $\theta = 0.177 \text{ deg}$  away from G070.29+1.60.

I measure a parallax of  $\varpi = 0.097 \pm 0.011 \text{ mas}$  towards G070.29+1.60 (Table 3.2). Inverting this parallax suggests the most likely distance is  $D = 11.2^{+1.2}_{-1.1} \text{ kpc}$ . Additionally, I measured a proper motion of  $\mu_x = -1.45 \pm 0.04$  and  $\mu_y = -3.69 \pm 0.05 \text{ mas/yr}$  which convert to  $\mu_{l*} = -3.89 \pm 0.06$  and  $\mu_b = -0.74 \pm 0.02 \text{ mas/yr}$ .

G070.18+1.74 has a published parallax and proper motion of  $\varpi = 0.136 \pm 0.014 \text{ mas}$  and  $\mu_x = -2.88 \pm 0.15 \text{ mas/yr}$ ,  $\mu_y = -5.18 \pm 0.18 \text{ mas/yr}$  (giving  $\mu_{l*} = -5.92 \pm 0.15$  and  $\mu_b = -0.33 \pm 0.08 \text{ mas/yr}$ ; Zhang et al., 2019). These data was collected in BR149R. The parallaxes of the two masers are not statistically different, suggesting that the distance to W58a as a whole the average of  $D = 8.3 \pm 1.4 \text{ kpc}$ .

The proper motions of the two masers do not agree within error and I suggest that this is most likely due to internal motions of the water maser. Unfortunately there is not more than a single phase reference feature visible in enough epochs to determine motions directly. As many water maser are associated with outflows, they do not reliably trace the systemic velocity of gas. Class II 6.7 GHz methanol are associated with embedded stars and they have been found to trace the gas velocity  $\pm 3 \text{ km s}^{-1}$  (Green & McClure-Griffiths, 2011). Therefore, I assume the proper motions measured in BR149 more accurately represent to motion of the gas cloud as a whole and calculate the inferred internal motions of G070.29+1.60. This gives  $\mu_{x,int} = +1.33 \pm 0.16$  and  $\mu_{y,int} = +1.42 \pm 0.19 \text{ mas/yr}$  (or  $\mu_{l*,int} = +1.9 \pm 0.3$  and  $\mu_{b,int} = -0.36 \pm 0.06 \text{ mas/yr}$ ). At the distance of W58a this would be give  $v_x = +52 \pm 14$  and  $v_y = +55 \pm 15 \text{ km s}^{-1}$  (or  $v_{l*} = 75 \pm 20$  and  $v_b = -14 \pm 4$ ). The line-of-sight velocity spread of transient spectral features in G070.29+1.60 over the 16 epochs was  $v = -40$  to  $-15 \text{ km s}^{-1}$ .

Using the Bayesian distance estimator from Reid et al. (2014, 2019), I can compared the measured parallax distance to that expected from known Galactic structure and dynamics (Figure 3.13). In the left-hand panel I have also used the measured values for the proper motion of the single water maser component. In the right-hand panel I assume that the methanol maser proper motions represent a better estimate for the region. It should be noted that this programme uses known parallaxes around the line of sight; in this case the solid blue line is the previously determined parallax for the methanol maser G070.18+1.74 and should be ignored. With the raw measurement of the proper motion, the expected distance is ambiguous between  $D = 1.35 \pm 0.8$ ,  $6.75 \pm 0.92$  and  $13.36 \pm 0.74 \text{ kpc}$ . Taken alone, the  $\mu_b$  proper motion even favours a fourth distance of  $D \sim 4 \text{ kpc}$  in the local arm, however this is unfavoured by the other components. Using the modified proper motion as above, the number of plausible distances is reduced to only  $D = 6.77 \pm 0.78 \text{ kpc}$  which agrees with the averaged distance of  $D = 8.3 \pm 1.4 \text{ kpc}$ .

G070.29+1.60 was quite a weak maser with a dynamic and variable spectrum. As far as I could determine there was only a single component that could be reliably located and used for phase referencing between epochs 3 and F, with the exception of epochs 4, 5 and D. Strong spectral features were visible in epoch 1, 2 around  $v = -37 \text{ km s}^{-1}$ , heavily diminished in epoch 3, 4 then completely missing from 5 onwards. There was a persistent weak spectral feature (in scalar

### 3.3. RESULTS AND DISCUSSION

average cross-correlated spectra) at  $v = -23.34 \text{ km s}^{-1}$ , visible in 14 epochs, however the spatial position of this feature could not be reliably located after exhaustive searching. This spectral feature is very close to assumed systemic velocity of the region as traced by the methanol maser.

Due to the strength of the phase reference feature ( $S \leq 1 \text{ Jy}$ ) phases were referenced from the two quasars. Unfortunately this approach had the effect of reducing the SNR on the maser by an additional factor  $\sqrt{2}$ . This appears to be the primary reason why it was not possible to reliably image the weak maser feature at multiple epochs along with maser variability. It is likely that the phase reference feature first emerged above the noise at epoch 3.

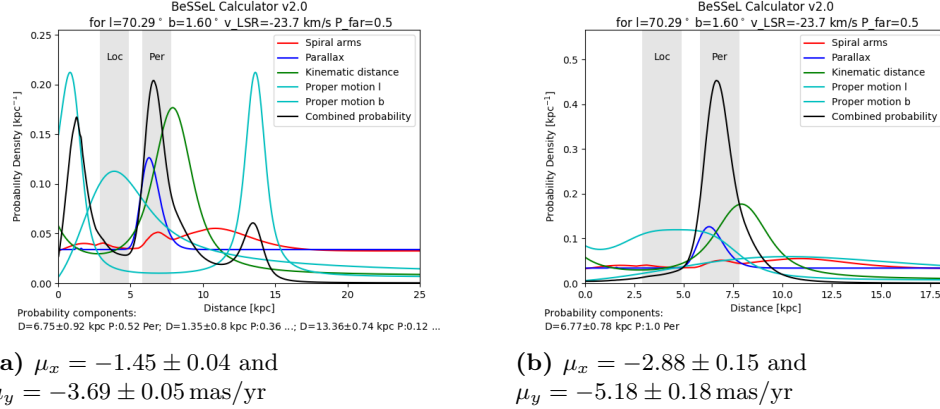
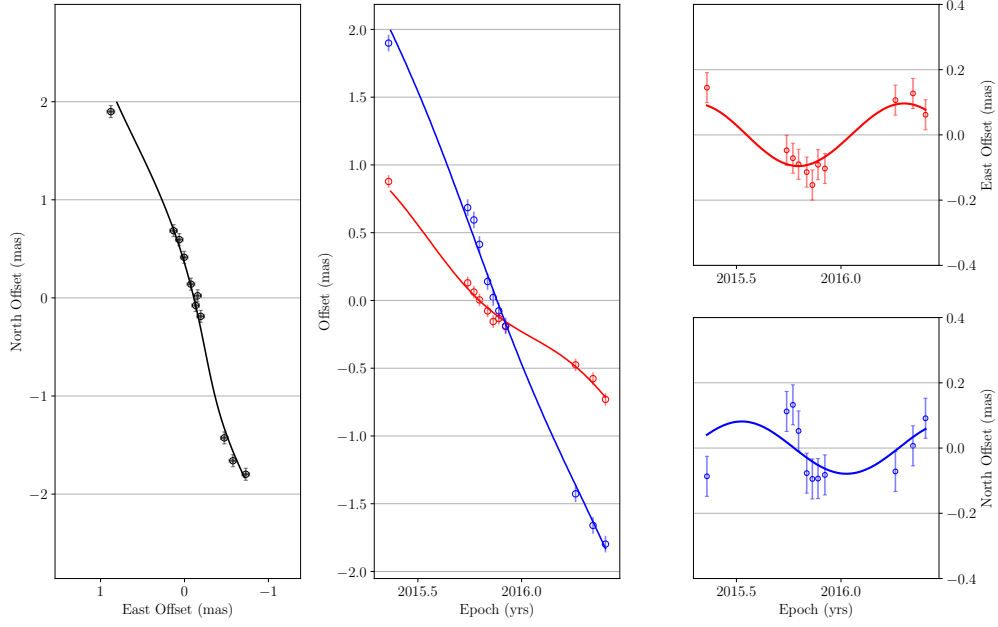


**Figure 3.13:** Bayesian distance estimator output from Reid et al. (2019) for G070.29+1.60 for respective proper motions. Line colours indicate different components of the probability density— **Red:** spiral arm locations; **Blue:** previous parallaxes; **Green:** kinematic distance; **Cyan:**  $l$  and  $b$  proper motions; **Black:** multiplicatively-combined probability density.

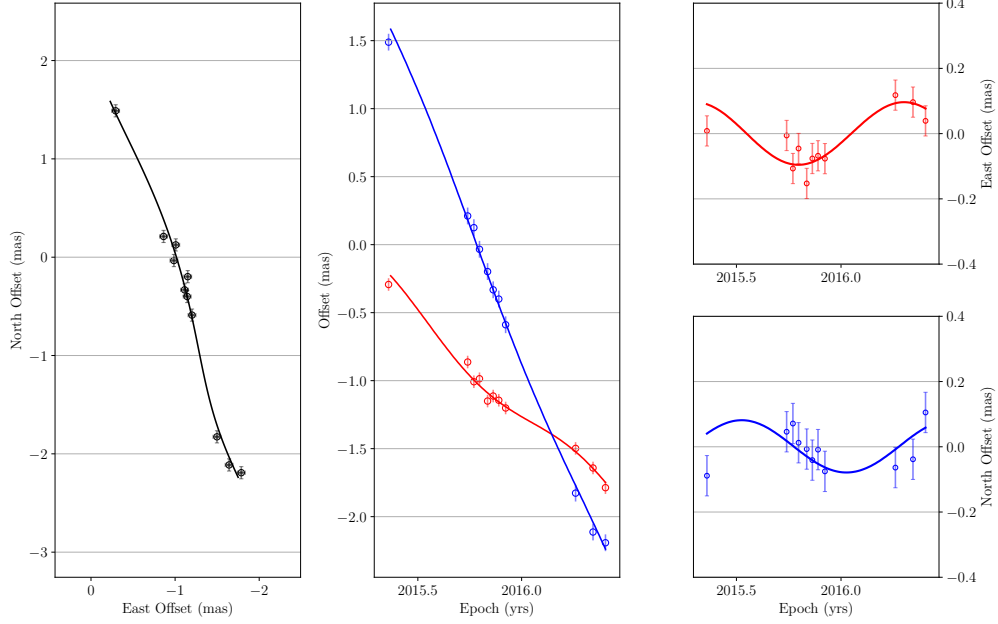
The parallax fit (Figure 3.11) depends disproportionately on the astrometry attained at epoch 3 compared to other epochs. This is due to the aforementioned spot variability and overall correlation of proper motion and parallax if the peaks are not sampled correctly. With the current fit for the parallax and proper motion of G070.29+1.60, the correlation coefficient between parallax  $\varpi$  and proper motions  $\mu$  are  $\rho(\varpi, \mu_x) = -0.48$  and  $\rho(\varpi, \mu_y) = -0.06$  for the East–West and North–South respectively. Removal of this point has serious implications for all variables and correlations. The parallax fit without epoch 3 becomes  $\varpi = 0.209 \pm 0.029 \text{ mas}$ ,  $\mu_x = -1.84 \pm 0.08 \text{ mas/yr}$  and  $\mu_y = -3.90 \pm 0.04 \text{ mas/yr}$  with  $\rho(\varpi, \mu_x) = -0.95$  and  $\rho(\varpi, \mu_y) = -0.42$ ! Inverting this alternate parallax would suggest the most likely distance is  $D = 3.85^{+0.21}_{-0.19} \text{ kpc}$  and would imply the maser is in the Local arm and a full 3 kpc away from the distance measured. This suggests formal parallax fitting errors for under-sampled parallax curves are underestimated at best.

As I will show in the next section, the apparent height above the plane for G070.29+1.60 is  $z - z_\odot = 247 \text{ pc}$  and has a  $Z$ -velocity  $\dot{Z} = -14 \text{ km s}^{-1}$  (or  $-29 \text{ km s}^{-1}$  using measured values). This is quite an atypical region, far above the plane and with dynamics that are complex and difficult to interpret.

### 3.3. RESULTS AND DISCUSSION



(a) With respect to J1957+3338.



(b) With respect to J2001+3323.

**Figure 3.11:** Parallax and proper motion for target G070.29+1.60 referenced to corresponding calibrators.

### 3.3. RESULTS AND DISCUSSION

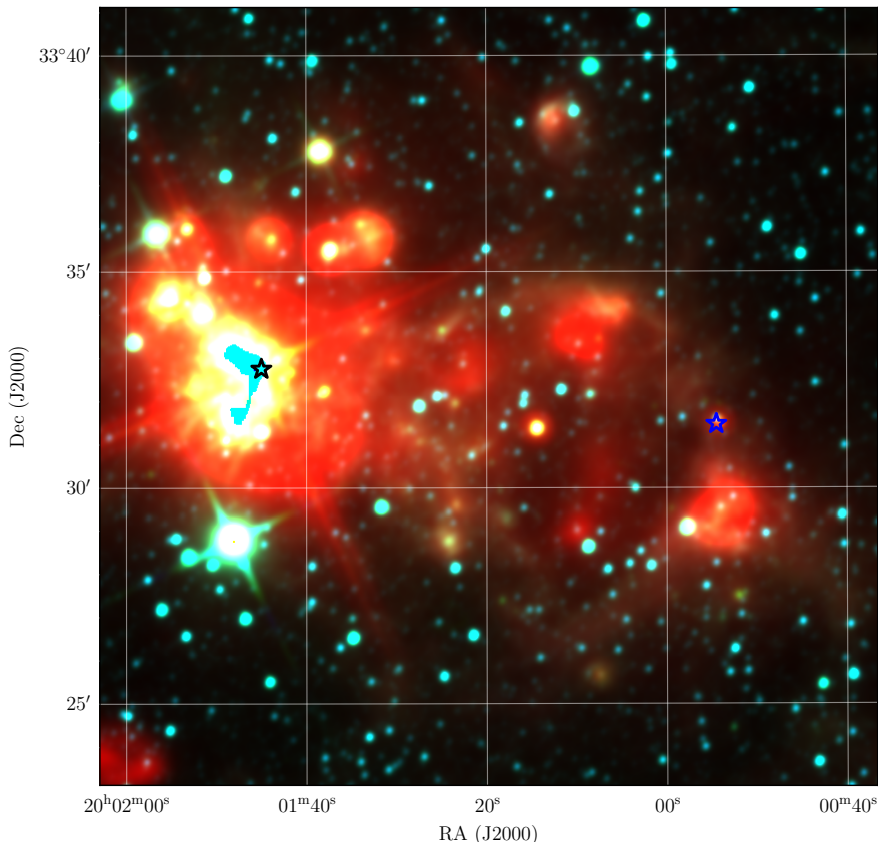


**Figure 3.12:** K3-50A/W58a giant molecular cloud region. **RGB image:** WISE W4,W2,W1 (22, 4.6,  $3.4\mu\text{m}$ ); **Black star:** H<sub>2</sub>O maser G070.29+1.60; **Blue star:** CH<sub>3</sub>OH maser G070.18+1.74. Image size is  $9'\times 9'$  in J2000 coordinate system.

### 3.3. RESULTS AND DISCUSSION

#### 3.3.6 Kinematics and Spiral Arm Modelling

Following standard definitions, Galactic radius is  $R = 0$  kpc at the Galactic centre and Galactic azimuth is  $\beta = 0^\circ$  towards the Sun and increasing clockwise following Galactic rotation. Careful

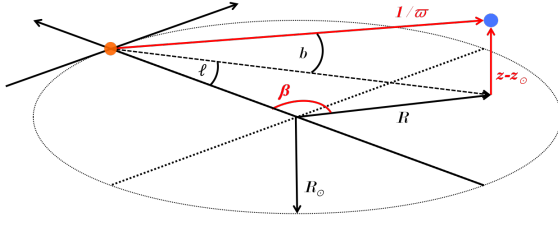


**Figure 3.14:** Schematic of the relationship between Galactic  $(l, b, \frac{1}{\omega})$  and Galactocentric  $(R, \beta, z)$  coordinate systems.

inspection of Figure 3.14 reveals the conversion from Galactic coordinates  $(l, b, \frac{1}{\omega})$  to cylindrical Galactocentric coordinates  $(R, \beta, z)$  are:

$$\begin{aligned} R &= \sqrt{R_\odot^2 + \frac{\cos^2 b}{\omega^2} - 2\frac{R_\odot}{\omega} \cos l \cos b} \\ \sin \beta &= \frac{\cos b \sin l}{\omega R} \\ z - z_\odot &= \frac{1}{\omega} \sin b \end{aligned}$$

again using  $R_\odot = 8.35 \pm 0.15$  kpc (Reid et al., 2014). Use of a cylindrical coordinate system and general disregard for the height variable  $z$  in spiral arm modelling is justified due to apparent solid body rotation and general constraint of maser regions to  $|b| < 5^\circ$ . The maser scale height is thought to be  $27 \pm 1$  (Green & McClure-Griffiths, 2011) or  $19 \pm 2$  pc (Reid et al., 2019) and this makes the ratio  $\frac{z}{D} \ll 1$  for all masers to good approximation.

The reader is left to convert to Galactocentric Cartesian as desired with  $X = -R \cos \beta$ ,  $Y = R \sin \beta$  and  $Z = z - z_\odot$ . Of note however are the instantaneous changes to  $X, Y, Z$  called  $U, V, W$  in  $\text{km s}^{-1}$ . I can now convert maser Galactic coordinates to Galactocentric cylindrical coordinates. Using the above it can be shown that the conversion from Galactic velocities  $(v, \mu_{l*}, \mu_b)$  to Galactocentric Cartesian velocities  $(U, V, W)$  requires the application of another rotation matrix:

$$\begin{bmatrix} U \\ V \\ W \end{bmatrix} = \begin{bmatrix} \cos b \cos l & -\sin l & -\cos l \sin b \\ \cos b \sin l & -\cos l & -\sin l \sin b \\ \sin b & 0 & \cos b \end{bmatrix} \begin{bmatrix} v \\ 4.7 D \mu_{l*} \\ 4.7 D \mu_b \end{bmatrix}$$

where  $v$  is the line-of-sight velocity in  $\text{km s}^{-1}$  and 4.7 is the approximate conversion from AU/yr to  $\text{km s}^{-1}$ . Galactocentric cylindrical coordinates are particularly useful for analysis of spiral arm pitch angles. These determinations are given in Table 3.3.

I consider spiral arms to take the classic log-spiral form as defined below:

$$\ln \left( \frac{R}{R_0} \right) = -\tan \psi (\beta - \beta_0)$$

where  $\psi$  is the spiral arm pitch angle and  $R_0$  and  $\beta_0$  are the values of the spiral arm distribution at some arbitrary reference position. When plotted as  $\ln R$  vs.  $\beta$ , maser distribution should

### 3.3. RESULTS AND DISCUSSION

**Table 3.3:** Measured position in Galactocentric coordinates for masers based off measured quantities. (1) Maser name in Galactic coordinates, (2) distance between Sun and maser, (3) Galactocentric radii, (4) Galactocentric azimuth, (5) relative Galactic height, (6)  $X$  velocity, (7)  $Y$  velocity, (8)  $Z$  velocity.

Maser	$D$ (kpc)	$R$ (kpc)	$\beta$ (deg)	$z - z_{\odot}$ (pc)	$U$ ( $\text{km s}^{-1}$ )	$V$ ( $\text{km s}^{-1}$ )	$W$ ( $\text{km s}^{-1}$ )
<b>G021.88+0.02</b>	14.1	7.1	131	4.2	173.7	398.7	-17.9
<b>G037.82+0.41</b>	11.9	7.4	97.5	86.4	266.1	324.8	+13.8
<b>G060.57-0.18</b>	7.7	8.1	55.3	-24.3	207.8	120.4	-3.3
<b>G070.29+1.60</b>	8.3	9.9	56.5	247	222.2	69.0	-14.7

form a straight line with slope  $= -\tan \psi$ . I also wish to only consider spiral change in a ‘small’ Galactic azimuthal section such that  $0 \leq \beta - \beta_0 < 360^\circ$ .

In addition to the distances calculated/measured in this chapter, I include known parallaxes thought to be associated with the Perseus arm. I aim to simultaneously confirm that the masers measured here indeed are Perseus-associated and also determine a Perseus arm pitch angle including them.

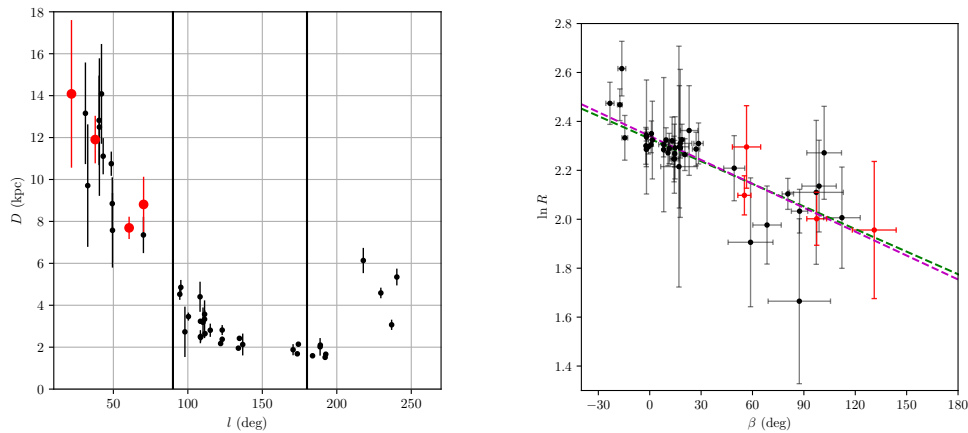


**Figure 3.15:** Spiral arm fitting. **Left:** Distribution of Galactic Longitude  $l$  vs. distance  $D$ . **Right:** Distance and  $l$  converted to  $\ln R$  and  $\beta$  with distance errors propagated and shown as  $1\sigma$ . **Black markers:** Perseus arm associated masers; **red markers:** masers reduced in this chapter; **green line:** fit from weighted least-squares; **magenta line:** from normal least squares.

Fitting  $(\ln R, \beta)$  with weighted least squares gives pitch angle for the Perseus arm of  $\psi_{p,w} = 10.77 \pm 0.04$  deg. Un-weighted least squares gives a more conservative estimate of with  $\psi_{p,uw} = 13.2 \pm 3.9$  deg. Both these values agree statistically with previous estimates  $\psi = 9.1 \pm 1.4$  deg from Reid et al. (2014) or  $\psi_< = 10.3 \pm 1.4$ ,  $\psi_> = 8.7 \pm 2.7$  from Reid et al. (2019). As a note on notation,  $\psi_<$  and  $\psi_>$  indicate values for the pitch angle before and after the so-called ‘kink’ in the spiral arms (see Reid et al., 2019, for details).

### 3.4. CONCLUDING REMARKS

## 3.4 Concluding Remarks

I have determined the distances to and calculated the Galactic dynamics of 4 HMSFR in the First Galactic Quadrant. I have also identified them with the Perseus spiral arm and calculated an updated pitch angle.

The analysis performed here has not only enhanced the knowledge pool in relation to Galactic structure visible from the Northern Hemisphere, but it is representative of the priorities necessary for accurate parallax measurements. Although interpolation of spiral structure is possible, S $\pi$ RALS will not be able to directly benefit from previously measured parallaxes or accurately known Galactic dynamics. S $\pi$ RALS aims to provide the measurements for future modelling and therefore it is important to learn lessons from BeSSeL.

Astrometry of G021.87+0.01 and G070.29+1.60 demonstrate the degrading influence of water maser variability and evolution. Both distance determinations would not have been possible without additional constraints otherwise unavailable for S $\pi$ RALS and these are due to maser evolution. Evolutionary and variability effects are only apparent once the data are observed and reduced and cannot be mitigated through calibration or other techniques.

Particular to these two masers is their low flux density, so astrometric observations would benefit greatly from more onsource time. Due to the large number of baselines available on the VLBA (36 or 45) shared tracks generally still provide sufficient onsource time and *uv*–coverage. It is also recognised that time has to be optimised for observations made using a competitive application–scheduled facility. S $\pi$ RALS will largely *not* be weighted down due to facility availability. The ASCI array is owned and operated by the University of Tasmania and therefore there will be ample time available for well–sampled parallax measurements. This is extremely important due to the much smaller number of baselines (6 or 10) with generally lower sensitivity suggesting that it is more important to focus on sampling few targets well.

G021.87+0.01 individually demonstrates the importance of high quality quasars. When inverse phase referencing was not possible, normal PR techniques were required. Unfortunately both reference quasars were too weak to get reliable fringe solutions and entire epochs had to be discarded. If at least one quasar had been bright enough with uncertain position or structure; calibration techniques exist to mitigate or model those effects. So intrinsically weak quasars limit the calibration approaches that can be used and are probably not worth using them at all because of this. G037.81+0.41 demonstrates that two ‘far’ quasars ( $\theta_{sep} \sim 1.8$  deg) at *K*–band still can give good parallaxes.

Finally from G070.29+0.01 it is demonstrated that correct sparse sampling is more important than intense sampling. In theory, intense sampling of parallax curvature about the peak is able to break the fit degeneracy in the case of a missing first or last peak. However, in practice this should not be relied upon, especially for potentially distant targets. The correlation of proper motion and parallax in these cases makes the parallax unreliable at best and misleading at worst.

Critical analysis of the parallax measurements undertaken for this thesis suggest that the formal parallax and proper motion uncertainties resulting from normal/weighted least–squares fitting are underestimated. Future work in trigonometric parallaxes will include an alternative fitting approach, most likely Markov–Chain Monte Carlo Bayesian orientated to accurately estimate parallax and proper motion curves and uncertainties from astrometric data in S $\pi$ RALS.



# 4

## SOUTHERN HEMISPHERE 6.7 GHz METHANOL MASER COMPACTNESS CATALOGUE

Many of the problems encountered during the BeSSeL VLBI maser astrometry analysis completed in the previous chapter are immediately resolved by using class II methanol masers instead of 22 GHz water masers. Class II 6.7 GHz methanol masers are almost as intrinsically bright as 22 GHz water masers and are known to be stable for periods much longer than a year.

There are over 1000 known individual 6.7 GHz class II methanol masers visible from the Southern Hemisphere, approximately half exclusively so. However, compared to water masers, methanol masers spots are typically larger– in many cases being resolved. If S $\pi$ RALS is to use 6.7 GHz masers as astrometric targets these diffuse, weak and/or structured masers need to be identified so that they can be avoided. The desirability of a maser target for astrometry is often summarised with a quantity called ‘compactness’.

In this chapter I determine a first target list for S $\pi$ RALS by modelling angular sizes of 6.7 GHz methanol maser spots and relating them with metrics that characterise compactness. In this way, I construct a VLBI compactness catalogue for all relevant Southern Hemisphere 6.7 GHz methanol masers.

## 4.1. INTRODUCTION

### 4.1 Introduction

Class II 6.7 GHz methanol masers are the second brightest maser transition observed in astronomy after 22 GHz water masers. However, it can be the case that a large fraction of the flux density emanates from large diffuse structures ( $> 0.1 - 1.5$  arcseconds at a distance of 4 kpc; Caswell, 1997) or many small velocity/spatially overlapping regions of low flux density. The surveys that discover these masers (e.g. Caswell et al., 2010, etc) will use single-dish observation and the intrinsic size of methanol maser emitting regions are much smaller than a single dish beam. Therefore the exact angular size, extent and compactness of many maser species are unknown until high resolution imaging with interferometry (e.g. Phillips et al., 1998) or VLBI (e.g. Minier et al., 2002; Goedhart et al., 2005; Bartkiewicz et al., 2009).

S $\pi$ RALS is scheduled to spend hundreds of hours observing class II 6.7 GHz methanol masers for the purpose of high-accuracy, high-precision astrometry. Therefore there is an initiative to find 6.7 GHz methanol masers that are the most compact, and can give the best astrometry. The Methanol Multibeam catalogue (MMB; Caswell et al., 2010; Green et al., 2010; Caswell et al., 2011; Green et al., 2012; Breen et al., 2015) contains all known Southern Hemisphere 6.7 GHz class II methanol masers as observed by the Parkes 64 m radio telescope. However, in order to determine which ones are the best for astrometry in S $\pi$ RALS, I must observe all appropriate masers from this list with VLBI.

### 4.2 Source Selection and Observations

As discussed in Section §1.4.3, the AuScope–Ceduna Interferometer (ASCI) array will be the instrument used for S $\pi$ RALS. The ASCI array is not specifically designed for maser astrometry and is comprised of sensitive but heterogeneous large telescopes and homogeneous geodetic 12 m telescopes. The new 6.7 GHz capable receivers being installed on the 12 m telescopes have a focus on broad frequency coverage and low maintenance, rather than maximising performance at 6.7 GHz (receiver temperature 70 K, SEFD estimations around 3500 Jy).

Considering these factors, I can estimate a detection limit for masers. The baseline sensitivity between Ceduna 30m (SEFD  $\approx$  650 Jy) to a geodetic 12 m antenna is expected to be

$$\sigma = \sqrt{\frac{S_1 S_2}{2 \tau_{\text{int}} \Delta \nu}} = \sqrt{\frac{3000 \times 650}{2 \times 60 \times 2 \times 10^3}} = 3.0 \text{ Jy} \quad (4.1)$$

for  $\tau_{\text{int}} = 60$  s integration and  $\Delta \nu = 2$  kHz spectral resolution ( $\Delta v = 0.09 \text{ km s}^{-1}$ ). Therefore, for a  $5\sigma$  detection ASCI needs to observe masers on baselines  $|\mathbf{B}|/\lambda = B_\lambda = 35 \text{ M}\lambda$  with a correlated flux density of at least  $S_{B_\lambda} \geq 15 \text{ Jy}$ .

As such, I take all masers with peak flux density catalogued  $S_0 \geq 10 \text{ Jy}$  for completeness and accounting for possible variability. Although it is unlikely the peak flux density will remain constant for all baselines, this sub-catalogue of targets then also provides sampling for weaker sources appropriate for the more sensitive Australian Long Baseline Array (LBA), Square-Kilometer Array (SKA) or potential future iterations of ASCI.

This subset of masers was observed using the LBA on 4th March 2016 and 22 March 2016 (project code V534). The participating telescope parameters are listed in Table 4.1 and the baselines and sensitivities are listed in Table 4.2. The LBA utilised a Data Acquisition System (DAS) which

## 4.2. SOURCE SELECTION AND OBSERVATIONS

**Table 4.1:** V534 LBA telescopes. **Columns:** (1) Telescope colloquial name; (2) two letter station code; (3) latitude; (4) longitude; (5) height above sea-level; (6) dish diameter; (7) 6.7 GHz primary beam size; (8) 6.7 GHz nominal SEFD; (9) owner/operating institute. All telescopes participated in both epochs of V534.

Station	Code	Latitude (deg)	Longitude (deg)	$z$ (m)	D (m)	$\theta_{6.7}$ (as)	SEFD (Jy)	Institute
<b>ATCA (tied)</b>	At	30.31288 S	149.56476 E	252	5×22	413	50	CSIRO
<b>Ceduna</b>	Cd	31.86769 S	133.80983 E	165	30	303	650	UTAS
<b>Hobart</b>	Ho	42.80358 S	147.44052 E	65	26	350	850	UTAS
<b>Mopra</b>	Mp	31.26781 S	149.09964 E	867	22	413	850	CSIRO
<b>Parkes</b>	Pa	32.99840 S	148.26352 E	415	64	142	110	CSIRO
<b>Warkworth</b>	Wa	36.43316 S	174.66295 E	123	30	303	650	WRAO

**Table 4.2:** **Left:** VLBI baselines for the Australian LBA participating telescopes. **Upper Left:** Linear distances (km) between the antennas as calculated by NRAO VLBI scheduling program SCHEDE. **Lower Left:** Approximate mean  $uv$ -distance ( $M\lambda$ ) for 6.7GHz observations. **Right:** Approximate ( $\pm 10\%$ ) baseline sensitivities (Jy) for a 1 min integration and 2 kHz spectral resolution.

	$ B $						$\sigma_s$ (Jy)					
	At	Cd	Ho	Mp	Pa	Wa	At	Cd	Ho	Mp	Pa	Wa
<b>At</b>	1508	1396	114	322	2409							
<b>Cd</b>	34		1702	1448	1361	3718	0.4					
<b>Ho</b>	31	38		1286	1089	2415	0.5	1.8				
<b>Mp</b>	2	32	29		207	2411	0.5	1.8	2.1			
<b>Pa</b>	7	30	24	5		2425	0.2	0.7	0.8	0.8		
<b>Wa</b>	54	83	54	54	54		0.4	1.6	1.8	1.8	0.7	

recorded two IF bands, each 16 MHz dual circular polarisation centred on 6308 and 6668 MHz at a total data rate of 256 Mbits/s.

Observational structure was 150 s scans on each of 187 separate 6.7 GHz maser targets distributed between  $l = 188 \rightarrow 360^\circ$  and  $|b| \leq 2^\circ$  over two epochs (Figures 4.1 and 4.2). Scans on fringe-finder quasars were also scheduled every  $\sim 3$  hours, with an average onsource time of  $\sim 5$  min.

Telescope baseband data was correlated with DiFX (Deller et al., 2007) at the Pawsey supercomputer facilities in association with Curtin University, WA. The data for each experiment was correlated in one pass with an integration time of  $\tau_{int} = 2$  s and 8192 spectral channels. This gave a frequency resolution of  $\Delta\nu = 1.95$  kHz or a velocity resolution of  $\Delta v = 0.09 \text{ km s}^{-1}$  at 6.7 GHz in each IF.

### 4.3. DATA REDUCTION

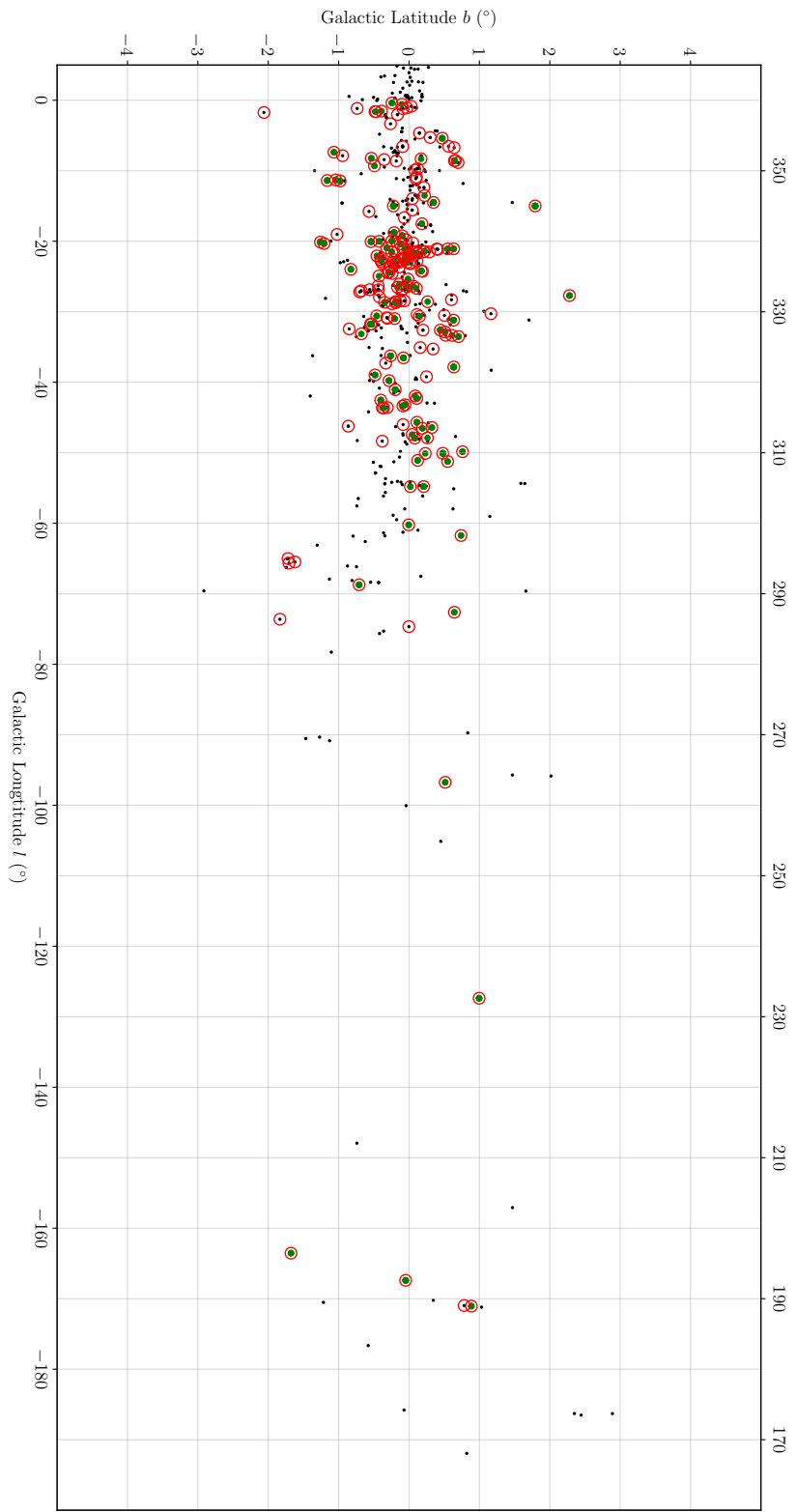


**Figure 4.1:** **Black:** The positions of all known Galactic 6.7 GHz methanol masers collected in Yang et al. (2019), primarily from Caswell et al. (2010); Green et al. (2010); Caswell et al. (2011); Green et al. (2012); Breen et al. (2015) (and additional referenced therein) between  $-200 < l < 20^\circ$ ,  $|b| < 5^\circ$ . Only 4 methanol masers ( $G206.542 - 16.355$ ,  $G208.996 - 19.386$ ,  $G209.016 - 19.398$ ,  $G213.705 - 12.597$ ) are catalogued  $-200 < l < 20^\circ$ ,  $|b| > 6^\circ$  and were not included in this survey. **Red circles:** The positions of all 6.7 GHz methanol masers included in this survey. **Green:** Positions of modelled masers.

#### 4.3. DATA REDUCTION

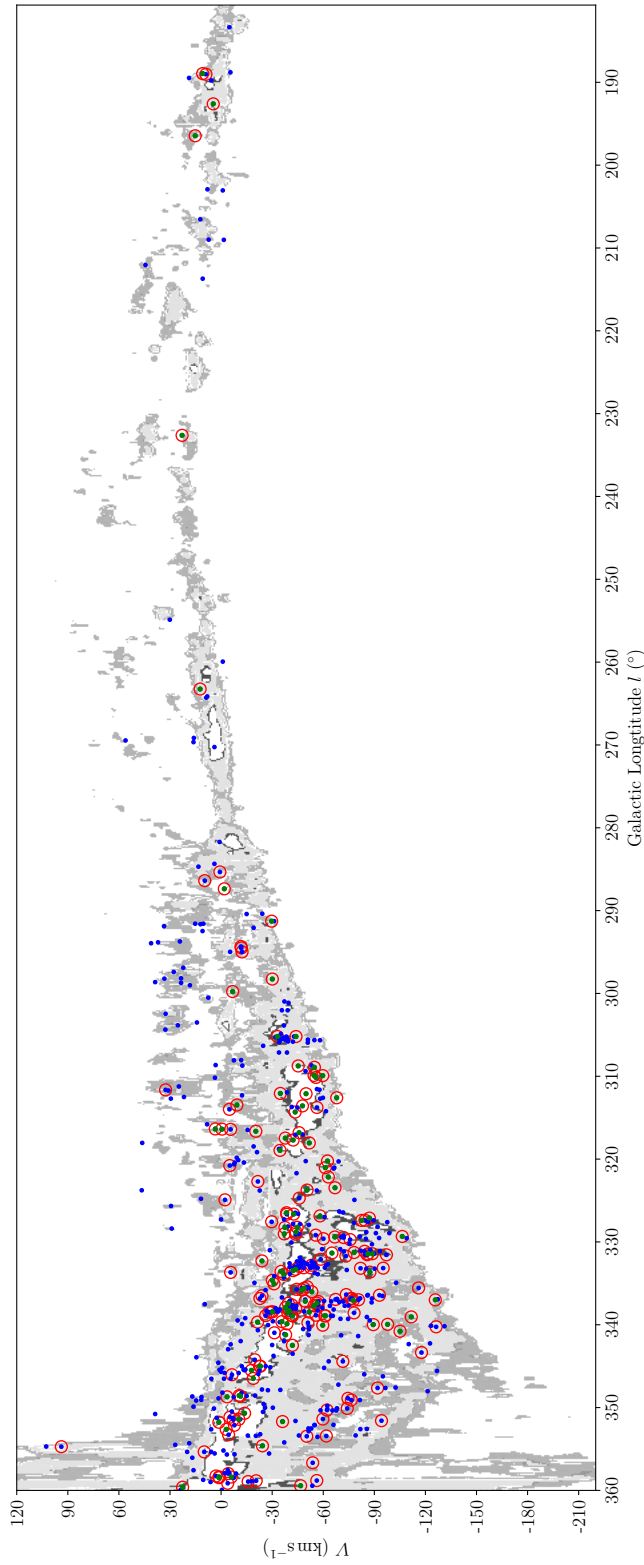


**Figure 4.2:** Longitude-velocity ( $l$ - $v$ ) diagram of the 3rd and 4th quadrants of the Milky Way. **Grey:** Greyscale CO integrated emission ( $\text{K}/\text{arcdeg}$ ) from the  $b \leq 4^\circ$  central strip of the Milky Way, adapted from Dame et al. (2001) (Figure 3 therein). **Blue:** Positions of all known 6.7 GHz methanol masers between  $270 < l \leq 360^\circ$ . **Red circles:** Positions of targeted masers. **Green:** Modelled masers.

## 4.3 Data Reduction

### 4.3.1 AIPS reduction

Data were reduced in *AIPS* using the procedure shown schematically in Figure 4.5. As a note on the nomenclature, some *AIPS* ‘tasks’ calculate and produce solution (*SN*) tables which can then be applied to multi-source data by being merged with a calibration (*CL*) table. New *CL* tables can be applied directly to the multi-source data upon inspection or further calibration/analysis. Descriptions of the various steps are given below.

1. Using the task ‘FITLD’, the data were loaded into *AIPS* from the correlated FITS files as *uv*–data sets and basic header tables.
2. The analog signal measured by a telescope is first digitised (in this case 2-bit) before being recorded. The task ‘ACCOR’ is used to calculate potential errors resulting from sampler thresholds by determining how much the autocorrelation spectra deviates from unity. This creates *SN1* which is merged with *CL1* using the task ‘CLCAL’ to create *CL2*.
3. Where available, the antenna temperatures over the experiment are extracted from the antenna .log files. *TY1* and *GC1* are created from the antenna temperatures and gain–curves (at  $\sim 6.7$  GHz) respectively by *AIPS* task ‘ANTAB’. *TY1* and *GC1* are then merged into an amplitude gain calibration table *SN2* which is merged with *CL2* via ‘CLCAL’ to make *CL3*. Where tsys information was not available, nominal SEFD values (Table 4.2) were added to *CL3* with task ‘CLCOR’. This approximate amplitude calibration procedure made *step 8* necessary.
4. Antenna .log files are used to determine off–source slewing times, windstows and downtime. Offending times are flagged with ‘UVFLG’ to produce flag table *FG1*.
5. Autocorrelation data on quasars was used to determine time–variable bandpass shape for each antenna IF/polarisation via task ‘BPASS’, creating a bandpass table *BP1*.
6. Bulk–electronic and instrumental delays for each antenna/polarisation/IF are solved for by task ‘FRING’. Scan chosen for this solution is a bright continuum source for which all antennas had onsource time. Rate solutions are zero–ed. This created *SN3* which is merged into *CL3* by ‘CLCAL’ to create *CL4*.
7. Task ‘FRING’ is used on the remaining continuum sources to calculate a time–variable multiband delay, the slope of which should approximate the antenna clock drift rate. This clock rate is externally calculated ( $\dot{\tau} \approx \frac{\Delta\tau}{\Delta t}$ ), then applied via task ‘CLCOR’ into *CL5*.
8. Externally, the ParselTongue script *maser\_amplitude\_calibrate.py* is run. The amplitudes of the cross–correlation data are corrected using the autocorrelation flux density of the masers, which in effect scales the antenna gains to that of the reference. This process generates *CL6*. See Section §4.3.2 for more information on this external processing.
9. Now that antenna gains, clock–rates and delays are approximately accounted for, the internal integration time for the *uv*–data is increased from  $\tau_{\text{int}} = 2$  s to 60 s with task ‘UVAVG’. This has the effect of averaging the data. This process applies all pre–existing calibration, bandpass and flag tables, and generates a new *uv*–data set.

### 4.3. DATA REDUCTION

10. Task ‘SETJY’ is used to set the reference frequency of the data to the rest–frequency of CH<sub>3</sub>OH 5<sub>1</sub> → 6<sub>0</sub> A<sup>+</sup>, at 6.6685192(8) GHz (Müller et al., 2004). This re–calculates Doppler velocities and results in spectra. ‘CVEL’ can then be used to shift the spectral line data to account for the rotation of the Earth and Solar System movement. This creates a final *uv*–data set.

#### 4.3.2 Notes on external *ParselTongue* scripts

**ParselTongue script *maser\_amplitude\_calibration.py*** is a custom alternative to the *AIPS*-task ‘ACFIT’. ‘ACFIT’ uses a well–calibrated template autocorrelation spectra from one antenna and a short time range to determine amplitude gain errors in the remaining spectra. This generates an *SN* table of time–variable gains to be reapplied to the data. Regrettably, ‘ACFIT’ is suited for a single/limited number of individual maser sources observed in one epoch. The alternative but approximate technique as introduced in Section §2.5.1 uses a similar approach to ‘ACFIT’ but tailored for observations of hundreds of masers in a single observing session. At each scan, for each antenna/polarisations the  $S_\nu > 10\sigma$  peaks are located in the baseline–subtracted autocorrelated spectra. A reference antenna is chosen (either Ho or Cd due to largest experiment participation time and stable gains) and matching–velocity peaks in the various spectra are divided by the reference. This gives a correction factor ( $\Gamma$ ) for that antenna/polarisation/time (equal to 1 for the reference). Similarly determining  $\Gamma$  for each scan gives a time–variable scaling factor for each antenna/polarisation. If no peaks can be found above the threshold for an antenna/polarisation at time  $t_{\text{ant,pol},i}$ , the final  $\Gamma_{\text{ant,pol}}$  is interpolated to that time. Finally  $\sqrt{\Gamma_{\text{ant,pol}}}$  are internally applied via task ‘CLCOR’ to generate a new *CL* table. The reason  $\sqrt{\Gamma_{\text{ant,pol}}}$  is applied to the visibility data ( $\bar{s}_i$ ) to correct is because  $\Gamma_{\text{ant,pol}}$  is determined from autocorrelation products ( $\bar{s}_i \cdot \bar{s}_i$ ).

As with ‘ACFIT’, this method re–weights the visibility data to a reference antenna without consolation of maser amplitude catalogues (e.g. MMB). As I discuss later, this advantageously can identify extreme cases of maser variability or flaring rather than blindly assuming static flux density. Figure 4.3 demonstrates that combined data collected over two epochs with independent amplitude calibration agree and indicate the method is sufficiently accurate at the 10% level.

**ParselTongue script *find\_peak\_uv.py*** is used to find potential maser spots of interest and extracts the relevant calibrated *uv*–data. Without appropriately precise gain and accurate polarisation calibration, true polarisation analysis as part of this survey is not feasible. In addition, Class II methanol masers are considered to be only weakly circularly polarised (< 1%; Stack & Ellingsen, 2011) and so in the interest of improving mean amplitude calibration, the polarisations are averaged together to form stokes–*I* in all further analysis. For each maser, baseline and scalar–averaged stokes *I* cross–correlated spectra are generated with a lower bound *uv*–distance of 20 M $\lambda$ . Large and diffuse physical structures are assumed to have a kinematic ‘continuum’ of emission centred at the mean LSR velocity. Down weighting the contribution from this can potentially reveal otherwise spectrally resolved maser components and generally bias the selection process towards compact candidates (Figure 4.4). Peaks in this averaged spectrum are identified via  $S_\nu > 20\sigma_m$  and the visibility information extracted to an external file for modelling (*uv* vs.  $S_\nu$ , including baseline–subtracted autocorrelations). As a note, in the instance that all antennas

### 4.3. DATA REDUCTION

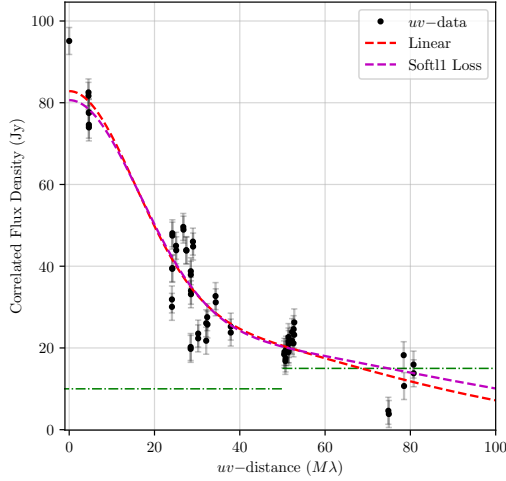


**Figure 4.3:** Example maser visibility fit on maser G345.010+1.792 velocity feature  $v = -17.46 \text{ km s}^{-1}$ . **Red line:** linear least-squares regression; **magenta line:** ‘SoftL1’/Huber Loss linear regression– robust fitting. **Green lines** indicate  $10\sigma$  sensitivity thresholds of the ASCI array

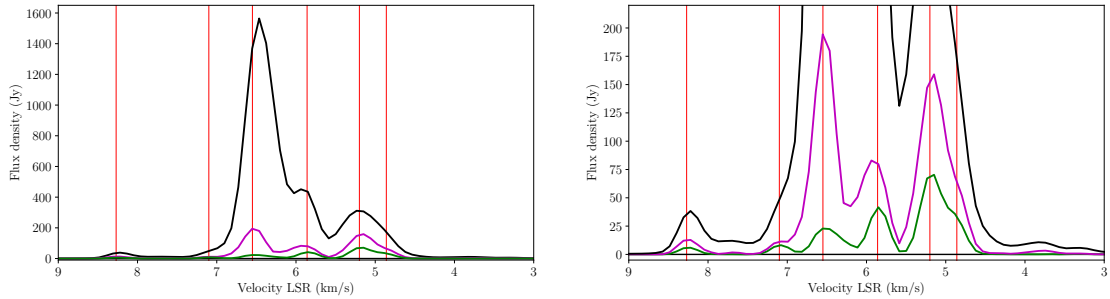


**Figure 4.4:** Comparison of various baseline/scalar-averaged spectra of G192.600–0.048. **Black:** Baseline, combined autocorrelated spectrum. **Magenta:** Scalar averaged cross-correlated spectrum from all 15 baselines. **Green:** Scalar averaged cross-correlated spectrum from 12 baselines, excluding baselines with  $B_\lambda \leq 20 \text{ M}\lambda$ . **Red:** Vertical lines indicated the derived position for potential compact structures by fitting the peak of the green spectrum. The reader is encouraged to note that the peaks of the green spectrum do not necessarily line up with peaks in the magenta or black spectra.

### 4.3. DATA REDUCTION



**Figure 4.5:** Data reduction process for V534 data involving AIPS (green), ParselTongue (red) and Python (white) steps.

### 4.3. DATA REDUCTION

are onsource for 2 scans, 2.5 min each, the scalar averaged spectral noise should be:

$$\frac{1}{\sqrt{5}} \frac{\sum_{i=1}^{12} \sigma_i}{12} \approx 0.5 \text{ Jy}$$

where  $\sigma_i$  are the appropriate baseline sensitivities ( $\text{Jy min}^{1/2}$ ; Table 4.2). Therefore a  $20\sigma$  detection in this spectrum implies an average spectral amplitude of  $\approx 10 \text{ Jy}$ .

As seen in Table 4.1, a  $uv = 20 \text{ M}\lambda$  cutoff removes At–Mp, At–Pa and Mp–Pa baselines. Therefore masers detected only on these baselines are automatically filtered out by this process and are automatically considered bad candidates.

#### 4.3.3 Maser Visibility Fitting

To avoid a degenerate naming scheme, I will refer to the whole region as the *maser*; emission from each extracted velocity channel an assumed separate *maser spot*; and different apparent emission structures at the same velocity channel as *maser components*. The `find_peak_uv.py` script ensures that only one channel from each peak/velocity feature has data extracted (see vertical red lines in Figure 4.4). Discrepancies to these assumptions are discussed in Section §4.5.4. So I aim to determine which masers have appropriate spots to use for inverse phase-referencing by analysing the spatial and energetic properties of their components.

In order to determine meaningful component properties, I require a model with realistic attributes. The model considered for a maser spot is a simple two-component Core/Halo model, where each component is estimated by a Gaussian brightness distribution:

$$I(r) = \frac{2 I_0}{\sqrt{\pi \ln 2 \theta^2}} \exp\left(-\frac{8 \ln 2 r^2}{2\theta}\right) \quad (4.2)$$

The Gaussian component has an unresolved flux density of  $\int_0^\infty I(r) = I_0$ ; where  $r$  is the radius from the centre of the distribution; and an angular diameter characterised by the FWHM of the Gaussian  $\theta$ . If I assume there are 2 components centrally co-located, then the corresponding visibility amplitude vs. baseline length ( $S_\nu(B_\lambda)$ ; which is the Fourier Transform of this model) is also a Gaussian and is given by:

$$S_\nu(B_\lambda) = S_C \exp\left(-\frac{2\pi^2}{8 \ln 2} (\theta_C B_\lambda)^2\right) + S_H \exp\left(-\frac{2\pi^2}{8 \ln 2} (\theta_H B_\lambda)^2\right) \quad (4.3)$$

where  $\theta_C, \theta_H$  are the Core/Halo angular sizes,  $S_C, S_H$  are the Core/Halo peak flux densities and  $B_\lambda$  is the baseline length expressed in units of the observing wavelength  $\lambda$  (aka  $uv$ -distance). The Core/Halo components are defined such that  $\theta_C < \theta_H$ . This is quite possibly the simplest model geometrically, computationally and for many sources on milliarcsecond scales will be a reasonable assumption (Minier et al., 2002).

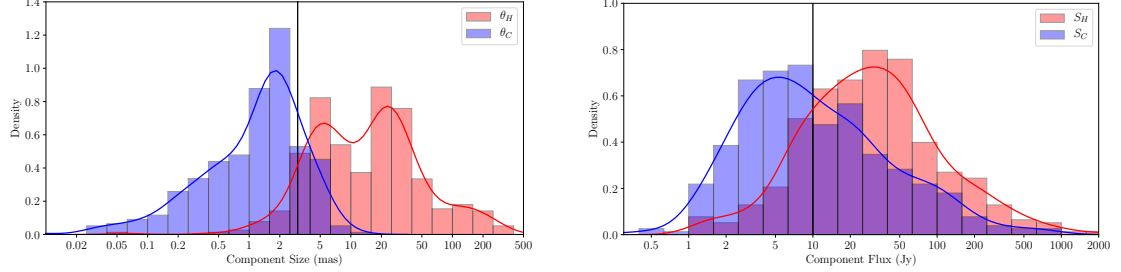
Non-linear least squares fitting techniques were deployed to determine parameters for each model with visibility amplitude uncertainties ( $\sigma_{S_\nu}$ ) estimated from spectral noise. Constraints imposed on the modelling process were  $\theta_H > \theta_C$ ,  $\theta_{\text{comp}} \in [0.1, 500]$ ,  $S_{\text{comp}} \geq 0.3$ .

Initial  $\chi^2$  values were produced from the fit, then the uncertainties were re-weighted such that they produced  $\chi^2 \approx 1$ . These more representative uncertainties (presumably accounting for

### 4.3. DATA REDUCTION

systematic model offsets) are shown as errors bars in visibility plots (Appendix B.3). Model parameters and modified uncertainties are included in Table B.2 .

All maser spot fits are shown in Appendix B.3.



**(a)** Distribution of modelled component size (mas) for all detected maser components.  $x$ -axis has  $\log_{10}$  scale and histogram bins are equally spaced in  $\log_{10}$  at 0.05 units.

**(b)** Distribution of modelled component flux density (Jy) for all detected maser components.  $x$ -axis has  $\log_{10}$  scale and histogram bins are equally spaced in  $\log_{10}$  at 0.1 units.

**Figure 4.6:** Global distributions for fitted parameters  $S_C$ ,  $\theta_C$ ,  $S_H$  and  $\theta_H$ . Blue components are attributed to a core and red to a halo, where the definition for each was assigned during modelling when  $\theta_H > \theta_C$ .

Figure 4.6 shows the global distribution of parameters for the 393 modelled maser spots in 104 masers. I find median  $\theta_H = 13.6^{+25.8}_{-9.8}$  mas and  $\theta_C = 1.3^{+1.9}_{-1.3}$  mas (error bars expressing 75% CI) which agrees with the expectation imposed by model constrains and definition of core vs. halo components ( $\theta_H > \theta_C$ ).

I find the component flux density of the halo structure is globally greater at  $S_H = 27.8^{+98.8}_{-20.4}$  Jy compared to  $S_C = 7.3^{+50.0}_{-5.2}$  Jy at 75% CI. While this was not strictly imposed, this follows expected trends. Now that the model parameters have been determined, I aim to compose them into a thorough categorisation which clearly hints at quality for parallax measurements, and which naturally relates to the ever elusive compactness.

## 4.4 Categorisation

Given the model parameters, I wish to categorise the maser spots and therefore their host masers on an intuitive grading scheme that quantifies compactness. Immer et al. (2011) conducted a VLBA survey to find quasar calibrators appropriate for BeSSeL maser astrometry and graded detections on a decreasing scale from  $A$  to  $D$ , and then  $F$  for non-detections. Compactness was solely associated with this grade and the grade determined by the baseline length at which the normalised visibility amplitude (NVA;  $S_{B_\lambda}/S_0$ ) fell below a threshold value of 20%. Following this, I will also grade the methanol masers on a scale from  $A$  to  $D$ , however, since masers have a more complex structure than quasars, I will use more than one metric. In the next few sections I will define these additional metrics and establish cutoffs in those metrics that encompass what characteristics I expect  $A-$ ,  $B-$ ,  $C-$  and  $D$ -grade masers to have.

To that end, I expect  $A$ -grade will represent as close to a perfect astrometric candidate as I can determine,  $B$  will be a good candidate,  $C$  will represent a possible but not recommended candidate, and  $D$  will be reserved for masers for which high accuracy astrometry is unlikely. Unmodelled masers are classed as such, having failed the basic detection constraints in *find\_peak\_uv.py*. Depending on the reason, they are classed as failed ( $F$ ) or undetected/unknown ( $U$ ). These masers are discussed in Section §4.5.1.

### 4.4.1 Fitting Results

In order to categorise the maser spots, I needed metrics that represented the physical properties attributed to compactness. Figure 4.7 shows the global distributions of model parameters against one another. A weak correlation between halo and core component flux density, but almost no correlation between core and halo sizes is implied. Seemingly apparent 1:1 correlation between  $\log_{10} \theta_H$  and  $\log_{10} \theta_C$  can be explained by a degenerate fit – the maser spot is well explained by a single Gaussian component with  $\theta_S = \theta_C \approx \theta_H$  and  $S_0 = S_C + S_H$ . The lack of an apparent global (and quite possibly inherent) correlation between core and halo parameters implies the ratios  $S_C/S_H$ ,  $\theta_C/\theta_H$  vary independently and possibly randomly for each spot. This unknown variability limits the independent inference power of NVA for compactness, and confirms that I must rely on multiple metrics to describe it fully.

### 4.4.2 Visibility Amplitude vs. $uv$ -distance

Possibly the most intuitive metric to characterise compactness are visibility amplitudes thresholds at fixed  $uv$ -distance cuts ( $S_{B_\lambda}$ ). To represent average Cd–AuScope12m, AuScope12m–AuScope12m and/or future Cd–Warkworth 30m (Petrov et al., 2015)  $uv$ -distances, baseline cuts are set at  $B_\lambda = 35$  and  $80\text{ M}\lambda$ . Global estimates for the median visibility amplitudes are  $S_{35\text{M}\lambda} = 5.6_{-3.9}^{+61.6}\text{ Jy}$  and  $S_{80\text{M}\lambda} = 2.2_{-2.2}^{+21.5}\text{ Jy}$  respectively (90% CI; Figure 4.8a).

Despite potentially weak individual inference power, I still will consider NVA ( $R_{B_\lambda} = \frac{S_{B_\lambda}}{S_0}$ ) evaluated at fixed baseline cuts of  $B_\lambda = 35$  and  $80\text{ M}\lambda$ . Global median estimates for the NVA are  $R_{35\text{M}\lambda} = 0.20_{-0.17}^{+0.45}$  and  $R_{80\text{M}\lambda} = 0.07_{-0.07}^{+0.36}$  (90% CI; Figure 4.8b).

#### 4.4. CATEGORISATION

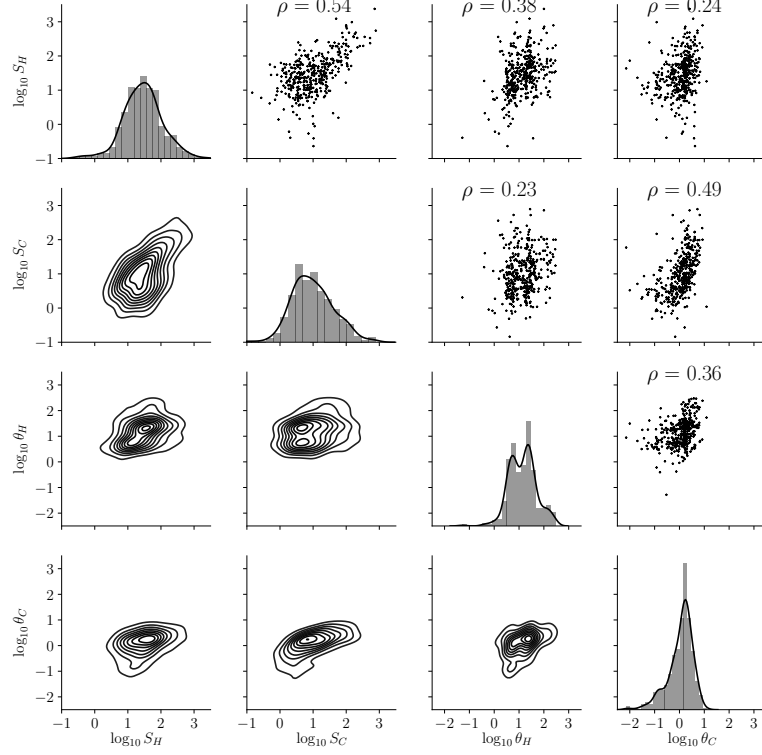


**Figure 4.7:** Correlation distributions between the 4 model parameters in the 2 component fit. All axis are in  $\log_{10}$  space to allow the visualisation of the full dynamic ranges and acts as more sensitive visual correlation probe. **Upper:** Scatter plot for parameters and associated correlation coefficients for the exponentiated populations ( $x$  not  $\log_{10}x$ ). **Diagonal:** Self-correlated histograms of parameter distribution density and single-variable KDE. **Lower:** KDE for two parameter comparison. Fit parameters are each randomly modulated with ‘weak’ Gaussian distribution to represent the respective uncertainty at the lower bound cutoffs. This smooths the visual transition at the bound edges (otherwise ‘unresolved’ cores stack at the  $\theta_C = 0.1$  mas level) and leaves the remaining distribution unchanged. Modulations are sampled from distribution  $P_m = \frac{1}{\sqrt{2\pi}} \exp\left(-\frac{1}{2}(x - \sigma)^2/(3\sigma^2)\right)$  for  $\sigma_\theta = 0.1$  mas,  $\sigma_S = 0.3$  Jy respectively.

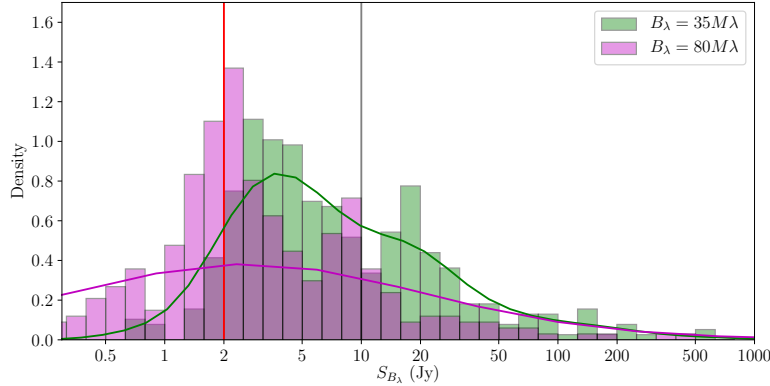
#### 4.4.3 Emission density/compactness index $\xi$

The next metric I use for maser spot classification is (pseudo) emission density,  $\xi$ :

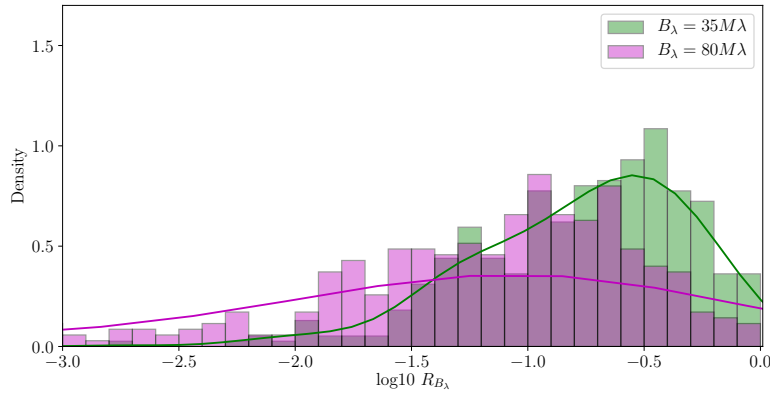
$$\xi_{comp} = \frac{S_{comp}}{(\theta_{comp}^2 + \theta_B^2)^4} \quad (4.4)$$

where  $\theta$  is the particular component size in mas,  $S$  is the flux density of the component in Jy and  $\theta_B$  is the synthesized beam size of the array in mas and  $\xi$  has units  $\text{Jy mas}^{-8}$ . This metric describes a size weighted surface flux density for each of the modelled components where the denominator  $(\theta^2 + \theta_B^2)^4$  was constructed in such a way that  $\xi$  does not diverge at small modelled sizes and is most sensitive to changes in component size  $\theta = \frac{\theta_B}{3}$  ( $\frac{\partial^2 \xi}{\partial \theta^2}|_{\theta_B/3} = 0$ ).

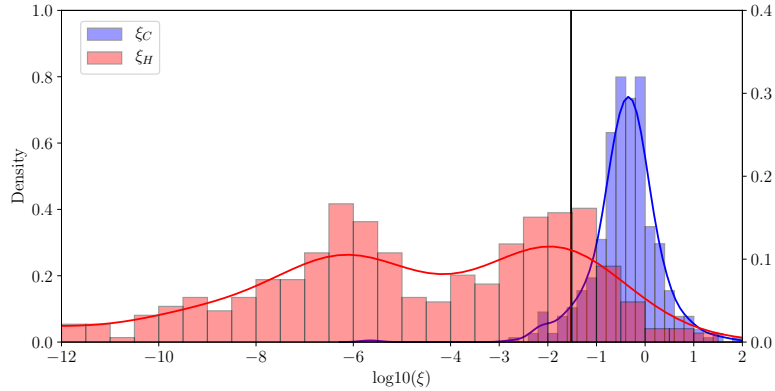
#### 4.4. CATEGORISATION



**(a)** Distribution of total spot flux (Jy) derived from model and model parameters at baseline lengths  $35 M\lambda$  (green) and  $80 M\lambda$  (magenta) respectively.  $x$ -axis has  $\log_{10}$  scale and histogram bins are equally spaced in  $\log_{10}$  at 0.1 units.



**(b)** Distribution of total spot flux to autocorrelated flux ratio ( $R_{B_\lambda} = S_{B_\lambda}/S_0$ ). Histogram has lower cut-off at  $R_{B_\lambda} = -3$  or 0.1%.



**(c)** Distribution of pseudo emission density  $\xi$ .  $x$ -axis has  $\log_{10}$  scale and histogram bins are equally spaced in  $\log_{10}$  space at 0.1 units. Vertical black line indicates  $\xi_{\min} = 0.06 \text{ Jy mas}^{-2}$ .

**Figure 4.8:** Distributions of various calculated metrics for the purposes of quantifying and therefore classifying compactness.

## 4.4. CATEGORISATION

Global median estimates for the emission density are  $\xi_H = 0.11_{-0.10}^{+1.22}$  Jy mas $^{-8}$  for the diffuse halo component and  $\xi_C = 0.38_{-0.27}^{+4.61}$  Jy mas $^{-8}$  for the core component (90% CI; Figure 4.8c), which expectedly implies core components typically have a higher concentration of emission compared to halo components.

### 4.4.4 Constraints and grades

As I wish to not only categorise masers, but to do so in a way which graduates them on a scale from most to least appropriate for my purposes, I will again consider the observational constraints. As calculated in Section §4.2, the baseline sensitivity from Ceduna 30m to an AuScope12m antenna would theoretically be 3 Jy (each  $\sqrt{\text{minute}}$  integration) at a  $uv$ -distance of  $35 \text{ M}\lambda$ . AuScope12m–AuScope12m baseline sensitivities can be calculated to be  $\sim 5 \text{ Jy min}^{\frac{1}{2}}$  and a possible Ceduna 30m–Warkworth 30m baseline would be  $\sim 1 \text{ Jy min}^{\frac{1}{2}}$ , both approximately at  $80 \text{ M}\lambda$ . Therefore, I define an A-grade maser spot as one that has a minimum  $3\sigma$  detection on every baseline (or  $S_{80} \geq 15 \text{ Jy}$ ). B-grade maser spots have a  $5\sigma$  detection detected on every Ceduna baseline, but not AuScope–AuScope baselines. Ceduna–AuScope baselines are  $B_\lambda \sim 35 \text{ M}\lambda$ , meaning the correlated flux density of the maser has to be  $S_{35} \geq 10 \text{ Jy}$ . Both A- and B-grade masers would be acceptable for S $\pi$ RALS in the current era.

Figure 4.9 are representative examples of maser spots which demonstrate a compactness grade from *A* to *D*. These masers serve as a general guide to the proportions and magnitudes of parameters that result in said grades. The aforementioned specific visibility amplitude cuts are shown for every maser compactness plot in Appendix B.3.

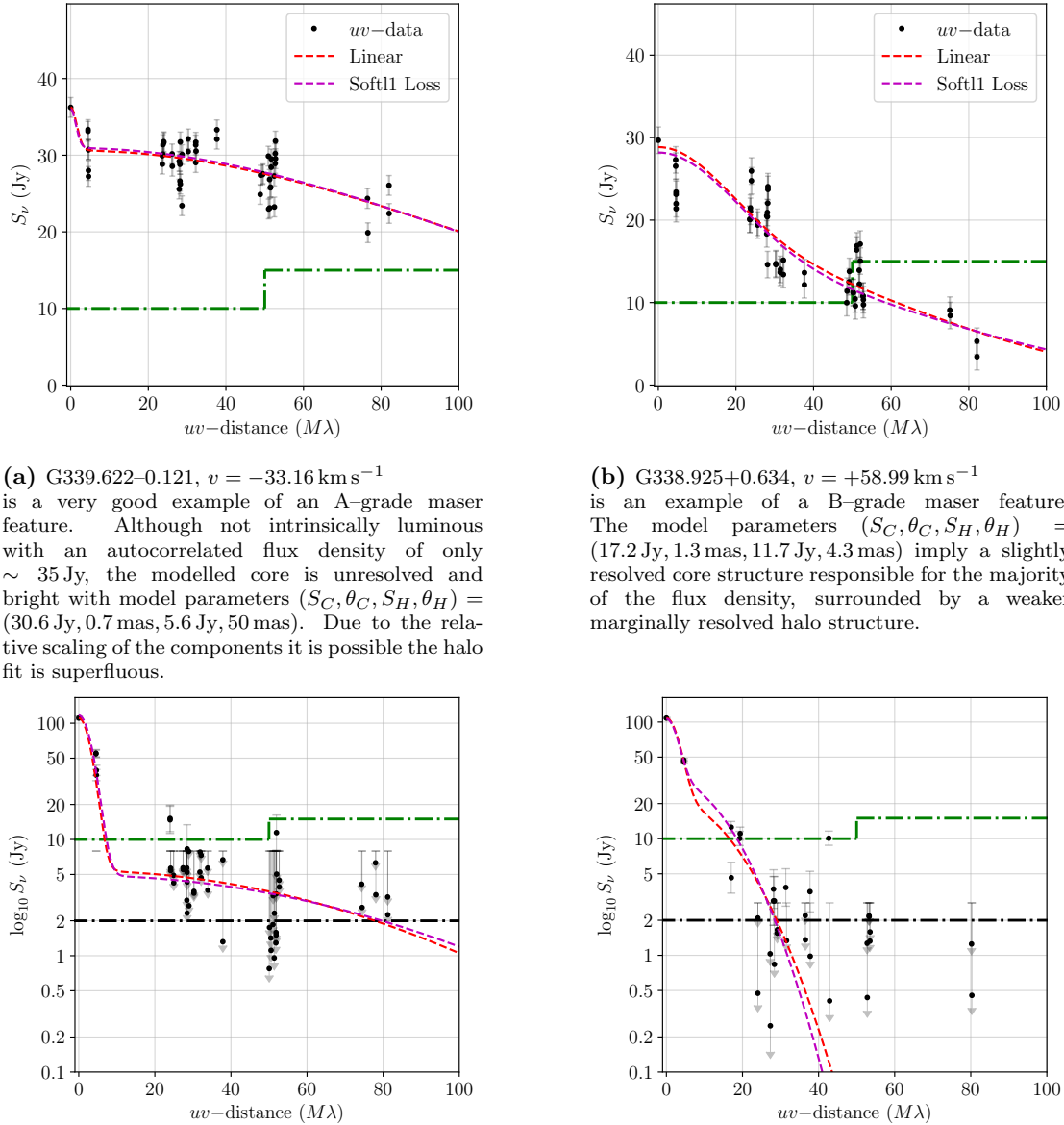
C-grade masers would fail both the previous constraints and therefore not be ideal first targets for S $\pi$ RALS. However, foreseeing possible future sensitivity upgrades, I further separate C-grade and D-grade maser spots. C-grade masers are classically weak, but compared to D-grade masers they are compact. D-grade masers are weak and almost immediately resolve out to fall below detection thresholds.

Figure 4.10 shows the distributions and correlations of the metrics explained above from the global sample of maser spots overlayed with the metrics derived from the ideal maser spots. I only include metrics  $S_{35}$ ,  $S_{80}$  and  $\xi_C$  and for all these cases the compactness grades are arranged left to right. A value of  $\xi_C \geq 0.3 \text{ mJy/mas}^8$  implies if  $S_C = 5 \text{ Jy}$ ,  $\theta_C/\theta_B \leq 0.5$  or if  $\theta_C/\theta_B \geq 1$ ,  $S_C \geq 30 \text{ Jy}$ . Since bright compact objects ( $\xi \gg 0.3$ ) have been most likely identified by either  $S_{80}$  or  $S_{35}$ ,  $\xi$  serves as a method to segregate fits to marginally weak cores from fits to Rice noise/baseline non-detections. This is because  $\xi$  simultaneously takes into account and weights the core component modelled flux density and size under a certain threshold.

### 4.4.5 Summary

Finally I categorise all modelled maser spots from these cuts. Figures B.1 and B.2 show correlations with the determined categorisations against the original modelled parameters and full range of metrics. It can be seen here that NVA ( $R_{35}$  and  $R_{80}$ ) do not clearly separate into the populations as determined by this method. This can likely be attributed to the inclusion of the diffuse flux density from the halo which is uncorrelated with the core size and flux density and therefore compactness. Maser regions are then categorised via the highest grade maser spot (Table B.2). Masers with multiple ‘equal’ grade spots (apart from D-grade) are all included.

#### 4.4. CATEGORISATION



**Figure 4.9:** Examples of the 4 categories of detected masers in the survey. **x-axis:** Projected wavelength-scaled baseline distance ( $M\lambda$ ). **Top y-axis:** Correlated flux density (Jy) of specified maser channel velocity. **Bottom y-axis:**  $\log_{10} S_\nu$  scaled axis. **Black dots:** 60 s-averaged  $uv$ -data with scaled errors bars to attain  $\chi^2 = 1$ . **Red:** Gaussian Core/Gaussian Halo model for maser structure with linear residual scaling. **Magenta:** GCGH model with robust residual loss. **Green:** Categorisation thresholds at 10 Jy and 15 Jy for  $35 \text{ M}\lambda$  and  $80 \text{ M}\lambda$  respectively. **Black line:** Rician noise detection threshold – values below are modelled but not considered detected.

#### 4.4. CATEGORISATION

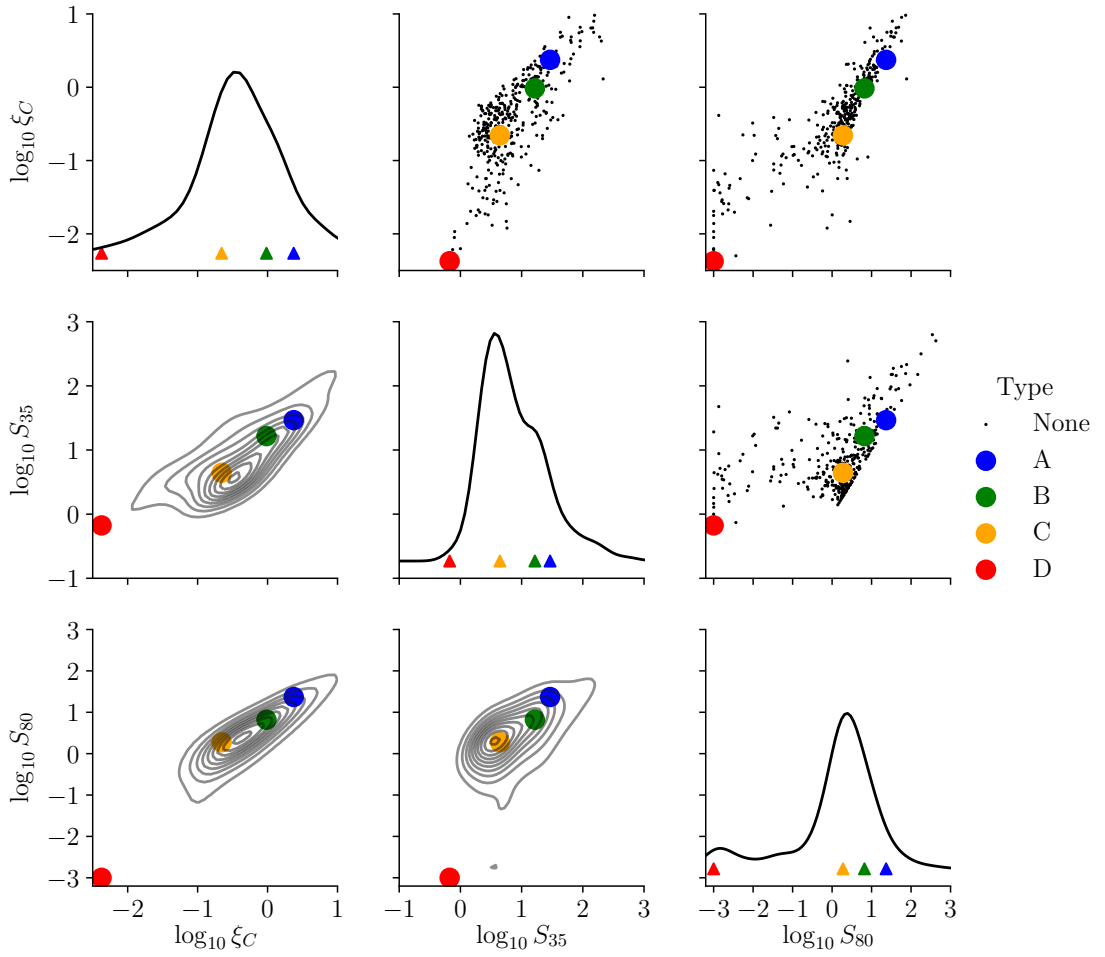


**Figure 4.10:** Correlation distributions between 3 compactness metrics for – **black**: All modelled maser spots; **blue**: A-grade maser spot G339.622–0.121  $v = -33.16 \text{ km s}^{-1}$ ; **green**: B-grade maser spot G338.925+0.634  $v = +58.99 \text{ km s}^{-1}$ ; **orange**: C-grade maser spot G345.003–0.223  $v = -26.84 \text{ km s}^{-1}$ ; **red**: and D-grade maser spot G359.436–0.104  $v = -46.66 \text{ km s}^{-1}$ . **Upper**: Scatter plot for parameters. **Diagonal**: Self-correlated single-variable KDE and markers indicating classic maser spot positions. **Lower**: KDE for two parameter comparison.

## 4.5. DISCUSSION

**Table 4.3:** Compact maser catagorisation descriptions. **Rows:** Condition that core–compactness index is greater than the threshold value  $\xi_C \geq 0.06 \text{ Jy mas}^{-4}$ , condition that correlated flux density at  $35 \text{ M}\lambda$  is greater than five times the detection limit  $5\sigma_S = 15 \text{ Jy}$ , condition that the correlated flux density at  $80 \text{ M}\lambda$  is greater than  $10 \text{ Jy}$ .

Grade	$S_{35} \geq 10$ (Jy)	$S_{80} \geq 15$ (Jy)	$\xi_C \geq 0.3$ (mJy mas $^{-8}$ )	Description
A	Y	Y	Y	Compact and strong on all baselines.
B	Y	N	Y	Compact, flux density tapers off on long baselines but still good for reverse–phase reference
C	N	N	Y	Compact but weak. Okay for normal phase referencing subject to quasars availability
D	N	N	N	Diffuse and weak.
F	N	N	-	Only detected on $uv < 20 \text{ M}\lambda$ baselines. Target maser was too weak to initially find peaks to fit $uv$ –data from
U	-	-	-	Unknown grade. Maser had insufficient valid $uv$ –data due to issues.

## 4.5 Discussion

### 4.5.1 Non-detections

I consider masers that were unable to have a single maser spot modelled successfully (degrees of freedom  $> 1$ ) as non-detections. Out of the 187 masers surveyed, 85 are considered as non-detections, and are given the grade of either F(ailed) or U(nknown) (Table 4.3). If maser is designated F-grade, it had no significant detection on non-At-Mp, At-Pa or Mp-Pa baselines ( $B_\lambda \geq 25 \text{ M}\lambda$ ). This implies that the angular size of any present components were much larger than the synthesized beam at that  $uv$ -distance  $\theta_C \gg \theta_B = 10 \text{ mas}$  or that any small angular components present were much weaker than the detection thresholds (Table 4.2). If given a U-grade, maser had no autocorrelated or cross correlated detection due to scheduling, correlation or observational issues.

## 4.5. DISCUSSION

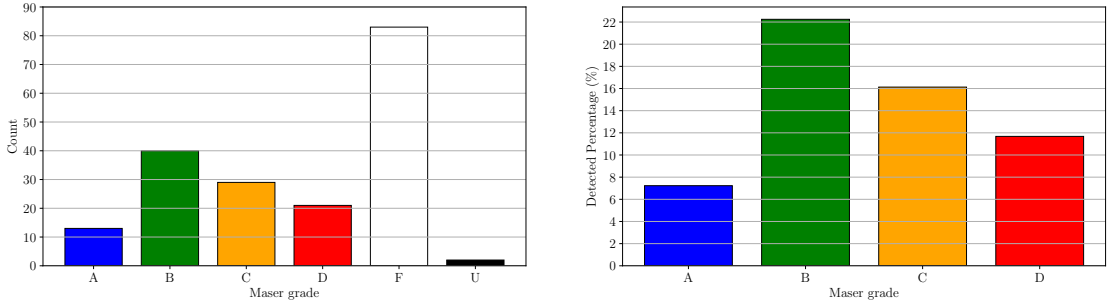


**Figure 4.11:** Histograms showing number/percentages of masers categorised into each grade. **Left:** Number of masers graded  $A \rightarrow D$  compared against non-detections  $F$  and unknown  $U$ . **Right:** Percentage of detected masers categorised into each grade.

### 4.5.2 Interstellar scattering

It is well known that multipath diffraction through the Interstellar Medium (ISM) causes scintillation and angular broadening (e.g. Cordes et al., 1991; Fey et al., 1991; Pushkarev & Kovalev, 2015). From Cordes (2001) the Galactic angular broadening ( $\Theta$ ; mas) at 6.7 GHz as a function of the scattering measure ( $SM$ ) and frequency ( $\nu$ ; GHz) is given by:

$$\Theta = 71 \frac{SM^{3/5}}{\nu^{11/5}} \text{ mas}$$

Minier et al. (2002) investigated whether the presence of extended emission (halos) around maser spots can be explained by scatter broadening. They argued that while some degree of scattering is expected ( $\Theta \sim 0.3$  and 1 mas at 12.2 and 6.7 GHz respectively), it is not large enough in magnitude to give rise to the 5–50 mas halos-like structures seen in their sample of 12.2 GHz masers. In addition, they found that the ratio of halo size at the two frequencies did not behave as  $\lambda^2$  as would be expected if the halo size originates primarily from scatter broadening. Therefore they concluded that apparent distinct core/halo structures are the result of either saturation in some uniform spherical cloud, physically different environments (dense gas vs. weak diffuse gas), or turbulence in a homogeneous medium. A similar argument was put forward by Menten et al. (1992), comparing the spot sizes of 6.7 GHz CH<sub>3</sub>OH against 12.2 GHz CH<sub>3</sub>OH and 1.665 GHz OH at the same velocities in W3(OH). The conclusion was that since a  $\lambda^2$  variation was not seen, the observed spot size was intrinsic.

Masers are confined to the plane of the Milky Way, however, not all to the same extent (Figure 4.1). Since HMSF-associated masers have a scale height from the Galactic Plane of  $19 \pm 2$  pc (Reid et al., 2019), masers at higher Galactic  $b$  are more biased towards being closer to us. In addition, regardless of whether the masers are actually closer, a higher Galactic Latitude line-of-sight passes through less of the Galactic Plane. Either way, it is not unreasonable to suggest that higher Galactic  $b$  masers might be effected less by scattering.

Pushkarev & Kovalev (2015) surveyed VLBI quasar size as a function of Galactic  $b$  and frequency. They found that there was a significant difference in the modelled angular size of AGN inside  $|b| < 10^\circ$  and outside the Galactic plane  $|b| > 10^\circ$ . While data at 5 GHz suffered from completeness issues, 2/8 GHz data were collected simultaneously allowing for the frequency dependence to be explored about 5 GHz. For sources within the plane, 33% had a frequency-dependant core size

## 4.5. DISCUSSION

ratio with index  $\sim 2$ , suggesting scatter broadening. The exact graduation of this effect was not explored, most likely due to diminishing sample size as  $|b| \rightarrow 0$ . However the maximum observed size of quasars at 2 GHz and 8 GHz at  $|b| = 2, 1, < 1$  were approximately 10, 10, 20 mas and 4, 6, 4, mas. From this I derive approximate max values of  $SM = 0.5, 0.5, 1.5$  for  $|b| = 2, 1, < 1$  (removing extreme values by consulting expected values for the scattering measure from Cordes et al. (1991)). This gives  $\Theta = 0.7, 0.7, 1.4$  mas.

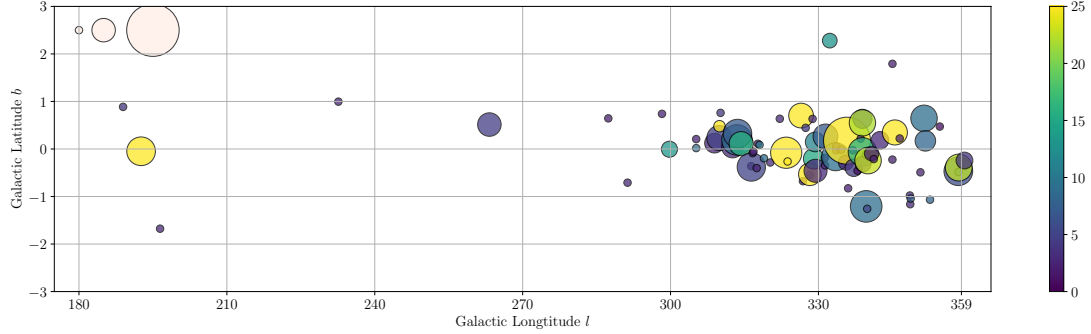


**Figure 4.12:** Distribution of maser minimum modelled size vs. Galactic coordinates. **Point size:** Radius scales with modelled size– Key top left: 0.1, 1.0, 5.0 mas left to right. **Colourmap:** Component flux density in Jy.

Next I compared modelled values against values in Cordes & Lazio (1991) Fig 2, where the expected angular broadening at 1 GHz is modelled against  $l$  and  $b$  towards the Galactic Centre. Values closer to  $\Theta = 0.5, 1.9, 3.8$  mas are implied, most likely due to Galactic Centre and/or Galactic Plane proximity ( $|b| < 10$ ). I take the geometric average and see that my graduated scale is approximated as  $\Theta = 0.6, 1.2, 2.3$  mas for  $|b| = 2, 1, < 1$ .

If there is a minimum size due to interstellar scattering, I expect to see a tendency for targets at low Galactic latitudes to have a larger minimum size than those at higher latitudes. Also, if that effect is larger than the intrinsic maser size and variations to it, I would expect to see a maser minimum size ‘cap’ at the values derived above. Taking the smallest ‘significant’ maser spot core size for each maser (no D-grade spots), I examine the distribution in both  $l$  and  $|b|$  (Figure 4.12). I have 8 masers outside of  $|b| > 1$ , 18 masers inside the range  $0.5 < |b| < 1$  and 56 masers inside  $|b| < 0.5$ . I find the average spot minimum spot size within those ranges as  $\theta_{|b|>1.0} = 0.22 \pm 0.17$  mas,  $\theta_{0.5 < |b| < 1.0} = 0.55 \pm 0.66$  mas and  $\theta_{|b|<0.5} = 0.58 \pm 0.59$  mas respectively.

I cannot detect any significant difference between minimum maser spot sizes as a function of  $|b|$ . In addition, is it clear that derived minimum spot sizes do not cap at the above values of  $\Theta = 0.6, 1.2, 2.3$  mas for  $|b| = 2, 1, < 1$ . Therefore, it is safe to infer that the values and variation between my modelled Core/Halo spot sizes are very unlikely the product of interstellar scattering at the level that can limit the astrometric accuracy. Therefore, maser spot size appears to be purely intrinsic at 6.7 GHz.

### 4.5.3 Class II Methanol Variability and Flaring

Class II methanol masers are known to be variable on time scales of more than months to years (Caswell et al., 1995a; Szymczak et al., 2018a). While this variability is normally by a factor

## 4.5. DISCUSSION

of less than 2 and rarely by a factor of less than 10, there have been some extreme examples in recent years. These rapid increases in flux density are called flares. G192.600 – 0.048 as observed in this survey serendipitously was undergoing flaring (Szymczak et al., 2018a).

In this survey the maser region G192.600–0.048 (also known as S255) is considered an *A*–grade candidate due to the  $v_1 = 5.20 \text{ km s}^{-1}$  and  $v_2 = 5.90 \text{ km s}^{-1}$  components, with the  $v_1$  component being the most compact and preferable for astrometry. In June 2015, S255 began to rapidly increase in luminosity. Szymczak et al. (2018b) presents a detailed overview of burst and Figure 4.13 is Fig. 3, page 3 from that article. Figure 4.13 shows that at the time of these observations (MJD 57451 and 57469) S255 was very close to the peak of the burst, especially the 5.2 and 5.9  $\text{km s}^{-1}$  velocity components. This coincidental occurrence explains the extremely enhanced flux density encountered for this source compared to that catalogued by the MMB, and the different spectral features and spectra. Although the previous methanol parallax was for a  $v = 4.6 \text{ km s}^{-1}$  component, that feature is no longer present in auto- or cross-correlation spectra. It is clear that the accretion event led to the appearance of some very compact emission regions at  $v_1 = 5.20 \text{ km s}^{-1}$  and  $v_2 = 5.90 \text{ km s}^{-1}$ .

Therefore, I acknowledge that in this relatively blind survey with a very short time baseline there is a non-zero chance that the derived compactness for some targets may appear significantly different at a later date due to un-monitored episodic accretion resulting in morphological, spectroscopic and luminous variations.

### 4.5.4 Variation from Model

Maser regions are complex dynamic structures, and it is possible for multiple emission regions in the field of view to coincide with a single line-of-sight velocity channel. The relatively high velocity resolution aims to combat this ambiguity without sacrificing thermal sensitivity. Nevertheless < 500 s worth of integration time spread over 2 to 4 scans per maser provides very little  $uv$ –coverage, especially continuous coverage required for accurate and precise imaging. As a consequence, it is very difficult to ascertain whether the measured flux density is due to more than one spatially separate emission region and to what fraction. Furthermore the determination of individual structure for each region becomes highly degenerate when one considers potential flux density variation due to component separation and position angle.

This point is clearly illustrated by Figures 2 and 3 from Goedhart et al. (2005), where the authors image the strong methanol maser G9.62+0.2E with the VLBA. This maser has a complex morphology— the diffuse components are quite elongated and it is easy to see that one or two cuts at different hour angles on structures like this are going to give quite different visibility amplitudes on similar baseline lengths. Therefore, there can be the case that there are multiple spatially distinct maser spots which overlap in velocity and/or there can be complex morphologies in a single maser spot. Both of these can produce results which may be confusing or inconsistent when there is only one or two small cuts.

#### 4.5. DISCUSSION

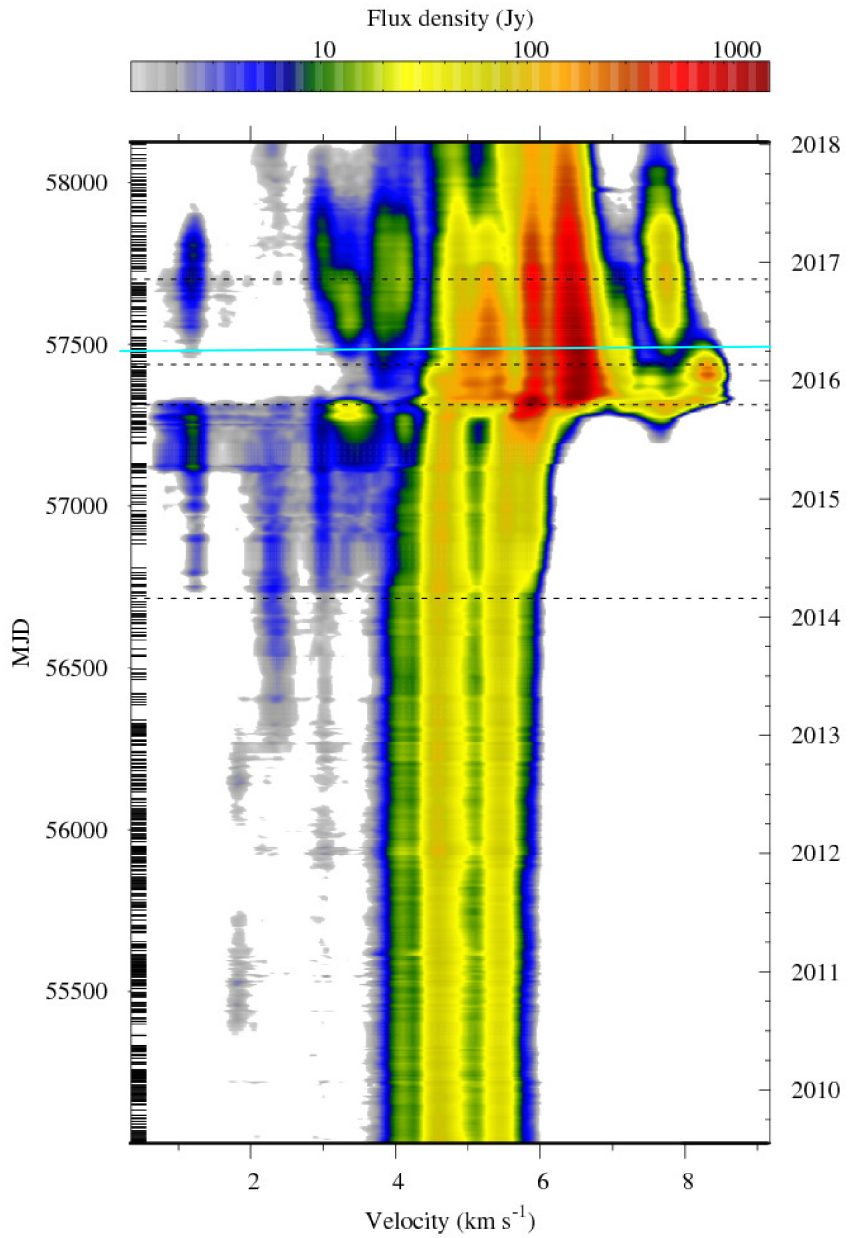


**Figure 4.13: Original Caption:** *Fig. 3. Dynamic spectrum of the 6.7 GHz methanol maser emission for S255IR-NIRS3. The color scale maps to the flux density as shown in the wedge on the top. The flux densities are linearly interpolated between consecutive 32 m telescope spectra. The velocity scale is relative to the local standard of rest. Individual observation dates are indicated by black tick marks near the left ordinates. The horizontal dashed lines from bottom to top mark the approximate times of the start first peak, dip, and second peak of the burst. Cyan line: Approximate dates for V534A and B epochs.*

## 4.6 Conclusion - First Targets

I have conducted a survey of 187 individual 6.7 GHz methanol masers from the Methanol Multi-beam Catalogue and have determined which ones are currently most appropriate for future S $\pi$ RALS observations that will culminate in a parallax measurement. I report successful detections of over 90% of the surveyed sources and have modelled structural parameters for over 50% of them. Table B.1 contains a list of the recommended first targets for VLBI parallax measurements set to begin mid-2020, while Figure 4.14 shows the distribution of first targets in  $l-v$  space. I find that out of the sample of 187 masers, 13 are categorised as  $A$ -grade, 40

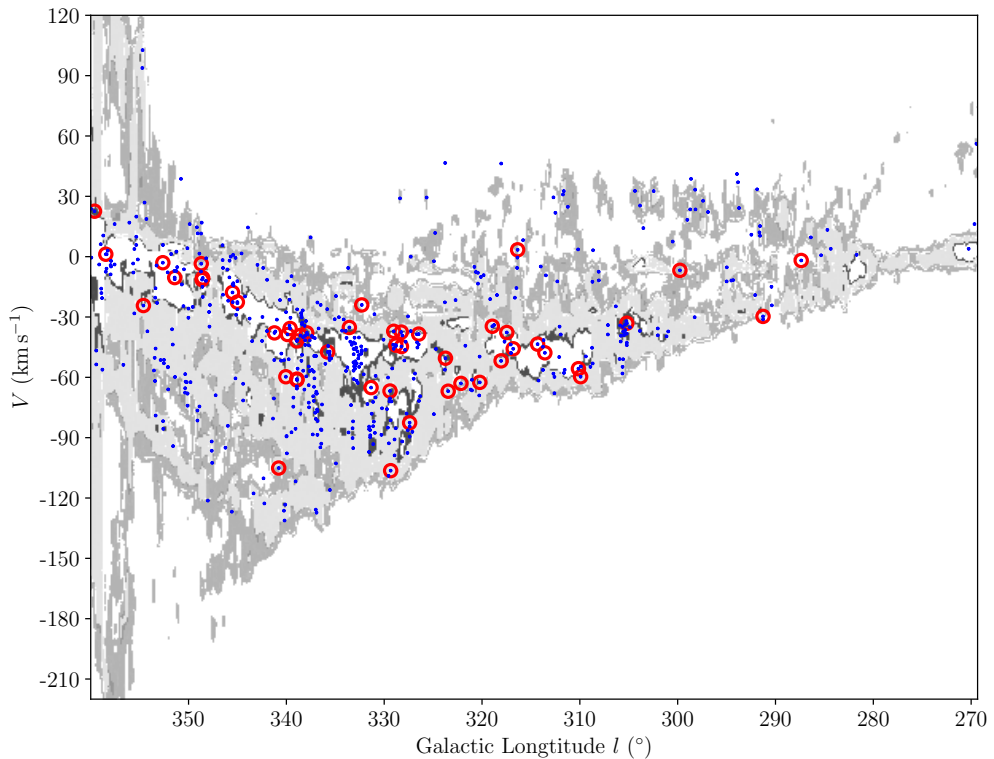


**Figure 4.14:**  $l-v$  distribution of 6.7 GHz visible from the Southern Hemisphere. **Blue:** Positions of all known masers between  $270 < l < 2^\circ$ . **Red:** Positions of best maser targets determined by this survey. The best masers appear to have a fairly good sampling of the 4th Galactic quadrant with the exception of  $l < 285^\circ$ .

as  $B$ -grade, 29 as  $C$ -grade and 21 as  $D$ -grade. A further 83 can be classed as unsuitable for milliarcsecond astrometry in the current era (if at all) due to extremely heavy resolution on small to intermediate baselines ( $10\text{--}20 M\lambda$ ), and a further 2 as unknown due to observational issues (Figure 4.11).



## MULTIVIEW

The ASCI array is a much sparser, less sensitive array containing fewer telescopes than the VLBA, European VLBI Network (EVN) or LBA. ASCI also cannot rely on sophisticated dual-beam receivers like those that assist VERA in atmospheric calibration. In order to achieve the same level of astrometric accuracy as BeSSeL or VERA, S $\pi$ RALS must rely on observational methods and calibration techniques to overcome the current limitations of ASCI.

In this chapter I will introduce the background, theory and observational methodology of the calibration technique to be tested in Chapter §6: MultiView. The core idea of the MultiView astrometric calibration technique is that if it were possible to simultaneously observe multiple calibrators positioned around the target, then all residual delays could be determined and perfectly removed.

Certain technology may allow direct use of Multiview in its purest conceptual form: phased array feeds or multi-beam receivers can simultaneously observe target and calibrator(s) providing direct calibration. However, as ASCI does not have access to any of these systems, I need to develop an observational-based version of MultiView.

Following a brief background, I step through the delay budget after calibration, each component in turn to explain how inverse MultiView can calibrate that effect. I finish off with an explanation on how I will structure the inverse MultiView part of observations and consequently solve for target positions.

## 5.1. BACKGROUND

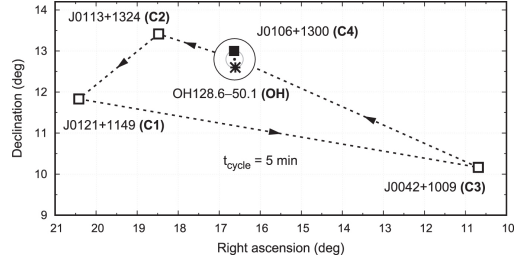
### 5.1 Background

MultiView is a relatively new approach to astrometric calibration. The first iteration of MultiView was called ‘cluster–cluster’ phase referencing (Rioja et al., 1997, 2002). This involved simultaneous observations of a target and multiple calibrators at low frequencies by utilising multi-element single stations. Unfortunately, the availability of such observing sites (let alone multiple sites for VLBI) is extremely limited, and therefore, modification was required. Despite this, cluster–cluster showed promise in removing residual ionospheric and tropospheric delays that plagued low-frequency astrometry.

The next iteration was the phase referencing stage demonstrated by Rioja et al. (2017). Observations were structured such that the calibrators and an OH maser were looped through as C1–C3–(M+C4)–C3–C1..., where the total duty cycle was  $\sim 5$  mins (Figure 5.1). The OH maser had an in-beam calibrator that was used as an astrometric comparison. This is what I will refer to as traditional MultiView – an important caveat is that all sources have to be observed in under the tropospheric and ionospheric coherence times (hence the 5 mins; Orosz et al., 2017) and this was considered the definition of simultaneity.

The method involved extracting phases from the 4 calibrators and 2D linear interpolating them to the position of the maser and in-beam calibrator. Phase ambiguities that were multiples of  $2\pi$  were iteratively removed from calibrator phases to minimise residuals and optimise image rms noise. Although effective at lower frequencies ( $\sim 1.5$  GHz) this technique has limited direct

**Figure 5.1:** Rioja et al. (2017) Figure 1. Original caption: *Sky distribution of the sources observed with the VLBA at 1.6 GHz ... Dashed lines and arrows mark the source switching order during the observations with 5 minute duty cycles. Star and solid symbols mark the simultaneously observed OH/C4 pair, with the VLBA antennas pointed halfway between the two. The two concentric circles represent the half-power beam width and full beam width of the antennas. Both OH and C4 are targets in the astrometric analyses ... C1 was used as the fringe finder.*



applicability at intermediate frequencies ( $\sim 7$  GHz) where tropospheric coherence times are shorter and in-beam calibrators are rare.

Inverse phase referencing (iPR) is commonplace in maser astrometry as it uses the strong maser as the fringe fit location rather than the often weak quasar calibrators. As the masers are strong, less on-source integration time is required to get sufficient SNR, and therefore observations of maser/calibrator can be kept within the increasingly shorter coherence times as the frequency increases. Doing so transfers the (opposite of the) positional information from the maser to calibrator and therefore, the offsets, proper motion and parallax. This technique is important as you can nod between a maser and calibrator in many different ways and also maximise the time on, and *uv*– coverage on the maser (for imaging and structure analysis).

Therefore, instead of MultiView, I will do *inverse MultiView* (iMV) using the maser as the reference. Again, time on and *uv*–coverage of the maser can be maximised and because the maser is strong, the individual scan on-source time can be minimised while still measuring fringe solutions. Calibration is achieved by iteratively nodding to various calibrators at different position

## 5.2. INVERSE MULTIVIEW THEORY

angles and angular separations, and then measuring phases referenced to the maser. Individual calibrators can be chosen less rigorously than normal PR/iPR: compactness and calibrators with more flux density are a higher priority than target–calibrator separation so as to achieve stable phase solutions with high SNR.

Finally a phase plane solution or wedge can be fit over the FoV above each telescope based on the measured phases and their change over time. As I will show, application of this solution to the target will return the positional information while minimising the effect of residual delays.

### 5.2 Inverse MultiView Theory

I want to establish how MultiView is expected to reduce phase referencing errors using a theoretical approach. To this end I am going to start by assume a target (T) separated  $\theta_{sep}$  radians away from a calibrator (C) on a single baseline. I will use  $\sigma$  to signify an error/uncertainty and  $\Delta$  to signify a difference.

Recall the total delay budget after phase referencing (Equation 2.11):

$$\begin{aligned}\tau_C(t_{i+1}) - \tau_T(t_i) &= \Delta\tau_{bl} + \Delta\tau_{tr} + \Delta\tau_{io} + \tau_{\theta,C} - \tau_{\theta,T} + \tau_{th} \\ &= \tau_{\theta,C} - \tau_{\theta,T} + \sigma_{\tau_{pr}}\end{aligned}\quad (5.1)$$

where  $\Delta\tau_{bl}$ ,  $\Delta\tau_{tr}$ ,  $\Delta\tau_{io}$  refer to difference in the respective LoS delays due to baseline, tropospheric and ionospheric residuals and  $\tau_{th}$  is the thermal uncertainty. Therefore the difference in delay between the target and calibrator gives the positional offset corrupted by a factor ‘ $\sigma_{\tau_{pr}}$ ’. If the positional offset of the calibrator is constant (e.g. for a quasar), then any change in the sum  $\tau_{\theta,C} - \tau_{\theta,T}$  over time/between epochs is due to the change in position of the target.

Accepted wisdom (e.g. Reid & Honma, 2014) is that delay errors are effectively reduced by phase referencing such that the final error becomes:

$$\sigma_{\tau_{pr}} \leq \theta_{sep}\sigma_\tau + \tau_{th} \quad (5.2)$$

where  $\sigma_\tau$  is the quadrature sum of all individual sources of delay uncertainty (calibration uncertainty). This function increases linearly with target–calibrator separation, and therefore, for a fixed upper limit on calibration delay uncertainty  $\sigma_\tau$ , smaller separations are expected to give increasingly better astrometry up to the thermal limit  $\tau_{th}$ .

The uncertainty  $\sigma_{\tau_{pr}}$  can be interpreted as ‘the maximum value residual delay could be over angular distance  $\theta_{sep}$ ’. Rather than accept this upper limit, MultiView is a technique to indirectly measure  $\sigma_\tau$  and subtract the effect it has on the data.

Following Rioja et al. (2017) I will be using 3D phase–planes in equatorial coordinates RA, DEC ( $\alpha$ ,  $\delta$ ) as the MultiView model. However, I would like to take a moment to justify why. In the following few sections, I will show that the residual LoS delay terms  $\Delta\tau_{bl}$  and  $\Delta\tau_{tr}$  can be modelled by 3D delay (or phase) planes out to reasonable target–calibrator separations.

#### 5.2.1 Baseline delay differential $\Delta\tau_{bl}$

The baseline component  $\Delta\tau_{bl}$  from Equation 5.1 is the difference in residual baseline error for each line of sight. The residual baseline delay for any LoS depends on the individual baseline

## 5.2. INVERSE MULTIVIEW THEORY

uncertainties, hour angle and declination, and is given in Equation 2.6. Target and calibrator are separated by  $\mathbf{a}$  radians in RA and  $\mathbf{b}$  radians in DEC:  $\alpha_C - \alpha_T = \mathbf{a}$ ,  $\delta_C - \delta_T = \mathbf{b}$  and  $\theta_{sep}^2 = \mathbf{a}^2 + \mathbf{b}^2$ . Subtracting the measured target delay from the calibrator data would give:

$$\begin{aligned} c(\tau_{bl,C} - \tau_{bl,T}) &= c\Delta\tau_{bl} = \Delta B_x \cos(t_{lst} - \alpha_1) \cos \delta_1 - \Delta B_y \sin(t_{lst} - \alpha_1) \cos \delta_1 + \Delta B_z \sin \delta_1 \\ &\quad - \Delta B_x \cos(t_{lst} - \alpha_2) \cos \delta_2 + \Delta B_y \sin(t_{lst} - \alpha_2) \cos \delta_2 - \Delta B_z \sin \delta_2 \end{aligned} \quad (5.3)$$

where  $\Delta B_i$  are the baseline errors in the geocentric coordinate system  $x, y, z$  and  $t_{lst}$  is the local sidereal time. Substitution of  $\alpha_C = \mathbf{a} + \alpha_T$  and  $\delta_C = \mathbf{b} + \delta_T$  gives:

$$\begin{aligned} c\Delta\tau_{bl} &= \mathbf{a} [\Delta B_x \sin(t_{lst} - \alpha_T) \cos \delta_T - \Delta B_y \cos(t_{lst} - \alpha_T) \cos \delta_T] \\ &\quad + \mathbf{b} [\Delta B_x \cos(t_{lst} - \alpha_T) \sin \delta_T - \Delta B_y \sin(t_{lst} - \alpha_T) \sin \delta_T + \Delta B_z \cos \delta_T] + \sigma_{O^2} \quad (5.4) \\ &= \mathbf{a}\mathcal{A}_{bl}(t_{lst}) + \mathbf{b}\mathcal{B}_{bl}(t_{lst}) + \sigma_{O^2} \end{aligned}$$

Where I have put the full derivation in Appendix C.1.1. This is an equation for a plane in Right Ascension offset and Declination offset from target position with respective time-variable slopes  $\mathcal{A}(t_{lst})$  and  $\mathcal{B}(t_{lst})$ . The  $\sigma_{O^2}$  is the error in this model due to ignoring  $O^2$  terms.

In traditional phase referencing, the slope  $c\Delta\tau_{bl}$  is entirely ignored. The maximum value the slope can take will be determined by the magnitude of baseline component errors  $\Delta B_i$  and the distances  $\mathbf{a}, \mathbf{b}$ . The error in ignoring the slope (which is the  $O^1$  term) is:

$$\begin{aligned} |\sigma_{O^1}| &\leq |\mathbf{a}(\Delta B_x + \Delta B_y) + \mathbf{b}(\Delta B_x + \Delta B_y + \Delta B_z)| \\ &\leq \sqrt{\mathbf{a}^2 + \mathbf{b}^2} \sqrt{\Delta B_x^2 + \Delta B_y^2 + \Delta B_z^2} \\ &= \theta_{sep}\sigma_{bl} \end{aligned} \quad (5.5)$$

where  $\sigma_{bl}$  is the quadrature sum of individual sources of uncertainty (in this case only baseline). This form is consistent with Equation 5.2.

If the error in phase referencing (effectively the  $O^0$ /DC solution) is the maximum values the  $O^1$  term can take, then it follows the (baseline) error in MultiView is the maximum value  $O^2$  term can take.  $\sigma_{O^2}$  is the error in the plane due to not accounting for higher order terms (aka. curvature) and is given by:

$$\sigma_{O^2} = \mathbf{a}\mathbf{b}\mathcal{C}_{bl} + \frac{1}{2}\mathbf{a}^2\mathcal{D}_{bl} + \frac{1}{2}\mathbf{b}^2\mathcal{E}_{bl} \quad (5.6)$$

where functions for the  $O^2$  coefficients  $\mathcal{C}_{bl}$ ,  $\mathcal{D}_{bl}$  and  $\mathcal{E}_{bl}$  are given in derivation (Appendix C.1.1). All high order coefficients depend linearly on  $\Delta B_i$  and have the same sinusoidal dependence on hour angle and declination. Therefore, they all have maximum values which only depend on

## 5.2. INVERSE MULTIVIEW THEORY

baseline uncertainty  $\Delta B_i$ :

$$\begin{aligned}
|\sigma_{O^2}| &= |\mathbf{a} \mathbf{b} \mathcal{C}_{bl} + \frac{1}{2} \mathbf{a}^2 \mathcal{D}_{bl} + \frac{1}{2} \mathbf{b}^2 \mathcal{E}_{bl}| \\
&\leq \left| \frac{1}{2} \mathbf{a}^2 (\Delta B_x + \Delta B_y) + \mathbf{a} \mathbf{b} (\Delta B_x + \Delta B_y) + \frac{1}{2} \mathbf{b}^2 (\Delta B_x + \Delta B_y + \Delta B_z) \right| \\
&\leq \left| \frac{1}{2} \mathbf{a}^2 + \mathbf{a} \mathbf{b} + \frac{1}{2} \mathbf{b}^2 \right| |\Delta B_x + \Delta B_y + \Delta B_z| \\
&\leq \frac{1}{2} (\mathbf{a} + \mathbf{b})^2 \sqrt{\Delta B_x^2 + \Delta B_y^2 + \Delta B_z^2} \\
&\leq \theta_{sep}^2 \sigma_{bl}
\end{aligned} \tag{5.7}$$

This implies that even in the presence of baseline errors  $\Delta B = 3$  cm, MultiView plane fitting uncertainty is at the level of  $\sigma_{O^2} = 0.0002$  cm at  $\theta_{sep} = 5$  deg, equivalent to an astrometric uncertainty of  $\sigma_\theta = 13\mu\text{as}$  with a baseline of  $B = 3500$  km. This is opposed to the case of not fitting the plane in traditional phase referencing and getting values  $\sigma_{O^1} = 0.002$  cm and  $\sigma_\theta = 150\mu\text{as}$ .

Equation 5.7 describes the minimum value for baseline delay uncertainty. In practice the total delay uncertainty will be larger as it depends on how accurately the delay slopes can be measured, and this depends on other delay slopes such as the one due to the residual dry tropospheric path delay.

### 5.2.2 Dry Tropospheric delay differential $\Delta\tau_{dtr}$

The total difference in delay between a target and calibrator due to the troposphere is

$$\Delta\tau_{tr} = \Delta\tau_{dtr} + \Delta\tau_{wtr}$$

given in Equation 5.1 and as mentioned, will have two components, dry (*dtr*) and wet (*wtr*). For the moment I will only consider the difference between residual dry tropospheric delay  $\Delta\tau_{dtr}$ . For a single source at some zenith angle  $Z$ , the residual dry tropospheric zenith delay will be:

$$\tau_{dtr} = \sigma_{\tau_z}(t) \sec Z \tag{5.8}$$

where  $\sigma_{\tau_z}(t)$  is the zenith delay error arising from either uncertainty in geoblock fitting or systematic effects like ionosphere (see Section §2.4.2 for more information of geoblock fitting). I have used the dry tropospheric mapping function  $m_3 = \sec Z$  (Equation 2.15) as it is quantitatively easy to deal with (and I have previously shown various mapping functions  $m_1$ ,  $m_2$  and  $m_3$  equivalent; see Figure 2.4).

After phase referencing from the target at some zenith angle  $Z_T$  to the calibrator at another zenith angle  $Z_C$ , the hypothetical delay difference for the two positions for a *single antenna* is:

$$\begin{aligned}
\Delta\tau_{dtr} &= \sigma_{\tau_z} \left( \frac{1}{\cos Z_C} - \frac{1}{\cos Z_T} \right) \\
&= \frac{\sigma_{\tau_z}}{\sin \delta_C \sin \varphi + \cos \delta_C \cos \varphi \cos(t_{lst} - \alpha_C)} \\
&\quad - \frac{\sigma_{\tau_z}}{\sin \delta_T \sin \varphi + \cos \delta_T \cos \varphi \cos(t_{lst} - \alpha_T)}
\end{aligned} \tag{5.9}$$

## 5.2. INVERSE MULTIVIEW THEORY

where I have used  $\cos Z = \sin \delta \sin \varphi + \cos \delta \cos \varphi \cos(t_{lst} - \alpha)$  and  $\varphi$  is the antenna latitude. I make this substitution because I want to determine a plane in equatorial coordinates As in the previous example, the calibrator is arbitrarily offset from the target  $\alpha_C = \alpha_T + \mathbf{a}$  and  $\delta_C = \delta_T + \mathbf{b}$ . In Appendix C.1.1 I detail the expansion leading to:

$$\begin{aligned}\Delta\tau_{dtr} &= \frac{\sigma_{\tau_z}}{\cos^2 Z_T} (\mathbf{a} [-\cos \delta_T \cos \varphi \sin(t_{lst} - \alpha_T)] \\ &\quad + \mathbf{b} [\cos \varphi \cos(t_{lst} - \alpha_T) \sin \delta_T - \sin \varphi \cos \delta_T]) + \sigma_{O^2} \\ &= \mathbf{a}\mathcal{A}_{dtr}(t_{lst}) + \mathbf{b}\mathcal{B}_{dtr}(t_{lst}) + \sigma_{O^2}\end{aligned}\quad (5.10)$$

As before, the  $\sigma_{O^2}$  term is the error in the plane fit due to omission of higher-order terms that describe curvature. Unlike in the plane due to a baseline residual,  $\sigma_{O^2}$  is difficult to interpret in the equatorial coordinate system. Instead I will interpret this in a local telescope local coordinate system.

The worse case scenario leading to the largest value for  $\sigma_{O^2}$  is that as the target moves towards  $Z_T \rightarrow 90$  deg at a particular antenna location (aka. sets), target and calibrator are coincidentally aligned in the direction of maximum elevation change. This depends on the antenna location, for example, at the equator this will always be in the RA direction. So in order to retain generality I assume that in this scenario only the difference in zenith angles between the two sources is needed to parametrize the difference in residual delay.

In this case the difference in residual delay between the two sources can be described by:

$$\begin{aligned}\Delta\tau_{dtr} &= \sigma_{\tau_z} \left( \frac{1}{\cos(Z_T + \theta_{sep})} - \frac{1}{\cos Z_T} \right) \\ &= \sigma_{\tau_z} \sec^2 Z_T \sin Z_T \theta_{sep} + \sigma_{\tau_z} (\sin^2 Z_T + 1) \sec^3 Z_T \frac{\theta_{sep}^2}{2} + \sigma_{O^3}\end{aligned}\quad (5.11)$$

The  $O^1$  term is the same as that previously identified in Section 2.4.2, Equation 2.16 and would be the error if no plane fitting was performed (aka. the error in phase referencing). Therefore, it stands to reason that the maximum error in plane fitting from ignoring curvature is:

$$|\sigma_O^2| \leq \sigma_{\tau_z} (\sin^2 Z_T + 1) \sec^3 Z_T \left( \frac{\theta_{sep}^2}{2} \right)\quad (5.12)$$

Figure 5.2 shows a comparison between theoretical uncertainties in phase referencing and inverse MultiView. At  $Z_T = 60$  deg, with residual zenith troposphere  $\sigma_{\tau_z} = 3$  cm and a target-calibrator separation  $\theta_{sep} = 3$  deg, normal phase referencing at this elevation would yield:

$$\sigma_{O^1} = \sigma_{\tau_z} \sec^2 Z_T \sin Z_T \theta_{sep} = 0.55 \text{ cm}$$

equivalent to an astrometric accuracy of  $\sigma_\theta = 312 \mu\text{as}$  with a maximum baseline  $|\mathbf{B}| = 3500$  km. Alternatively, with MultiView plane fitting and the same parameters, this becomes

$$\sigma_{O^2} = \sigma_{\tau_z} (\sin^2 Z_T + 1) \sec^3 Z_T \left( \frac{\theta_{sep}^2}{2} \right) = 0.06 \text{ cm}$$

equivalent to an astrometric accuracy of  $\sigma_\theta = 33 \mu\text{as}$ , an order of magnitude improvement!

## 5.2. INVERSE MULTIVIEW THEORY

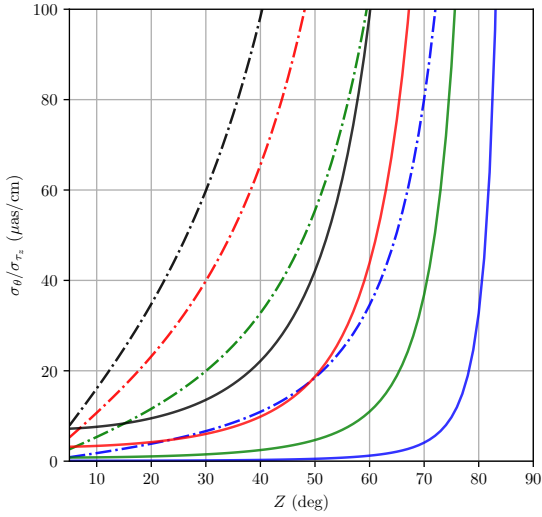


**Figure 5.2:** Comparison of theoretical maximum residual dry troposphere effect in inverse MultiView and phase referencing for different target–calibrator separations. **y-axis:** Positional uncertainty  $\sigma_\theta$  per unit residual zenith delay  $\sigma_{\tau_z}$ ; **x-axis:** Observing zenith angle. **Dotted lines:** phase referencing ( $\sigma_{O^1}$ ). **Solid lines:** inverse MultiView ( $\sigma_{O^2}$ ). **Blue, green, red and black lines** indicated target–calibrator separations  $\theta_{sep} = 1, 3, 6, 9$  deg respectively. All values are calculated with maximum ASCI baseline of  $|\mathbf{B}| \sim 3500$  km.

Inverse MultiView performs better than phase referencing for dry tropospheric calibration, especially in the presence of large residual tropospheric delay uncertainties ( $\sigma_{\tau_z} \geq 1 - 2$  cm), low-elevations and/or large target–calibrator separations. Theoretically, inverse MultiView should be able to give astrometric accuracy better than  $10\mu\text{as}$  at  $\sim 15$  deg elevation in the presence of well-calibrated zenith delays ( $\sim 1$  cm), and given proximal calibrators ( $\sim 1$  deg) on a baseline  $|\mathbf{B}| = 3500$  km.

### 5.2.3 Positional delay difference

So far I have shown that  $\Delta\tau_{bl}$  and  $\Delta\tau_{dtr}$  terms can be expressed by planes with uncertainties which depend on  $\sigma_{O^2} \propto \theta_{sep}^2$  and are in general smaller than equivalent uncertainties for normal phase referencing. Now I want to discuss how positional errors in target and calibrator affect the inverse MultiView method.

Equation 2.7 gives the delay uncertainty expected due to a source position error:

$$\begin{aligned} c\tau_\theta &= \sigma_\alpha \cos \delta_C (B_x \sin(t - \alpha) + B_y \cos(t - \alpha)) \\ &\quad + \sigma_\delta (-B_x \cos(t - \alpha) \sin \delta + B_y \sin(t - \alpha) \sin \delta_C + B_z \cos \delta) \end{aligned}$$

where  $\sigma_\alpha$  and  $\sigma_\delta$  are the positional uncertainties in Right Ascension and Declination;  $B_i$  are the baseline components in geocentric coordinates  $x, y, z$ ; and  $\alpha$  and  $\delta$  are again source Right Ascension and Declination.

Inverse phase referencing subtracts delay of the target from the calibrator, which serves to

## 5.2. INVERSE MULTIVIEW THEORY

subtract the above respective expressions for the target and calibrator:

$$\begin{aligned} c(\tau_{\theta,C} - \tau_{\theta,T}) = & \sigma_{\alpha,C} \cos \delta_C (B_x \sin(t - \alpha_C) + B_y \cos(t - \alpha_C)) \\ & + \sigma_{\delta,C} (-B_x \cos(t - \alpha_C) \sin \delta_C + B_y \sin(t - \alpha_C) \sin \delta_C + B_z \cos \delta_C) \\ & - \sigma_{\alpha,T} \cos \delta_T (B_x \sin(t - \alpha_T) + B_y \cos(t - \alpha_T)) \\ & - \sigma_{\delta,T} (-B_x \cos(t - \alpha_T) \sin \delta_T + B_y \sin(t - \alpha_T) \sin \delta_T + B_z \cos \delta_T) \end{aligned} \quad (5.13)$$

The target and calibrator will always be separated by some  $\theta_{sep}^2 = \mathbf{a}^2 + \mathbf{b}^2$  s.t  $\alpha_C = \alpha_T + \mathbf{a}$  and  $\delta_C = \delta_T + \mathbf{b}$ . I can substitute these expansions, and as shown in Appendix C.1.1, it then simplifies to:

$$\begin{aligned} c\Delta\tau_\theta = & [(\sigma_{\alpha,C} - \sigma_{\alpha,T}) \cos \delta_T (B_x \sin(t - \alpha_T) + B_y \cos(t - \alpha_T)) \\ & + (\sigma_{\delta,C} - \sigma_{\delta,T}) (B_x \sin \delta_T \cos(t - \alpha_T) - B_y \sin \delta_T \sin(t - \alpha_T) - B_z \cos \delta_T)] \\ & + \mathbf{a} [\sigma_{\alpha,C} \cos \delta_T (B_x \cos(t - \alpha_T) - B_y \sin(t - \alpha_T)) \\ & - \sigma_{\delta,C} \sin \delta_T (B_x \sin(t - \alpha_T) + B_y \cos(t - \alpha_T))] \\ & + \mathbf{b} [\sigma_{\alpha,C} \sin \delta_T (B_x \sin(t - \alpha_T) - B_y \cos(t - \alpha_T)) \\ & + \sigma_{\delta,C} (B_x \cos \delta_T \cos(t - \alpha_T) - B_y \cos \delta_T \sin(t - \alpha_T) - B_z \sin \delta_T)] \end{aligned} \quad (5.14)$$

This expression describes a plane, however, there is more nuance in this case than encountered in planes arising from dry tropospheric or baseline uncertainties. Firstly, there is an additional time-variable ‘constant’ offset term  $\tau_0(t_{lst})$  that depends on the difference in positional offsets of the two sources:

$$\begin{aligned} c\tau_0(t_{lst}) = & (\sigma_{\alpha,C} - \sigma_{\alpha,T}) \cos \delta_T (B_x \sin(t - \alpha_T) + B_y \cos(t - \alpha_T)) \\ & + (\sigma_{\delta,C} - \sigma_{\delta,T}) (B_x \sin \delta_T \cos(t - \alpha_T) - B_y \sin \delta_T \sin(t - \alpha_T) - B_z \cos \delta_T) \end{aligned}$$

This is the astrometric result. Synthesising an image (say of the target) with only this delay applied (subtracted) would give the astrometric offset  $\Delta\alpha_T = \sigma_{\alpha,T} - \sigma_{\alpha,C}$  and  $\Delta\delta_T = \sigma_{\delta,T} - \sigma_{\delta,C}$ . If the target was a maser and the calibrator a quasar,  $\sigma_{\alpha,C}$  and  $\sigma_{\delta,C}$  are constant over consecutive epochs and the  $\sigma_{\alpha,T}$  and  $\sigma_{\delta,T}$  over time give the parallax and proper motion (see Equations 2.29).

The second nuance is that there is not a ‘shared plane’ for multiple calibrators. In planes arising from residual dry troposphere or baseline offsets, RA or DEC slopes  $\mathcal{A}$  and  $\mathcal{B}$  can be solved for by using multiple calibrators and sampling the effect at different positions ( $\mathbf{a}$ ,  $\mathbf{b}$ ). In the case of planes arising from positional uncertainties:

$$c\Delta\tau_\theta = c\tau_0(t_{lst}) + \mathbf{a}\mathcal{A}_{\theta,i}(t_{lst}) + \mathbf{b}\mathcal{B}_{\theta,i}(t_{lst}) \quad (5.15)$$

there will be slopes  $\mathcal{A}_{\theta,i}$  and  $\mathcal{B}_{\theta,i}$  for each calibrator (represented with  $i$  subscript) and they will not necessarily correlate between calibrators. If the positional uncertainty of all calibrators is very small or zero  $\sigma_{\alpha,C,i} = \sigma_{\delta,C,i} \approx 0.0\mu\text{as}$  then there are ‘no slopes’ to measure at the calibrator position, only the negative of the target positional offset. This is the desired result in normal phase referencing.

Therefore, the uncertainty in the inverse MultiView measurement of the target–calibrator offset  $\Delta\tau_\theta$  will be the first order term  $\sigma_{O^1}$  as in the case of normal phase referencing:

$$c\Delta\tau_\theta = c\tau_0(t_{lst}) + \sigma_{O^1} \quad (5.16)$$

## 5.2. INVERSE MULTIVIEW THEORY

where the uncertainty is the average quadrature sum of source planes:

$$|\sigma_{O^1}| \leq \left| \frac{1}{N} \sum_{i=1}^N (a_i \mathcal{A}_{\theta,i} + b_i \mathcal{B}_{\theta,i}) \right| \quad (5.17)$$

These planes are a strong function of calibrator uncertainty, which nominally are  $0.1 - 0.3$  mas if taken from astrometric catalogues. However, these positions can be updated over the course of calibration and checked in consecutive epochs, getting the relative calibrator positions to the  $10 - 20\mu\text{as}$  level.

### 5.2.4 Final delays

The only delays from Equation 2.9 that I have not yet discussed are those associated with the wet-tropospheric delay and the ionosphere. As previously discussed in Section §2.4.3, the wet-troposphere is close to a stochastic system and depends on clumpy structures moving across the line-of-sight. This makes it difficult to theoretically predict what amount of residual water vapour will be along a line-of-sight ( $\mathbf{a}, \mathbf{b}$ ) degrees away from the phase reference position.

Nevertheless, if the angular distance between target and calibrator is smaller than the angular size of wet-tropospheric structures, there should be a smooth change in residual delay with angular distance from the phase reference position. Therefore, it stands to reason that there is a valid distance that this can be modelled by a plane in a first-order expansion:

$$\Delta\tau_{wtr} = \mathbf{a}\mathcal{A}_{wtr} + \mathbf{b}\mathcal{B}_{wtr} + \sigma_{wtr} \quad (5.18)$$

Within this distance inverse MultiView will give similar or better calibration results than inverse phase referencing as it accounts for the smooth change and removes it.

It has already been shown that the ionospheric structure is very well described by planar structure (Rioja et al., 2018, ; Figure 5). Therefore, I assume that the residual ionosphere (after TEC GPS correction; see Section §2.4.4) is also well-described by a 3D plane in RA and DEC:

$$\Delta\tau_{io} = \mathbf{a}\mathcal{A}_{io} + \mathbf{b}\mathcal{B}_{io} + \sigma_{io} \quad (5.19)$$

However, as with the case of the wet-troposphere, the expected angular distance or time-scale over which this is valid is unknown.

### 5.2.5 Total delay/phase solution

I have derived delay-plane solutions for the known potential causes for an angular delay difference. Each of these (apart from source position error) was derived for a particular antenna at a fixed location and is expected to change based on the hour angle  $h = t_{lst} - \alpha$ . However, in reality, a delay can only be measured relative to another telescope and is a baseline quantity. Each antenna will have an individual set of time-variable slopes  $\mathcal{A}, \mathcal{B}$  which depend on  $\alpha, \delta, t_{lst}, \varphi$  and the various potentially time dependent/variable (e.g.  $\delta\tau_z, \delta\tau_I, \dots$ ), or time independent/stable (e.g.  $\Delta B_x, \Delta\alpha, \dots$ ) sources of delay. The measured delay difference between target (observed at time  $t_{j+1}$ ) and calibrator (observed at time  $t_j$ ), will be the delay difference above antenna  $i$

### 5.3. OBSERVING METHOD AND PHASE–FITTING

minus the delay difference above the reference antenna  $r$ :

$$\begin{aligned}
(\tau_T(t_{j+1})_i - \tau_T(t_{j+1})_r) - (\tau_C(t_j)_i - \tau_C(t_j)_r) &= \tau_0(t_{gst}) + \tau_{th} \\
&\quad + \mathbf{a} [\mathcal{A}_{bl,i} - \mathcal{A}_{bl,r} + \mathcal{A}_{dt,i} - \mathcal{A}_{dt,r} \dots] (t_{gst}) \\
&\quad + \mathbf{b} [\mathcal{B}_{bl,i} - \mathcal{B}_{bl,r} + \dots] (t_{gst}) \\
&= \tau_0(t_{gst}) + \mathbf{a} \mathbf{A}(t_{gst}) + \mathbf{b} \mathbf{B}(t_{gst})
\end{aligned} \tag{5.20}$$

where  $t_{gst} = t_{lst} - \psi_i$  is Greenwich sidereal time and  $\psi_i$  is the antenna East–Longitude in hours for antenna  $i$ .

Thus far I have limited discussion to the idea of slopes in delay. However, if maximum the delay difference between target and calibrator are kept within a observing wavelength ( $c\tau \ll \lambda$ ), then phase is an effective tool to sample the changes more accurately. Recall:

$$\begin{aligned}
\phi &= 2\pi\nu\tau \\
\therefore \frac{\partial\phi}{\partial\tau} &= 2\pi\nu
\end{aligned} \tag{5.21}$$

which shows that phase is  $2\pi\nu$  times more sensitive to changes in delay than the delay itself, with the caveat that phase is subject to  $2\pi$  measurement ambiguities. As phase referencing is the standard procedure, a phase–plane will be the assumed model and phases are expected to be  $-\pi < \phi < \pi$ .

## 5.3 Observing Method and Phase–Fitting

In the previous section I theorised that after solving for phase and rate on a target and applying that solution to surrounding calibrators, any and all residual delay can be treated as a phase plane in RA and DEC offset from the target position:

$$\phi(\alpha, \delta, t) = \phi_0(t) + \mathbf{A}(t)(\alpha - \alpha_T) + \mathbf{B}(t)(\delta - \delta_T) \tag{5.22}$$

where  $\mathbf{A}$  and  $\mathbf{B}$  are the phase–gradients in  $\alpha$  and  $\delta$  directions respectively. Simultaneous observations of target and calibrator are unavailable. Observational structure will be T–C1–T–C2–T–C3–T such that target and calibrators are observed within the tropospheric coherence time to approximate simultaneity.

As the calibrator sources are not observed simultaneously, there cannot be an exact solution for the entire plane for each time-stamp. Rather I will consider a moving solution for each cluster of sources. Say if there are  $n$  calibrators in the ring (henceforth orbit sources) then the measured phase for each loop (and each baseline) will be:

$$\Phi(\bar{t}_i) = \begin{bmatrix} \phi_1(t_{i,1}) \\ \phi_2(t_{i,2}) \\ \phi_3(t_{i,3}) \\ \vdots \\ \phi_{n-1}(t_{i,n-1}) \\ \phi_n(t_{i,n}) \end{bmatrix}$$

### 5.3. OBSERVING METHOD AND PHASE-FITTING

Where  $t_{ij} = t_{i,j-1} + 2(t_{\text{dwell}} + t_{\text{slew}})$ . Practically, this implies that the time-stamp for the solution is  $\bar{t} = t_{i,\frac{n}{2}}$ . Despite the fact that each loop around the ring will take  $t = 2n(t_{\text{dwell}} + t_{\text{slew}})$  and I practically want to use all  $n$  points to solve for the plane at a given time, I can sample the time more regularly than every loop. If I take the next phase solution from the same quasar in the following loop, I can set finer time sampling of  $\delta t \approx 2(t_{\text{dwell}} + t_{\text{slew}})$ . Then the next phase vector is:

$$\Phi(\bar{t}_{i+1}) = \begin{bmatrix} \phi_2(t_{i+1,2}) \\ \phi_3(t_{i+1,3}) \\ \phi_4(t_{i+1,4}) \\ \vdots \\ \phi_n(t_{i+1,n}) \\ \phi_1(t_{i+1,1}) \end{bmatrix}$$

At each time step  $i$ , the problem and solutions are:

$$\Phi(\bar{t}_i) = [\phi_{i,j}] = \begin{bmatrix} 1 & \alpha_1 - \alpha_0 & \delta_1 - \delta_0 \\ 1 & \alpha_2 - \alpha_0 & \delta_2 - \delta_0 \\ \vdots & & \\ 1 & \alpha_j - \alpha_0 & \delta_j - \delta_0 \end{bmatrix} \begin{bmatrix} \phi_{0,i} \\ \mathbf{A}_i \\ \mathbf{B}_i \end{bmatrix} = \mathbb{M}\boldsymbol{\lambda}_i$$

$$\therefore \boldsymbol{\lambda}_i = (\mathbb{M}^T \mathbb{M})^{-1} \mathbb{M}^T \Phi_i \quad (5.23)$$

This solution weights all points equally, which makes sense if all data is equally certain. However ‘weaker’ calibrators will have a less certain phase solution and that measurement error has to be taken into account. If a calibrator is measured to have a phase of  $\phi$  with a signal-to-noise of SNR; then I consider the uncertainty in that measurement to be:

$$\sigma_\phi = \frac{1}{\text{SNR}} \quad (5.24)$$

in radians. Finally I assume that the weights will take the form

$$w_i = \frac{1}{\sigma^2}$$

$$\sigma^2 = \sigma_s^2 + \left( \frac{180}{\pi \text{SNR}} \right)^2 \quad (5.25)$$

where I have assumed a static error floor of  $\sigma_s \sim 10 \text{ deg}$ . This ensures that extremely luminous quasars do not dominate the solution while sufficiently weak quasars are rightfully down-weighted. Therefore, I have the diagonal weight matrix:

$$\mathbb{W} = \begin{bmatrix} w_1 & 0 & 0 & \dots & 0 \\ 0 & w_2 & 0 & \dots & 0 \\ 0 & 0 & w_3 & \dots & 0 \\ \vdots & \vdots & & \ddots & \vdots \\ 0 & 0 & \dots & \dots & w_n \end{bmatrix}$$

which is incorporated into the equation at each time step as:

### 5.3. OBSERVING METHOD AND PHASE-FITTING

$$\begin{aligned} \mathbb{W}\Phi_i &= \mathbb{W}\mathbb{M}\lambda_i \\ \therefore \lambda_i &= (\mathbb{M}^T \mathbb{W}\mathbb{M})^{-1} \mathbb{M}^T \mathbb{W}\Phi_i \end{aligned} \quad (5.26)$$

Hence, I can calculate a solution  $\lambda(\bar{t})$  for each baseline, which I can use to return positional information back to the target source while correcting for the presence of phase slopes between the orbit sources and target due to residual phase errors.



### 5.3. OBSERVING METHOD AND PHASE-FITTING

# 6

## MULTIVIEW–RING CALIBRATION

The lack of well-characterised VLBI calibrators in the Southern Hemisphere limits the number of targets available within a given radius of a target. This is especially detrimental when conducting astrometry within the Galactic Plane where there is additional obscuration and many radio continuum surveys stop as they approach the plane (usually  $|b| \leq 5$  deg). For traditional phase referencing, this means observations have to rely on ‘distant’ and/or poor quality quasars, or luck. The only alternative to these three is not to conduct observations at all. This is extremely unfortunate as the vast majority of the central Galaxy is visible from the Southern Hemisphere.

The standard approach for phase referencing observations is to seek calibrators as close as possible to the target so as to minimise the differential effects of uncompensated delays. However, as I have shown in the previous chapter, phase referencing using more distant quasars should be possible if the differential delay effects can be measured and hence corrected for.

In this chapter I present results of the first demonstration of inverse MultiView, the first phase referencing observations utilising the ASCI Array and first microarcsecond astrometric result in the Southern Hemisphere. I provide an overview of the processes I personally undertook to achieve this, including scheduling, observing, correlating, reduction and analysis. I then discuss results, uncertainty limitations of the technique and recommendations for future observations.

## 6.1 Introduction

The primary cause of residual delay at mid-frequencies ( $\sim 4 - 8$  GHz) is generally attributed to the ionosphere. While this is most likely accurate, it does not eliminate the existence of other unmodelled residual delays such as baseline errors or residual troposphere and they should not be discounted. Regardless, due to the much lower density of GPS receivers in the Southern Hemisphere relative to the North, Total Electron Content (TEC) maps have a much lower resolution and can include systematic offsets (Walker & Chatterjee, 1999). At centimetre wavelengths (e.g. 6.7 or 8.4 GHz) the contribution of tropospheric and ionospheric path delays is expected to be roughly equal, and without a method to remove dispersive and non-dispersive delays separately the residual dispersive delays are included in the solution of the zenith non-dispersive delays. While dual-frequency observations allow accurate tropospheric delays to be measured and applied to phase reference data, residual ionospheric delays will still be present and unmodelled. Therefore, this issue of unmodelled residual delays is shared between dual and single-frequency phase referencing observations and requires observational techniques to remove.

Only derivations of MultiView provide a method to calibrate out these residual ionospheric delays for phase referencing astrometry. These experiments provide the opportunity to not only develop and test these techniques, but to do so on a fledgling VLBI array. The array used for these observations is the AuScope–Ceduna Interferometer (ASCI) Array (Section 1.4.3). This array will also form the basis for the S $\pi$ RALS large project, and these observations serve as pilots in terms of array capabilities and technique.

The AuScope portion of this array is comprised of Katherine (Ke), Yarragadee (Yg) and Hobart26m (Ho). Ke/Yg are identical 12 m Patriot geodetic dishes equipped with S/X receivers, DBBC2 digitisers and Mark5B recording units (Lovell et al., 2013). Ho is a 26 m X/Y mount equipped with cryogenic cooled L, S, X, C(4.8 GHz), 6.7 GHz, 12 GHz, S/X and K-band receivers, DBBC2 and Fila10G/Flexbuf recorder. Ho/Ke and Yg all regularly participate in IVS geodetic observations. The final telescope, Ceduna (Cd; McCulloch et al., 2005) only participates in irregular LBA VLBI observations. It is a 30 m ex-telecommunications dish, equipped with uncooled L, S, X, C(4.8 GHz), 6.7 GHz, 12 GHz and K-band receivers, a DBBC2 and Fila10G/Mark5C recorder. This will be the first time these telescopes will be used in conjunction for VLBI astrometry and I am eager to show how they perform.

S $\pi$ RALS aims to achieve high accuracy astrometry for 6.7 GHz masers on the ASCI array, however, it will likely encounter the same large residual delays as Krishnan et al. (2015, 2017) on the LBA. Authors of those papers suspect the main cause of residual delay was the ionosphere and therefore MultiView may be the only way to remove those effects. In fact, as I have shown in Chapter 5 MultiView should be able to calibrate almost all causes of residual delay. Therefore I want to collect and analyse real data to test these predictions.

In this chapter I develop the methodology and reduction processes for inverse MultiView, allowing for high accuracy astrometry at intermediate frequencies in the presence of suspected large residual delays. The questions that I address are:

1. What is the astrometric accuracy of MultiView vs. what would be expected from inverse phase referencing at a similar target–calibrator separation. Does it perform better? As I will show, inverse MultiView increases calibration overheads and is non trivial to observe or reduce. Does it return a proportionally better result? I address this question in Section §6.5.1;

## 6.2. SOURCE SELECTION

2. What is the maximum separation between target and calibrators for which inverse MultiView can measure coherent solutions and what is the cause of this decoherence? There are generally fewer suitable (compact, high flux density) calibrators in the immediate neighbourhood of Galactic masers so the larger separation for which high accuracy astrometry can be undertaken, the better. Rioja et al. (2017) use a maximum separation between calibrators of  $\theta \sim 10$  deg at low frequencies for non-inverse MultiView, where the ionosphere is expected to be the largest source of error. At higher frequencies ( $> 6-8$  GHz) the troposphere is expected to be dominant, however, the residual effects of both can be equivalent in magnitude. So after including dry tropospheric calibration techniques (geoblocks) and GPS TEC maps, is MultiView at intermediate frequencies limited by ionosphere, dry/wet troposphere or some other factor? I address this question in Section §6.5.1.
3. Is it possible to use measured phase slopes to determine residual delays? The derived equations in the previous chapter provide clear relationships between instantaneous sources of residual delay, LST and/or UTC, longitude, latitude, RA and DEC. It is possible to decouple the relationships and approximate residual path delay and therefore estimate the calibration fidelity. The phase-slopes derived in the previous chapter are very sensitive to residual delay and therefore could be used as a delay probe. I discuss the nature of phase slopes and feasibility of delay determination in Section §6.5.2.
4. How should MultiView be conducted in the future? Is there an optimal number of calibrators, what calibrator parameters should be optimised and what spacing/positioning might give best results. I address this question in Section §6.5.3.

## 6.2 Source Selection

The ultimate aim of this chapter is to test the ability of inverse MultiView to measure and remove the residual delay for maser astrometry in S $\pi$ RALS, so the observing structure is nearly identical to that of a maser phase-referencing observation (see Section §6.3.2). The ASCI array does not currently have mutual frequency coverage over the rest frequencies of any known and/or appropriately bright maser species, so I have used quasars as both the calibrators and targets for these MultiView tests. Although this does not allow me to test MultiView under identical conditions as a parallax observation, it does present other advantages. In the next few sections I will discuss these advantages and quasar selection criteria.

### 6.2.1 Quasar benefits and Quality $Q$

The primary benefit of using quasars as targets is that their positions are constant with time. In addition, they have little to no structure and due to frequent observations by global VLBI arrays, often have known positional and flux density values. The lack of detectable proper motion and parallax implies any measured offsets that change over time are due to residual delay or phase-noise, which can be directly used for an estimate of calibration quality. This fact will be used to compare traditional phase referencing methods to inverse MultiView and determine the overall capability of the array.

Although many quasars can appear point-like, others can have jets that may offset the astrometric results. Care is taken to avoid resolved quasars or those with jets as they can make phase referencing solutions confusing or add positional uncertainty. Frequent VLBI observations of a

## 6.2. SOURCE SELECTION

subset of quasars places good constraints on their absolute positions. Henceforth I will refer to the positional uncertainty of a quasar as its quality  $Q$ . Generally speaking, the smaller  $Q$  is, the more desirable the quasar is for astrometry

Another advantageous characteristic of quasars is that they are very common compared to masers (referring to individual maser regions per species). The 2019a Radio Fundamental Catalogue contains 15740 objects\*, which gives an average sky density of  $\sim 0.38 \text{ deg}^{-2}$  or roughly 1.2 quasars per circle of radius 1 deg. In contrast, the catalogue of all known 6.7 GHz methanol masers (Yang et al., 2019, and referenced therin) contains 1085 masers largely confined to the Galactic Plane  $|b| < 5^\circ$  and only observable between 7 – 17 LST for the Southern Hemisphere. This difference not only allows for a larger pool to select from and a greater time window to observe, but allows one to have strict selection criteria.

While the total quasar sky-density remains  $0.38 \text{ deg}^{-2}$  at intermediate-to-high Declinations, at low Declinations ( $\delta < -30^\circ$ ) the total density drops to  $\sim 0.19 \text{ deg}^{-2}$  (Figure 6.1). This discrepancy is unlikely due to a lack of quasars, which are isotropically distributed but represents a relatively lower amount of regular and high-sensitivity quasar surveys in the Southern Hemisphere. In addition, due to the relative lack of frequent observations, the number of quasars known in the Southern Hemisphere is proportionally biased towards ‘low-quality’ quasars (Figure 6.1). In

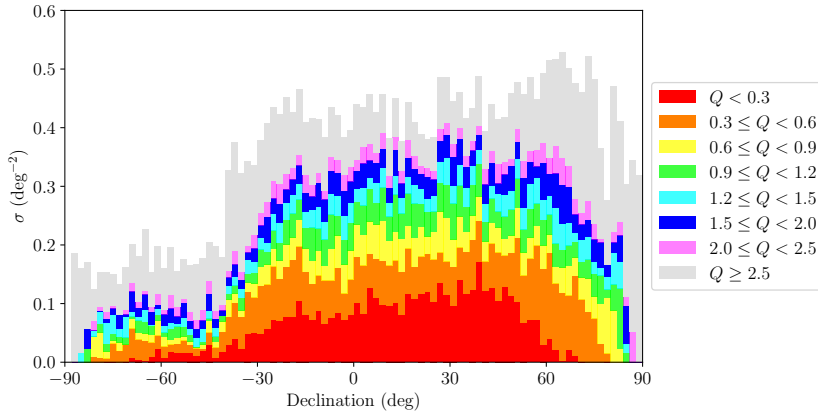


**Figure 6.1:** Stacked Declination-binned quasar density distribution. Colour represents relative contribution of each quasar- $Q$  (legend) to the Declination-binned quasar density.

catalogues, quasars are presented with estimated positional accuracies. As I want to focus on the atmospheric aspects of MultiView calibration, I chose only quasars with  $Q < 0.3$  mas. Finally, to limit the effects of target elevation, sources are only selected from the South celestial region  $\delta < 0$ . Next, I need to consider quasars from the perspective of array sensitivity.

### 6.2.2 Sensitivity Limitations

I want to use the nominal SEFDs of the telescopes to determine the detection limit. Taking the Cd–Ke baseline and nominal SEFD = 800 Jy and SEFD = 3500 Jy for Ceduna and Katherine respectively, a  $\tau = 40$  s integration with a spanned-bandwidth of  $\Delta\nu = 256$  MHz will yield a

---

\*<http://astrogeo.org/rfc/>

## 6.2. SOURCE SELECTION

noise level  $\sigma_S$  of:

$$\begin{aligned}\sigma_N &= 1.2 \sqrt{\frac{\text{SEFD}_i \text{SEFD}_j}{2\tau\Delta\nu}} = 1.2 \sqrt{\frac{800 \times 3500}{2 \times 40 \times 256 \times 10^6}} \\ &= 11 \text{ mJy}\end{aligned}$$

Therefore, for a strong, per-scan detection of  $\text{SNR} = \frac{S_c}{\sigma_N} > 10$ , I require quasars with a correlated flux density  $S_c > 110 \text{ mJy}$ . Constraining  $S_c$ ,  $\delta < 0.0^\circ$  deg and  $Q < 0.3 \text{ mas}$  I find there are a total of 824 available quasars. From this list of good quasars, I desire the ones which have a sky distribution favourable for testing inverse MultiView.

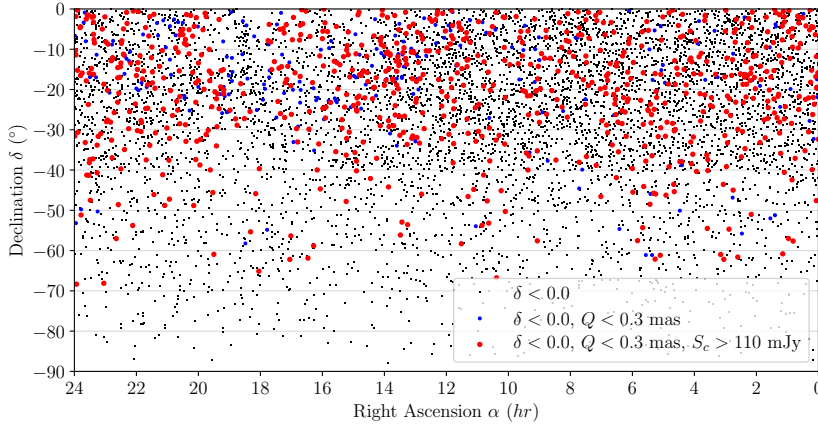


**Figure 6.2:** Sky positions of all  $\delta < 0.0^\circ$  quasars. **Black:** Non-suitable quasars due to positional uncertainty  $Q > 0.3 \text{ mas}$ . **Blue:** Non-suitable quasars on the basis of catalogued correlated flux  $S_c < 110 \text{ mJy}$ . **Red:** All suitable quasars.

### 6.2.3 Quasar Arrangement

The final determination is to choose which clusters of quasars I want to select as the targets and calibrators from this list of 824 quasars. The expectation is that for a clumpy and non-uniform residual ionosphere, there should be a maximum distance beyond which phase decoherence occurs. In order to test this theory I use the idea of a calibration ring with an approximate radius around a target quasar to compare the astrometric accuracy for each ring radii.

A search was conducted for quasars that had  $N \geq 6$  surrounding quasars within the sample, confined to ring radii or range 2–4, 4–5, 5–6, 6–7 and 7–8 degrees. The number of quasars in the ring was chosen for redundancy and in order to minimise the contribution from directionality. Quasar clusters were selected from the sample that had good position angle ( $\theta_i = \arctan(\Delta\delta, \Delta\alpha)$ ) sampling about the target such that the root sum of squares (RSS) of the angle was:

$$\text{RSS} = \frac{\sqrt{\sum \theta_i^2}}{2\pi} \leq 1.2$$

In total this gave a list of 29 potential rings. Visual inspection of the rings was performed to cut down list of candidates to 9. Three at around  $\alpha = 7$  hrs,  $\alpha = 14$  hrs and  $\alpha = 20$  hrs. The three

## 6.2. SOURCE SELECTION

rings would share a 7 hour track over a  $\sim 24$  hour experiment, sampling the different radii and effects due to Local Time.

Largely for historical and internal reasons, sources names are indicated via the following rules: Source names starting with G indicates a target at the centre of a ring, J indicates a calibrator (orbit source) within the ring and F a fringe finder. In all cases the name of the sources is based on the J2000 right ascension and declination.

Pathfinder observations MV022 and MV025 revealed that some of these rings contained poorly constrained calibrator and target positions and/or lower flux density sources than expected from the catalogued values. Therefore the final list of rings was cut down to the best 3 at differing LST and radii in experiments MV026, 27 and 28. These rings were centred at the quasar positions of: G0634–2335 with a mean radius of  $\bar{R} = 3$  deg; G1901–0809 with  $\bar{R} = 6.5$  deg and; G1336–0829 with  $\bar{R} = 7.5$  deg (see Figures 6.3, 6.4 and 6.5, respectively). Considering the isoplatonic radius for the wet–troposphere is considered to be smaller than  $R = 7–9$  deg, this was expected to give a good idea of the limitations of inverse MultiView calibration before and after this transitional point.

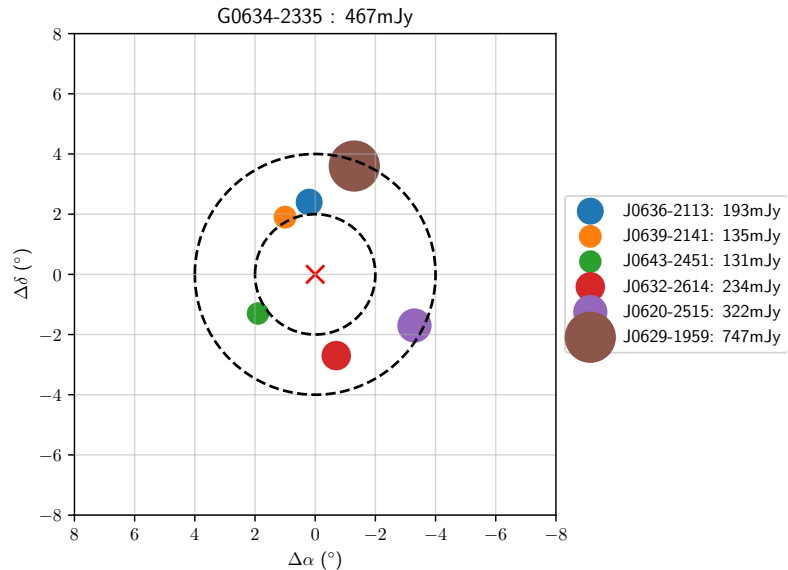


**Figure 6.3:** Ring plot for target quasar G0634–2335. This ring is between  $2^\circ$  and  $4^\circ$  as smaller rings with sufficient quasars that fit the criteria did not exist. The catalogued correlated flux density for G0634–2335 is 467 mJy.

## 6.2. SOURCE SELECTION

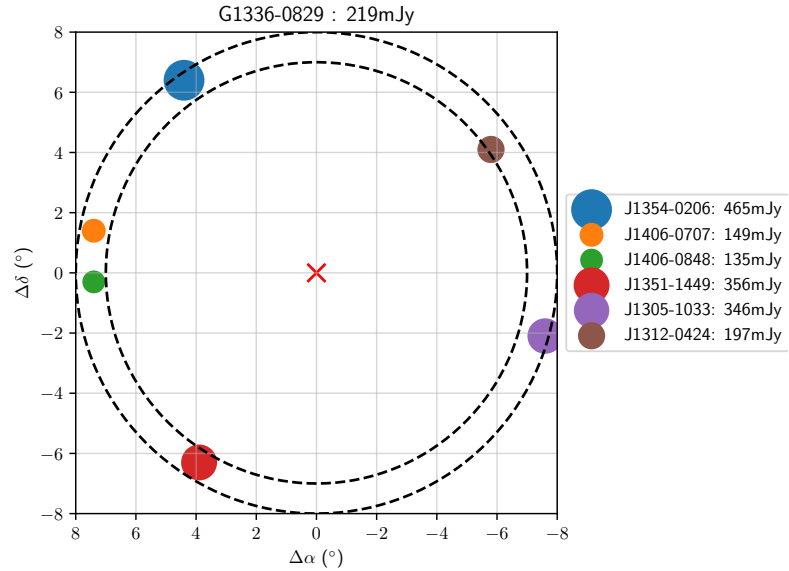


**Figure 6.4:** Ring plot for target quasar G1336–0829. This ring is between  $7^\circ$  and  $8^\circ$  and the central quasar has flux density 219 mJy.

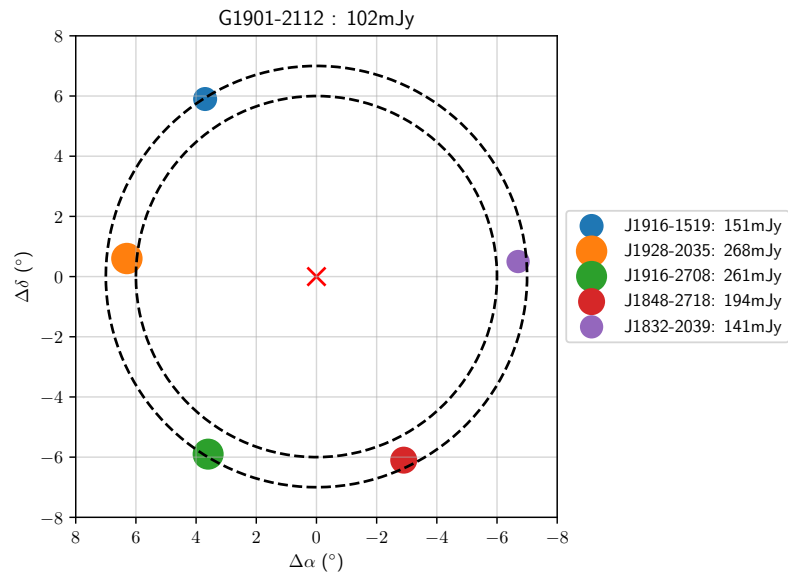


**Figure 6.5:** Ring plot for target quasar G1901–2112. This ring is between  $6^\circ$  and  $7^\circ$  and the central quasar has flux density 120 mJy.

## 6.3 Method and Observations

### 6.3.1 Array and Frequency

Observations were conducted using the ASCI Array (Section §1.4.3). Baselines and approximate sensitivities are given in Table 6.1. The ASCI Array is quite sparse, lacking baselines  $uv < 45 \text{ M}\lambda$ . For compact targets and calibrators such as those determined in Chapter §4 or chosen in the previous section, this sparse  $uv$ -sampling should prove less of an issue, with the exception of potentially higher sidelobe levels than an array with more elements.

**Table 6.1:** **Left:** VLBI baselines for the ASCI Array. **Upper Left:** Linear distances (km) between the antennas as calculated by NRAO VLBI scheduling program SCHEd. **Lower Left:** Approximate mean  $uv$ -distance ( $\text{M}\lambda$ ) for 8.34 GHz observations. **Right:** Baseline sensitivites ( $\pm 10\%$ , mJy) for a 40 s integration and  $\Delta\nu = 256 \text{ MHz}$ .

	$ \mathbf{B} $				$\sigma_s \text{ (Jy)}$			
	Cd	Ho	Ke	Yg	Cd	Ho	Ke	Yg
<b>Cd</b>	-	1703	1937	1792	-			
<b>Ho</b>	47.3	-	3432	3211	5	-		
<b>Ke</b>	53.9	95.4	-	2360	11	9	-	
<b>Yg</b>	49.8	89.3	65.6	-	11	9	21	-

The optimal frequency range to observe the quasars was deemed to be X–band due to mutual frequency coverage, ionospheric/tropospheric stability and most importantly, frequency–proximity to the planned observing frequency of 6.7 GHz methanol masers. S–band was also an available option for mutual frequency coverage, but lacked other factors. If the aims had been to test ionospheric residual delay and compensation by MultiView, perhaps future observations could involve this. However, in order to test inverse MultiView as applicable to maser phase referencing, X–band was the best option.

All observations were recorded with  $16 \times 16 \text{ MHz}$  packed bands, single polarisation RCP, giving 256 MHz sky frequency and the following setup:

$$\nu_L = 8196.99 + 16 \times (0, 1, 2, 3, 4, 5, 6, 7, 8, 9, 10, 11, 12, 13, 14, 15) \text{ MHz}$$

where  $\nu_L$  is the lower edge frequency for each band. Single polarisation 256 MHz was chosen over the optional 128 MHz dual polarisation as the former prioritises delay sensitivity and the latter discrete frequency sensitivity. As quasars emit in continuum, wide–band single polarisation was prioritised.

### 6.3.2 Observing Structure

The general observing structure is modelled on that used for the VLBA BeSSeL BR210 epochs (see Section §2.7 and Chapter 3) and consists of three full tracks spanning  $\sim 23$  hours. Each 7 hour track is defined as the time in which the target source is at an elevation above  $30^\circ$  at all stations, bracketed by 45 mins for calibration (see Figure 6.6).

### 6.3. METHOD AND OBSERVATIONS

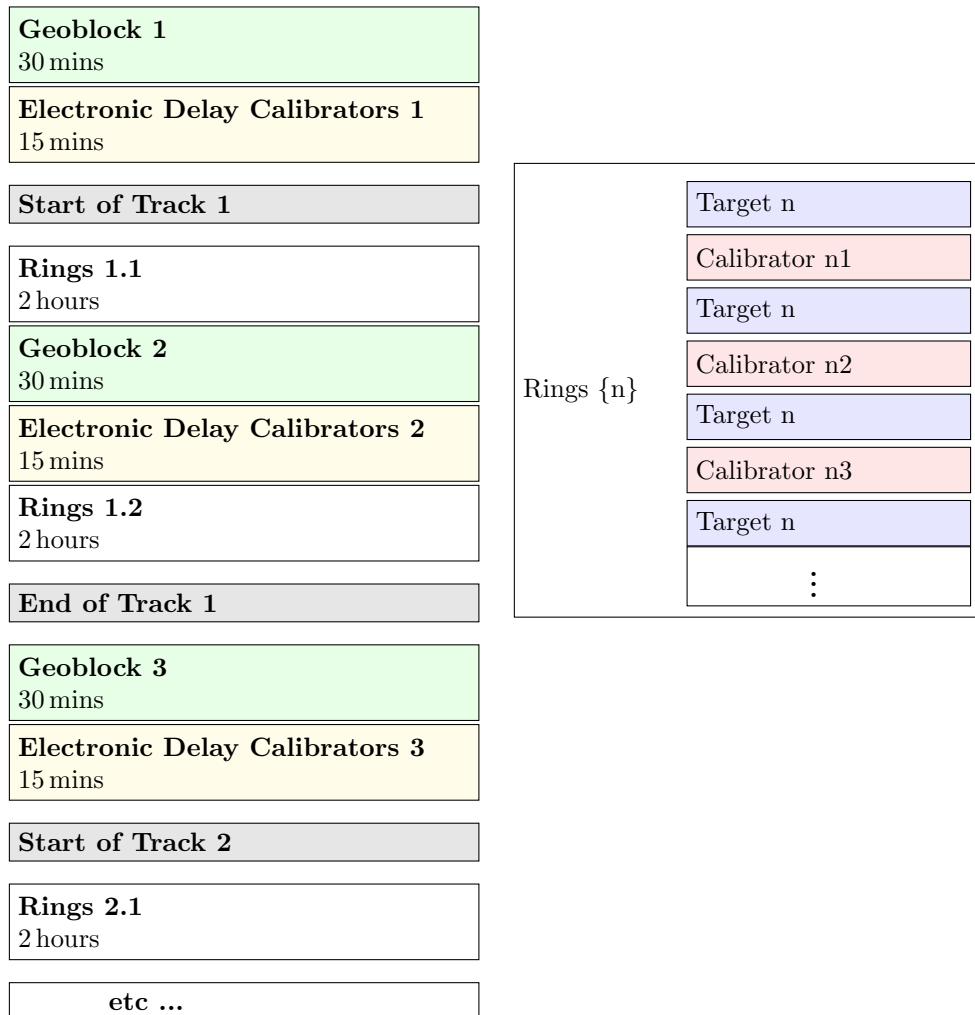


**Figure 6.6:** Block Diagram for the MV02\* observing structure.

### 6.3. METHOD AND OBSERVATIONS

Observations begin with a 30 minute geoblock, followed by a  $\sim$ 15 min block with electronic delay calibrators (EDC). For redundancy, 3–4 bright fringe finder quasars sources were scheduled in each EDC to ensure that one or more is sufficiently bright and has enough onsource time. Slewing accounts for the remaining time. Potentially overzealous redundancy was due to uncertain quasar brightness and array performance. The fringe finders were used to calculate clock drift–rate, bulk clock–offsets and confirm fringes during correlation, calibrate individual telescope electronic delays (manual phase calibration) as well as check delay residuals after application of global atmospheric delay solution. Although the pre–calibration (geoblock + fringe finder) overhead is about 30%, good *a priori* solutions for the delays and fringe–rates are required to avoid the possibility of phase–wrap ambiguities. As seen in the previous chapter, the magnitude of the delay/phase planes depends on residual delay and might cause general loss of coherence in the phase domain if left uncalibrated.

At beginning of the track after the first geoblock and EDC block, the target source was at an elevation  $\varepsilon \gtrsim 30^\circ$  at all sites and the MultiView nodding began. The observing mode here was Target, Calibrator 1, Target, Calibrator 2, ... and so on. For eventual fringe–fitting on the target (inverse phase referencing), target source scans observations bracket the calibrator scans to ensure long–term phase coherence. I decided it was best to observe orbit sources in a ‘star’ pattern rather than progressing azimuthally around the ring. This was to minimise the effect of a possible directional sampling bias and ensuring that the slope measured at any time was representative. There may be more a optimal time–spatial sampling for a given quasar distribution that accounts for likely slope differential changes over the loop interval, however, that investigation is a refinement on the basic method and is a potential topic for future study.

The above process was repeated once, with a second geoblock in the centre of the track to avoid loosing time due to tracking the target source through the zenith at the larger, more slowly slewing antennas. The third geoblock and electronic delay calibrator blocks are directly after the target was below  $30^\circ$  at at least two stations. Geoblocks must also bracket ring blocks for interpolation of clock and tropospheric delay solutions, with a minimum of 3 geoblocks necessary for a reasonable estimate for the clock–rate and residuals at each station. Tracks can be tiled together, sharing the middle and fringe–finder blocks such that observations can contain at least 3 tracks per day for a total of approximately 23 hrs.

Table 6.2 summaries the results of epochs MV020 through to MV028. Only epochs MV025 through to MV028 are used in further analysis for the reasons outlined in the bottom section of Table 6.2.

### 6.3. METHOD AND OBSERVATIONS

**Table 6.2:** MV02\* epochs. **Top:** Successful epochs, characterised by minimal or acceptable issues and or loss of data. **Bottom:** Unsuccessful MV02X epochs where one or more major telescope, backend or data problems caused the loss of almost all the data at one or more antennas.

Epoch	Date	$N_r$	Notes
<b>Used:</b>			
MV025	17-Feb-2019	9	9 ring experiment, otherwise no issues
MV026	17-Mar-2019	3	Ceduna 30m power failure in last 3 hours and subsequent clock jump
MV027	13-Apr-2019	3	No issues to note
MV028	4-May-2019	3	No issues to note
<b>Unused:</b>			
MV022	9-Feb-2019	9	Unexplained $> 2\text{ ns}$ clock oscillation at Ceduna 30m
<b>Unsuccessful:</b>			
MV020	20-Jul-2018	9	6 hour pilot observation. No Hobart 26m fringes
MV021	23-Sep-2018	9	Incorrect Hobart26m mode and bitmask
MV023	9-Feb-2019	9	Incorrect receiver configuration at Ceduna 30m
MV024	10-Feb-2019	9	Incorrect Mark5B frame size at Ceduna 30m, data recorded incorrectly; Katherine taken offline after 6 hours for maser maintenance

## 6.4 Reduction Processes

The data were all reduced in an identical manner over the four epochs (MV025, 26, 27 and 28) with the Standard VLBI calibration method (Section 2.7) with minor variation:

1. Some antenna positions needed to be corrected and updated. This was performed by fitting the residual multiband delays for a diurnal sinusoidal offset in addition to geodetic delays;
2. The amplitudes were initially calibrated with antenna system temperature measurements from the telescope sites, and then again using an iterative method (see Section §2.5.2);
3. After manual phase calibration, data is fit with inverse phase referencing (iPR) and can proceed to be split out and imaged. Then, post-iPR data is fit with inverse MultiView methods and this data is also split out and imaged.

### 6.4.1 Correlation

I correlated the baseband data from the telescopes with DiFX-2.6.1 (Deller et al., 2011) running on a local cluster. As per Section 2.3.1 this process involved fringe verification and manual clock-searching. For fringe-finding, a strong source from the EDC blocks (optimally near the centre of the observation; EDC block 2 or 3) with all telescopes onsource is correlated at a high spectral resolution (often  $\delta\nu < 0.0625\text{MHz}/\text{channel}$ , or 256 channels in a 16 MHz band). The detection of fringes on this source indicates that telescopes had a correct frequency setup and indeed was on source for this time (potentially eliminating extreme pointing issues). In addition, high spectral resolution correlation allows the detection of higher single band delays which might otherwise wrap over a channel. The maximum detectable delay goes as  $\tau = 2\pi/\delta\nu < 100\ \mu\text{s}$ , so failure to find fringes might indicate a too low correlation resolution such that the phases are decorrelating over the channels. Once fringes are found, the antenna delays for that scan can be used to zero the delays (within measurement uncertainty of the delay determination). Once clocks were zeroed about the middle of the experiment, all fringe-finder scans were correlated and clock rates were fit with least-squares regression (Figure 6.7). Fitted clock-rates were applied and final correlation was performed in one pass - all sources correlated over the full bandwidth (16 MHz) with 32 spectral channels per IF, giving a spectral resolution of 0.5 MHz.

### 6.4.2 Antenna Position Corrections

For correlation I used antenna positions and velocities determined from the information on the AstroGeo website<sup>†</sup> given in Table 6.3. These positions come from past IVS and geodesy-style experiments nominally involving the 4 stations of interest as part of the LBA. Hobart 26m, Katherine 12m and Yarragadee 12m partake in IVS experiments at least once per week, and therefore their positions are known to the level of  $|\Delta B| \sim 1\ \text{cm}$ . Ceduna 30m does not regularly partake in IVS-style experiments and therefore has a more uncertain position.

Single-frequency geoblock fitting nominally takes measured LoS delay (after manual phase calibration, EOP and TEC corrections; see Section §2.7) and fits for a likely clock rate and zenith non-dispersive delay. If other delays are present, they will be included in this fitting process and

---

<sup>†</sup><http://astrogeo.org/vlbi/solutions/>

## 6.4. REDUCTION PROCESSES

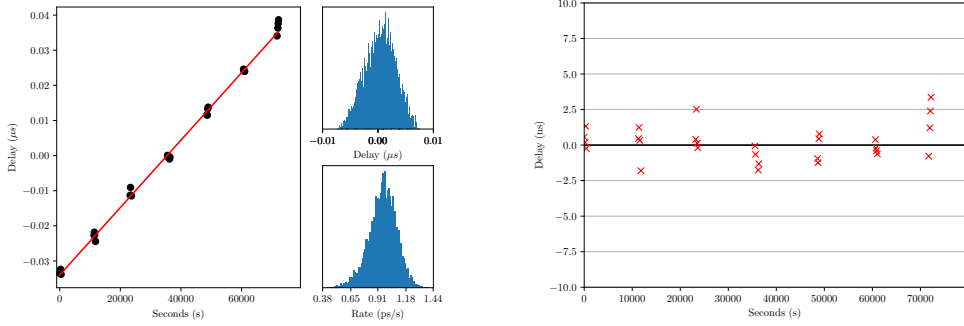


**Figure 6.7:** Delays measured on fringe-finder quasars for experiment MV028, baseline Ho–Cd. **Left:** fitting and removing clock drift rate between stations. Measured and removed clock rate is  $\frac{d\tau}{dt} = 97 \pm 13 \text{ ps/s}$  in this case. The fit for residual electronic delay  $\tau_e = 1 \pm 30 \text{ ns}$ . **Right:** Residual delay after clock removal is  $|\delta\tau| < 3 \text{ ns}$  which can be explained by individual IF electronic delays or atmospheric effects. This will be removed in *ATPS* calibration. The low residual delay allows for a much coarser correlation resolution in FITS output at 0.5 MHz/chan as this will still allow this small delay to be easily detected and corrected during processing.

**Table 6.3:** Correlated antenna positions and velocities at epoch 2000.0 from AstroGeo RFC\_2018. Ceduna velocity taken from RFC\_2009. **Columns (1)** Antenna name; **(2-3)**  $X$  position and velocity; **(4-5)**  $Y$  position and velocity; **(6-7)**  $Z$  position and velocity.

Antenna	$X$ (m)	$\dot{X}$ (m/yr)	$Y$ (m)	$\dot{Y}$ (m/yr)	$Z$ (m)	$\dot{Z}$ (m/yr)
Ceduna 30m	-3753442.7457	-0.04173	3912709.7530	0.00267	-3348067.6095	0.04990
Hobart 26m	-3950237.5960	-0.03834	2522347.7530	0.00849	-4311561.6600	0.03942
Katherine 12m	-4147354.8680	-0.03477	4581542.3320	-0.01545	-1573302.9130	0.05427
Yarragadee 12m	-2388896.4240	-0.04673	5043350.0760	0.00824	-3078590.5910	0.04838

skew the zenith delay estimate (see Section §2.4.2). In the presence of suspected baseline errors, I used an alternate programme (written by Mark J. Reid) to simultaneously fit for tropospheric dispersive delay, clock rate and positional offsets in the Ceduna 30m correlated position  $\Delta X$ ,  $\Delta Y$ ,  $\Delta Z$ . Results of this fitting are shown in Table 6.4.

I measured the Ceduna 30m position offset to be  $(\Delta X, \Delta Y, \Delta Z) = (7, -9, 22) \text{ cm}$ . The reason behind this difference is attributed to offsets in the used AstroGeo catalogues for the position of Ceduna 30m. Figure 6.8 shows Ceduna 30m  $X$ ,  $Y$ ,  $Z$  position vs. time for my two primary sources of telescope position measurements: AstroGeo and ATNF (Australia Telescope National Facility) scheduling programme SCHED. It is clear the catalogued positions in SCHED are much closer to those measured, however are given without uncertainty measurements. AstroGeo is far more generous in terms of errors estimation, quoting large errors  $\sigma = 25 \text{ cm}$  and therefore are always going to be consistent with most measurements. However assuming a conservative estimate of 3 cm in the SCHED positions easily leaves them consistent with the measurements here. Therefore for all future S $\pi$ RALS correlation, ATNF SCHED positions will be used. Further position measurement-dedicated sessions should nevertheless be undertaken to confirm this.

Individual coordinate offset errors in the delay measurements are approximately  $\sim 3 \text{ cm}$ , however I confidently report that the consistent measurements over the 4 epochs allows the accurate estimation at around  $\sim 1 \text{ cm}$  considering the maximum position change due to station velocity is

## 6.4. REDUCTION PROCESSES

**Table 6.4:** Measured position offsets and formal uncertainty for Ceduna 30m over the 4 epochs. \*The Y component had a necessary sign reversal when applied. Positional accuracy in epoch MV026 is understandably lower due to positional determination from 6 geoblocks rather than 7 (data flagged following clock jump).

Epoch	$\Delta X$ (cm)	$\sigma_{\Delta X}$ (cm)	$\Delta Y$ (cm)	$\sigma_{\Delta Y}$ (cm)	$\Delta Z$ (cm)	$\sigma_{\Delta Z}$ (cm)
MV025	5.31	2.67	9.24	2.66	24.23	2.31
MV026	8.69	2.88	10.97	2.99	21.43	2.94
MV027	6.09	2.64	6.87	2.68	20.55	2.60
MV028	6.83	2.67	9.13	2.72	22.87	2.62
AVG	6.7	1.4	-9.1*	1.4	22.3	1.3

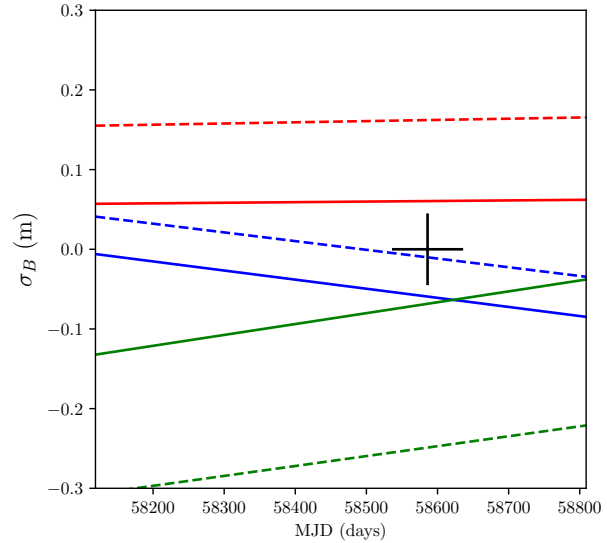


**Figure 6.8:** Ceduna X (red), Y (blue) and Z (green) position vs. time for SCED (solid) and AstroGeo (dotted) catalogued positions as compared to the mean position determined at all MV02\* epochs (black + error bars).

< 1 cm over the 70 day time period. Figure 6.9 shows images with identical calibration processes with the exception of the baseline offsets being applied or not. There is an extremely clear increase in image fidelity for the case where the improved position for Ceduna is used.

#### 6.4. REDUCTION PROCESSES

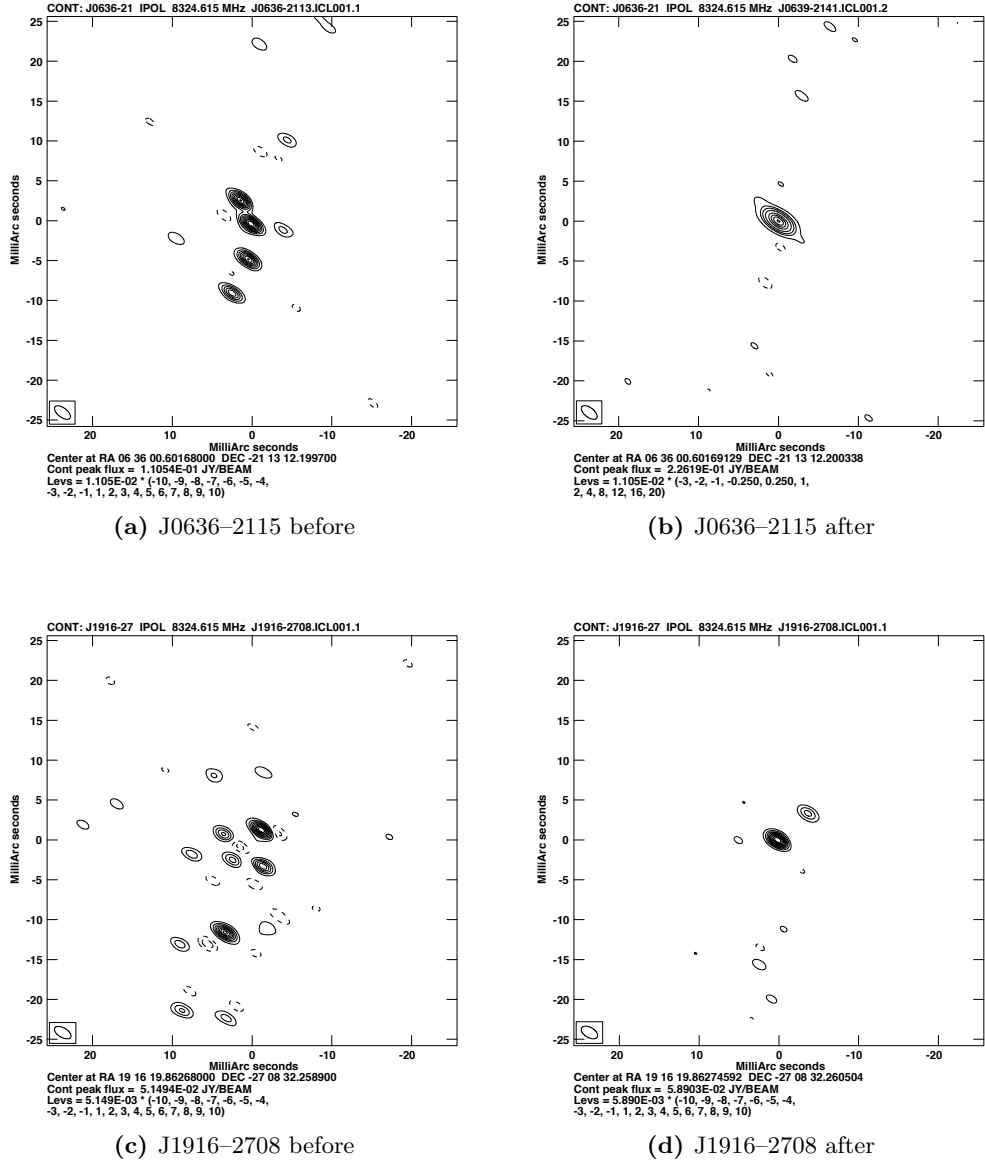


**Figure 6.9:** Phase referenced images of J0636-2113 and J1916-2708 from epoch MV027 with and without the estimated Ceduna position solutions applied. Apart from differing Ceduna position and resultant tropospheric delay solutions, analysis process is identical for all images. J0636-2113 is at distance  $R = 2.4$  deg from centre while J1916-2708 is  $R = 6.9$ . No self-calibration has been applied.

## 6.4. REDUCTION PROCESSES

### 6.4.3 Antenna Amplitude Calibration

Where available, system temperatures were extracted from telescope logs and applied in conjunction with gain curves. Where system temperature information was not available, nominal SEFD values were applied. This provided a rough conversion between raw voltages to flux density values. To improve the amplitude calibration where no system temperature information was available, additional steps were required.

Certain IFs at Ceduna 30m presented a practical difficulty. There was an unexplained drop ('notch') in apparent sensitivity of some of the IFs in the frequency range observed. This is thought to be due to a power-slope input into the DBBC unit. Nevertheless since it was very unlikely originating from the target quasars, the method described in Section §2.5.2.2 was used to calibrate the spectral data pre-imaging. Source F1256–0547 (aka. 3C279) was used to correct amplitude over frequency as it is exceptionally luminous  $S_c \sim 10$  Jy. A custom ParselTongue script was written and used for this purpose (Figure 6.10).

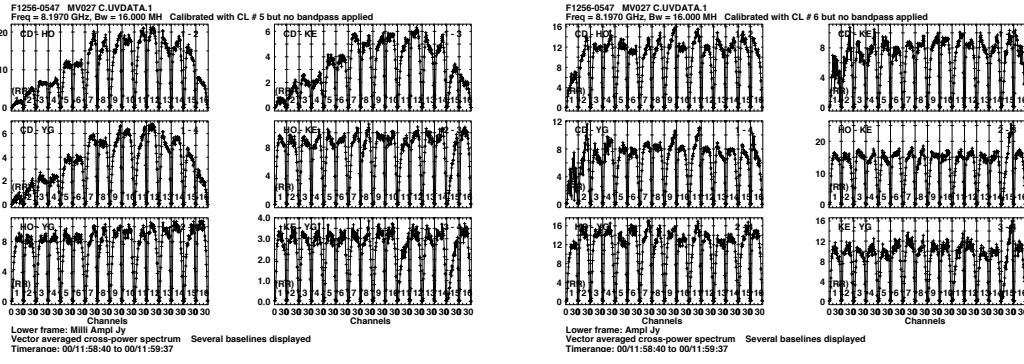


**Figure 6.10:** IF calibration for Ceduna 30m. **Left:** Amplitude of F1256–0547 after system temperature calibration but before IF calibration; **Right:** After IF calibration.

Although F1256–0547 (3C279) is a very strong, compact source, it is also quite variable and hosts a large luminous jet. So while it is useful for estimating the relative amplitude of the IFs on a particular baseline, it is not suitable for amplitude calibration of baseline relative to the others. The quasar G0634–2335 is less variable, more compact and was used as the centre target source in the  $R = 2 - 4$  degree ring. The catalogued flux density for this source was tabulated as  $S_c = 620$  mJy in December 2012, however in MV02\* epochs it was observed to have a total flux density of approximately 1 Jy on most baselines after nominal SEFD's and/or  $T_{sys}$  were applied. It is unlikely that the ASCI array sensitivity is almost twice as high as the expected or nominal values, therefore either G0634–2335 has brightened, or catalogued flux densities are systematically lower. Nevertheless, the quasar is known to be quite bright, have a 0.1 mas positional uncertainty and be very compact for the array. Figure 6.11 shows a core-halo model fit for G0634–2335 used in the amplitude vs. baseline calibration:

$$S(B_\lambda) = S_c \exp\left(\frac{-2\pi^2}{8 \ln 2} \theta_C^2 B_\lambda^2\right) + S_H \exp\left(\frac{-2\pi^2}{8 \ln 2} \theta_H^2 B_\lambda^2\right)$$

One can derive that the likely core size is  $\theta_c = 0.145$  mas with a flux density  $S_c = 400$  mJy, which represents about 70% of the flux density.

With the core/halo size parameters considered reliable and flux density parameters set to  $S_c =$

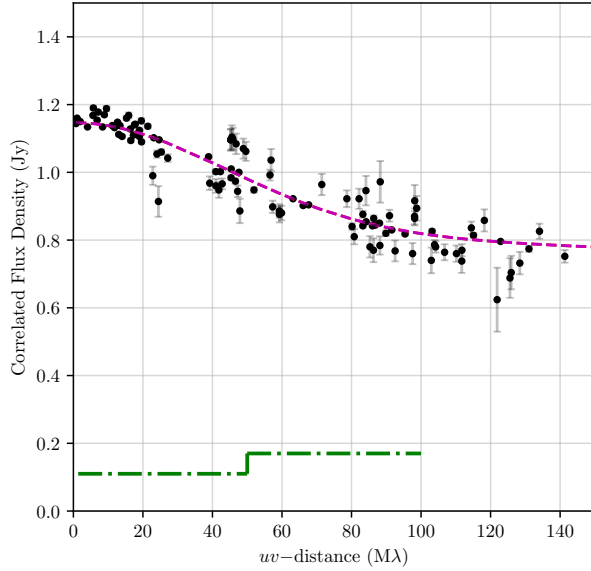


**Figure 6.11:** Radplot of G0634–2335 extracted from AstroGeo and my fit to visibility data. Derived parameters are  $S_c = 810$  mJy,  $S_H = 340$  mJy,  $\theta_c = 0.145$  mas and  $\theta_H = 1.75$  mas for a core/halo model for the source. The least-squares fits are plotted on top of the  $uv$ –flux data (magenta). Green lines indicate  $10\sigma$  sensitivity threshold for baselines Cd-Ke/Yg (lower) and Ke-Yg (higher) in a single  $\tau = 40$  s scan.

0.81 Jy and  $S_H = 0.34$  Jy, G0634–2335 was used as an amplitude calibrator for all four epochs using the custom ParselTongue script and method described in Section §2.5.2.2.

#### 6.4.4 Initial Phase Referencing and Orbit Source Position Corrections

After I had completed and checked amplitude and pre-delay calibration, I used F1256–0547 (3C279) as the manual phase calibrator for all epochs. After application of these solutions, I averaged the data in frequency and split the rings into separate catalogues. For each ring, I fringe fit the target source for a phase  $\phi$  and rate  $\frac{d\phi}{dt}$  over the entire observational period (e.g. Figure 6.12). Positional offsets present in orbit calibrators cannot be removed by MultiView as they cause uncorrelated source-specific plane structures in the measured phases. If an orbit source has a small positional offsets, the resultant slope in the phase domain is dominated by the position offset of the target source and all orbit source position slopes become correlated (see Section 5.2.3). Therefore, the positions of the orbit sources need to be checked and corrected using iPR prior to an astrometric campaign using MultiView. While the initial positional uncertainty in some MultiView calibrators may be quite large, provided there are some calibrators with accurate positions nearby, these should be sufficient to correct for large offsets before later refinement with iMV.

To this end I used epoch MV027 to determine the position of any ring sources without good *a priori* position determination. I applied the fringe fit solution from the target to each of the orbit sources, imaged them and fitted elliptical Gaussians to the peak emission. For the largest ring it was difficult to determine which peak corresponded to the ‘real’ quasar as phase

## 6.4. REDUCTION PROCESSES

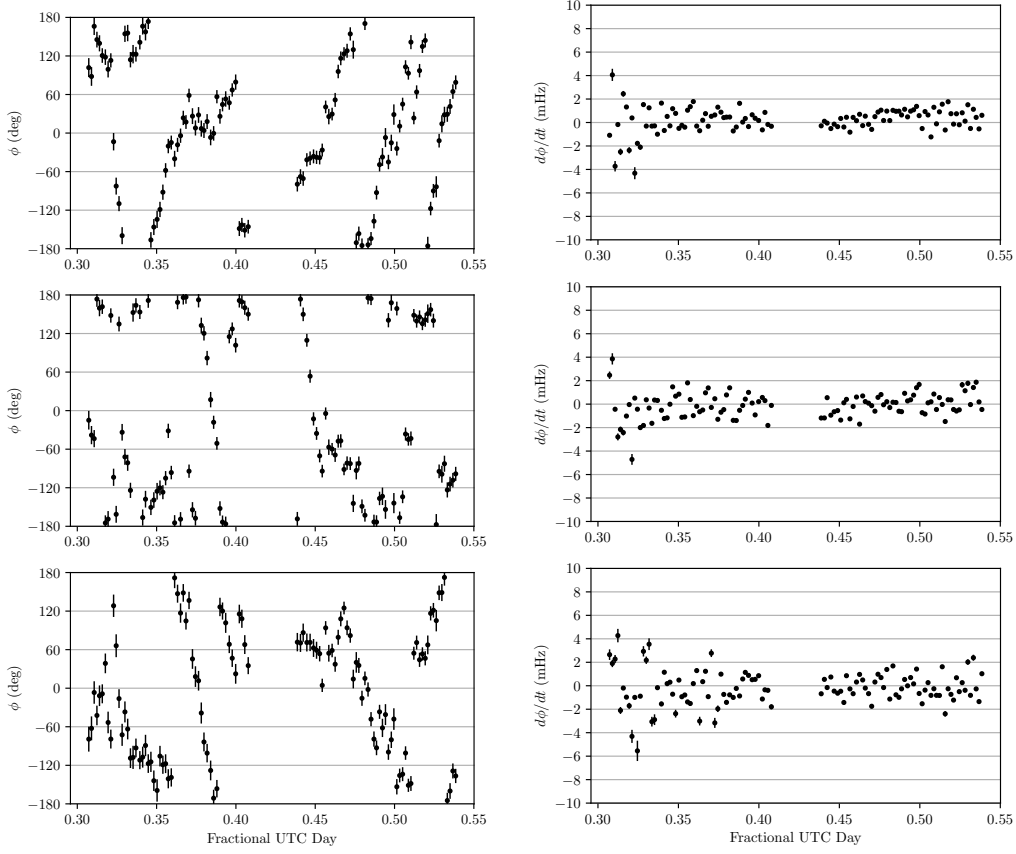


**Figure 6.12:** Example phase and rate solutions before MultiView fitting. **Left:** Phase and **right:** rate solutions for centre source G0634–2335 for the experiment MV026. **Top to bottom:** baselines Cd–Ho, Ke–Ho and Yg–Ho.

referencing imaging was very unreliable. Final determined offsets are given in Table 6.5. These position offsets were applied for all epochs to check and a little trial and error was necessary. As discussed, the quasars observed were taken from the RFC\_2018 with  $S > 110 \text{ mJy}$  and with nominal positional quality  $Q < 0.3 \text{ mas}$ . However, despite this positional offsets were on average much larger than expected (median shift 0.73 mas, minimum 0.2 mas, maximum of 1.48 mas).

### 6.4.5 MultiView Fitting

I fringe fit orbit sources for phase, one solution per scan and output phase vs. time data. All principle data used for fitting is shown in Appendix C.2. These phases are fed into a custom ParselTongue fitting script that performs a weighted least-squares fit at each time step for a the phase plane on each baseline referenced to the reference antenna. This is the same as the procedure described in Section 5.3. Figure 6.13 shows a 3D representation of the phase plane fit for a few time steps over the observation.

The MultiView fitting script outputs an *AIPS*–compatible input file (SN table) containing

## 6.4. REDUCTION PROCESSES

**Table 6.5:** Correlated and shifted positions of orbit quasars. All shifts are applied in AIPS task CLCOR. **Columns (1):** Quasar name in J2000 format; **(2):** correlated Right Ascension J2000; **(3):** correlated Declination J2000; **(4):** updated Right Ascension J2000; **(5):** updated Declination J2000; **(6):** Right Ascension shift; **(7):** Declination shift; **(8):** total shift.

Source	$\alpha_B$ (hh:mm:ss)	$\delta_B$ (dd:mm:ss)	$\alpha_A$ (hh:mm:ss)	$\delta_A$ (dd:mm:ss)	$\Delta\alpha$ (mas)	$\Delta\delta$ (mas)	$\Delta\theta$ (mas)
J0636-2113	06:36:00.60168	-21:13:12.1997	06:36:00.601601	-21:13:12.200019	0.079	-0.319	0.329
J0643-2451	06:43:07.46892	-24:51:21.3120	06:43:07.469343	-24:51:21.313112	-0.423	-1.112	1.190
J0620-2515	06:20:32.11700	-25:15:17.4851	06:20:32.117785	-25:15:17.486352	-0.785	-1.252	1.478
J0639-2141	06:39:28.72567	-21:41:57.8045	06:39:28.725476	-21:41:57.805075	0.194	-0.575	0.607
J0632-2614	06:32:06.50180	-26:14:14.0353	06:32:06.501723	-26:14:14.034143	0.077	1.157	1.160
J0629-1959	06:29:23.76186	-19:59:19.7236	06:29:23.761793	-19:59:19.723399	0.067	0.201	0.212
J1354-0206	13:54:06.89532	-02:06:03.1906	13:54:06.895183	-02:06:03.190118	0.137	0.482	0.501
J1351-1449	13:51:52.64960	-14:49:14.5569	13:51:52.649078	-14:49:14.557691	0.522	-0.791	0.948
J1312-0424	13:12:50.90123	-04:24:49.8923	13:12:50.901495	-04:24:49.891692	-0.265	0.608	0.663
J1406-0848	14:06:00.70186	-08:48:06.8806	14:06:00.700617	-08:48:06.881194	1.243	-0.594	1.378
J1305-1033	13:05:33.01504	-10:33:19.4281	13:05:33.014697	-10:33:19.427271	0.343	0.829	0.897
J1406-0707	14:06:00.70186	-08:48:06.8806	14:06:00.702585	-07:07:06.880665	-0.725	-0.065	0.728
J1916-1519	19:16:52.51100	-15:19:00.0716	19:16:52.510923	-15:19:00.071417	0.077	0.183	0.199
J1848-2718	18:48:47.50417	-27:18:18.0722	18:48:47.504007	-27:18:18.072451	0.163	-0.251	0.299
J1928-2035	19:28:09.18336	-20:35:43.7843	19:28:09.183320	-20:35:43.784797	0.040	-0.497	0.499
J1832-2039	18:32:11.04649	-20:39:48.2033	18:32:11.045556	-20:39:48.202587	0.934	0.713	1.175
J1916-2708	19:16:52.51100	-15:19:00.0716	19:16:52.510560	-27:08:00.072402	0.440	-0.802	0.915

phase corrections for the target source and orbit quasars. I applied these solutions directly to the target and orbit sources in  $\mathcal{AIPS}$ . Finally, target and orbit sources are imaged in  $\mathcal{AIPS}$  and the peak emission in CLEANed images fit with elliptical Gaussians. The measured positions of targets and orbit sources are given in Appendix C.3.2.

### 6.4.6 Inverse Phase Referencing and Self-Calibrating

In order to compare inverse MultiView with inverse phase referencing, I imaged the central targets and orbit sources directly after the initial fringe fit to the central target. I fitted the emission within the central 25% of CLEANed images with elliptical Gaussians. This was in order to have a reasonable comparison between iMV and iPR, because while there was still emission at the centre of such images, the peak emission was sometimes  $\theta \geq 5$  mas away. This effect can be seen in the fractional flux density recovery (FFR), which I defined as the fraction of integrated flux density in a phase referenced image region compared to the same region in a self-calibrated image. In order to get the FFR metric, single-cycle self calibration was applied to all quasar sources. Again, the peak emission in the central 25% was fit with elliptical Gaussians. The results of the iPR and self-calibration astrometry are presented in Appendices C.3.1 and C.3.3.

#### 6.4. REDUCTION PROCESSES

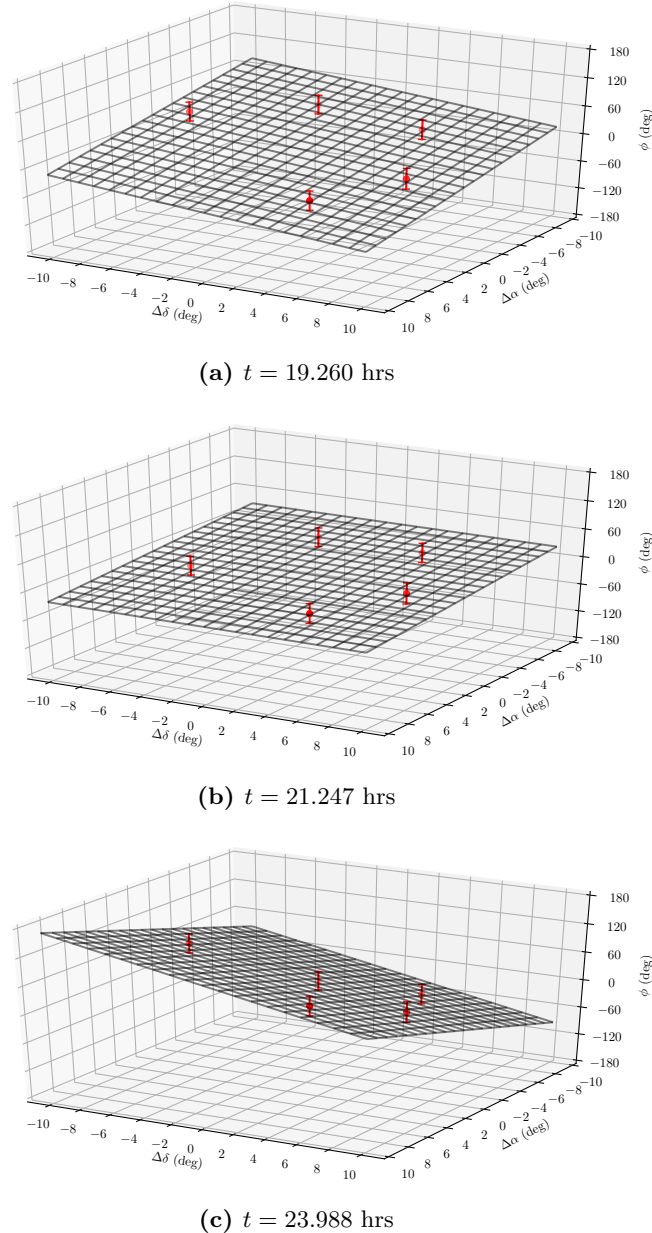


**Figure 6.13:** Phase plane for baseline Cd–Ho for ring G1901–2112 for epoch MV027 at given time steps. Time steps are given in UTC.

## 6.5 Results and Discussion

### 6.5.1 Astrometry

Figure 6.14 shows the astrometric accuracy of inverse MultiView compared to inverse phase referencing as it pertains to the observations. As the only fair comparison to make is between the orbit sources with inverse phase referencing applied against MultiView as applied to the centre source, that is what I have shown in this figure. That is because the position of the target quasar is always at the centre of the image in iPR after application of the phase and rate solution to itself. Similarly the fitting of the phase planes to the orbit source in iMV is very close to self-calibration.

Despite the fact that quasar positions were updated to be centred for the MV027 epoch, the astrometric accuracy of iPR decreased as calibrator-target distance increased. The quality of the results obtained from iPR look quite reasonable if Figure 6.14 is considered in isolation, however, Figure 6.15 which shows the fraction flux density recovery (FFR) better demonstrates the significant degradation in the image quality produced on average by iPR. The FFR was  $\sim 70\%$  for iPR at radii  $R < 7$  deg, dropping off rapidly for  $R > 7$  deg.

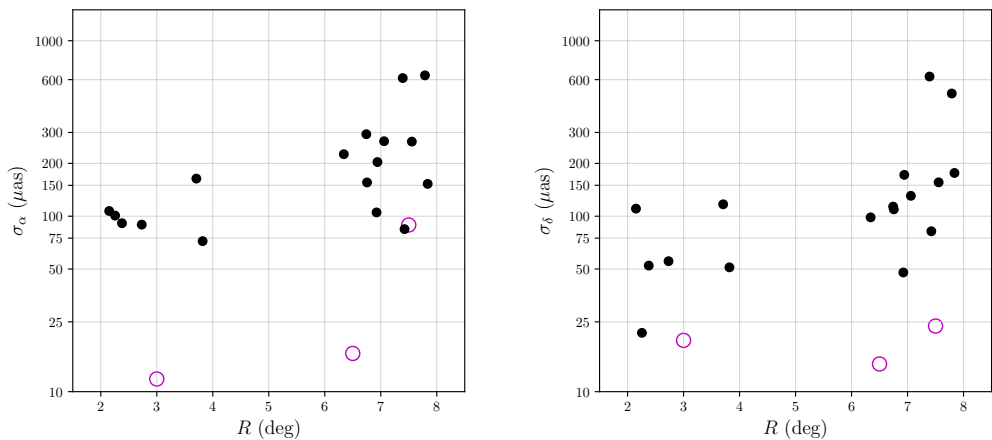


**Figure 6.14:** Positional accuracy vs. radius for inverse MultiView (magenta) and inverse PR (black). **Left:** Results from East–West and; **Right:** North–South directions. Both plots have a  $\log_{10}$ –scaled y–axis to fit all data.

Conversely, all images of target sources after inverse MultiView had been applied had high FFR  $\sim 0.95$  and repeatable positions. Orbit sources after iMV had been applied had FFR  $\sim 0.85$ , suggesting that the fitting process evenly spreads the noise over all calibrators at the level of 15%. This also suggests that residual phases were at the level of around  $180/\pi * 0.15 \approx 9$  deg in rough agreement with the assumed 10 deg phase noise floor for fitting. Taking the worst case FFR of 0.6, the upper limit on systematic deviations from the planar approximation are 20 deg at a target–calibrator separation of 8 deg (which does not take into account the likely influence of phase noise). The thermal noise in the synthesised images is  $\sigma_{th} = \frac{\theta_B}{2 \text{ SNR}} \gtrsim \frac{2.0}{2 \times 100} = 10 \mu\text{as}$  suggesting that thermal uncertainty is not a predominant source of astrometric error.

In order to investigate whether MultiView is robust to small positional offsets (such of those due to maser proper motions) I perturbed target sources positions by  $\Delta\alpha = 0.2$  and  $\Delta\delta = 0.4$  mas

## 6.5. RESULTS AND DISCUSSION

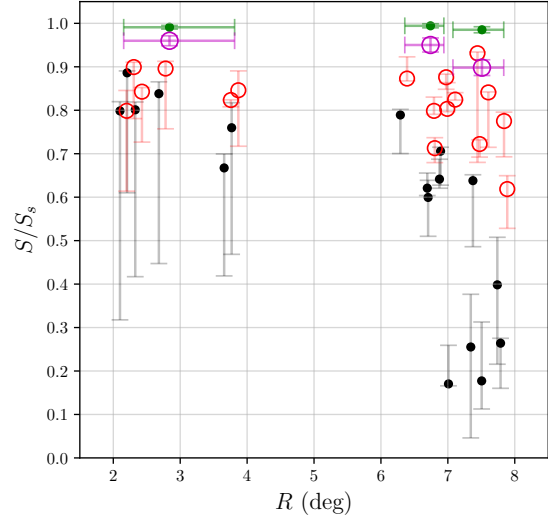


**Figure 6.15:** Fractional flux density recovery against radial target-calibrator separation. Orbit sources **black**: for inverse phase-referencing **red**: for MVRC. Target **green**: for iPR **magenta**: for MVRC. Points are the median FFR and error bars indicate the upper and lower quartile range for all three epochs.

for all rings and epochs excluding MV025. In the case of inverse phase referencing this will move all orbit sources by the negative of both offsets. In the case of MultiView I expect that this offset is returned to the centre source after application of the inverse MultiView solution. The application of this position shift is performed in *AIPS* with task CLCOR then reduction is continued onwards from EOP/PANG corrections (see Section §2.7).

Figure 6.16 shows the results of this perturbation for the MV026, 27 and 28 epochs. The position shift has clearly been translated into the orbit sources for iPR and returned to the target source in iMV. While there are cases where iPR returns the position shift more precisely, iMV more

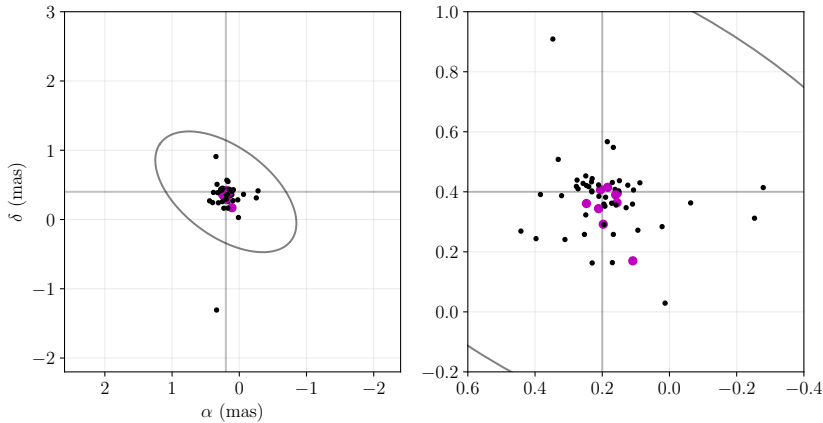


**Figure 6.16:** Measured position shifts for iPR (black) and iMV (magenta). Applied position shifts were  $\Delta\alpha = 0.2$ ,  $\Delta\delta = 0.4$  mas and this is indicated on the plot as vertical and horizontal black lines. The measured position shifts for iPR have had a sign reversal. Also included is the mean synthesised beam ( $2.4 \times 1.4$  mas position angle  $60^\circ$ ).

consistently provides an answer closer to the applied offset.

### 6.5.2 Phase Slopes

As derived in Chapter 5, the phase/delay slopes at any given time depends on the instantaneous residual delay modulated by the effects of various locational parameters such as latitude, longitude, RA, DEC, hour angle and local time. In this section I discuss the measured slopes over the four epochs, what they mean and might be useful for.

Figure 6.17 shows measured phase slopes and phase on the Katherine 12m–Hobart 26m baseline for all four epochs. All measured slopes and phases for Hobart 26m baselines for epochs MV025, 26, 27 and 28 are given in Appendix C.2.2. In many cases the measured phase slopes have a clear trend with time, and one that is different for the slope in RA and DEC. I am going to compare the trends and shapes with those expected from residual ionosphere, dry troposphere and baseline offsets.

While it is well known that the total ionospheric delay is at a maximum around local midday and a minimum at midnight local time, the residual ionosphere is expected to have a maximum about sunrise and sunset. This is due to changes in the ionosphere being most rapid around those times. Combined with this is the realisation that sunrise and sunset are not necessarily shared for pair of telescopes. Therefore a baseline may have a sunrise/sunset affected period approximately stretching  $\leq 3$  hrs (for the ASCI Array). Mutual night time periods are hypothesised to have a minimum total- and residual ionospheric delay. Therefore any delay slope that is observed these times are not *expected* to be significantly affected by residual ionosphere and must be explained by other sources.

The local night–time period at the telescope sites changes over the course of the year at the sidereal rate (0.00273 s/s or 3m56s/day). The total time–baseline for the four experiments observations is 76 days, or 0.208 yrs. This amounts to an Local Sidereal/UTC shift of 4 hrs 59 min. Over this time sunrise/sunset shifted a maximum of +1.5/-2 hrs at Hobart and a minimum at Katherine of +0.2/-0.8 hrs (days receding and nights increasing). This caused the ‘sunrise affected’ period to change from the middle of the G1336–0809 ( $\bar{R} = 7.5$  deg ring) track into the G1901–2112 ( $\bar{R} = 6.5$  deg ring) track (see Figure 6.17). The ‘sunset affected’ period was only every time–coincident with the G0634–2335 ( $\bar{R} = 3$  deg ring) track, however, it moved from affecting the beginning to the end of the track.

The smallest ring  $R = 2 \rightarrow 4$  (blue) has the highest scatter in measured slope however, this is mostly bounded by the larger error bars. The error bars themselves are weighted least–squares formal errors:

$$\sigma_A = \sqrt{\frac{\sum_{i=1}^N (\phi_i - \bar{\phi})^2}{N - 2}} / \sqrt{\sum_{i=1}^N (a_i - \bar{a})^2}$$

where  $a_i$  is an example RA coordinate offset and  $\sigma_A$  is the uncertainty in the measured RA slope. While I will explore this in more detail soon, for a larger sampled distance the slope measurement is expected to be more accurate and therefore the slope measurement uncertainty is largest for the smallest ring.

## 6.5. RESULTS AND DISCUSSION

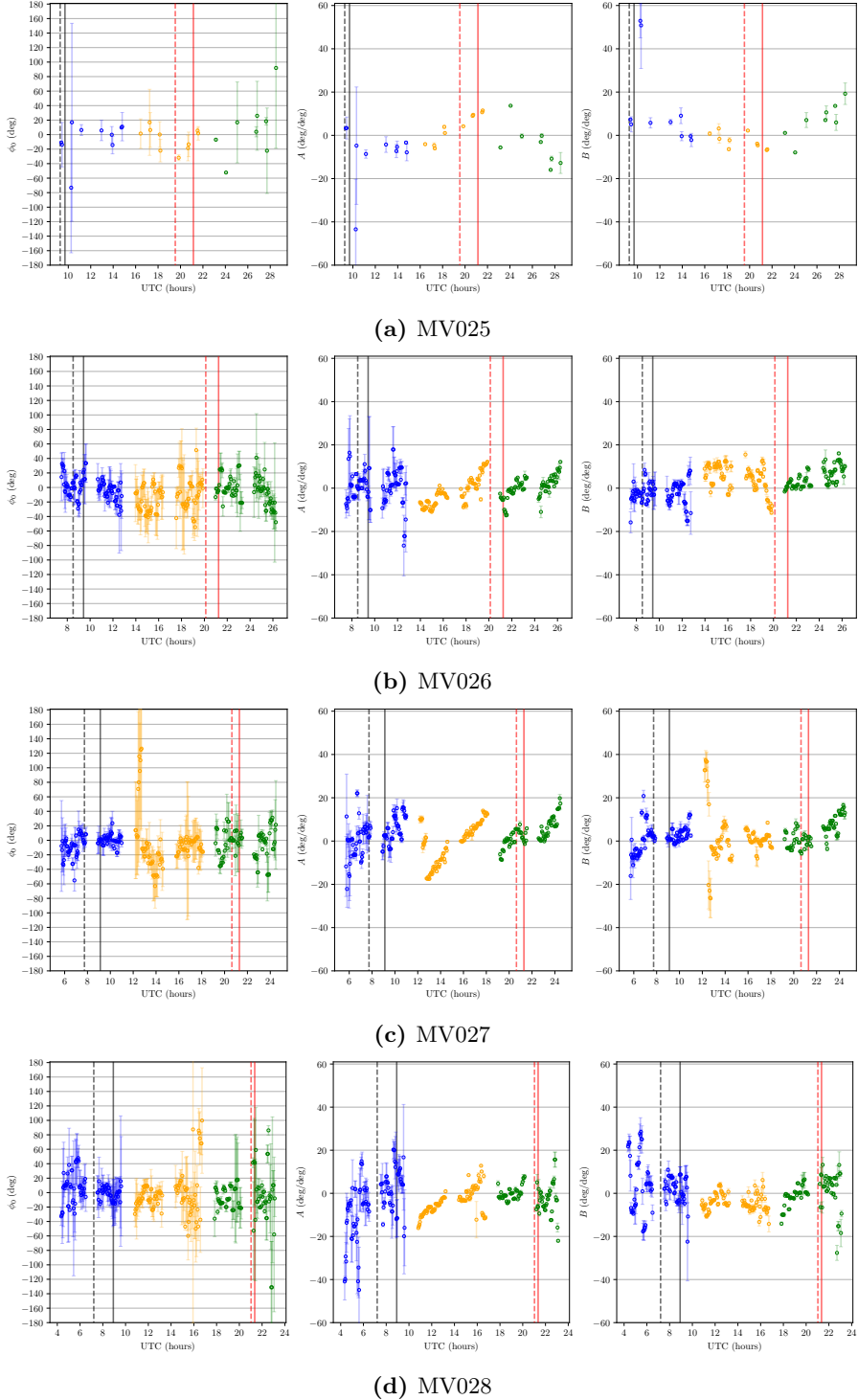


**Figure 6.17:** Measured target source phases and slopes for baseline Ke-Ho. **Columns:** (1) Phases; (2) Slopes in East-West (RA) and; (3) North-South (DEC). **Rows:** Epochs MV025; MV026; MV027; MV028. **Colours:** Rings (blue) G0634-2335  $\bar{R} = 3$  deg; (yellow) G1336-0809  $\bar{R} = 7.5$  deg and; (green) G1901-2112  $\bar{R} = 6.5$  deg. **Vertical lines:** Local sunrise (red) and sunset (black) for antenna (solid; e.g. Katherine) and reference antenna (dotted; e.g. Hobart). Error bars are given by weighted-least-squared fitting.

## 6.5. RESULTS AND DISCUSSION

There does not seem to be any clear correlation between local sunrise/sunset time and phase slope magnitude and/or stability or derived phase stability (see all plots Appendix C.2.2). While there appears to enhanced slope scatter about the sunset period for some epochs/baselines, it is not repeatable nor necessarily outside the slope measurement error. The larger inherent uncertainty in slope measurement for the smallest ring appears to explain almost all scatter rather than coincident observational period with local sunset. Therefore, based on the prediction that residual ionosphere will have a local sunrise/sunset dependant enhancement, I find it difficult to ascertain whether this prediction is false or the effect of the enhancement on phase slope magnitude is smaller than that due to other effects (residual dry troposphere or baseline offset).

All experiments coincide with solar cycle 24, which began December 2008, peaked April 2014 and ended December 2019. This solar cycle was one of the least active in recent history, with a maximum of 81 sunspots compared to 180 in the previous cycle (solar cycle 23). In addition, the 2018–2019 period where observation take place are at the very tail end of the cycle, with a maximum monthly sunspot number of less than 7 (<https://www.swpc.noaa.gov/products/solar-cycle-progression>).

Katherine–Hobart and Yarragadee–Hobart baselines are nearly identical in terms of sensitivity and total length. However Katherine–Hobart baselines appear to have generally greater phase and phase-slope stability for all rings and epochs. The main differences between the baselines are orientation and latitude. Baseline orientation is unlikely to be the contributing factor as many targets all over the sky should not necessarily have the same structure/compactness. Therefore it is not unreasonable to conclude that the Katherine antenna latitude and resultant elevation over the track is the separating factor. All targets and resultant rings have declinations  $\delta \pm 5 \approx \varphi_{\text{Ke}} = -14.3$  deg implying that they track relatively high at Katherine compared to Yarragadee. However if elevation alone was the culminating factor, I would expect to see increased phase scatter and increased magnitude and/or scatter of phase slopes increasing at both ends of the track which is not evident. Therefore, I cannot find a reason for this disparity and it should be investigated further as more data is collected in future S $\pi$ RALS observations.

Despite the fact that residual ionospheric delay is expected to be at a minimum at ‘mutual’ midnight, clear phase slopes are measured at all epochs at this time. In addition, the phase slopes have obvious time-dependant trends. I want to determine whether a phase slopes such as these can be explained purely by either a baseline offset or residual dry tropospheric error. Since I have already derived equations for the delay slopes caused by either of these two effects (see Chapter 5) I will compare these models to the measured phase slopes to ascertain the feasibility that these effects could be a major contributors.

The first phase plane I will model and compare to data is that arising from a baseline offset. Taking Equation 5.4, for a four-telescope array there are 12 antenna position offsets  $\Delta X_i, \Delta Y_i, \Delta Z_i$  for  $i = \text{Cd}, \text{Ho}, \text{Ke}$  and  $\text{Yg}$ . Figure 6.18 shows baseline offset phase slope model against measured data for epoch MV027, target ring G1336–0809 on baselines referenced to Hobart.

## 6.5. RESULTS AND DISCUSSION

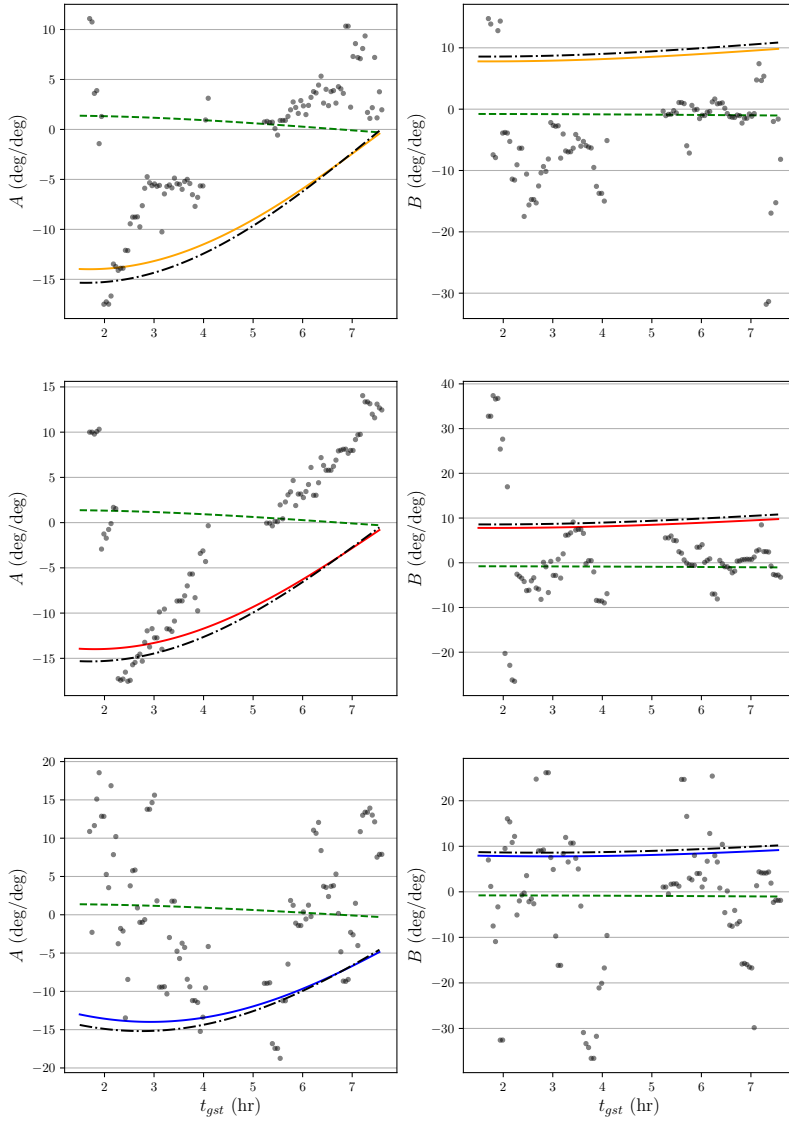


**Figure 6.18:** Measured slopes vs. baseline slope model. **Left column:** Phase slopes in RA; **right column:** in DEC. **Green line (all plots):** modelled phase slope above reference antenna Hobart. **Yellow, red and blue solid lines:** modelled phase slopes above Ceduna, Katherine and Yarragadee. **Dashed black line:** resultant modelled phase slope above baseline (coloured antenna slope minus green reference slope). **Black points:** Measured phase slopes on G1336–0809 at epoch MV027.

## 6.5. RESULTS AND DISCUSSION

Model parameters were unable to replicate the measured phase slope trends or magnitudes. The example shown uses parameters  $(\Delta X_i, \Delta Y_i, \Delta Z_i) = (10, 10, 10)$  cm for Cd, Ke and Yg and  $(-1, -1, -1)$  cm for Ho, however, this is because this combination gives results which show some similarity to the measured RA trend unlike many others. In order to match magnitude more closely  $\Delta X$  and  $\Delta Y$  have to be increased over 20 cm which is far outside the realm of possibility given IVS observations at Ke, Yg and Ho and reduction processed here for Cd. In addition  $\Delta X$  and  $\Delta Y$  are the coordinates geodetic observations are most sensitive to. Therefore I find it safe to conclude that baseline errors (even if present on the 5 cm level) do not significantly contribute to the phase slopes.

The next comparison I want to make is for a phase slope purely arising from a residual (zenith) dry tropospheric delay. Taking the equation for a likely residual dry tropospheric phase slope (Equation 5.10), the model parameters will be residual zenith delay errors  $\sigma_{\tau_z,i}$  above each telescope  $i = \text{Cd}, \text{Ho}, \text{Ke}$  and  $\text{Yg}$ . I will be using a constant value for  $\sigma_{\tau_z,i}$  over the track, however, this is unlikely to be the case. Each geoblock solves for a  $\tau_{z,i}$ , so for a track there will be a measured values at the beginning, middle and end. Instantaneous values are interpolated between these three.

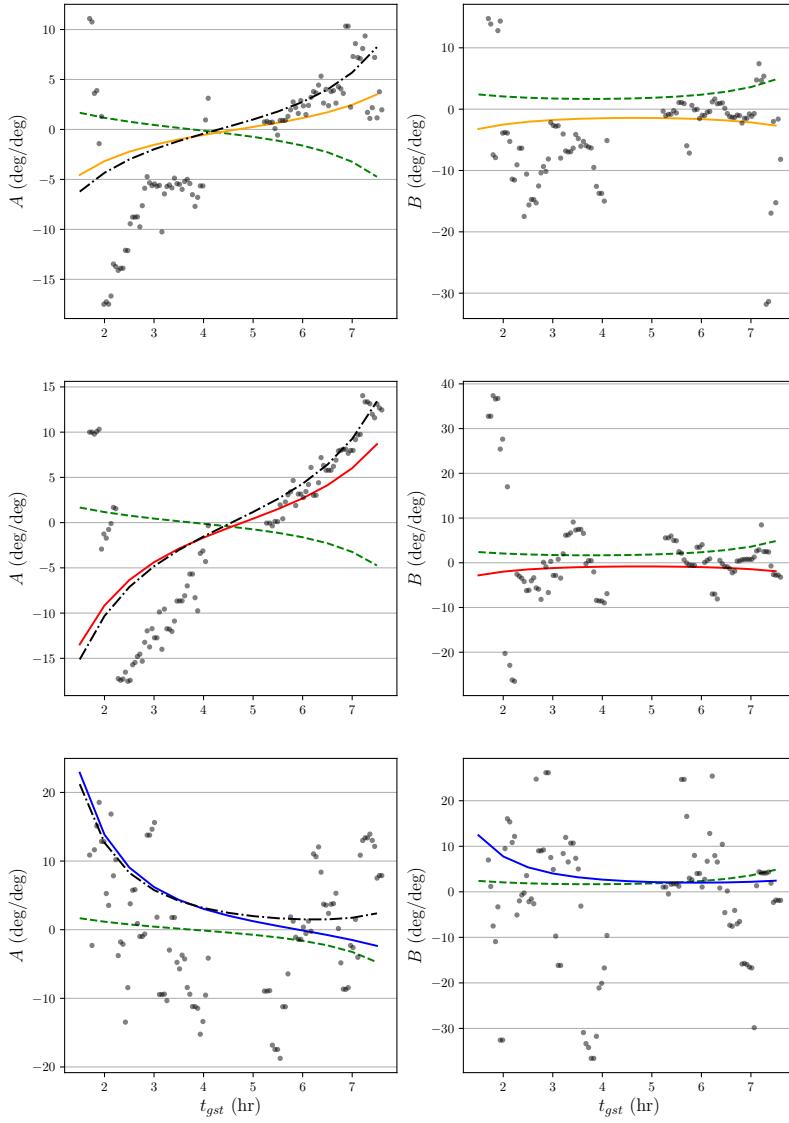
While in theory there can be a different and changing value for  $\sigma_{\tau_z,i}$  for each half of the track resulting from interpolating the derived value in each geoblock fit, I will only consider some average value for each telescope over the whole time range.

Figure 6.19 shows an example of this modelling with parameters  $\sigma_{\tau_z,i} = -2, 3, 8, -5$  cm against measured data for epoch MV027, target ring G1336–0809 on baselines referenced to Hobart. These model parameters ( $\pm 1$  cm) give a consistent match to the trend and magnitudes of the phase slopes, especially when compared against the phase slopes arising from baseline offsets.

The tropospheric plane models are relatively degenerate even just considering this single source of delay error, as the slopes are the difference between the planes above the antennas (Cd, Ke or Yg) and the plane above the reference (Ho). Model parameters were adjusted using realistic values ( $-15 < \sigma_{\tau_z} \leq 15$  cm) to best match data. While it seems apparent that the tropospheric model presented is able to explain the trends it does not fully encapsulate the magnitudes over time with a single value of delay. Adding further complexity (such as a time-variable version of the residual tropospheric delay  $\sigma_{\tau_z}$ ) will of course match the measured slopes more closely, however, there is no guarantee that this is representatively of the true delay.

In summary: seems possible to use the measured slopes to deduce what residual delays were present in the phase data, however, as it was not the primary focus of this testing, it should be investigated more closely in future studies. The most feasible method would be a Bayesian Markov–Chain Monte Carlo to solve for the parameters baseline errors, residual zenith troposphere (per geoblock per antenna) and potentially some additional terms to include ionosphere. Therefore at this time measured slopes serve two purposes; to roughly estimate the degree that residuals delays from any source had been pre-calibrated and; calculate phase solutions for orbit sources and re-apply thereby determining an estimate for residual phases.

## 6.5. RESULTS AND DISCUSSION



**Figure 6.19:** Measured slopes vs. tropospheric slope model. **Left column:** Phase slopes in RA; **right column:** in DEC. **Green dotted line (all plots):** modelled phase slope above reference antenna Hobart. **Yellow, red and blue solid lines:** modelled phase slopes above Ceduna, Katherine and Yarragadee. **Dashed black line:** resultant modelled phase slope above baseline (antenna slope minus reference slope). **Black points:** Measured phase slopes on G1336–0809 at epoch MV027.

## 6.5. RESULTS AND DISCUSSION

### 6.5.3 Astrometric Uncertainty

I would like to understand how the details of inverse MultiView calibrations such as the number of calibrators, target–calibrator separation and SNR affects the astrometric accuracy of the results from a theoretical standpoint and compare it to the observational results.

At each time-step, the phase uncertainty on the target source should be:

$$\sigma_\phi^2 = \bar{R}^2 (\sigma_A^2 + \sigma_B^2) + \sigma_{O^2}^2 \quad (6.1)$$

where there is the measurement uncertainty in the slope fits  $\sigma_A$  and  $\sigma_B$  and the systematic error due to assuming purely planar structure.

The measurement uncertainty in the slope from a least squares fit is:

$$\sigma_A = \frac{\sigma_\phi}{\sqrt{\sum_i^N (\mathbf{a}_i - \bar{\mathbf{a}})^2}} \quad (6.2)$$

and the same for  $\sigma_B$  and  $\mathbf{b}_i$ . Since I have approximately identical radii and uniformly distributed position angles ( $\sqrt{\sum_{i=1}^N \theta_i^2} \approx 2\pi$ ), all  $\mathbf{a}_i$  (or  $\mathbf{b}_i$ ) coordinates can be expressed as the combination of radius and position angle relative to the target at the centre:  $\mathbf{a}_i = R_i \cos(\theta_i + \psi)$  and  $\bar{\mathbf{a}} \approx 0$ .  $\psi$  is an arbitrary constant rotational offset from the designated coordinate system. Therefore I am left with:

$$\sum_i^N (\mathbf{a}_i - \bar{\mathbf{a}})^2 = \sum_{i=1}^N (R_i \cos(\theta_i + \psi))^2 = \left( \frac{\bar{R}^2 + \sigma_R^2}{2} \right) N$$

where I go through the simplification in Appendix C.1.2.

I use the well established expression  $\sigma_\phi = \frac{180/\pi}{\text{SNR}}$  to estimate the uncertainty in phase measurement. For each quasar, SNR only depends on integration time  $\tau$ :  $\text{SNR} \propto \sqrt{\tau}$ . Therefore the slope measurement error will look something like

$$\sigma_A = \frac{360/\pi}{\text{SNR} \sqrt{\left( \frac{\bar{R}^2 + \sigma_R^2}{2} \right) N}} \quad (6.3)$$

where the phase slope uncertainty has units degree of phase per degree of separation and where I consider the average SNR of sampled quasars. So the slope measurement uncertainty decreases with a higher average radius  $\bar{R}$ , radial scatter  $\sigma_R$ , average SNR and  $\sqrt{N}$  number of orbit sources. This assumes ‘perfect’ azimuthal sampling and slope measurement uncertainty increases in a complex manner depending on  $N$  and the magnitude of azimuthal under-sampling. Quantitatively, the best quasar configuration would optimise azimuthal sampling, time/spatial-coherence and onsource time for both target and orbit sources weighted by their flux density. To first order, a near-perfect linear configuration target and two orbit sources would be a very interesting case. Instead of a plane, a simple linear slope could be fit. While previous authors suggest such a strategy (Reid et al., 2017), such configurations of reference quasars with respect to target sources of interest will be relatively uncommon.

For 3D slope fitting as prescribed here, the theoretical minimum is 4 quasars in a perfect cross pattern with the target source at the centre. Such a configuration would give the highest sampling rate of the phase slope and determination of the 3 parameter fit with a free parameter to constrain

## 6.5. RESULTS AND DISCUSSION

residuals. Again, I expect this configuration to be quite rare and in almost all cases the number of calibrators is expected to be  $N \geq 5$ .

The other consideration is that there is a trade-off between onsource time (which improves SNR) and number of calibrators  $N$ . The total time to observe a single loop comprises of all dwell and slew times. For every calibrator scan there are 2 target scans and 2 slews. Atmospheric terms will have temporal variability, so there must be an upper limit to the time over which a solution to the phase plane can be determined. If this time is the ‘spatial coherence time’  $T_{coh}$ , then it must be the case that:

$$\begin{aligned} T_{coh} &\geq N(\tau_t + \tau_s + \tau_c + \tau_s) + \tau_t \\ &\geq (N+1)\tau_t + 2N\tau_s + N\tau_c \end{aligned} \quad (6.4)$$

where  $\tau_t$ ,  $\tau_c$  are dwell times for the calibrators and target respectively,  $\tau_s$  is the slew time and  $T_{coh}$  is the total plane approximate coherence time. I consider the slowest slewing telescope to be the limiting factor in the slew times such that the slew time is the angular distance between target and calibrator (aka.  $R$ ) divided by that telescopes slew time:

$$\tau_s = \frac{R}{v_s}$$

I note that in the case of short slews, the slew times can be dominated by the antennas acceleration and settling time, so in these instances there might not be a simple relationship with the target-calibrator separation. However, these cases also are unlikely to be coherence limited due to the small separations.

For MV02\* epochs, the target and calibrator had the same integration time of  $\tau_t = \tau_c = 40$  s and I find coherent plane solutions for  $\bar{R} = 7.5$  deg and  $N = 6$  which gives a lower-limit coherence time of  $T_{coh} = 10.9$  min at 8.4 GHz. Considering this limit, I investigate if there exists a theoretically ideal number of quasars and respective distance.

The average  $\overline{\text{SNR}}$  is given by the radiometry equation and target quasar strength:

$$\overline{\text{SNR}} = \frac{\overline{S_c}}{\sigma_S} = \overline{S_c} \sqrt{\frac{2\tau\Delta\nu}{\overline{\text{SEFD}}}} \quad (6.5)$$

where  $\sigma_S$  is the noise,  $\overline{S_c}$  is the average quasar strength,  $\Delta\nu$  is the integrated bandwidth and  $\overline{\text{SEFD}}$  is the average baseline SEFD. Solving Equation 6.4 for quasar onsource integration time  $\tau$  and assuming that  $\tau_c = \tau_m = \tau$ :

$$\begin{aligned} T_{coh} &= (N+1)\tau + 2N\frac{R}{v_s} + N\tau \\ \therefore \tau &= \frac{T_{coh} - 2N\frac{R}{v_s}}{2N+1} \end{aligned} \quad (6.6)$$

Substituting Equation 6.5 and 6.6 into Equation 6.3 the final form for the uncertainty is:

$$\sigma_A = \frac{360/\pi}{S_c} \sqrt{\frac{\overline{\text{SEFD}}}{2\Delta\nu}} \frac{1}{\sqrt{\bar{R}^2 + \sigma_R^2}} \sqrt{\frac{2N+1}{N(T_{coh} - 2N\frac{\bar{R}}{v_s})}} \quad (6.7)$$

## 6.5. RESULTS AND DISCUSSION

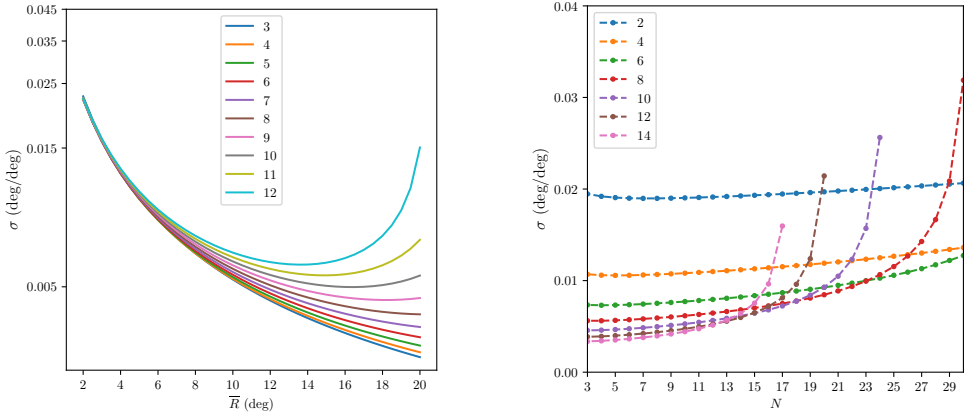


**Figure 6.20:** Slope uncertainty  $\sigma$  as a function of **Left:**  $\bar{R}$ , with different lines correspond to different values of  $N$  given in legend; and **Right:**  $N$ , with lines corresponding to different values of  $\bar{R}$  given in legend. For all lines  $SEFD = 2000$  Jy,  $\sigma_R = 1$  deg,  $T_{coh} = 11$  min,  $v_s = 40$  deg/min,  $S_c = 250$  mJy and  $\Delta\nu = 256$  MHz. Note: left figure is  $\log_{10}$  scaled however retaining natural units.

Figure 6.20 shows the theoretical measurement uncertainty in the slopes introduced by increasing mean radius  $\bar{R}$  or number of quasars  $N$  for the ASCI array sensitivities. The slope measurement uncertainty is a strong function of radius and a weak function of quasar number provided loops are kept within coherence time. In addition, the slope measurement uncertainty is as strong a function of mean quasar correlated flux density  $\bar{S}_c$  as it is of radius. The reasons for the turn up that occurs at extreme values of  $\bar{R}$  and  $N$  is as the total loop time approaches the spatial coherence time, scans have to be increasingly shorter and SNR rapidly decreases.

It is clear that there is no theoretical detriment as viewed purely from a slope measurement uncertainty perspective to increasing the angular offset of the orbit sources and adding more calibrators. The interpretation is that compact luminous quasars are extremely beneficial to have and worth the time investment to slew to if phase slope measurement uncertainty is the limiting factor.

I have not yet addressed the systematic error  $\sigma_O^2$  in Equation 6.1. While theoretically it makes sense to push the limit and increase mean radius to sample the slope more precisely, in practice it is understood that this will run the risk of a breakdown in the planar assumption and introduce other systematics. From the equations derived in Chapter 5, it is clear that the systematic underestimation of the phase while plane fitting (if positions have been pre-corrected by iPR) should take the form:

$$\sigma_{O^2} \leq \bar{R}^2 \frac{|c\sigma_\tau|}{\lambda} \left( \frac{\pi}{180} \right)$$

for phase in radians, where  $|c\sigma_\tau|$  is the quadrature sum of all possible sources of unmodelled residual delay towards the target and  $\bar{R}$  is the average target–calibrator separation. For moderate elevations  $\varepsilon \geq 30$  deg during the track, this function should serve as an upper bound for the natural deviation from planar structure.

The only factor not included in either modelling or planar systematics is the spatial decoherence due to the wet troposphere. As discussed in Chapters 2 and 5, temporal and spatial variation in the wet troposphere are very difficult to predict or model, particularly on the scales we desire for this analysis. For early BeSSeL pilot observations and testing periods, target–calibrator

## 6.5. RESULTS AND DISCUSSION

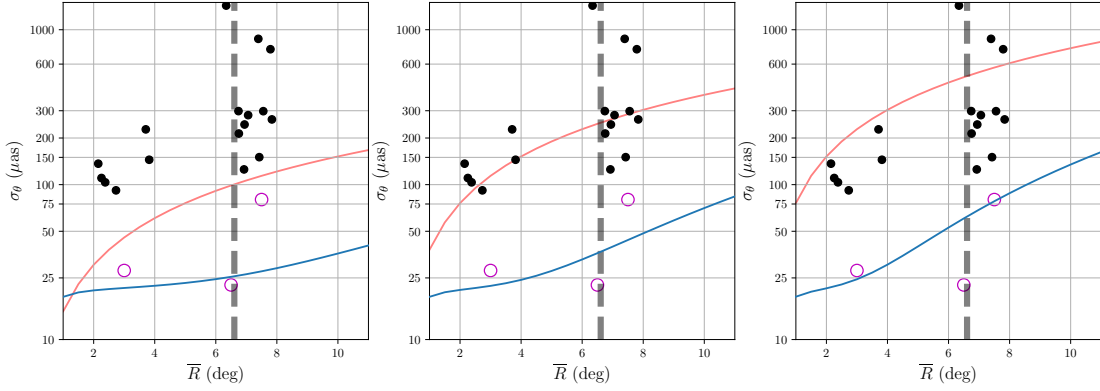


**Figure 6.21:** Astrometry vs. empirically modelled uncertainty at 8.2 GHz. **Black and magenta points:** Astrometric uncertainty  $\sigma_\theta = \sqrt{\sigma_\delta^2 + \sigma_\alpha^2}$  for phase reference quasars in iPR and target sources in iMV respectively. **Red line:** Uncertainty expected from iPR  $\sigma_\theta = \theta_{sep} |c\tau_r|$  and; **blue line:** Uncertainty expected from iMV with  $\sigma_\theta = \theta_{sep}^2 |c\tau_r|$  with  $N = 5.65$  (average of 3 ring  $N$ 's),  $T_{coh} = 11$  min,  $SEFD = 2000$  Jy and  $\bar{S} = 250$  mJy as consistent with MV02\* epochs; **black dashed line:** expected radius that wet-tropospheric decoherence occurs  $\theta_{wt,8.2}$ . **Left to right:** Assuming residual delay of  $|c\tau_r| = 2, 5, 10$  cm respectively.

separations of  $\theta_{sep} \geq 2.5$  deg were found to regularly fail (Mark J. Reid, private communication) due to phase decoherence. If I assume this spatial coherence scale  $\theta_{wt,\nu}$  scales linearly with wavelength:

$$\frac{\theta_{wt,\nu}}{\theta_{wt,22}} = \frac{22 \text{ GHz}}{\nu}$$

then we can establish values for other wavelengths;  $\theta_{wt,8.2} = 6.6$  deg and  $\theta_{wt,6.7} = 8.3$  deg.

The total astrometric accuracy expected from inverse MultiView should therefore be:

$$\sigma_\theta^2 = \left( \frac{\lambda}{|\mathbf{B}|} \right)^2 \left( \left( \frac{360/\pi}{S_c} \right)^2 \frac{SEFD}{2\Delta\nu} \frac{\bar{R}^2}{\bar{R}^2 + \sigma_R^2} \frac{2N+1}{N \left( T_{coh} - 2N \frac{\bar{R}}{v_s} \right)} \right) + \left( \bar{R}^2 \frac{|c\sigma_\tau|}{|\mathbf{B}|} \right)^2 \quad (6.8)$$

where  $\sigma_\theta$  is the astrometric accuracy,  $\lambda$  is the observing wavelength and  $|\mathbf{B}|$  is the array max baseline.

Figure 6.21 shows Equation 6.8 plotted against the measured astrometric accuracy from the 4 epochs of analytical data, MV025 to MV028. There seems to be moderate agreement between model and astrometric trends, and numerical agreement for certain parameter combinations. This modelling implies the most likely amount of residual delay present in calibrated data was approximately  $|c\tau| \sim 5$  cm, and likely a combination of residual ionosphere and troposphere, however, the cause of the residual delay  $|c\tau|$  does not appear to matter as it was removed regardless.

## 6.6 Final comments

The VLBA achieves astrometric accuracy for parallax observations that can be better than  $10\mu\text{as}$ . Key to this accuracy is that they are able to use wideband system to get good estimates of the zenith tropospheric delay and that there is also a good *a priori* ionospheric delay model available from GPS measurements. They also benefit from a good quasar catalogues which mean that they are generally able to find multiple quasars within 1–2 degrees of the target source. We have an array where some of the antennas do not have dual-band or wideband receiver systems which reduces the accuracy of the tropospheric zenith delay determination significantly (further exacerbated by slow slewing of some antennas reducing the sampling of the sky in geoblocks). The ionospheric models and the quasar catalogues are poorer. So to achieve the same sort of accuracy that they have with the VLBA we either need a VLBA in the south and the time to expand the quasar catalogue or a different method.

I have shown the methodology and reduction processes to achieve microsecond astrometry in the Southern Hemisphere. Inverse MultiView appears extremely promising as a method to achieve high astrometric accuracy even in the suspected presence of large residual delays, almost regardless of the cause. Using the empirical model (Equation 6.8) as applicable to S $\pi$ RALS observing frequency of 6.7 GHz with target quasars  $\bar{S} = 250 \text{ mJy}$  in the presence of  $|c\tau| = 5 \text{ cm}$  residual delays, I predict a per-epoch astrometric uncertainty  $\sigma_\theta \leq 50\mu\text{as}$ . With 8 parallax epochs spread over a year this would give a parallax error  $\sigma_\varpi \approx \frac{\sigma_\theta}{2\sqrt{n-3}} = 11\mu\text{as}$ . While this is a conservatively high estimate for the astrometric uncertainty of the array, it demonstrates that a high astrometric accuracy can reasonably be achieved from a reasonable number of epochs.

Therefore inverse MultiView will be the astrometric calibration scheme for S $\pi$ RALS. The selected masers (Chapter 4) are compact and luminous, allowing for easy phase detection within a scan. Immediate future work is quasar classification within  $\sim 10$  deg of target masers. While quasar classifications exist, additional surveys to measure quasars as detectable by the ASCI array would be very beneficial.

The ideal number of orbit sources is that which optimally samples azimuthally while staying under a total loop time of 10 min. While 4 is the minimum, not only is it unlikely to have 4 orbit sources in optimal spacing, it only leaves one free parameter for estimating residuals. A good rule of thumb is 5 orbit sources if optimally spaced or 6 to achieve it. As astrometric uncertainty depends on slope measurement certainty and therefore SNR, I recommend strong  $\text{SNR} = 10 - 15$  detections.

While inverse MultiView appears able to calibrate residual delay up to the measurement error, it appears beneficial to include calibration overhead of manual phase calibration, geoblocks and GPS TEC maps etc. Good *a priori* delay calibration is key to solving for position offsets in the phase domain- too much residual delay will cause phase planes to be too steep and phases to wrap.

I have applied MultiView 12 times (4 epochs x 3 sources) and it has worked on each occasion, even out to target-calibrator separations of 7–8 degrees. Therefore the technique seems robust. The observations to date only span a limited range of times and a single frequency, but there is no reason to expect that comparable observations at other frequencies and other arrays cannot be similarly successful. MultiView should increase the centimetre wavelength accuracy achievable with heterogeneous arrays such as the LBA, EVN and East-Asian VLBI Network (EAVN) - which at the moment perform much less well than the VLBA astrometrically.



# CONCLUSION

Since the inception of BeSSeL and resultant accurate determination of Galactic structure as visible from the Northern Hemisphere, the astrometric community has strived to do the same in the Southern Hemisphere. Early attempts on the LBA were affected by suspected ionospheric effects, limited mutual bandwidth on the heterogeneous array and time unavailability. With the material contained within this thesis, it should now be possible to determine the structure and kinematics of the Galaxy as visible from Southern Hemisphere. This is a significant breakthrough.

## 7.1 Summary of Results

I reduce BeSSeL data and measure the proper motion and parallax for three 22 GHz water masers and a 6.7 GHz methanol maser. With these measurements I determine distances for the host star forming regions and use these distances to place all four masers in the Perseus arm of the Galaxy. Finally, I combine my results with previously known Perseus arm maser parallaxes to calculate a Perseus spiral arm pitch angle.

I conduct a targeted VLBI survey of all known Southern Hemisphere 6.7 GHz methanol masers with flux density  $> 10$  Jy. I model spatial and energetic properties for each maser velocity feature and determine overall maser compactness. I catalogue the individual maser properties and compactness for future studies and select out the best targets for astrometry.

I introduce and discuss inverse MultiView calibration. I derive relationships to predict how inverse MultiView will be able to remove residual delays. I find that inverse MultiView is robust to target source positional uncertainties, baseline, ionosphere and troposphere delay uncertainties given prior calibration. I expect uncertainty in inverse MultiView calibration to increase as  $\theta^2$  rather than  $\theta$  for traditional phase referencing.

Finally, I conduct pilot S $\pi$ RALS observations using quasars to test inverse MultiView and the BeSSeL observation/calibration approach as applicable to the new ASCI array. This process involves scheduling, observing, correlating, data reduction, inverse MultiView application and astrometric analysis. I find that inverse MultiView allows the ASCI array to achieve microarc-second astrometry out to average target–calibrator separations  $\sim 7.5$  deg.

## 7.2 Current and Future work

S $\pi$ RALS began pilot observations of 6.7 GHz methanol masers in September 2019 and fully began taking observations in May 2020. At the time of writing, over 400 hours of data have been collected. All S $\pi$ RALS targets have been *A*–grade sources as catalogued. Early astrometric estimates show that inverse MultiView is working at the level of  $40 - 60\mu\text{as}$  per epoch, in-line with expectations.

Before pilot observations begun, Warkworth Radio Astronomical Observatory, New Zealand joined the S $\pi$ RALS collaboration. They brought access to the Warkworth 30m radio telescope into ASCI. This extends the maximum baseline from Hobart–Katherine at  $|B| = 3500$  km to Yarragadee–Warkworth at  $|B| = 5500$  km and increases the array sensitivity.

Ceduna 30m, Yarragadee 12m and Warkworth 30m have a planned receiver upgrade. While all three upgrades are at various stages, all three are very likely to be completed in the next year. All receivers will have a mutual spanned bandwidth of at least 3–7 or 8 GHz. This spanned bandwidth will allow dispersive delay removal during geoblock fitting and consequential accurate zenith tropospheric delay determination. I presented evidence to suggest a large amount of residual zenith delay (5 cm) in inverse MultiView test observations from the phase slopes, so accurate determination would most likely leave only ionosphere residuals above 1 cm. As residual dry tropospheric delay has a tendency to diverge at a elevation dependant target–calibrator radius compared to the delay slopes expected from the much thinner ionosphere, this may allow either an extension to how low in elevation tracks can be or an observing scheme comprised of only one low-elevation track.

The parallax measured for the 22 GHz water maser G021.87+0.01 was not sufficiently constrained by the astrometry to directly determine a distance. This was largely due to observed source evolution and/or flux density variability common in water masers. It would be beneficial to independently confirm the distance of  $D = 13.7$  kpc as I determined from kinematic models of recession velocity and proper motion. The region in question appears to have a nearby 6.7 GHz methanol maser G021.880+0.014 (Caswell et al., 1995b; Breen et al., 2015). The methanol maser G021.880+0.014 is offset 0.6 amin from water maser G021.87+0.01 with identical velocity range  $v = 17$  to  $22\text{ km s}^{-1}$ . However, the methanol maser has a catalogued flux density between  $S = 15$  and 5 Jy with unknown compactness. Therefore, it is not immediately obvious whether it is suitable for inverse phase referencing or inverse MultiView.

As I saw from the reduction of G021.87+0.01, only the nearby calibrator J1825–0737 at  $\Delta\theta = 2.566$  deg was suitable for phase referencing (at  $\sim 200$  mJy). The other calibrator J1835–1115 at  $\Delta\theta = 1.793$  deg was too–weak ( $\sim 20$  mJy). In the neighbourhood of  $\Delta\theta < 6$  deg there are 9 quasars suitable for phase referencing; all appear compact and have flux densities  $S > 80$  mJy. Depending on the compactness of the quasar, this could prove to be a very good chance to test non-inverse MultiView (by phase referencing on a quasar and interpolating phase slopes to maser) or inverse MultiView on the VLBA.

I chose to conduct the MultiView tests at X-band, however, there is little preventing a repeat of observations at S-band ( $\sim 2$  GHz). All ASCI array telescopes (and the possible inclusion of Warkworth 12m) have access to S-band receivers, so there is the possibility to test whether MultiView holds up as residual delays increase on the target (due to the ionosphere). I attributed the measured phase slopes at X-band to residual dry troposphere, however, at S-band the ionosphere and variations to it should be dominant. I intend to pursue this in a future study.

## 7.2. CURRENT AND FUTURE WORK

If dry tropospheric residuals, baseline offsets and ionospheric residuals were brought down to VLBA levels of 1 cm, for a target–calibrator separation of 3 deg I calculate the inverse MultiView should be able to achieve an astrometric accuracy of  $\sigma_\theta = 1\mu\text{as}$ . This also implies that inverse MultiView on the VLBA should be approaching this astrometric accuracy already.

The application of the high astrometric accuracy provided by MultiView carrying the most impact may be the ability to measure parallaxes to masers in the Large Magellanic Cloud (Green et al., 2008, 2009; Imai et al., 2013). While this is not currently possible from a logistical perspective, it is no longer impossible. The ability to directly measure distances to star formation regions at  $\sim 50$  kpc would affect the whole cosmic distance ladder by almost an order of magnitude; allowing the whole Universe to be brought into sharper focus.

Other very promising avenues are low-frequency astrometry, which struggle to surpass the limits of the ionosphere. Pulsar astrometry (Deller et al., 2019) rely heavily on in-beam calibrators to achieve microsecond astrometry due to the overwhelming influence of the ionosphere at low frequencies (1.66 GHz). Even for target–calibrator separations 0.5 deg, which would be an in-beam calibrator on the VLBA, a residual TEC of only 1 TECU at 1.66 GHz would mean a delay difference of almost 15 cm! At 0.5 deg separation this constitutes an astrometric accuracy of  $35\mu\text{as}$ , however, this requires the existence of an in-beam calibrator. The ionosphere is largely planar at even lower frequencies ( $\leq 150$  MHz; Rioja et al., 2018, and given good weather) so MultiView should be able to achieve the  $\theta^2$  dependence of plane fitting. With a similar setup at 1 deg separation, MultiView should achieve  $1\mu\text{as}$  astrometric accuracy.

I have confidence in saying that the most significant result of this thesis is the demonstration of inverse MultiView calibration. Trigonometric parallax is the gold standard for distance estimates in astronomy and any ability to increase the accuracy that parallaxes can be determined affects all aspects of astronomy and cosmology. Inverse MultiView has the potential to be the next big leap in astrometric calibration that can allow accurate distance determination an order of magnitude larger.



## BIBLIOGRAPHY

- Amaral, L. H., & Lepine, J. R. D. 1997, MNRAS, 286, 885
- Antoja, T., Figueras, F., Romero-Gómez, M., et al. 2011, MNRAS, 418, 1423
- Asaki, Y., Imai, H., Sobolev, A. M., & Parfenov, S. Y. 2014, ApJ, 787, 54
- Asiaain, R., Figueras, F., & Torra, J. 1999, A&A, 350, 434
- Bailer-Jones, C. A. L. 2015, PASP, 127, 994
- Barnard, E. E. 1916, AJ, 29, 181
- Bartkiewicz, A., Szymczak, M., van Langevelde, H. J., Richards, A. M. S., & Pihlström, Y. M. 2009, A&A, 502, 155
- Benjamin, R. A. 2008, in Astronomical Society of the Pacific Conference Series, Vol. 387, Massive Star Formation: Observations Confront Theory, ed. H. Beuther, H. Linz, & T. Henning, 375
- Bhat, N. D. R., Cordes, J. M., Camilo, F., Nice, D. J., & Lorimer, D. R. 2004, ApJ, 605, 759
- Blitz, L. 1979, ApJ, 231, L115
- Breen, S. L., Ellingsen, S. P., Caswell, J. L., et al. 2016, MNRAS, 459, 4066
- Breen, S. L., Ellingsen, S. P., Contreras, Y., et al. 2013, MNRAS, 435, 524
- Breen, S. L., Fuller, G. A., Caswell, J. L., et al. 2015, MNRAS, 450, 4109
- Bronfman, L., Nyman, L. A., & May, J. 1996, A&AS, 115, 81
- Brunthaler, A., Reid, M. J., Menten, K. M., et al. 2011, Astronomische Nachrichten, 332, 461
- Burns, R. A., Handa, T., Nagayama, T., Sunada, K., & Omodaka, T. 2016, MNRAS, 460, 283
- Burns, R. A., Handa, T., Imai, H., et al. 2017, MNRAS, 467, 2367
- Burns, R. A., Sugiyama, K., Hirota, T., et al. 2020a, Nature Astronomy, 10

## BIBLIOGRAPHY

- Burns, R. A., Orosz, G., Bayandina, O., et al. 2020b, MNRAS, 491, 4069
- Capitaine, N., Klioner, S., & McCarthy, D. 2012, in IAU Joint Discussion, Vol. 7, IAU Joint Discussion, 40
- Caswell, J. L. 1997, MNRAS, 289, 203
- Caswell, J. L., & Haynes, R. F. 1987, A&A, 171, 261
- Caswell, J. L., Vaile, R. A., & Ellingsen, S. P. 1995a, PASA, 12, 37
- Caswell, J. L., Vaile, R. A., Ellingsen, S. P., Whiteoak, J. B., & Norris, R. P. 1995b, MNRAS, 272, 96
- Caswell, J. L., Fuller, G. A., Green, J. A., et al. 2010, MNRAS, 404, 1029
- . 2011, MNRAS, 417, 1964
- Cheung, A. C., Rank, D. M., Townes, C. H., Thornton, D. D., & Welch, W. J. 1969, Nature, 221, 626
- Choi, Y. K., Hachisuka, K., Reid, M. J., et al. 2014, ApJ, 790, 99
- Cordes, J. 2001, Ap&SS, 278, 11
- Cordes, J. M. 2004, in Astronomical Society of the Pacific Conference Series, Vol. 317, Milky Way Surveys: The Structure and Evolution of our Galaxy, ed. D. Clemens, R. Shah, & T. Brainerd, 211
- Cordes, J. M., & Lazio, T. J. 1991, ApJ, 376, 123
- Cordes, J. M., Weisberg, J. M., Frail, D. A., Spangler, S. R., & Ryan, M. 1991, Nature, 354, 121
- Dame, T. M., Hartmann, D., & Thaddeus, P. 2001, ApJ, 547, 792
- de Bruijne, J. H. J., Allen, M., Azaz, S., et al. 2015, A&A, 576, A74
- de Vaucouleurs, G. 1959, Handbuch der Physik, 53, 275
- de Vaucouleurs, G., de Vaucouleurs, A., Corwin, Jr., H. G., et al. 1991, Third Reference Catalogue of Bright Galaxies. Volume I: Explanations and references. Volume II: Data for galaxies between  $0^h$  and  $12^h$ . Volume III: Data for galaxies between  $12^h$  and  $24^h$ .
- de Vaucouleurs, G., & Pence, W. D. 1978, AJ, 83, 1163
- Deller, A. T., Tingay, S. J., Bailes, M., & West, C. 2007, PASP, 119, 318
- Deller, A. T., Brisken, W. F., Phillips, C. J., et al. 2011, PASP, 123, 275
- Deller, A. T., Goss, W. M., Brisken, W. F., et al. 2019, ApJ, 875, 100
- Dickey, J. M., & Lockman, F. J. 1990, ARA&A, 28, 215
- Dodson, R., Rioja, M., Asaki, Y., et al. 2013, AJ, 145, 147
- Dodson, R., Rioja, M. J., Molina, S. N., & Gómez, J. L. 2017, ApJ, 834, 177
- Dos Santos, P. M., & Lepine, J. R. D. 1979, Nature, 278, 34
- Draine, B. T. 2010, Physics of the Interstellar and Intergalactic Medium (Princeton University Press)
- Drimmel, R. 2000, A&A, 358, L13
- Drimmel, R., & Spergel, D. N. 2001, ApJ, 556, 181

## BIBLIOGRAPHY

- Elitzur, M. 1992, ARA&A, 30, 75
- Ellingsen, S. P. 1996, PhD thesis, Physics Department, University of Tasmania, GPO Box 252C, Hobart 7001, Australia
- . 2006, ApJ, 638, 241
- Ellingsen, S. P., Voronkov, M. A., Cragg, D. M., et al. 2007, in IAU Symposium, Vol. 242, IAU Symposium, ed. J. M. Chapman & W. A. Baan, 213–217
- Ellsworth-Bowers, T. P., Rosolowsky, E., Glenn, J., et al. 2015, ApJ, 799, 29
- Englmaier, P. 2000, in Reviews in Modern Astronomy, Vol. 13, Reviews in Modern Astronomy, ed. R. E. Schielicke, 97
- Englmaier, P., & Gerhard, O. 1999, in Astronomical Society of the Pacific Conference Series, Vol. 182, Galaxy Dynamics - A Rutgers Symposium, ed. D. R. Merritt, M. Valluri, & J. A. Sellwood
- Englmaier, P., Pohl, M., & Bissantz, N. 2011, Memorie della Societa Astronomica Italiana Supplementi, 18, 199
- Fernández, D., Figueras, F., & Torra, J. 2001, A&A, 372, 833
- Fey, A. L., Spangler, S. R., & Cordes, J. M. 1991, ApJ, 372, 132
- Fich, M., Blitz, L., & Stark, A. A. 1989, ApJ, 342, 272
- Foster, T., & Cooper, B. 2010, in Astronomical Society of the Pacific Conference Series, Vol. 438, The Dynamic Interstellar Medium: A Celebration of the Canadian Galactic Plane Survey, ed. R. Kothes, T. L. Landecker, & A. G. Willis, 16
- Francis, C., & Anderson, E. 2009, Proceedings of the Royal Society of London Series A, 465, 3425
- Gaia Collaboration, Brown, A. G. A., Vallenari, A., et al. 2018, A&A, 616, A1
- Georgelin, Y. M., & Georgelin, Y. P. 1976, A&A, 49, 57
- Goedhart, S., Minier, V., Gaylard, M. J., & van der Walt, D. J. 2005, MNRAS, 356, 839
- Gómez, G. C. 2006, AJ, 132, 2376
- Gordon, J. P., Zeiger, H. J., & Townes, C. H. 1955, Physical Review, 99, 1264
- Gray, M. 2012, Maser Sources in Astrophysics
- Green, J., Van Langevelde, H. J., Brunthaler, A., et al. 2015, Advancing Astrophysics with the Square Kilometre Array (AASKA14), 119
- Green, J. A., & McClure-Griffiths, N. M. 2011, MNRAS, 417, 2500
- Green, J. A., Caswell, J. L., Fuller, G. A., et al. 2008, MNRAS, 385, 948
- Green, J. A., Caswell, J. L., Fuller, G. A., et al. 2009, in The Magellanic System: Stars, Gas, and Galaxies, ed. J. T. Van Loon & J. M. Oliveira, Vol. 256, 227–232
- . 2010, MNRAS, 409, 913
- Green, J. A., Caswell, J. L., McClure-Griffiths, N. M., et al. 2011, ApJ, 733, 27
- Green, J. A., Caswell, J. L., Fuller, G. A., et al. 2012, MNRAS, 420, 3108

## BIBLIOGRAPHY

- Green, J. A., Breen, S. L., Fuller, G. A., et al. 2017, MNRAS, 469, 1383
- Greisen, E. W. 1990, in Acquisition, Processing and Archiving of Astronomical Images, 125–142
- Hachisuka, K., Brunthaler, A., Menten, K. M., et al. 2009, ApJ, 696, 1981
- Hachisuka, K., Choi, Y. K., Reid, M. J., et al. 2015, ApJ, 800, 2
- Hawarey, M., Hobiger, T., & Schuh, H. 2005, Geophys. Res. Lett., 32, L11304
- Henderson, A. P. 1977, A&A, 58, 189
- Honma, M. 2013, in Astronomical Society of the Pacific Conference Series, Vol. 476, New Trends in Radio Astronomy in the ALMA Era: The 30th Anniversary of Nobeyama Radio Observatory, ed. R. Kawabe, N. Kuno, & S. Yamamoto, 81
- Honma, M., Nagayama, T., & Sakai, N. 2015, PASJ, 67, 70
- Honma, M., Tamura, Y., & Reid, M. J. 2008, PASJ, 60, 951
- Honma, M., Fujii, T., Hirota, T., et al. 2003, PASJ, 55, L57
- Honma, M., Bushimata, T., Choi, Y. K., et al. 2007, PASJ, 59, 889
- Hou, L. G., & Han, J. L. 2014, A&A, 569, A125
- Hou, L. G., Han, J. L., & Shi, W. B. 2009, A&A, 499, 473
- Hubble, E. 1926, Contributions from the Mount Wilson Observatory / Carnegie Institution of Washington, 324, 1
- Hubble, E. P. 1936, Realm of the Nebulae
- Hyland, L. J. 2015, Master's thesis, Physical Sciences
- Hyland, L. J., Ellingsen, S. P., & Reid, M. J. 2018, in IAU Symposium, Vol. 336, Astrophysical Masers: Unlocking the Mysteries of the Universe, ed. A. Tarchi, M. J. Reid, & P. Castangia, 154–157
- Imai, H., Burns, R. A., Yamada, Y., et al. 2016, ArXiv e-prints, arXiv:1603.02042
- Imai, H., Katayama, Y., Ellingsen, S. P., & Hagiwara, Y. 2013, MNRAS, 432, L16
- Immer, K., Reid, M. J., Menten, K. M., Brunthaler, A., & Dame, T. M. 2013, A&A, 553, A117
- Immer, K., Brunthaler, A., Reid, M. J., et al. 2011, ApJS, 194, 25
- Jansen, P., Kleiner, I., Xu, L.-H., Ubachs, W., & Bethlem, H. 2011, Physical Review A - PHYS REV A, 84, doi:10.1103/PhysRevA.84.06250
- Junqueira, T. C., Chiappini, C., Lépine, J. R. D., Minchev, I., & Santiago, B. X. 2015, MNRAS, 449, 2336
- Kellermann, K. I., Pauliny-Toth, I. I. K., & Williams, P. J. S. 1969, ApJ, 157, 1
- Kettenis, M., van Langevelde, H. J., Reynolds, C., & Cotton, B. 2006, Astronomical Society of the Pacific Conference Series, Vol. 351, ParselTongue: AIPS Talking Python, ed. C. Gabriel, C. Arviset, D. Ponz, & S. Enrique, 497
- Kohoutek, L. 1965, Bulletin of the Astronomical Institutes of Czechoslovakia, 16, 221
- Kounkel, M., Hartmann, L., Loinard, L., et al. 2017, ApJ, 834, 142

## BIBLIOGRAPHY

- Krishnan, V., Ellingsen, S. P., Reid, M. J., et al. 2017, MNRAS, 465, 1095
- . 2015, ApJ, 805, 129
- Lépine, J. R. D., Mishurov, Y. N., & Dedikov, S. Y. 2001, ApJ, 546, 234
- Lépine, J. R. D., Roman-Lopes, A., Abraham, Z., Junqueira, T. C., & Mishurov, Y. N. 2011, MNRAS, 414, 1607
- Levine, E. S., Blitz, L., & Heiles, C. 2006, Science, 312, 1773
- Lin, C. C., & Shu, F. H. 1964, ApJ, 140, 646
- Lockman, F. J. 1979, ApJ, 232, 761
- Lockman, F. J. 2002, in Astronomical Society of the Pacific Conference Series, Vol. 276, Seeing Through the Dust: The Detection of HI and the Exploration of the ISM in Galaxies, ed. A. R. Taylor, T. L. Landecker, & A. G. Willis, 107
- Lovell, J. E. J., McCallum, J. N., Reid, P. B., et al. 2013, Journal of Geodesy, 87, 527
- Lutz, T. E., & Kelker, D. H. 1973, PASP, 85, 573
- Malkin, Z., Jacobs, C., Arias, F., et al. 2015, in Journées 2014 “Systèmes de référence spatio-temporels”, ed. Z. Malkin & N. Capitaine, 3–8
- Marochnik, L. S., Mishurov, Y. N., & Suchkov, A. A. 1972, Ap&SS, 19, 285
- Martin-Pintado, J., Bachiller, R., & Fuente, A. 1992, A&A, 254, 315
- Martos, M., Hernandez, X., Yáñez, M., Moreno, E., & Pichardo, B. 2004, MNRAS, 350, L47
- McClure-Griffiths, N. M., & Dickey, J. M. 2007, ApJ, 671, 427
- . 2016a, ApJ, 831, 124
- . 2016b, ArXiv e-prints, arXiv:1608.03683
- McCulloch, P. M., Ellingsen, S. P., Jauncey, D. L., et al. 2005, AJ, 129, 2034
- Melis, C., Reid, M. J., Mioduszewski, A. J., Stauffer, J. R., & Bower, G. C. 2013, in IAU Symposium, Vol. 289, Advancing the Physics of Cosmic Distances, ed. R. de Grijs, 60–65
- Melis, C., Reid, M. J., Mioduszewski, A. J., Stauffer, J. R., & Bower, G. C. 2014, Science, 345, 1029
- Menten, K. M. 1991a, in Astronomical Society of the Pacific Conference Series, Vol. 16, Atoms, Ions and Molecules: New Results in Spectral Line Astrophysics, ed. A. D. Haschick & P. T. P. Ho, 119–136
- Menten, K. M. 1991b, ApJ, 380, L75
- Menten, K. M., Reid, M. J., Pratap, P., Moran, J. M., & Wilson, T. L. 1992, ApJ, 401, L39
- Merritt, D. 1999, PASP, 111, 129
- Minier, V., Booth, R. S., & Conway, J. E. 2002, A&A, 383, 614
- Moran, J. M., & Rosen, B. R. 1981, Radio Science, 16, 235
- Moscadelli, L., Reid, M. J., Menten, K. M., et al. 2009, ApJ, 693, 406
- Müller, H. S. P., Menten, K. M., & Mäder, H. 2004, A&A, 428, 1019

## BIBLIOGRAPHY

- Nakanishi, H. 2005, Astronomical Herald, 98, 670
- Nakanishi, H., & Sofue, Y. 2003, PASJ, 55, 191
- . 2006, PASJ, 58, 847
- . 2016, PASJ, 68, 5
- Naudet, C. J. 1996, Telecommunications and Data Acquisition Progress Report, 126, 1
- Neufeld, D. A., Melnick, G. J., Kaufman, M. J., et al. 2017, ApJ, 843, 94
- Oh, C. S., Kobayashi, H., Honma, M., et al. 2010, PASJ, 62, 101
- Oort, J. H., Kerr, F. J., & Westerhout, G. 1958, MNRAS, 118, 379
- Orosz, G., Dodson, R., Imai, H., et al. 2014, Testing methods for accurate OH maser astrometry, ATNF Proposal
- Orosz, G., Imai, H., Dodson, R., et al. 2017, AJ, 153, 119
- Orosz, G., Gómez, J. F., Imai, H., et al. 2019, MNRAS, 482, L40
- Osterbrock, D. E. 2005, Astrophysics Of Gas Nebulae and Active Galactic Nuclei (University Science Books)
- Oudmaijer, R. D., Groenewegen, M. A. T., & Schrijver, H. 1998, MNRAS, 294, L41
- Perryman, M. 2012, European Physical Journal H, 37, 745
- Perryman, M. A. C. 2002, Ap&SS, 280, 1
- Perryman, M. A. C., Lindegren, L., Kovalevsky, J., et al. 1997, A&A, 500, 501
- Perryman, M. A. C., de Boer, K. S., Gilmore, G., et al. 2001, A&A, 369, 339
- Petrov, L., Natusch, T., Weston, S., et al. 2015, PASP, 127, 516
- Phillips, C. J., Norris, R. P., Ellingsen, S. P., & McCulloch, P. M. 1998, MNRAS, 300, 1131
- Poleski, R. 2013, arXiv e-prints, arXiv:1306.2945
- Pradel, N., Charlot, P., & Lestrade, J. F. 2006, A&A, 452, 1099
- Pushkarev, A. B., & Kovalev, Y. Y. 2015, MNRAS, 452, 4274
- Quiroga, R. J. 1977, Ap&SS, 50, 281
- Quiroga-Nuñez, L. H., Immer, K., van Langevelde, H. J., Reid, M. J., & Burns, R. A. 2019, A&A, 625, A70
- Radcliffe, J. F., Garrett, M. A., Beswick, R. J., et al. 2016, A&A, 587, A85
- Reid, M. J. 1993, ARA&A, 31, 345
- Reid, M. J. 2008, in Revista Mexicana de Astronomia y Astrofisica Conference Series, Vol. 34, Revista Mexicana de Astronomia y Astrofisica Conference Series, 53–59
- Reid, M. J., & Honma, M. 2014, ARA&A, 52, 339
- Reid, M. J., Menten, K. M., Brunthaler, A., & Moellenbroek, G. A. 2009a, in ArXiv Astrophysics e-prints, Vol. 2010, astro2010: The Astronomy and Astrophysics Decadal Survey

## BIBLIOGRAPHY

- Reid, M. J., Menten, K. M., Brunthaler, A., et al. 2009b, *ApJ*, 693, 397
- Reid, M. J., Schneps, M. H., Moran, J. M., et al. 1988, *ApJ*, 330, 809
- Reid, M. J., Menten, K. M., Zheng, X. W., et al. 2009c, *ApJ*, 700, 137
- Reid, M. J., Menten, K. M., Brunthaler, A., et al. 2014, *ApJ*, 783, 130
- Reid, M. J., Brunthaler, A., Menten, K. M., et al. 2017, *AJ*, 154, 63
- Reid, M. J., Menten, K. M., Brunthaler, A., et al. 2019, *ApJ*, 885, 131
- Rioja, M., Dodson, R., Porcas, R. W., et al. 2009, in 8th International e-VLBI Workshop, 14
- Rioja, M. J., Dodson, R., & Franzen, T. M. O. 2018, *MNRAS*, 478, 2337
- Rioja, M. J., Dodson, R., Orosz, G., Imai, H., & Frey, S. 2017, *AJ*, 153, 105
- Rioja, M. J., Porcas, R. W., Desmurs, J. F., et al. 2002, in Proceedings of the 6th EVN Symposium, 57
- Rioja, M. J., Stevens, E., Gurvits, L., et al. 1997, *Vistas in Astronomy*, 41, 213
- Rix, H.-W., & Bovy, J. 2013, *A&A Rev.*, 21, 61
- Rodgers, A. W., Campbell, C. T., & Whiteoak, J. B. 1960, *MNRAS*, 121, 103
- Rohlfs, K. 1986, *Tools of Radio Astronomy* (Berlin : Springer-Verlag)
- Russeil, D. 2003a, in IAU Symposium, Vol. 212, *A Massive Star Odyssey: From Main Sequence to Supernova*, ed. K. van der Hucht, A. Herrero, & C. Esteban, 431
- Russeil, D. 2003b, *A&A*, 397, 133
- Rygl, K. L. J., Brunthaler, A., Reid, M. J., et al. 2010, *A&A*, 511, A2
- Rygl, K. L. J., Brunthaler, A., Sanna, A., et al. 2012, *A&A*, 539, A79
- Sakai, N. 2015, in *Revista Mexicana de Astronomia y Astrofisica Conference Series*, Vol. 46, *Revista Mexicana de Astronomia y Astrofisica Conference Series*, 56–60
- Sakai, N., Honma, M., Nakanishi, H., Sakanoue, H., & Kurayama, T. 2013, in IAU Symposium, Vol. 289, *Advancing the Physics of Cosmic Distances*, ed. R. de Grijs, 95–98
- Sakai, N., Honma, M., Nakanishi, H., et al. 2012, *PASJ*, 64, 108
- Sakai, N., Reid, M. J., Menten, K. M., Brunthaler, A., & Dame, T. M. 2019, *ApJ*, 876, 30
- Sakai, N., Sato, M., Motogi, K., et al. 2014, *PASJ*, 66, 3
- Sakai, N., Nakanishi, H., Matsuo, M., et al. 2015, *PASJ*, 67, 69
- Sanna, A., Reid, M. J., Dame, T. M., Menten, K. M., & Brunthaler, A. 2017, *Science*, 358, 227
- Sanna, A., Reid, M. J., Dame, T. M., et al. 2012, *ApJ*, 745, 82
- Sanna, A., Menten, K. M., Carrasco-González, C., et al. 2015, *ApJ*, 804, L2
- Sevenster, M. N. 1999, *MNRAS*, 310, 629
- Shaviv, N. J. 2003, *New A*, 8, 39

## BIBLIOGRAPHY

- Sobolev, A. M., Cragg, D. M., Ellingsen, S. P., et al. 2007, in IAU Symposium, Vol. 242, IAU Symposium, ed. J. M. Chapman & W. A. Baan, 81–88
- Sofue, Y., & Fujimoto, M. 1983, ApJ, 265, 722
- Stack, P. D., & Ellingsen, S. P. 2011, PASA, 28, 338
- Stotskii, A., Elgered, K. G., & Stotskaya, I. M. 1998, Astronomical and Astrophysical Transactions, 17, 59
- Stotskii, A. A., & Stotskaya, I. M. 1992, Astronomical and Astrophysical Transactions, 2, 327
- Szymczak, M., Hrynek, G., & Kus, A. J. 2000, A&AS, 143, 269
- Szymczak, M., & Kus, A. J. 2000, A&A, 360, 311
- Szymczak, M., Kus, A. J., Hrynek, G., Kępa, A., & Pazderski, E. 2002, A&A, 392, 277
- Szymczak, M., Olech, M., Sarniak, R., Wolak, P., & Bartkiewicz, A. 2018a, MNRAS, 474, 219
- Szymczak, M., Olech, M., Wolak, P., Gérard, E., & Bartkiewicz, A. 2018b, A&A, 617, A80
- Taylor, J. H., & Cordes, J. M. 1993, ApJ, 411, 674
- Titmarsh, A. M., Ellingsen, S. P., Breen, S. L., Caswell, J. L., & Voronkov, M. A. 2013, ApJ, 775, L12
- Townes, C. H., & Schawlow, A. L. 1955, Microwave Spectroscopy
- Tralli, D. M., & Lichten, S. M. 1990, Bulletin Geodesique, 64, 127
- Urquhart, J. S., Hoare, M. G., Purcell, C. R., et al. 2010, PASA, 27, 321
- Vallee, J. P. 1995, ApJ, 454, 119
- Vallée, J. P. 2002, ApJ, 566, 261
- van de Hulst, H. C., Muller, C. A., & Oort, J. H. 1954, Bull. Astron. Inst. Netherlands, 12, 117
- VERA Collaboration, Hirota, T., Nagayama, T., et al. 2020, PASJ, arXiv:2002.03089
- Walker, C., & Chatterjee, S. 1999, in VLBA Scientific Memo 23
- Weaver, H., Williams, D. R. W., Dieter, N. H., & Lum, W. T. 1965, Nature, 208, 29
- Wilson, T. L., Rohlf, K., & Hüttemeister, S. 2009, Tools of Radio Astronomy (Springer-Verlag), doi:10.1007/978-3-540-85122-6
- Wink, J. E., Altenhoff, W. J., & Mezger, P. G. 1982, A&A, 108, 227
- Wright, E. L., Eisenhardt, P. R. M., Mainzer, A. K., et al. 2010, AJ, 140, 1868
- Wu, Y. W., Sato, M., Reid, M. J., et al. 2014, A&A, 566, A17
- Wu, Y. W., Reid, M. J., Sakai, N., et al. 2019, ApJ, 874, 94
- Wynn-Williams, C. G. 1969, Astrophys. Lett., 3, 195
- Xu, Y., Reid, M. J., Zheng, X. W., & Menten, K. M. 2006, Science, 311, 54
- Xu, Y., Reid, M. J., Moscadelli, L., et al. 2012, in IAU Symposium, Vol. 287, Cosmic Masers - from OH to H<sub>0</sub>, ed. R. S. Booth, W. H. T. Vlemmings, & E. M. L. Humphreys, 368–376

## BIBLIOGRAPHY

- Xu, Y., Li, J. J., Reid, M. J., et al. 2013, ApJ, 769, 15  
Yang, K., Chen, X., Shen, Z.-Q., et al. 2019, ApJS, 241, 18  
Yao, J. M., Manchester, R. N., & Wang, N. 2017, ApJ, 835, 29  
Yao, X., & Liu, Q.-h. 2018, Chinese Astron. Astrophys., 42, 155  
Zhang, B., Reid, M. J., Menten, K. M., et al. 2013, ApJ, 775, 79  
Zhang, B., Reid, M. J., Zhang, L., et al. 2019, AJ, 157, 200  
Zinnecker, H., & Yorke, H. W. 2007, ARA&A, 45, 481



A

# FIRST QUADRANT PARALLAXES

## A.1 Additional Figures

### A.1.1 Maser and Calibrator Synthesised Maps

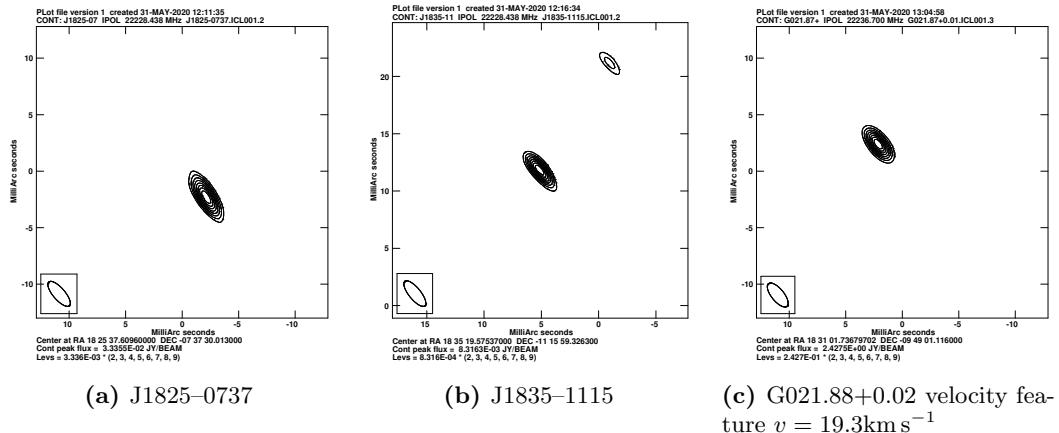


**Figure A.1:** Phase referenced images at epoch BR210B3. J1825-0737 and J1835-1115 are phase referenced against G021.87+0.01  $v = 19.3 \text{ km s}^{-1}$  feature. G021.87+0.01  $v = 19.3 \text{ km s}^{-1}$  map is phase referenced from J1825-0737.

## A.1. ADDITIONAL FIGURES

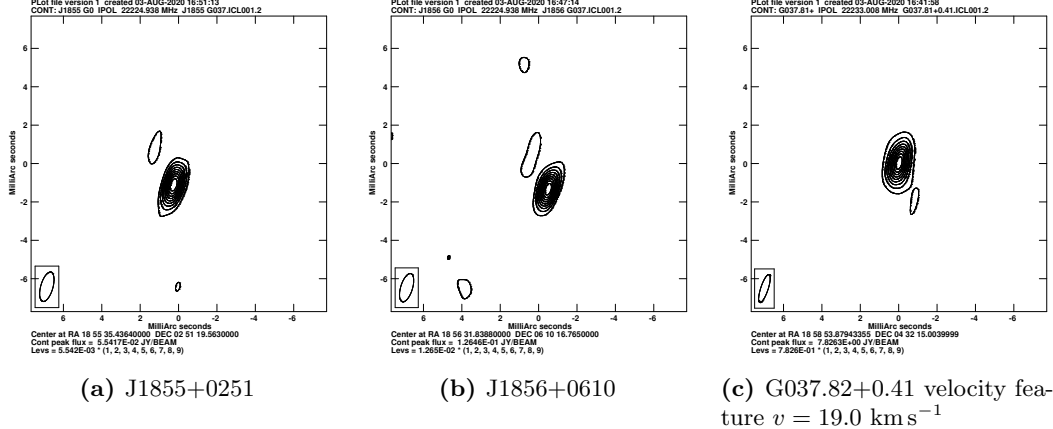


**Figure A.2:** Phase referenced images at epoch BR210C8. Both quasars J1855+0251 and J1856+0610 are phase referenced from G037.82+0.41  $v = 19.0 \text{ km s}^{-1}$  feature.

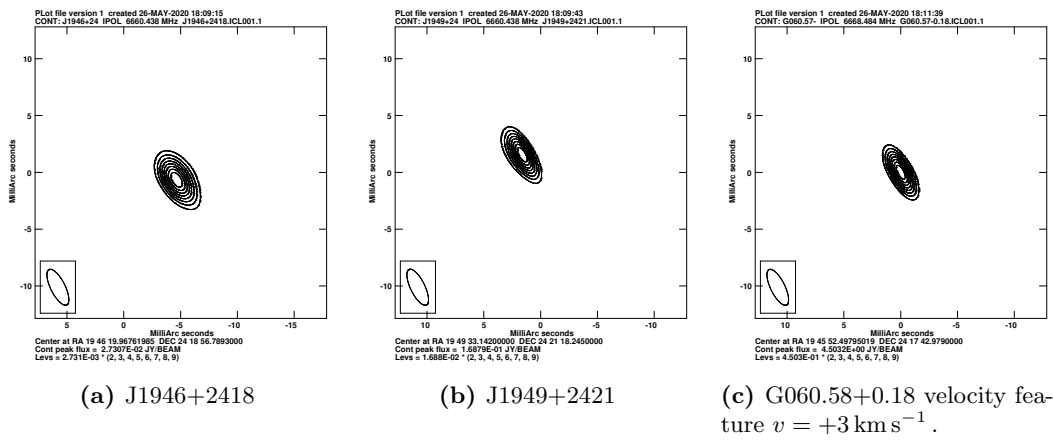


**Figure A.3:** Calibrators J1946+2418 and J1949+2421 phase referenced to G060.58+0.18 on epoch BR210FA. The channel used for fringe fit is also shown.

## A.1. ADDITIONAL FIGURES

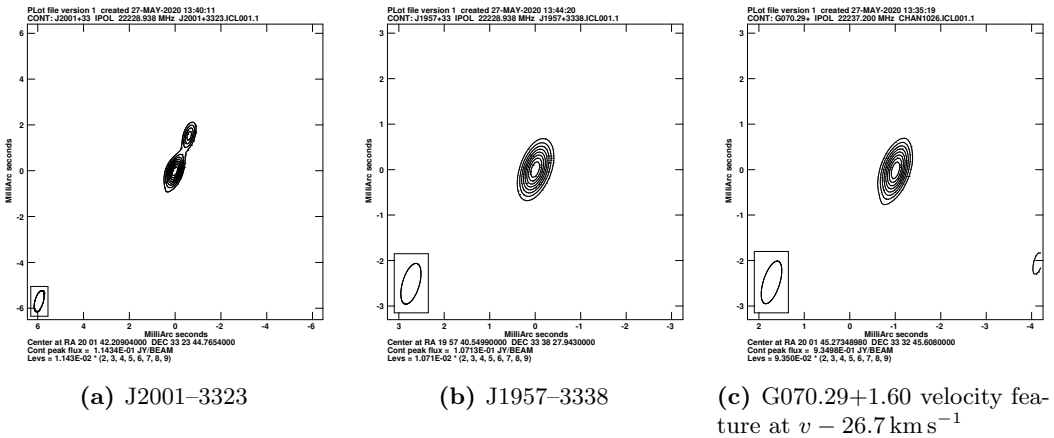


**Figure A.4:** Synthesised maps of G070.29+1.60 and calibrators.

### A.1. ADDITIONAL FIGURES

## A.1. ADDITIONAL FIGURES

### A.1.2 G021.87+0.01 Time-Series Spectra and Maps

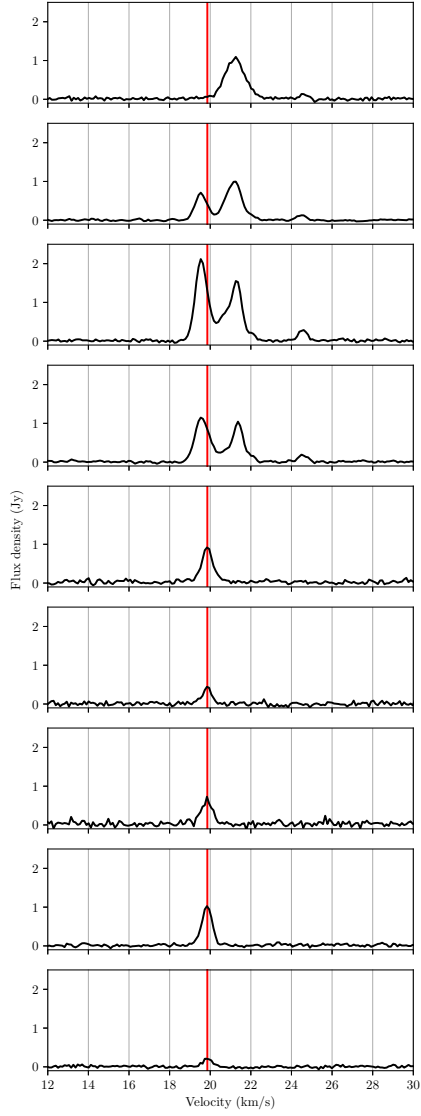


**Figure A.5:** Spectra of G021.88+0.01 on epochs 1, 2, 3, 4, 5, 6, 7, 8 and 12 (C) respectively; **y-axis:** scalar-averaged cross-power flux density (Jy) for antennas BR, FD, KP, LA, NL, OV and PT; **x-axis:** LSR recession velocity (km/s). Spectra undergoes almost no changes between epochs 8 and 12 apart from slight flux density variation. Time spacings from epoch 1 are  $t \simeq 0, 19, 44, 63, 166, 185, 196, 209, 256$  days respectively.

## A.1. ADDITIONAL FIGURES

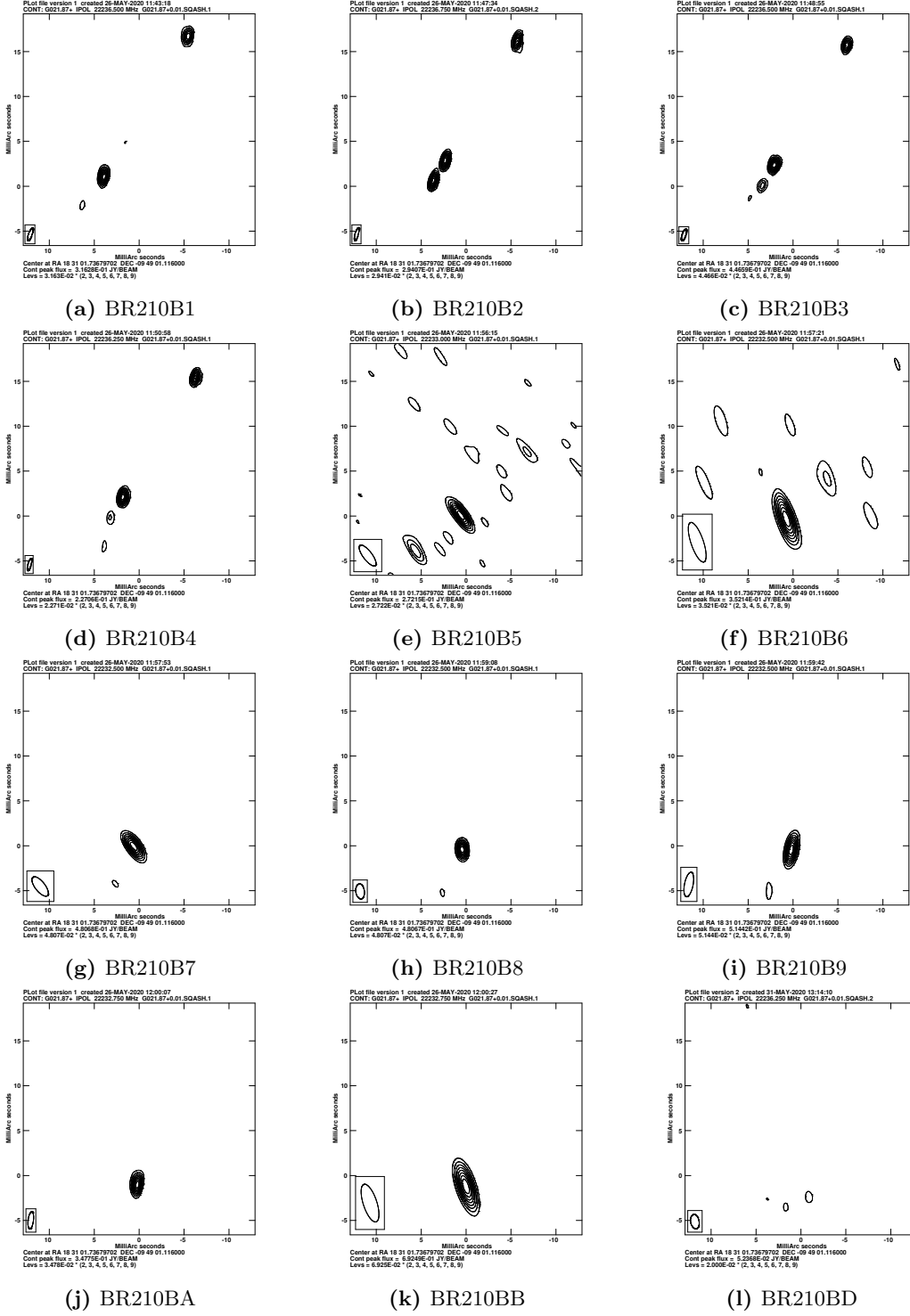


**Figure A.6:** G021.881+0.017 spotmaps over the coarse of the first 12 epochs. Maser region apparently undergoes relatively major morphological changes between the 4th and 5th epoch which are spaced  $\sim 103$  days apart. Due to fringe solution on both calibrator, astrometry not available for epoch 12/C despite clear maser detection in spectrum. Finally BR210BD is shows to illustrate the maser spot disappearance far below the detectable level

## A.2 Additional Tables

### A.2.1 BR210 Epochs

**Table A.1:** Observational epochs for relevant BR210 experiments.

Epoch	BR210B (yr)	BR210C (yr)	BR210D (yr)	BR210F (yr)
1	2015.178	2015.183	2015.189	2015.164
2	2015.230	2015.235	2015.277	2015.238
3	2015.298	2015.301	2015.359	2015.307
4	2015.350	2015.367	2015.408	2015.383
5	2015.632	2015.660	2015.698	2015.657
6	2015.684	2015.701	2015.739	2015.693
7	2015.715	2015.742	2015.769	2015.723
8	2015.750	2015.772	2015.797	2015.756
9	2015.780	2015.813	2015.835	2015.791
A	2015.819	2015.838	2015.862	2015.821
B	2015.846	2015.868	2015.890	2015.849
C	2015.879	2015.895	2015.923	2015.876
D	2016.134	2016.153	2016.197	2016.156
E	2016.205	2016.225	2016.260	2016.233
F	2016.279	2016.293	2016.345	2016.298
G	2016.350	2016.400	2016.405	2016.402

## A.2. ADDITIONAL TABLES

### A.2.2 Astrometric Products

**Table A.2:** Final astrometric values for G021.87+0.02.

QSO	Epoch (yr)	X offset (mas)	$\sigma_x$ (mas)	Y offset (mas)	$\sigma_y$ (mas)	Flux (Jy)	Experiment
J1825 – 0737	2015.230	2.260	0.010	2.872	0.022	0.55	B2
	2015.299	1.968	0.017	2.306	0.017	0.67	B3
	2015.351	1.704	0.015	2.118	0.026	0.57	B4
	2015.633	0.586	0.019	0.404	0.042	0.77	B5
	2015.715	0.589	0.027	-0.191	0.051	0.50	B7
	2015.751	0.425	0.015	-0.425	0.026	0.99	B8
	2015.781	0.212	0.012	-0.530	0.030	1.03	B9
	2015.819	0.260	0.022	-0.838	0.040	0.86	BA

## A.2. ADDITIONAL TABLES

**Table A.3:** Final astrometric values for G037.81+0.41

QSO	Epoch (yr)	X offset (mas)	$\sigma_x$ (mas)	Y offset (mas)	$\sigma_y$ (mas)	Flux (mJy)	Experiment
							BR210
J1855 + 0251	2015.184	1.485	0.004	4.391	0.006	86.5	C1
	2015.236	1.346	0.005	4.118	0.009	110.2	C2
	2015.301	1.151	0.006	3.791	0.008	107.8	C3
	2015.367	0.951	0.008	3.438	0.013	64.2	C4
	2015.660	0.026	0.015	1.712	0.023	38.0	C5
	2015.701	-0.066	0.007	1.554	0.009	56.0	C6
	2015.742	-0.240	0.007	1.161	0.008	65.2	C7
	2015.773	-0.265	0.006	1.125	0.010	57.7	C8
	2015.814	-0.373	0.005	0.786	0.007	70.2	C9
	2015.838	-0.335	0.005	0.616	0.008	67.3	CA
	2015.868	-0.508	0.007	0.457	0.012	64.4	CB
	2015.896	-0.518	0.007	0.324	0.011	52.3	CC
	2016.153	-1.134	0.004	-1.245	0.005	85.0	CD
	2016.224	-1.253	0.005	-1.633	0.009	70.0	CE
	2016.292	-1.420	0.009	-1.970	0.016	41.5	CF
	2016.399	-1.744	0.007	-2.665	0.009	75.7	CG
J1856 + 0610	2015.184	2.175	0.004	4.655	0.006	109.5	C1
	2015.236	2.005	0.006	4.383	0.010	119.7	C2
	2015.301	1.852	0.007	4.027	0.009	122.4	C3
	2015.367	1.685	0.008	3.657	0.012	97.5	C4
	2015.660	0.684	0.010	1.890	0.013	98.0	C5
	2015.701	0.727	0.008	1.744	0.011	118.3	C6
	2015.742	0.561	0.006	1.571	0.007	155.1	C7
	2015.773	0.490	0.007	1.334	0.011	132.2	C8
	2015.814	0.356	0.005	1.149	0.007	164.6	C9
	2015.838	0.241	0.005	1.089	0.007	157.0	CA
	2015.868	0.190	0.005	0.828	0.009	175.6	CB
	2015.896	0.146	0.005	0.736	0.008	137.2	CC
	2016.153	-0.393	0.004	-0.742	0.005	189.4	CD
	2016.224	-0.596	0.004	-1.071	0.007	148.2	CE
	2016.292	-0.751	0.009	-1.459	0.013	89.1	CF
	2016.399	-1.128	0.007	-2.017	0.008	132.8	CG

## A.2. ADDITIONAL TABLES

**Table A.4:** Final astrometric values for G060.57–0.18

QSO	Epoch (yr)	X offset (mas)	$\sigma_x$ (mas)	Y offset (mas)	$\sigma_y$ (mas)	Flux (mJy)	Experiment
							BR210
J1946 + 2418	2015.164	7.001	0.005	4.295	0.007	23.9	F1
	2015.238	6.832	0.007	3.924	0.011	30.0	F2
	2015.307	6.620	0.005	3.466	0.008	23.0	F3
	2015.384	6.323	0.007	3.190	0.010	21.5	F4
	2015.658	5.288	0.007	1.627	0.011	28.4	F5
	2015.693	5.169	0.007	1.368	0.010	23.3	F6
	2015.723	5.024	0.004	1.220	0.005	21.7	F7
	2015.756	4.853	0.004	0.972	0.005	28.8	F8
	2015.792	4.722	0.005	0.857	0.007	22.7	F9
	2015.822	4.713	0.008	0.640	0.010	32.5	FA
	2015.849	4.643	0.006	0.384	0.010	29.3	FB
	2015.877	4.480	0.010	0.183	0.013	25.4	FC
	2016.156	3.865	0.006	-1.407	0.010	22.2	FD
	2016.232	3.564	0.007	-1.732	0.012	23.4	FE
	2016.298	3.440	0.005	-2.194	0.007	31.2	FF
	2016.402	2.992	0.004	-2.671	0.006	21.8	FG
J1949 + 2421	2015.164	0.698	0.006	2.117	0.009	103.1	F1
	2015.238	0.397	0.005	1.717	0.008	161.7	F2
	2015.307	0.288	0.005	1.372	0.008	131.4	F3
	2015.384	0.005	0.007	0.987	0.010	116.7	F4
	2015.658	-0.999	0.006	-0.448	0.010	136.8	F5
	2015.693	-1.184	0.006	-0.709	0.010	114.9	F6
	2015.723	-1.335	0.002	-0.922	0.004	105.5	F7
	2015.756	-1.425	0.003	-1.134	0.004	140.5	F8
	2015.792	-1.577	0.006	-1.285	0.010	107.7	F9
	2015.822	-1.665	0.006	-1.531	0.008	181.3	FA
	2015.849	-1.725	0.006	-1.705	0.010	136.8	FB
	2015.877	-1.873	0.008	-1.878	0.011	115.2	FC
	2016.156	-2.471	0.004	-3.497	0.008	125.9	FD
	2016.232	-2.697	0.006	-3.896	0.011	122.7	FE
	2016.298	-3.030	0.005	-4.243	0.008	141.0	FF
	2016.402	-3.244	0.006	-4.695	0.010	124.4	FG

## A.2. ADDITIONAL TABLES

**Table A.5:** Final astrometric values for G070.29+1.60

QSO	Epoch (yr)	X offset (mas)	$\sigma_x$ (mas)	Y offset (mas)	$\sigma_y$ (mas)	Flux (Jy)	Experiment
							BR210
J1957 + 3338	2015.359	0.878	0.023	1.899	0.035	0.207	D3
	2015.740	0.130	0.003	0.685	0.004	1.593	D6
	2015.770	0.062	0.002	0.594	0.006	1.085	D7
	2015.797	0.004	0.002	0.414	0.004	1.566	D8
	2015.836	-0.077	0.004	0.140	0.004	2.142	D9
	2015.863	-0.156	0.003	0.022	0.003	2.355	DA
	2015.890	-0.133	0.003	-0.077	0.003	2.378	DB
	2015.923	-0.193	0.002	-0.188	0.004	2.156	DC
	2016.260	-0.475	0.003	-1.427	0.004	1.710	DE
	2016.344	-0.577	0.010	-1.660	0.027	0.555	DF
	2016.404	-0.730	0.006	-1.798	0.009	0.874	DG
J2001 + 3323	2015.359	-0.293	0.016	1.489	0.024	0.211	D3
	2015.740	-0.863	0.004	0.211	0.006	1.331	D6
	2015.770	-1.008	0.004	0.125	0.009	0.945	D7
	2015.797	-0.986	0.010	-0.034	0.013	0.745	D8
	2015.836	-1.150	0.004	-0.198	0.005	1.819	D9
	2015.863	-1.113	0.005	-0.332	0.006	2.112	DA
	2015.890	-1.144	0.003	-0.400	0.003	1.921	DB
	2015.923	-1.201	0.002	-0.589	0.004	1.862	DC
	2016.260	-1.498	0.003	-1.827	0.006	1.297	DE
	2016.344	-1.642	0.012	-2.113	0.017	0.891	DF
	2016.404	-1.787	0.011	-2.192	0.011	0.745	DG





# MASER COMPACTNESS

## B.1 Maser Compactness Tables

**Table B.1:** First target masers as determined by this survey. **Columns:** (1) Source name in galactic coordinates, maser spot LSR in  $\text{km s}^{-1}$ , flux density of core component with uncertainty in Jy, flux density of halo component and uncertainty in Jy, angular size of halo component with uncertainty in mas, equivalent Chi-Squared for fit and degrees of freedom for fit

N	Name	RA (J2000) hh:mm:ss	DEC (J2000) dd:mm:ss	V ( $\text{km s}^{-1}$ )	$S_0$ (Jy)	Grade	$D_{\text{near}}$ (kpc)	$D_{\text{far}}$ (kpc)	$D_{\text{outer}}$ (kpc)
1	$192.600 - 0.048$	06 : 12 : 53.99	+17 : 59 : 23.7	+5.90 +5.20	291.7 144.4	A			0.76
2	$232.620 + 0.996$	07 : 32 : 09.79	-16 : 58 : 12.4	+22.89	157.7	A			1.72
3	$287.371 + 0.644$	10 : 48 : 04.44	-58 : 27 : 01.0	-1.89	83.4	A			5.18
4	$291.274 - 0.709$	11 : 11 : 53.35	-61 : 18 : 23.7	-30.69	42.0	A	2.62	3.85	
5	$299.772 - 0.005$	12 : 23 : 48.97	-62 : 42 : 25.3	-6.68	22.6	A			8.14
6	$309.921 + 0.479$	13 : 50 : 41.78	-61 : 35 : 10.2	-57.85 -58.46 -58.81 -59.69	102.5 244.5 161.1 447.3	A	4.22	6.85	
7	$318.050 + 0.087$	14 : 53 : 42.67	-59 : 08 : 52.4	-51.47	12.1	A	2.97	9.77	
8	$323.740 - 0.263$	15 : 31 : 45.45	-56 : 30 : 50.1	-47.93 -48.46 -48.98 -50.39 -51.18 -52.41 -49.34	118.3 552.2 743.8 2412.8 1123.0 69.4 815.0	A A A A A A A	2.91	10.84	
9	$326.475 + 0.703$	15 : 43 : 16.64	-54 : 07 : 14.6	-38.43	64.1	A	2.25	11.94	
10	$327.402 + 0.445$	15 : 49 : 19.50	-53 : 45 : 13.9	-81.76 -82.02 -82.90 -83.25	18.8 33.3 72.3 37.6	A A A A	4.72	9.61	
11	$328.237 - 0.547$	15 : 57 : 58.28	-53 : 59 : 22.7	-44.48 -44.74	778.3 676.6	A A	2.68	11.77	
12	$328.254 - 0.532$	15 : 57 : 59.75	-53 : 58 : 00.4	-36.83	90.1	A	2.25	12.21	

Continued on Next Page...

## B.1. MASER COMPACTNESS TABLES

**Table B.1 – Continued...**

N	Name	RA (J2000) hh:mm:ss	DEC (J2000) dd:mm:ss	V (km s <sup>-1</sup> )	S <sub>0</sub> (Jy)	Grade	D <sub>near</sub> (kpc)	D <sub>far</sub> (kpc)	D <sub>outer</sub> (kpc)
13	329.029 – 0.205	16 : 00 : 31.80	–53 : 12 : 49.6	–36.12	50.0	A	2.25	12.32	
14	332.295 + 2.280	16 : 05 : 41.72	–49 : 11 : 30.3	–23.67	79.0	A	1.51	13.50	
				–24.02	117.7	A			
15	337.920 – 0.456	16 : 41 : 06.05	–47 : 07 : 02.5	–38.62	34.5	A	2.84	12.82	
16	339.622 – 0.121	16 : 46 : 05.99	–45 : 36 : 43.3	–33.16	31.0	A	2.85	12.98	
16	339.884 – 1.259	16 : 52 : 04.67	–46 : 08 : 34.2	–34.84	306.6	A	3.07	12.78	
				–35.63	858.9	A			
				–36.51	309.1	A			
				–37.39	523.5	A			
17	345.010 + 1.792	16 : 56 : 47.58	–40 : 14 : 25.8	–17.02	132.1	A	2.47	13.79	
				–17.46	82.8	A			
				–20.18	121.4	A			
				–21.76	277.4	A			
				–22.03	299.1	A			
18	345.505 + 0.348	17 : 04 : 22.91	–40 : 44 : 21.7	–14.06	242.3	A	2.06	14.24	
				–19.06	190.8	A			
19	348.550 – 0.979	17 : 19 : 20.41	–39 : 03 : 51.6	–10.41	29.3	A	1.58	14.88	
20	351.417 + 0.645	17 : 20 : 53.37	–35 : 47 : 01.2	–9.71	621.2	A	2.18	14.41	
				–10.32	1597.3	A			
21	352.630 – 1.067	17 : 31 : 13.91	–35 : 44 : 08.7	–2.91	134.8	A	0.59	16.03	
				–3.27	127.8	A			
22	263.250 + 0.514	08 : 48 : 47.84	–42 : 54 : 28.3	+12.35	46.9	B			2.11
23	188.946 + 0.886	06 : 08 : 53.32	+21 : 38 : 29.1	+10.85	602.9	B			2.98
24	305.200 + 0.019	13 : 11 : 16.93	–62 : 45 : 55.1	–32.04	39.7	B	1.77	8.23	
				–33.09	37.3	B			
25	310.144 + 0.760	13 : 51 : 58.43	–61 : 15 : 41.3	–55.89	36.9	B	3.67	7.45	
26	313.577 + 0.325	14 : 20 : 08.58	–60 : 42 : 00.8	–47.80	67.9	B	2.77	9.08	
27	314.320 + 0.112	14 : 26 : 26.20	–60 : 38 : 31.3	–43.42	34.9	B	2.43	9.57	
				–43.69	19.2	B			
28	316.359 – 0.362	14 : 43 : 11.20	–60 : 17 : 13.3	+3.38	65.3	B			12.65
29	316.811 – 0.057	14 : 45 : 26.43	–59 : 49 : 16.3	–45.61	46.6	B	2.57	9.93	
30	318.948 – 0.196	15 : 00 : 55.40	–58 : 58 : 52.1	–34.63	435.3	B	1.83	11.08	
				–36.30	63.1	B			
31	320.231 – 0.284	15 : 09 : 51.94	–58 : 25 : 38.5	–62.28	49.7	B	3.65	9.49	
32	322.158 + 0.636	15 : 18 : 34.64	–56 : 38 : 25.3	–54.51	58.6	B	3.65	9.83	
				–62.94	166.0	B			
				–63.29	115.5	B			
				–64.08	125.0	B			
33	323.459 – 0.079	15 : 29 : 19.33	–56 : 31 : 22.8	–67.15	112.1	B	3.87	9.83	
				–68.29	189.0	B			
				–68.99	204.5	B			
				–69.26	326.5	B			
				–70.48	59.1	B			
				–66.98	121.6	B			
34	328.808 + 0.633	15 : 55 : 48.45	–52 : 43 : 06.6	–44.40	251.8	B	2.66	11.87	
				–45.10	63.3	B			
				–46.24	154.0	B			
				–46.59	78.3	B			
35	329.339 + 0.148	16 : 00 : 33.13	–52 : 44 : 39.8	–106.28	19.9	B	6.05	8.56	
36	329.407 – 0.459	16 : 03 : 32.65	–53 : 09 : 26.9	–66.64	76.2	B	3.92	10.70	
37	331.342 – 0.346	16 : 12 : 26.45	–51 : 46 : 16.4	–67.08	19.9	B	3.90	10.99	
38	333.562 – 0.025	16 : 21 : 08.80	–49 : 59 : 48.0	–35.30	32.9	B	2.36	12.81	
39	335.789 + 0.174	16 : 29 : 47.33	–48 : 15 : 51.7	–47.39	303.6	B	3.23	12.20	
				–48.53	199.2	B			
40	338.561 + 0.218	16 : 40 : 37.96	–46 : 11 : 25.8	–39.05	31.3	B	2.98	12.75	
41	338.925 + 0.634	16 : 40 : 13.56	–45 : 38 : 33.2	–58.99	25.5	B	4.16	11.60	

Continued on Next Page...

## B.1. MASER COMPACTNESS TABLES

**Table B.1** – Continued...

N	Name	RA (J2000) hh:mm:ss	DEC (J2000) dd:mm:ss	V (km s <sup>-1</sup> )	S <sub>0</sub> (Jy)	Grade	D <sub>near</sub> (kpc)	D <sub>far</sub> (kpc)	D <sub>outer</sub> (kpc)
42	338.920 + 0.550	16 : 40 : 34.01	-45 : 42 : 07.1	-60.75	51.8	B			
43	338.935 - 0.062	16 : 43 : 16.01	-46 : 05 : 40.2	-61.29	50.8	B	4.18	11.58	
44	340.054 - 0.244	16 : 48 : 13.89	-45 : 21 : 43.5	-41.87	32.9	B	3.17	12.59	
				-59.36	38.7	B	4.21	11.66	
				-60.86	23.3	B			
45	340.785 - 0.096	16 : 50 : 14.84	-44 : 42 : 26.3	-108.02	764.9	B	5.94	9.99	
46	341.218 - 0.212	16 : 52 : 17.86	-44 : 26 : 52.3	-44.42	539.1	B	3.16	12.81	
47	348.617 - 1.162	17 : 20 : 18.65	-39 : 06 : 50.8	-11.47	38.9	B	1.72	14.75	
48	348.703 - 1.043	17 : 20 : 04.06	-38 : 58 : 30.9	-3.40	42.0	B	0.24	16.23	
				-7.36	84.6	B			
				-9.90	47.6	B			
50	354.615 + 0.472	17 : 30 : 17.13	-33 : 13 : 55.1	-24.21	164.4	B			
51	358.460 - 0.391	17 : 43 : 26.76	-30 : 27 : 11.3	+1.26	48.0	B	4.07	12.63	
52	359.615 - 0.243	17 : 45 : 39.09	-29 : 23 : 30.0	+24.50	26.4	B			
				+19.58	59.3	B			

## B.1. MASER COMPACTNESS TABLES

**Table B.2:** Determined parameters for detected maser spots. **Columns:** (1) Source name in galactic coordinates; (2) maser spot LSR (km/s); (3) flux density of core component with uncertainty (Jy); (4) flux density of halo component and uncertainty (Jy); angular size of halo component with uncertainty (mas), equivalent Chi-Squared for fit and degrees of freedom for fit

Name	$\alpha_{\text{J2000}}$ hh:mm:ss	$\delta_{\text{J2000}}$ dd:mm:ss	$V$ (km s $^{-1}$ )	$S_H$ (Jy)	$\theta_H$ (mas)	$S_C$ (Jy)	$\theta_C$ (mas)	Error (Jy)	DF (N-4)	Grade
192.600 - 0.048	06 : 12 : 53.99	+17 : 59 : 23.7	5.90	246	40.0	46	1.5	5	38	A
192.600 - 0.048	06 : 12 : 53.99	+17 : 59 : 23.7	5.20	70	7.3	74	1.6	12	38	A
196.454 - 1.677	06 : 14 : 37.03	+13 : 49 : 36.6	14.73	14	48.2	7	1.2	3	56	C
232.620 + 0.996	07 : 32 : 09.79	-16 : 58 : 12.4	22.89	50	21.3	108	2.0	7	32	A
263.250 + 0.514	08 : 48 : 47.84	-42 : 54 : 28.3	12.35	21	143.6	26	2.4	6	23	C
188.946 + 0.886	06 : 08 : 53.32	+21 : 38 : 29.1	10.85	482	7.0	121	2.7	31	15	B
287.371 + 0.644	10 : 48 : 04.44	-58 : 27 : 01.0	-1.89	59	13.4	25	0.5	14	47	A
291.274 - 0.709	11 : 11 : 53.35	-61 : 18 : 23.7	-30.69	31	20.4	11	0.0	6	28	B
298.262 + 0.739	12 : 11 : 47.65	-61 : 46 : 20.9	-30.13	8	18.8	2	0.0	2	38	D
298.262 + 0.739	12 : 11 : 47.65	-61 : 46 : 20.9	-29.86	5	22.9	3	0.9	1	16	D
299.772 - 0.005	12 : 23 : 48.97	-62 : 42 : 25.3	-6.68	9	2.3	13	0.5	3	48	A
305.199 + 0.005	13 : 11 : 17.20	-62 : 46 : 46.0	-32.04	31	3.6	9	0.0	5	20	B
305.199 + 0.005	13 : 11 : 17.20	-62 : 46 : 46.0	-33.09	12	31.1	25	1.8	3	20	B
305.208 + 0.206	13 : 11 : 13.71	-62 : 34 : 41.4	-44.04	43	7.5	10	1.2	7	26	C
308.754 + 0.549	13 : 40 : 57.60	-61 : 45 : 43.4	-39.21	3	3.6	0	3.6	2	4	D
308.754 + 0.549	13 : 40 : 57.60	-61 : 45 : 43.4	-45.27	6	6.6	2	0.0	3	16	D
308.918 + 0.123	13 : 43 : 01.85	-62 : 08 : 52.2	-54.25	28	49.9	4	1.9	2	32	D
308.918 + 0.123	13 : 43 : 01.85	-62 : 08 : 52.2	-54.60	19	9.9	3	0.9	2	32	D
308.918 + 0.123	13 : 43 : 01.85	-62 : 08 : 52.2	-54.78	20	8.9	3	0.7	1	32	D
309.901 + 0.231	13 : 51 : 01.05	-61 : 49 : 56.0	-54.29	3	7.1	5	1.1	2	4	D
309.921 + 0.479	13 : 50 : 41.78	-61 : 35 : 10.2	-57.85	43	8.7	59	0.2	13	32	A
309.921 + 0.479	13 : 50 : 41.78	-61 : 35 : 10.2	-58.46	120	78.8	125	1.8	48	32	A
309.921 + 0.479	13 : 50 : 41.78	-61 : 35 : 10.2	-58.81	55	13.3	106	0.5	17	32	A
309.921 + 0.479	13 : 50 : 41.78	-61 : 35 : 10.2	-59.69	391	3.0	56	0.0	113	32	A
310.144 + 0.760	13 : 51 : 58.43	-61 : 15 : 41.3	-55.89	19	33.9	18	1.7	5	32	C
312.071 + 0.082	14 : 08 : 58.20	-61 : 24 : 23.8	-34.18	25	6.3	1	0.0	1	8	D
312.071 + 0.082	14 : 08 : 58.20	-61 : 24 : 23.8	-34.80	2	6.0	33	6.0	2	8	D
312.108 + 0.262	14 : 08 : 49.31	-61 : 13 : 25.1	-49.94	11	4.9	5	1.6	2	20	D
312.598 + 0.045	14 : 13 : 15.03	-61 : 16 : 53.6	-67.78	9	7.3	3	0.9	1	20	D
313.469 + 0.190	14 : 19 : 40.94	-60 : 51 : 47.3	-9.44	28	7.2	9	1.7	6	20	C
313.469 + 0.190	14 : 19 : 40.94	-60 : 51 : 47.3	-11.81	12	29.7	10	1.9	3	20	C
313.577 + 0.325	14 : 20 : 08.58	-60 : 42 : 00.8	-47.80	32	7.3	36	1.8	4	32	B
314.320 + 0.112	14 : 26 : 26.20	-60 : 38 : 31.3	-43.42	19	5.2	16	1.1	4	20	B
316.412 - 0.308	14 : 43 : 23.34	-60 : 13 : 09.9	-3.38	42	3.0	23	1.4	12	32	B
316.640 - 0.087	14 : 44 : 18.45	-59 : 55 : 11.5	-20.36	109	57.1	3	0.0	3	32	D
316.640 - 0.087	14 : 44 : 18.45	-59 : 55 : 11.5	-19.77	67	40.5	3	0.0	1	8	D
316.640 - 0.087	14 : 44 : 18.45	-59 : 55 : 11.5	-19.95	62	16.3	3	1.2	1	8	D
316.811 - 0.057	14 : 45 : 26.43	-59 : 49 : 16.3	-22.23	49	73.1	3	1.3	1	8	D
317.466 - 0.402	14 : 51 : 19.69	-59 : 50 : 50.7	-38.87	10	6.9	8	0.0	8	20	C
317.466 - 0.402	14 : 51 : 19.69	-59 : 50 : 50.7	-39.57	14	5.9	9	0.0	11	20	C
317.701 + 0.110	14 : 51 : 11.69	-59 : 17 : 02.1	-42.15	9	4.2	5	0.0	6	12	C
318.050 + 0.087	14 : 53 : 42.67	-59 : 08 : 52.4	-51.47	2	4.1	10	0.0	3	22	B
318.948 - 0.196	15 : 00 : 55.40	-58 : 58 : 52.1	-34.63	356	9.0	79	2.2	40	32	B
318.948 - 0.196	15 : 00 : 55.40	-58 : 58 : 52.1	-36.30	31	34.8	32	1.9	12	32	B
320.231 - 0.284	15 : 09 : 51.94	-58 : 25 : 38.5	-62.28	29	9.9	21	1.3	7	32	B
321.033 - 0.483	15 : 15 : 52.63	-58 : 11 : 07.7	-60.88	12	3.4	0	3.4	5	8	D
321.033 - 0.483	15 : 15 : 52.63	-58 : 11 : 07.7	-61.23	10	4.0	0	3.2	4	8	D
322.158 + 0.636	15 : 18 : 34.64	-56 : 38 : 25.3	-62.94	107	11.7	59	2.5	16	29	B
322.158 + 0.636	15 : 18 : 34.64	-56 : 38 : 25.3	-63.29	79	50.4	37	2.8	10	29	B
322.158 + 0.636	15 : 18 : 34.64	-56 : 38 : 25.3	-64.08	74	54.7	51	2.8	13	29	B
323.459 - 0.079	15 : 29 : 19.33	-56 : 31 : 22.8	-67.15	70	67.2	42	2.2	9	20	B
323.459 - 0.079	15 : 29 : 19.33	-56 : 31 : 22.8	-68.29	124	8.3	65	1.9	25	32	B
323.459 - 0.079	15 : 29 : 19.33	-56 : 31 : 22.8	-68.99	112	9.7	92	3.3	12	32	B
323.459 - 0.079	15 : 29 : 19.33	-56 : 31 : 22.8	-69.26	227	81.6	100	3.8	15	32	B
323.459 - 0.079	15 : 29 : 19.33	-56 : 31 : 22.8	-70.48	33	8.3	26	1.8	10	32	B
323.459 - 0.079	15 : 29 : 19.33	-56 : 31 : 22.8	-66.98	83	9.5	39	2.1	12	8	B
323.740 - 0.263	15 : 31 : 45.45	-56 : 30 : 50.1	-47.93	83	11.0	35	1.5	16	26	A
323.740 - 0.263	15 : 31 : 45.45	-56 : 30 : 50.1	-48.46	337	8.7	215	1.9	74	26	A
323.740 - 0.263	15 : 31 : 45.45	-56 : 30 : 50.1	-48.98	640	93.4	104	1.3	30	26	A
323.740 - 0.263	15 : 31 : 45.45	-56 : 30 : 50.1	-50.39	1420	3.7	993	1.7	237	26	A
323.740 - 0.263	15 : 31 : 45.45	-56 : 30 : 50.1	-51.18	975	7.8	148	0.0	106	26	A
323.740 - 0.263	15 : 31 : 45.45	-56 : 30 : 50.1	-52.41	47	10.2	22	1.1	8	14	A
323.740 - 0.263	15 : 31 : 45.45	-56 : 30 : 50.1	-49.34	717	149.5	98	2.0	32	8	A
326.475 + 0.703	15 : 43 : 16.64	-54 : 07 : 14.6	-38.43	38	52.8	26	1.1	5	14	A
326.641 + 0.611	15 : 44 : 33.33	-54 : 05 : 31.5	-42.64	6	43.4	11	3.1	2	14	D
326.859 - 0.677	15 : 51 : 14.19	-54 : 58 : 04.8	-58.03	18	8.9	2	0.0	2	20	D
327.120 + 0.511	15 : 47 : 32.73	-53 : 52 : 38.4	-83.60	7	6.0	2	0.0	1	20	D
327.120 + 0.511	15 : 47 : 32.73	-53 : 52 : 38.4	-87.03	15	5.2	2	0.0	4	20	D
327.402 + 0.445	15 : 49 : 19.50	-53 : 45 : 13.9	-81.76	8	0.8	11	0.8	4	10	A
327.402 + 0.445	15 : 49 : 19.50	-53 : 45 : 13.9	-82.90	31	54.3	42	0.0	9	22	A
327.402 + 0.445	15 : 49 : 19.50	-53 : 45 : 13.9	-83.25	13	16.6	24	0.7	6	22	A
328.237 - 0.547	15 : 57 : 58.28	-53 : 59 : 22.7	-44.48	475	37.4	304	2.1	36	22	A
328.237 - 0.547	15 : 57 : 58.28	-53 : 59 : 22.7	-44.74	482	25.6	194	1.7	37	22	A
328.254 - 0.532	15 : 57 : 59.75	-53 : 58 : 00.4	-36.83	57	9.0	33	0.9	13	23	A
328.809 + 0.633	15 : 55 : 48.70	-52 : 43 : 05.5	-44.40	151	9.4	101	2.3	27	34	B
328.809 + 0.633	15 : 55 : 48.70	-52 : 43 : 05.5	-45.10	30	28.9	33	2.5	6	34	B
328.809 + 0.633	15 : 55 : 48.70	-52 : 43 : 05.5	-46.24	126	29.1	28	1.7	12	34	B
329.031 - 0.198	16 : 00 : 30.32	-53 : 12 : 27.3	-35.06	15	5.3	18	1.2	9	28	B
329.031 - 0.198	16 : 00 : 30.32	-53 : 12 : 27.3	-36.12	35	18.6	15	0.8	12	16	B
329.031 - 0.198	16 : 00 : 30.32	-53 : 12 : 27.3	-37.17	25	5.0	16	1.0	12	28	B

Continued on Next Page...

## B.1. MASER COMPACTNESS TABLES

**Table B.2 – Continued...**

Name	$\alpha_{\text{J2000}}$ hh:mm:ss	$\delta_{\text{J2000}}$ dd:mm:ss	$V$ (km s $^{-1}$ )	$S_H$ (Jy)	$\theta_H$ (mas)	$S_C$ (Jy)	$\theta_C$ (mas)	Error (Jy)	DF (N-4)	Grade
329.339 + 0.148	16 : 00 : 33.13	-52 : 44 : 39.8	-106.28	9	5.9	11	0.7	3	22	C
329.407 - 0.459	16 : 03 : 32.65	-53 : 09 : 26.9	-66.64	47	21.7	29	1.6	8	34	B
331.278 - 0.188	16 : 11 : 26.59	-51 : 41 : 56.7	-77.63	30	10.8	15	2.8	2	22	D
331.278 - 0.188	16 : 11 : 26.59	-51 : 41 : 56.7	-77.98	55	6.2	5	2.2	2	34	D
331.278 - 0.188	16 : 11 : 26.59	-51 : 41 : 56.7	-78.16	35	12.5	19	3.4	2	22	D
331.278 - 0.188	16 : 11 : 26.59	-51 : 41 : 56.7	-78.77	37	13.2	18	3.3	2	22	D
331.278 - 0.188	16 : 11 : 26.59	-51 : 41 : 56.7	-83.25	25	3.7	1	0.0	2	22	D
331.278 - 0.188	16 : 11 : 26.59	-51 : 41 : 56.7	-84.31	15	3.3	1	0.0	2	22	D
331.278 - 0.188	16 : 11 : 26.59	-51 : 41 : 56.7	-85.09	17	14.1	14	3.4	2	22	D
331.342 - 0.346	16 : 12 : 26.45	-51 : 46 : 16.4	-67.08	13	2.2	7	0.0	11	26	C
331.442 - 0.187	16 : 12 : 12.49	-51 : 35 : 10.1	-88.72	11	19.3	7	1.1	5	20	C
332.295 + 2.280	16 : 05 : 41.72	-49 : 11 : 30.3	-23.67	56	28.0	23	1.2	7	40	A
333.315 + 0.105	16 : 19 : 29.01	-50 : 04 : 41.3	-43.86	5	0.7	1	0.7	3	36	D
333.466 - 0.164	16 : 21 : 20.18	-50 : 09 : 48.6	-41.96	8	1.4	2	1.4	2	36	D
333.562 - 0.025	16 : 21 : 08.80	-49 : 59 : 48.0	-35.30	15	4.8	18	1.1	7	48	B
333.646 + 0.058	16 : 21 : 09.14	-49 : 52 : 45.9	-87.39	4	6.9	4	0.0	6	18	D
333.900 - 0.099	16 : 22 : 57.39	-49 : 48 : 35.1	-36.94	9	4.3	2	1.0	2	36	D
334.635 - 0.015	16 : 25 : 45.73	-49 : 13 : 37.4	-29.13	15	4.4	2	0.0	2	36	D
334.635 - 0.015	16 : 25 : 45.73	-49 : 13 : 37.4	-30.18	14	4.3	2	0.0	2	36	D
335.060 - 0.427	16 : 29 : 23.13	-49 : 12 : 27.1	-46.93	28	15.3	18	4.2	4	42	D
335.585 - 0.285	16 : 30 : 57.28	-48 : 43 : 39.7	-43.88	21	3.6	2	0.4	3	36	D
335.585 - 0.285	16 : 30 : 57.28	-48 : 43 : 39.7	-48.19	10	5.2	2	0.0	2	36	D
335.585 - 0.285	16 : 30 : 57.28	-48 : 43 : 39.7	-48.62	7	5.8	3	1.2	1	36	D
335.585 - 0.285	16 : 30 : 57.28	-48 : 43 : 39.7	-51.43	63	24.9	5	1.9	6	36	D
335.789 + 0.174	16 : 29 : 47.33	-48 : 15 : 51.7	-47.39	209	48.1	95	4.1	25	42	B
336.018 - 0.827	16 : 35 : 09.26	-48 : 46 : 47.4	-41.34	101	20.6	6	2.7	6	36	D
336.018 - 0.827	16 : 35 : 09.26	-48 : 46 : 47.4	-45.11	27	17.8	2	0.0	2	36	D
336.018 - 0.827	16 : 35 : 09.26	-48 : 46 : 47.4	-47.83	44	15.2	4	1.7	2	36	D
336.018 - 0.827	16 : 35 : 09.26	-48 : 46 : 47.4	-53.28	55	11.7	3	1.2	2	36	D
336.994 - 0.027	16 : 35 : 33.98	-47 : 31 : 12.0	-120.47	13	18.0	3	0.0	3	8	D
336.994 - 0.027	16 : 35 : 33.98	-47 : 31 : 12.0	-125.74	25	16.6	3	0.0	2	24	D
337.052 - 0.226	16 : 36 : 40.17	-47 : 36 : 38.4	-77.19	7	19.4	4	1.8	1	8	D
337.052 - 0.226	16 : 36 : 40.17	-47 : 36 : 38.4	-77.54	8	30.0	3	1.7	1	8	D
337.153 - 0.395	16 : 37 : 48.86	-47 : 38 : 56.5	-49.32	12	5.0	4	0.6	3	48	D
337.404 - 0.402	16 : 38 : 50.52	-47 : 28 : 00.2	-39.70	50	30.2	7	2.2	2	48	D
337.388 - 0.210	16 : 37 : 56.01	-47 : 21 : 01.2	-55.92	23	25.4	6	2.3	2	48	D
337.705 - 0.053	16 : 38 : 29.63	-47 : 00 : 35.5	-50.19	80	21.4	6	2.5	2	48	D
337.705 - 0.053	16 : 38 : 29.63	-47 : 00 : 35.5	-51.07	29	27.8	2	0.0	1	8	D
337.705 - 0.053	16 : 38 : 29.63	-47 : 00 : 35.5	-52.74	46	128.9	18	5.5	2	48	D
337.705 - 0.053	16 : 38 : 29.63	-47 : 00 : 35.5	-53.26	25	24.9	3	1.7	1	8	D
337.705 - 0.053	16 : 38 : 29.63	-47 : 00 : 35.5	-53.62	18	18.7	2	0.0	1	8	D
337.705 - 0.053	16 : 38 : 29.63	-47 : 00 : 35.5	-54.58	66	21.6	67	6.1	4	48	D
337.920 - 0.456	16 : 41 : 06.05	-47 : 07 : 02.5	-38.62	12	6.2	23	1.0	6	48	A
338.287 + 0.120	16 : 40 : 00.13	-46 : 27 : 37.1	-40.01	5	4.2	7	1.9	2	38	D
338.396 - 0.007	16 : 40 : 58.41	-46 : 27 : 47.8	-30.10	27	5.6	2	0.0	2	48	D
338.497 + 0.207	16 : 40 : 25.89	-46 : 14 : 43.5	-49.35	17	6.2	2	0.7	2	48	D
338.497 + 0.207	16 : 40 : 25.89	-46 : 14 : 43.5	-49.79	27	12.3	21	4.0	3	48	D
338.497 + 0.207	16 : 40 : 25.89	-46 : 14 : 43.5	-51.81	30	5.0	2	0.0	10	48	D
338.497 + 0.207	16 : 40 : 25.89	-46 : 14 : 43.5	-52.43	45	5.7	1	0.0	7	48	D
338.497 + 0.207	16 : 40 : 25.89	-46 : 14 : 43.5	-52.95	30	20.6	3	2.0	1	8	D
338.497 + 0.207	16 : 40 : 25.89	-46 : 14 : 43.5	-54.62	13	16.9	4	2.3	1	8	D
338.497 + 0.207	16 : 40 : 25.89	-46 : 14 : 43.5	-62.79	5	8.0	3	0.7	2	8	D
338.561 + 0.218	16 : 40 : 37.96	-46 : 11 : 25.8	-39.05	16	4.1	15	1.9	3	56	C
338.925 + 0.634	16 : 40 : 13.56	-45 : 38 : 33.2	-58.99	9	3.5	17	1.3	3	48	B
338.920 + 0.550	16 : 40 : 34.01	-45 : 42 : 07.1	-61.29	29	18.3	22	1.3	5	40	B
338.935 - 0.062	16 : 43 : 16.01	-46 : 05 : 40.2	-41.87	17	3.3	16	1.5	4	48	B
339.053 - 0.315	16 : 44 : 48.99	-46 : 10 : 13.0	-111.63	143	14.0	5	0.5	4	56	D
339.053 - 0.315	16 : 44 : 48.99	-46 : 10 : 13.0	-111.81	148	13.9	4	0.5	3	56	D
339.053 - 0.315	16 : 44 : 48.99	-46 : 10 : 13.0	-111.05	33	16.5	5	0.5	6	36	D
339.622 - 0.121	16 : 46 : 05.99	-45 : 36 : 43.3	-33.16	18	1.0	14	0.0	3	48	A
339.681 - 1.208	16 : 51 : 06.21	-46 : 16 : 02.9	-21.42	40	14.8	9	1.8	6	48	D
339.681 - 1.208	16 : 51 : 06.21	-46 : 16 : 02.9	-22.21	34	16.4	5	1.9	2	48	D
339.681 - 1.208	16 : 51 : 06.21	-46 : 16 : 02.9	-34.33	24	5.7	2	0.0	3	48	D
339.681 - 1.208	16 : 51 : 06.21	-46 : 16 : 02.9	-37.52	5	3.9	7	1.6	2	28	D
339.884 - 1.259	16 : 52 : 04.67	-46 : 08 : 34.2	-34.84	190	5.8	117	1.6	47	56	A
339.884 - 1.259	16 : 52 : 04.67	-46 : 08 : 34.2	-35.63	334	29.3	525	0.6	40	56	A
339.884 - 1.259	16 : 52 : 04.67	-46 : 08 : 34.2	-36.51	228	5.0	81	1.0	28	56	A
339.884 - 1.259	16 : 52 : 04.67	-46 : 08 : 34.2	-37.39	197	4.5	326	1.1	58	56	A
339.949 - 0.539	16 : 49 : 07.97	-45 : 37 : 58.8	-91.07	38	4.7	3	4.7	4	46	D
339.949 - 0.539	16 : 49 : 07.97	-45 : 37 : 58.8	-91.51	38	4.2	3	4.2	2	46	D
339.949 - 0.539	16 : 49 : 07.97	-45 : 37 : 58.8	-96.51	9	22.0	25	4.4	2	46	D
339.949 - 0.539	16 : 49 : 07.97	-45 : 37 : 58.8	-97.39	31	20.1	3	2.7	1	14	D
339.949 - 0.539	16 : 49 : 07.97	-45 : 37 : 58.8	-97.83	41	34.2	12	3.6	3	46	D
339.949 - 0.539	16 : 49 : 07.97	-45 : 37 : 58.8	-100.46	22	15.2	17	3.4	2	46	D
339.949 - 0.539	16 : 49 : 07.97	-45 : 37 : 58.8	-103.88	12	3.1	3	3.1	2	46	D
339.949 - 0.539	16 : 49 : 07.97	-45 : 37 : 58.8	-91.98	9	3.7	3	3.7	2	28	D
339.949 - 0.539	16 : 49 : 07.97	-45 : 37 : 58.8	-97.25	26	25.9	8	4.0	1	28	D
339.986 - 0.425	16 : 48 : 46.31	-45 : 31 : 51.3	-87.70	31	20.0	2	0.0	1	56	D
339.986 - 0.425	16 : 48 : 46.31	-45 : 31 : 51.3	-88.49	27	113.3	46	6.3	3	56	D
339.986 - 0.425	16 : 48 : 46.31	-45 : 31 : 51.3	-89.19	59	30.9	4	1.8	2	56	D
340.054 - 0.244	16 : 48 : 13.89	-45 : 21 : 43.5	-59.36	8	6.0	30	1.8	4	56	B
340.054 - 0.244	16 : 48 : 13.89	-45 : 21 : 43.5	-60.86	7	1.3	17	1.3	3	56	B
340.785 - 0.096	16 : 50 : 14.84	-44 : 42 : 26.3	-108.02	133	6.0	632	6.0	18	56	B
341.218 - 0.212	16 : 52 : 17.86	-44 : 26 : 52.3	-44.42	373	11.0	166	4.0	13	56	B
342.446 - 0.072	16 : 55 : 59.94	-43 : 24 : 22.5	-41.24	22	13.7	4	1.6	1	56	D
342.446 - 0.072	16 : 55 : 59.94	-43 : 24 : 22.5	-42.03	44	27.6	3	0.6	2	56	D
342.446 - 0.072	16 : 55 : 59.94	-43 : 24 : 22.5	-42.30	42	20.6	3	0.9	2	56	D
345.012 + 1.797	16 : 56 : 46.82	-40 : 14 : 08.9	-17.02	113	5.0	19	0.8	9	56	A
345.012 + 1.797	16 : 56 : 46.82	-40 : 14 : 08.9	-17.46	54	5.1	29	1.3	7	56	A
345.012 + 1.797	16 : 56 : 46.82	-40 : 14 : 08.9	-20.18	67	3.5	55	1.4	13	56	A
345.012 + 1.797	16 : 56 : 46.82	-40 : 14 : 08.9	-21.76	2						

## B.1. MASER COMPACTNESS TABLES

**Table B.2 – Continued...**

Name	$\alpha_{\text{J}2000}$ hh:mm:ss	$\delta_{\text{J}2000}$ dd:mm:ss	$V$ ( $\text{km s}^{-1}$ )	$S_H$ (Jy)	$\theta_H$ (mas)	$S_C$ (Jy)	$\theta_C$ (mas)	Error (Jy)	DF (N-4)	Grade
345.003 – 0.223	17 : 05 : 10.89	-41 : 29 : 06.2	-22.37	57	34.7	4	1.1	4	56	D
345.003 – 0.223	17 : 05 : 10.89	-41 : 29 : 06.2	-22.89	98	30.5	19	3.1	10	56	D
345.003 – 0.223	17 : 05 : 10.89	-41 : 29 : 06.2	-23.68	60	34.0	3	1.0	5	56	D
345.003 – 0.223	17 : 05 : 10.89	-41 : 29 : 06.2	-26.05	72	26.0	4	1.2	7	56	D
345.003 – 0.223	17 : 05 : 10.89	-41 : 29 : 06.2	-26.41	72	31.3	2	0.0	4	56	D
345.003 – 0.223	17 : 05 : 10.89	-41 : 29 : 06.2	-26.84	106	28.5	5	1.4	8	56	D
345.003 – 0.223	17 : 05 : 10.89	-41 : 29 : 06.2	-27.64	56	22.3	3	0.9	6	56	D
345.487 + 0.314	17 : 04 : 28.24	-40 : 46 : 28.7	-14.06	193	27.9	49	1.1	27	56	A
345.487 + 0.314	17 : 04 : 28.24	-40 : 46 : 28.7	-19.06	49	23.7	142	2.1	16	56	A
346.480 + 0.221	17 : 08 : 00.11	-40 : 02 : 15.9	-19.04	20	4.5	2	0.0	3	28	D
348.579 – 0.920	17 : 19 : 10.61	-39 : 00 : 24.2	-10.41	19	3.1	10	0.0	3	16	A
348.617 – 1.162	17 : 20 : 18.65	-39 : 06 : 50.8	-11.47	13	6.8	26	1.5	3	36	B
348.727 – 1.037	17 : 20 : 06.54	-38 : 57 : 09.1	-7.36	60	18.3	25	1.4	10	11	B
350.686 – 0.491	17 : 23 : 28.63	-37 : 01 : 48.8	-13.76	24	5.9	5	0.0	6	28	C
351.417 + 0.645	17 : 20 : 53.37	-35 : 47 : 01.2	-9.71	441	6.9	181	1.3	93	28	A
351.417 + 0.645	17 : 20 : 53.37	-35 : 47 : 01.2	-10.32	1232	7.7	365	2.0	399	28	A
351.688 + 0.171	17 : 23 : 34.52	-35 : 49 : 46.3	-36.07	11	5.2	8	0.8	5	28	C
351.775 – 0.536	17 : 26 : 42.57	-36 : 09 : 17.6	1.80	77	6.6	16	6.6	13	28	D
351.775 – 0.536	17 : 26 : 42.57	-36 : 09 : 17.6	1.27	43	23.8	3	1.4	2	28	D
352.630 – 1.067	17 : 31 : 13.91	-35 : 44 : 08.7	-2.91	121	4.1	14	0.0	12	28	A
352.630 – 1.067	17 : 31 : 13.91	-35 : 44 : 08.7	-3.27	53	4.4	75	1.6	19	28	A
354.615 + 0.472	17 : 30 : 17.13	-33 : 13 : 55.1	-24.21	60	165.3	105	4.2	6	22	B
358.371 – 0.468	17 : 43 : 31.95	-30 : 34 : 10.7	-5.98	6	53.9	7	0.0	3	14	C
358.460 – 0.393	17 : 43 : 27.24	-30 : 27 : 14.6	1.26	26	15.4	22	1.3	4	22	B
359.436 – 0.102	17 : 44 : 40.21	-29 : 28 : 12.5	-46.66	86	26.3	22	5.8	3	28	D
359.615 – 0.243	17 : 45 : 39.09	-29 : 23 : 30.0	24.50	5	34.6	21	1.8	3	28	B
359.615 – 0.243	17 : 45 : 39.09	-29 : 23 : 30.0	19.58	0	2.5	59	2.5	4	28	B

## B.1. MASER COMPACTNESS TABLES

**Table B.3:** Non-detections and unknown sources surveyed. **Columns:** (1) Maser name in Galactic coordinates, (2) Right Ascension (J2000), (3) Declination (J2000), (4) peak velocity (km/s) from MMB - confirmed same peak in this survey, (5) MMB autocorrelated peak flux density (Jy). Notes: Both U-grade masers 332.963–0.679 and 353.410–0.360 were observed at incorrect coordinates,  $\Delta\delta = 1$  amin and  $\Delta\alpha = 10$  amin offset respectively.

Name	$\alpha_{\text{J2000}}$ (hh:mm:ss)	$\delta_{\text{J2000}}$ (dd:mm:ss)	$V_p$ (km s $^{-1}$ )	$S_p$ (Jy)	Grade
285.337 – 0.002	10 : 32 : 09.62	-58 : 02 : 04.6	+0.7	17.9	F
286.383 – 1.834	10 : 31 : 55.12	-60 : 08 : 38.6	+9.6	17.6	F
294.337 – 1.706	11 : 33 : 49.91	-63 : 16 : 32.5	-11.7	14.5	F
294.511 – 1.621	11 : 35 : 32.25	-63 : 14 : 43.2	-11.9	9.0	F
311.643 – 0.380	14 : 06 : 38.77	-61 : 58 : 23.1	32.6	11.13	F
313.767 – 0.863	14 : 25 : 01.73	-61 : 44 : 58.1	-56.3	9.0	F
313.994 – 0.084	14 : 24 : 30.78	-60 : 56 : 28.3	-4.9	15.2	F
320.780 + 0.248	15 : 11 : 23.48	-57 : 41 : 25.1	-5.1	40.0	F
322.705 – 0.331	15 : 25 : 47.52	-57 : 09 : 15.5	-21.6	2.0	F
324.716 + 0.342	15 : 34 : 57.47	-55 : 27 : 23.6	-45.9	10.8	F
324.915 + 0.158	15 : 36 : 51.17	-55 : 29 : 22.9	-2.3	12.1	F
326.662 + 0.520	15 : 45 : 02.95	-54 : 09 : 03.1	-38.6	29.1	F
327.392 + 0.199	15 : 50 : 18.48	-53 : 57 : 06.3	-84.5	11.4	F
327.566 – 0.850	15 : 55 : 47.61	-54 : 39 : 11.4	-29.7	15.0	F
329.066 – 0.308	16 : 01 : 09.93	-53 : 16 : 02.6	-43.8	21.9	F
329.183 – 0.314	16 : 01 : 47.01	-53 : 11 : 43.3	-55.6	10.7	F
329.469 + 0.503	15 : 59 : 40.71	-52 : 23 : 27.3	-72.0	21.6	F
329.610 + 0.114	16 : 02 : 03.14	-52 : 35 : 33.5	-60.1	49.9	F
329.719 + 1.164	15 : 58 : 07.09	-51 : 43 : 32.6	-75.8	24.4	F
331.132 – 0.244	16 : 10 : 59.76	-51 : 50 : 22.6	-84.3	37.4	F
331.542 – 0.066	16 : 12 : 09.02	-51 : 25 : 47.6	-85.8	7.0	F
331.556 – 0.121	16 : 12 : 27.21	-51 : 27 : 38.2	-97.1	69.3	F
331.710 + 0.603	16 : 10 : 01.77	-50 : 49 : 32.3	-73.3	13.0	F
332.094 – 0.421	16 : 16 : 16.45	-51 : 18 : 25.7	-58.5	21.8	F
332.813 – 0.701	16 : 20 : 48.12	-51 : 00 : 15.6	-53.1	12.9	F
332.963 – 0.679	16 : 21 : 22.92	-50 : 52 : 58.5	-45.9	63.3	U
333.128 – 0.560	16 : 21 : 35.38	-50 : 40 : 56.5	-52.7	18.0	F
333.121 – 0.434	16 : 20 : 59.66	-50 : 35 : 51.9	-48.5	54.59	F
333.163 – 0.101	16 : 19 : 42.67	-50 : 19 : 53.2	-95.2	11.8	F
333.184 – 0.091	16 : 19 : 45.62	-50 : 18 : 35.0	-81.9	12.5	F
333.683 – 0.437	16 : 23 : 29.78	-50 : 12 : 08.6	-5.6	40.6	F
335.426 – 0.240	16 : 30 : 05.58	-48 : 48 : 44.8	-50.6	91.2	F
335.556 – 0.307	16 : 30 : 55.98	-48 : 45 : 50.2	-116.0	25.0	F
335.726 + 0.191	16 : 29 : 27.37	-48 : 17 : 53.2	-44.4	75.4	F
336.358 – 0.137	16 : 33 : 29.17	-48 : 03 : 43.9	-73.5	13.2	F
336.433 – 0.262	16 : 34 : 20.22	-48 : 05 : 32.2	-93.0	32.0	F
336.526 – 0.156	16 : 34 : 15.00	-47 : 57 : 07.4	-94.8	0.7	F
336.864 + 0.005	16 : 34 : 54.44	-47 : 35 : 37.3	-76.0	66.2	F
336.830 – 0.375	16 : 36 : 26.19	-47 : 52 : 31.1	-22.8	33.9	F
336.864 + 0.005	16 : 34 : 54.44	-47 : 35 : 37.3	-76.0	66.2	F
336.941 – 0.156	16 : 35 : 55.19	-47 : 38 : 45.4	-67.2	22.0	F
336.983 – 0.183	16 : 36 : 12.41	-47 : 37 : 58.2	-80.7	14.9	F
337.202 – 0.094	16 : 36 : 41.22	-47 : 24 : 40.2	-71.7	1.7	F
337.613 – 0.060	16 : 38 : 09.54	-47 : 04 : 59.9	-41.6	19.5	F
337.632 – 0.079	16 : 38 : 19.12	-47 : 04 : 53.3	-56.9	13.6	F
338.069 + 0.011	16 : 39 : 37.95	-46 : 41 : 45.3	-39.3	4.0	F
338.566 + 0.110	16 : 41 : 07.03	-46 : 15 : 28.3	-78.1	10.0	F
338.875 – 0.084	16 : 43 : 08.25	-46 : 09 : 12.8	-41.4	21.2	F
338.850 + 0.409	16 : 40 : 54.29	-45 : 50 : 52.0	-55.7	1.4	F
338.902 + 0.394	16 : 41 : 10.06	-45 : 49 : 05.4	-26.2	1.7	F
339.762 + 0.054	16 : 45 : 51.56	-45 : 23 : 32.6	-51.0	11.7	F
340.249 – 0.046	16 : 48 : 05.18	-45 : 05 : 08.4	-126.3	10.1	F
340.970 – 1.022	16 : 54 : 57.32	-45 : 09 : 05.2	-31.3	10.1	F
343.354 – 0.067	16 : 59 : 04.23	-42 : 41 : 35.0	-117.7	20.3	F
344.419 + 0.044	17 : 02 : 08.62	-41 : 47 : 10.3	-63.2	2.3	F
346.036 + 0.048	17 : 07 : 20.02	-40 : 29 : 49.0	-6.4	10.4	F
347.628 + 0.149	17 : 11 : 50.92	-39 : 09 : 29.2	-96.5	19.0	F
348.884 + 0.096	17 : 15 : 50.13	-38 : 10 : 12.4	-74.5	12.9	F
349.092 + 0.105	17 : 16 : 24.74	-37 : 59 : 47.2	-76.5	23.1	F
350.104 + 0.084	17 : 19 : 26.68	-37 : 10 : 53.1	-68.1	14.6	F
350.299 + 0.122	17 : 19 : 50.87	-36 : 59 : 59.9	-62.2	31.2	F
351.161 + 0.697	17 : 19 : 57.50	-35 : 57 : 52.8	-5.2	12.0	F
351.382 – 0.181	17 : 24 : 09.58	-36 : 16 : 49.3	-59.8	16.9	F
351.581 – 0.353	17 : 25 : 25.12	-36 : 12 : 46.1	-94.2	47.5	F
352.133 – 0.944	17 : 29 : 22.32	-36 : 05 : 00.2	-7.8	15.7	F
353.273 + 0.641	17 : 26 : 01.58	-34 : 15 : 15.4	-4.4	12.7	F
353.410 – 0.360	17 : 30 : 26.18	-34 : 41 : 45.6	-20.4	109.0	F
353.429 – 0.090	17 : 29 : 23.48	-34 : 31 : 50.3	-61.8	13.0	N
353.464 + 0.562	17 : 26 : 51.53	-34 : 08 : 25.7	-50.3	12.8	F
354.724 + 0.300	17 : 31 : 15.55	-33 : 14 : 05.7	+93.8	12.2	F
355.346 + 0.149	17 : 33 : 28.91	-32 : 47 : 49.5	+9.9	9.2	F
356.662 – 0.263	17 : 38 : 29.16	-31 : 54 : 38.8	-53.8	10.1	F
357.967 – 0.163	17 : 41 : 20.26	-30 : 45 : 06.9	-4.2	55.1	F
358.263 – 2.061	17 : 49 : 37.63	-31 : 29 : 18.0	+3.0	0.0	F
358.809 – 0.085	17 : 43 : 05.40	-29 : 59 : 45.8	-56.2	12.0	F
358.841 – 0.737	17 : 45 : 44.29	-30 : 18 : 33.6	-20.6	13.1	F
358.931 – 0.030	17 : 43 : 10.02	-29 : 51 : 45.8	-15.9	10.1	F
359.138 + 0.031	17 : 43 : 25.67	-29 : 39 : 17.3	-3.9	19.6	F

## B.2 Maser Compactness Statistics

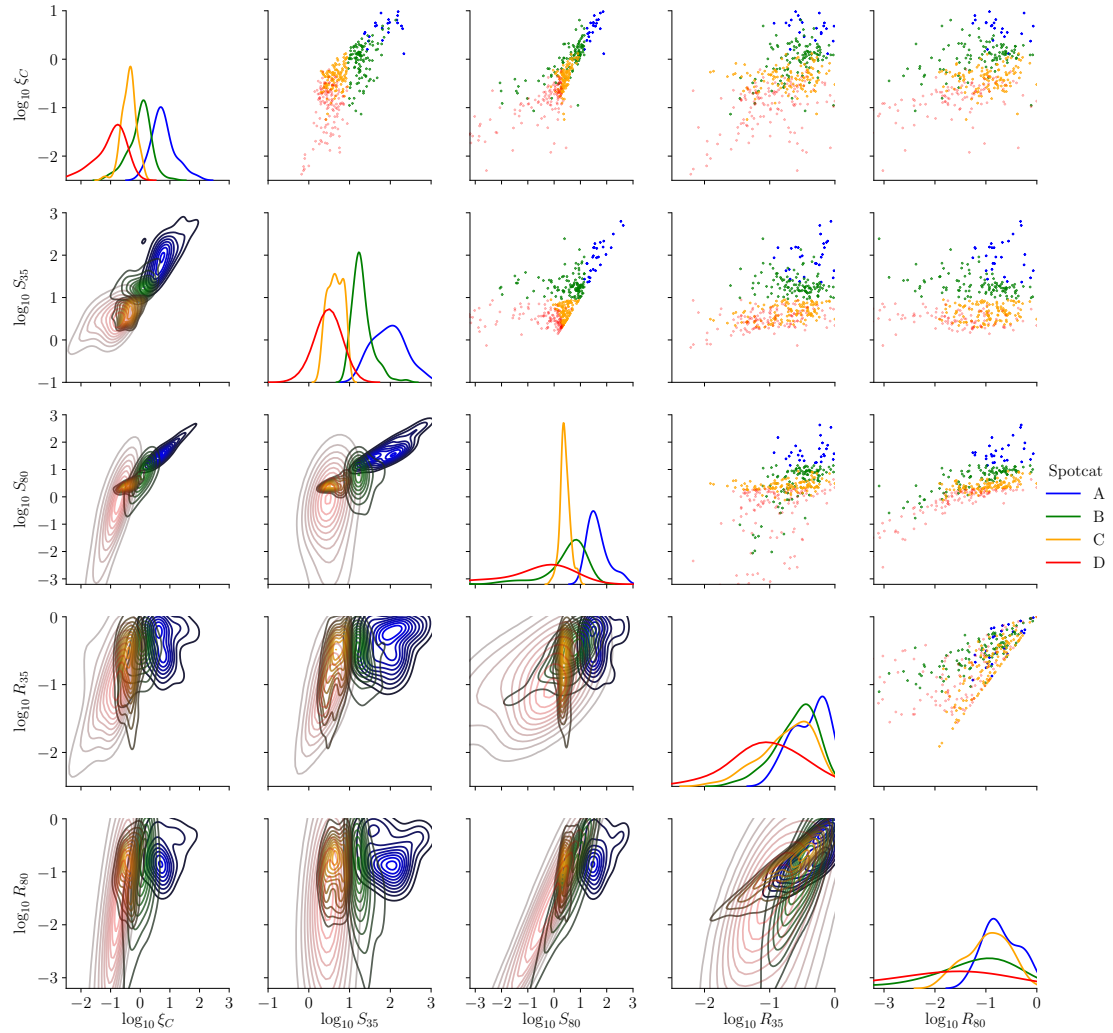


**Figure B.1:** Final distributions of metrics categorised by compactness

## B.2. MASER COMPACTNESS STATISTICS

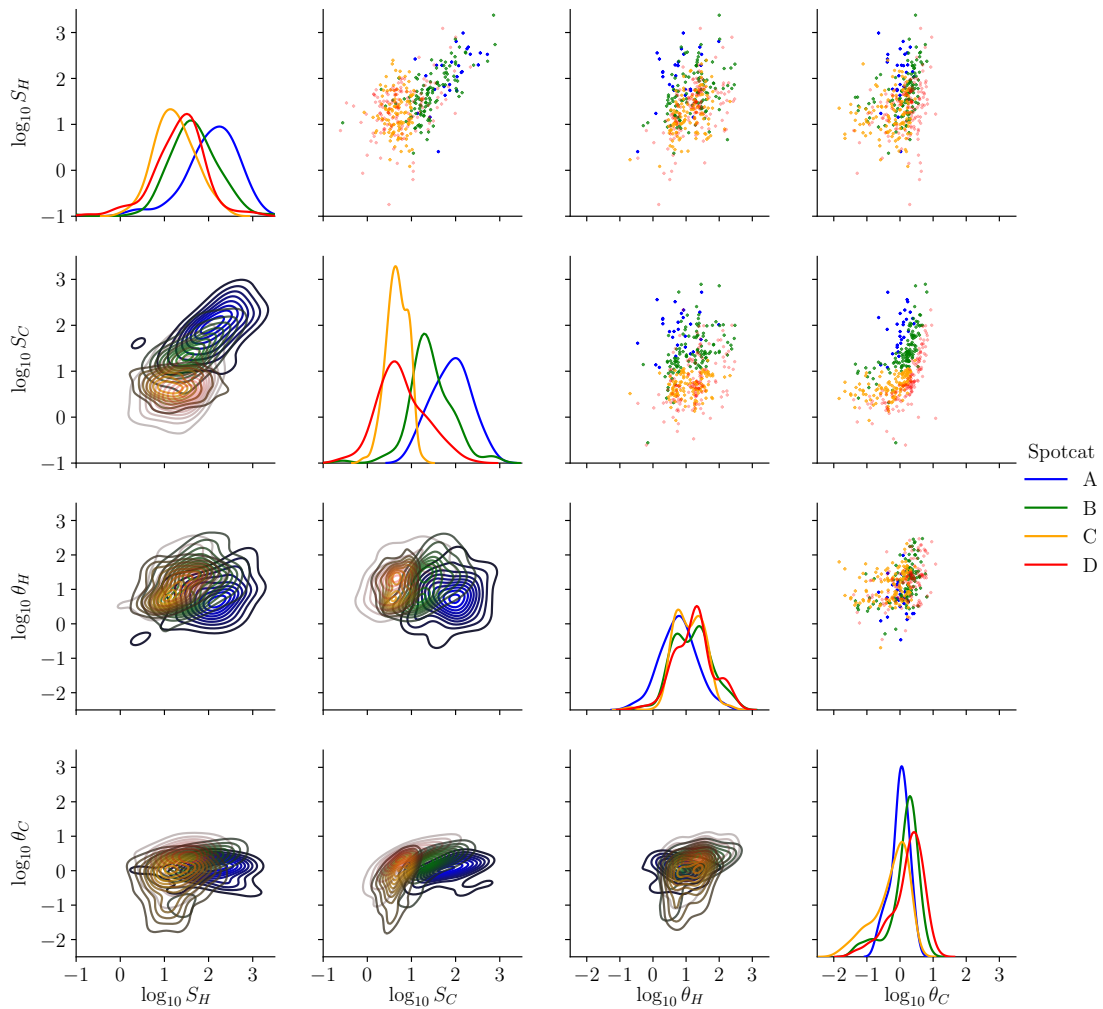
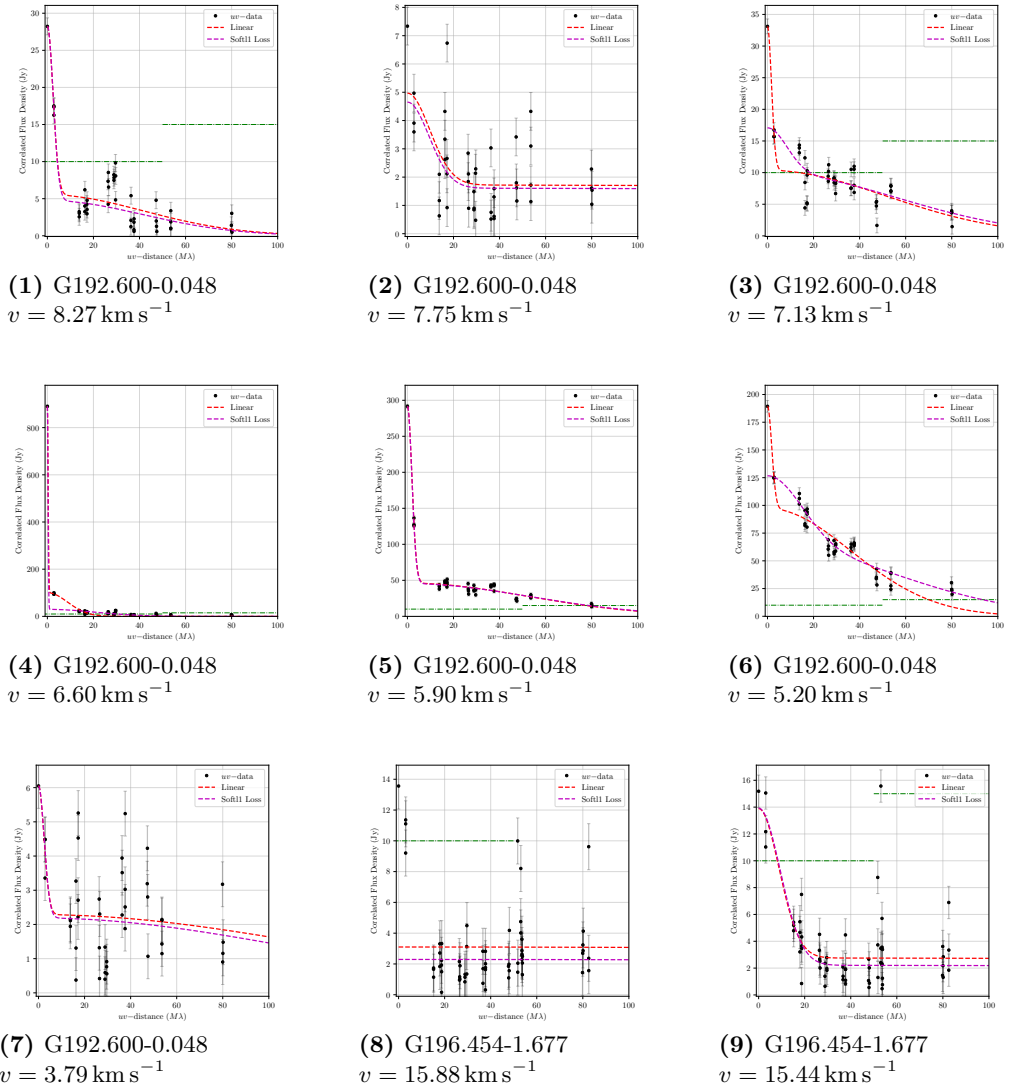


**Figure B.2:** Final distributions of metrics categorised by compactness

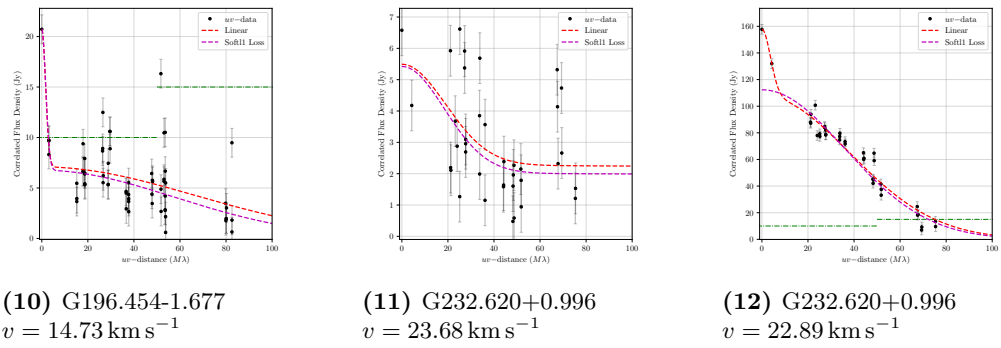
### B.3. ALL MASER SPOT COMPACTNESS

## B.3 All Maser Spot Compactness

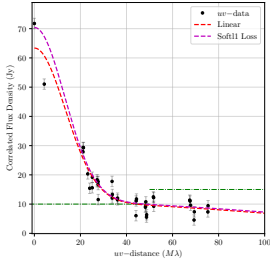
**Figure B.3**



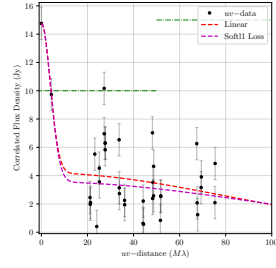
### B.3. ALL MASER SPOT COMPACTNESS



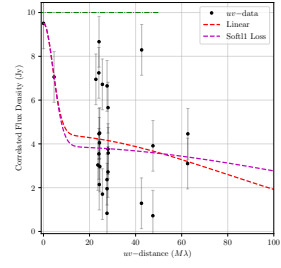
### B.3. ALL MASER SPOT COMPACTNESS



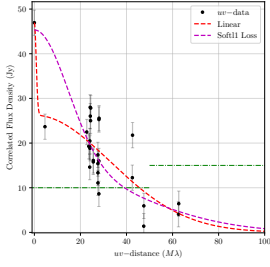
(13) G232.620+0.996  
 $v = 22.36 \text{ km s}^{-1}$



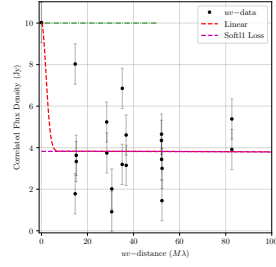
(14) G232.620+0.996  
 $v = 21.66 \text{ km s}^{-1}$



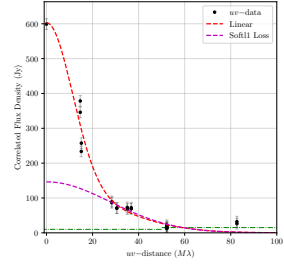
(15) G263.250+0.514  
 $v = 13.14 \text{ km s}^{-1}$



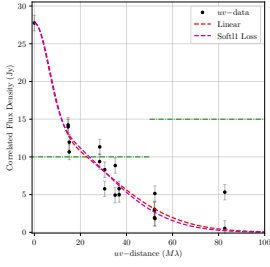
(16) G263.250+0.514  
 $v = 12.35 \text{ km s}^{-1}$



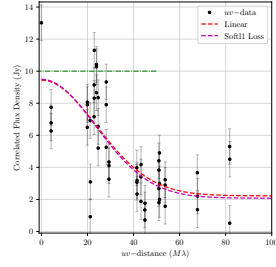
(17) G188.946+0.886  
 $v = 11.82 \text{ km s}^{-1}$



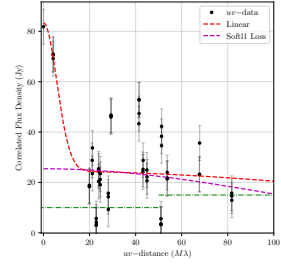
(18) G188.946+0.886  
 $v = 10.85 \text{ km s}^{-1}$



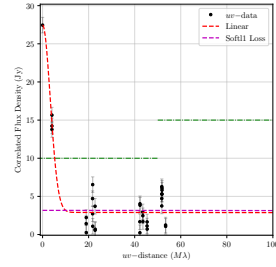
(19) G188.946+0.886  
 $v = 9.71 \text{ km s}^{-1}$



(20) G287.371+0.644  
 $v = -0.92 \text{ km s}^{-1}$

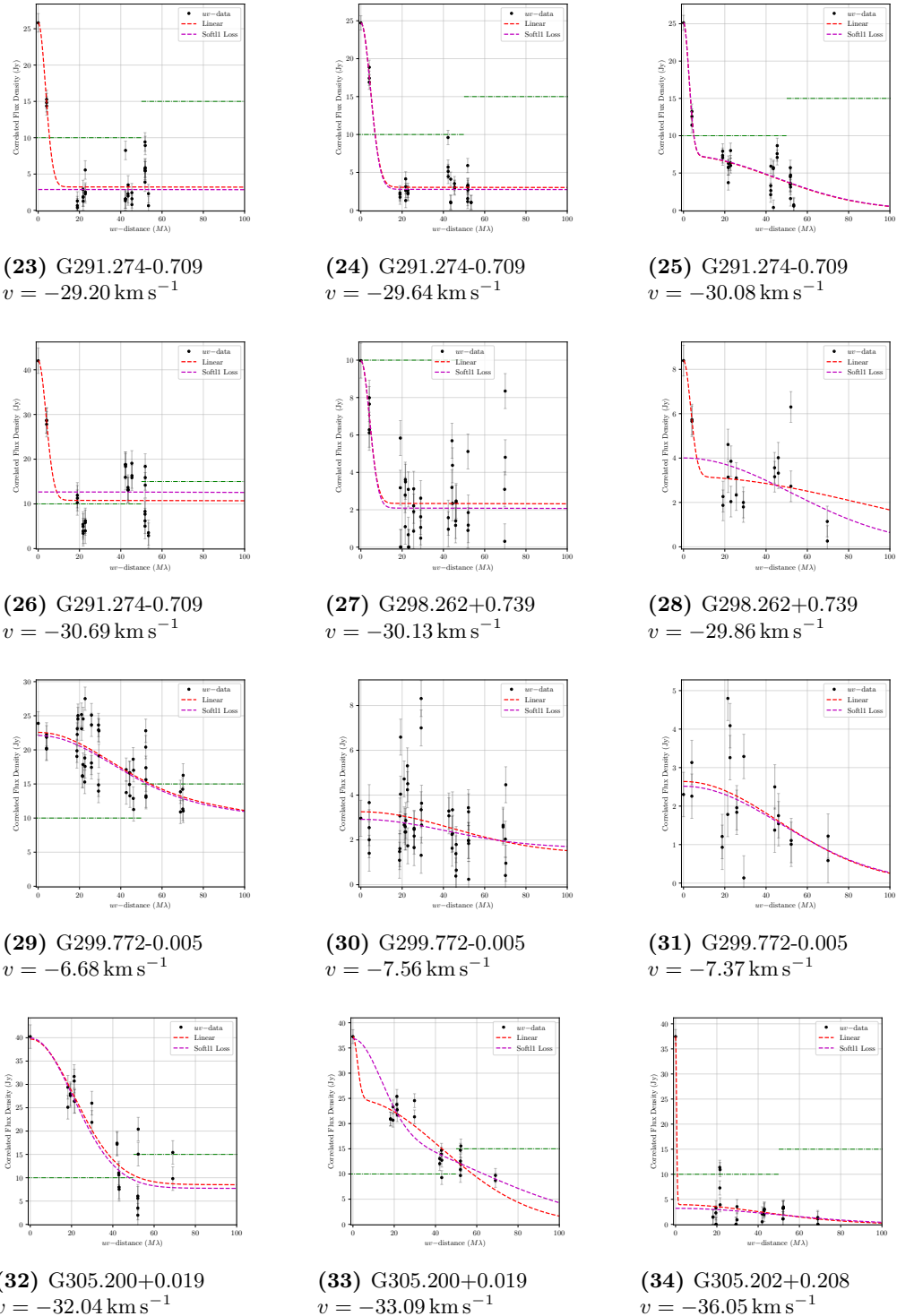


(21) G287.371+0.644  
 $v = -1.89 \text{ km s}^{-1}$

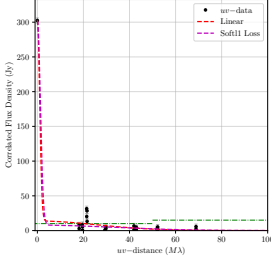


(22) G291.274-0.709  
 $v = -28.85 \text{ km s}^{-1}$

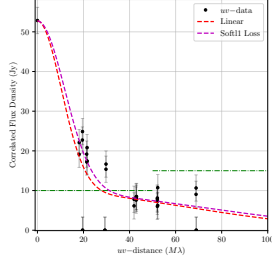
### B.3. ALL MASER SPOT COMPACTNESS



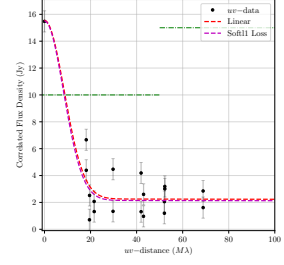
### B.3. ALL MASER SPOT COMPACTNESS



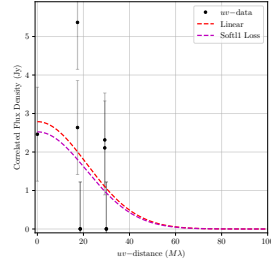
(35) G305.202+0.208  
 $v = -38.34 \text{ km s}^{-1}$



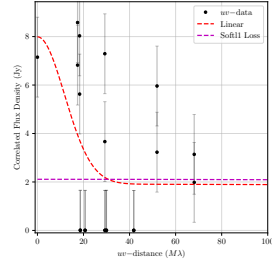
(36) G305.202+0.208  
 $v = -44.04 \text{ km s}^{-1}$



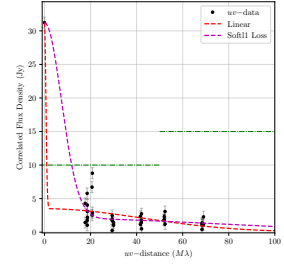
(37) G305.202+0.208  
 $v = -44.57 \text{ km s}^{-1}$



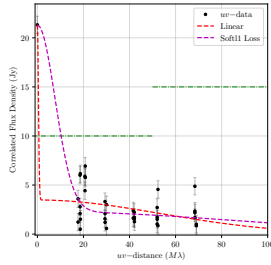
(38) G308.754+0.549  
 $v = -39.21 \text{ km s}^{-1}$



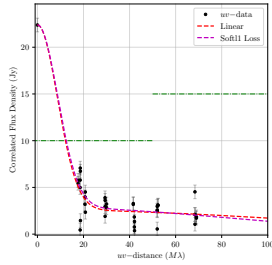
(39) G308.754+0.549  
 $v = -45.27 \text{ km s}^{-1}$



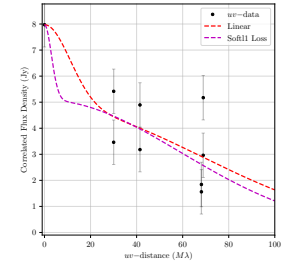
(40) G308.918+0.123  
 $v = -54.25 \text{ km s}^{-1}$



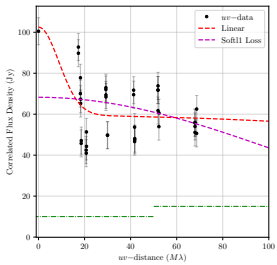
(41) G308.918+0.123  
 $v = -54.60 \text{ km s}^{-1}$



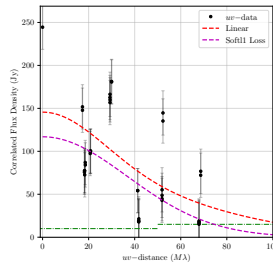
(42) G308.918+0.123  
 $v = -54.78 \text{ km s}^{-1}$



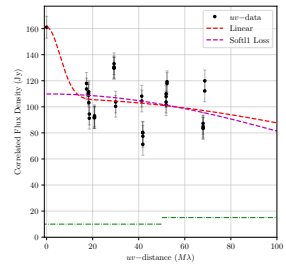
(43) G309.901+0.231  
 $v = -54.29 \text{ km s}^{-1}$



(44) G309.921+0.479  
 $v = -57.85 \text{ km s}^{-1}$

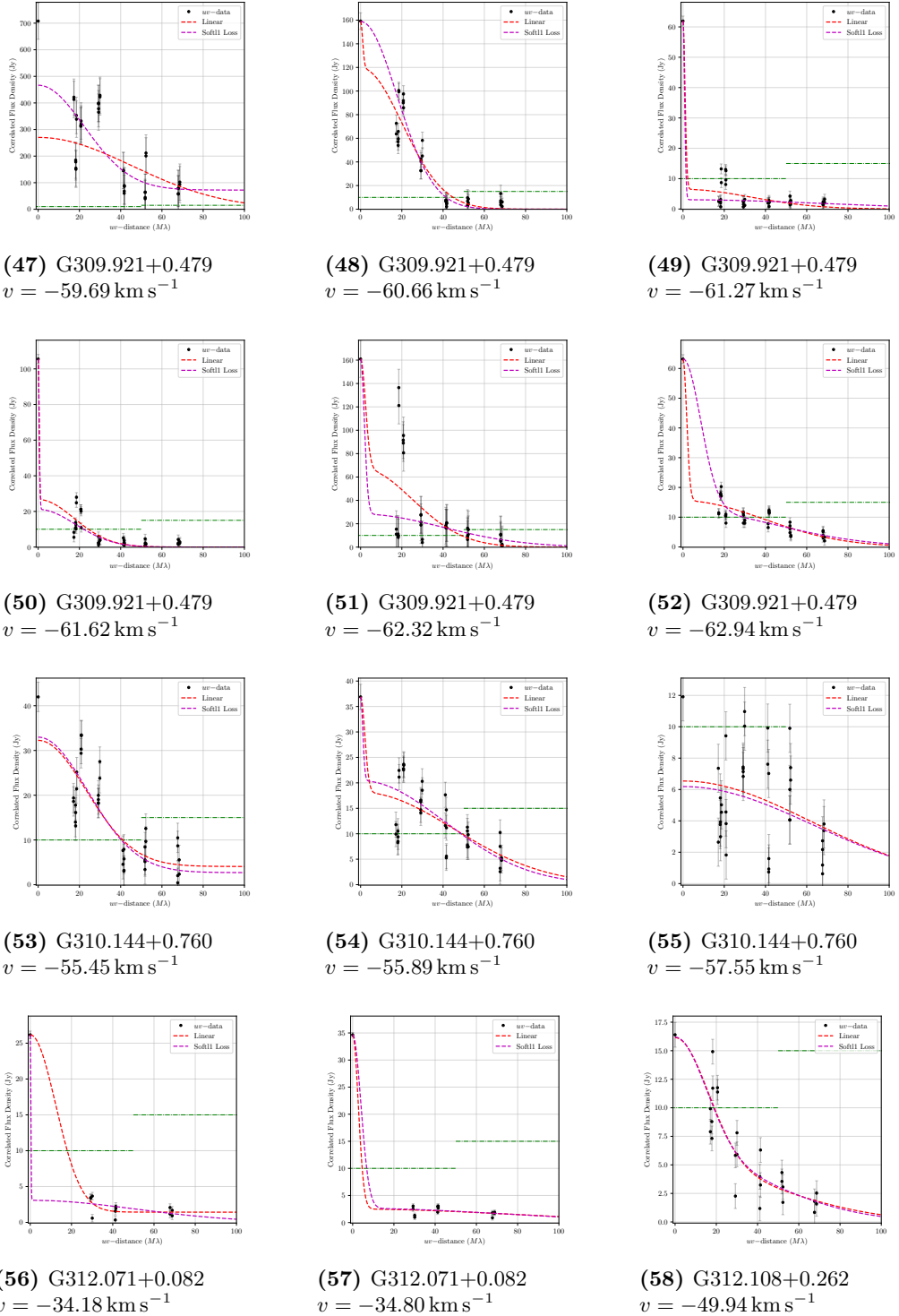


(45) G309.921+0.479  
 $v = -58.46 \text{ km s}^{-1}$

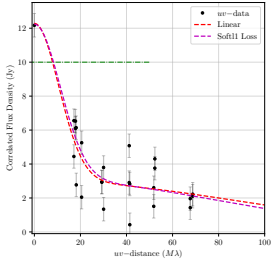


(46) G309.921+0.479  
 $v = -58.81 \text{ km s}^{-1}$

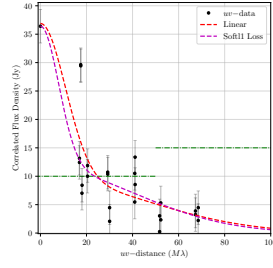
### B.3. ALL MASER SPOT COMPACTNESS



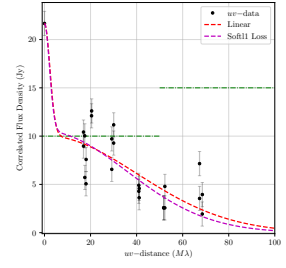
### B.3. ALL MASER SPOT COMPACTNESS



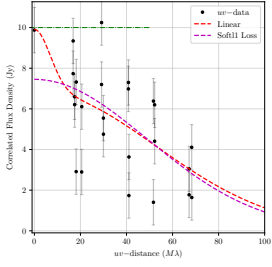
(59) G312.598+0.045  
 $v = -67.78 \text{ km s}^{-1}$



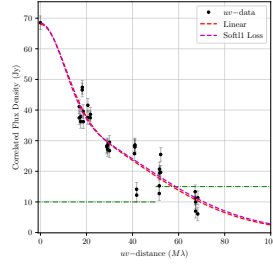
(60) G313.469+0.190  
 $v = -9.44 \text{ km s}^{-1}$



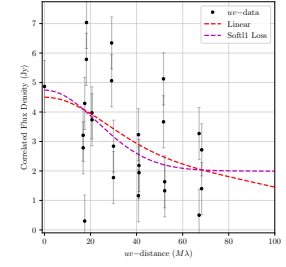
(61) G313.469+0.190  
 $v = -11.81 \text{ km s}^{-1}$



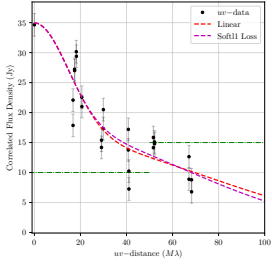
(62) G313.577+0.325  
 $v = -47.10 \text{ km s}^{-1}$



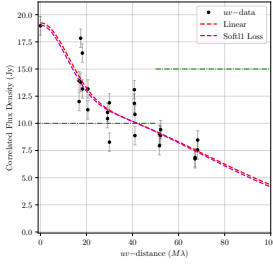
(63) G313.577+0.325  
 $v = -47.80 \text{ km s}^{-1}$



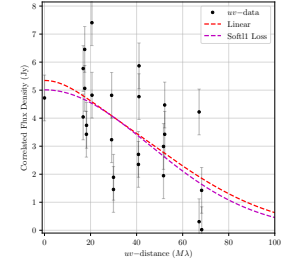
(64) G314.320+0.112  
 $v = -42.98 \text{ km s}^{-1}$



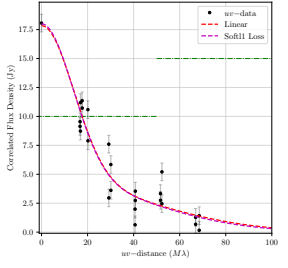
(65) G314.320+0.112  
 $v = -43.42 \text{ km s}^{-1}$



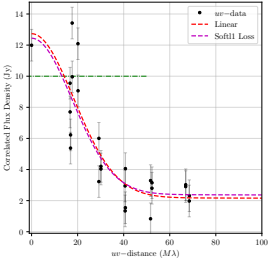
(66) G314.320+0.112  
 $v = -43.69 \text{ km s}^{-1}$



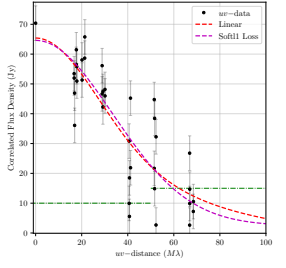
(67) G314.320+0.112  
 $v = -44.21 \text{ km s}^{-1}$



(68) G316.359-0.362  
 $v = 6.98 \text{ km s}^{-1}$

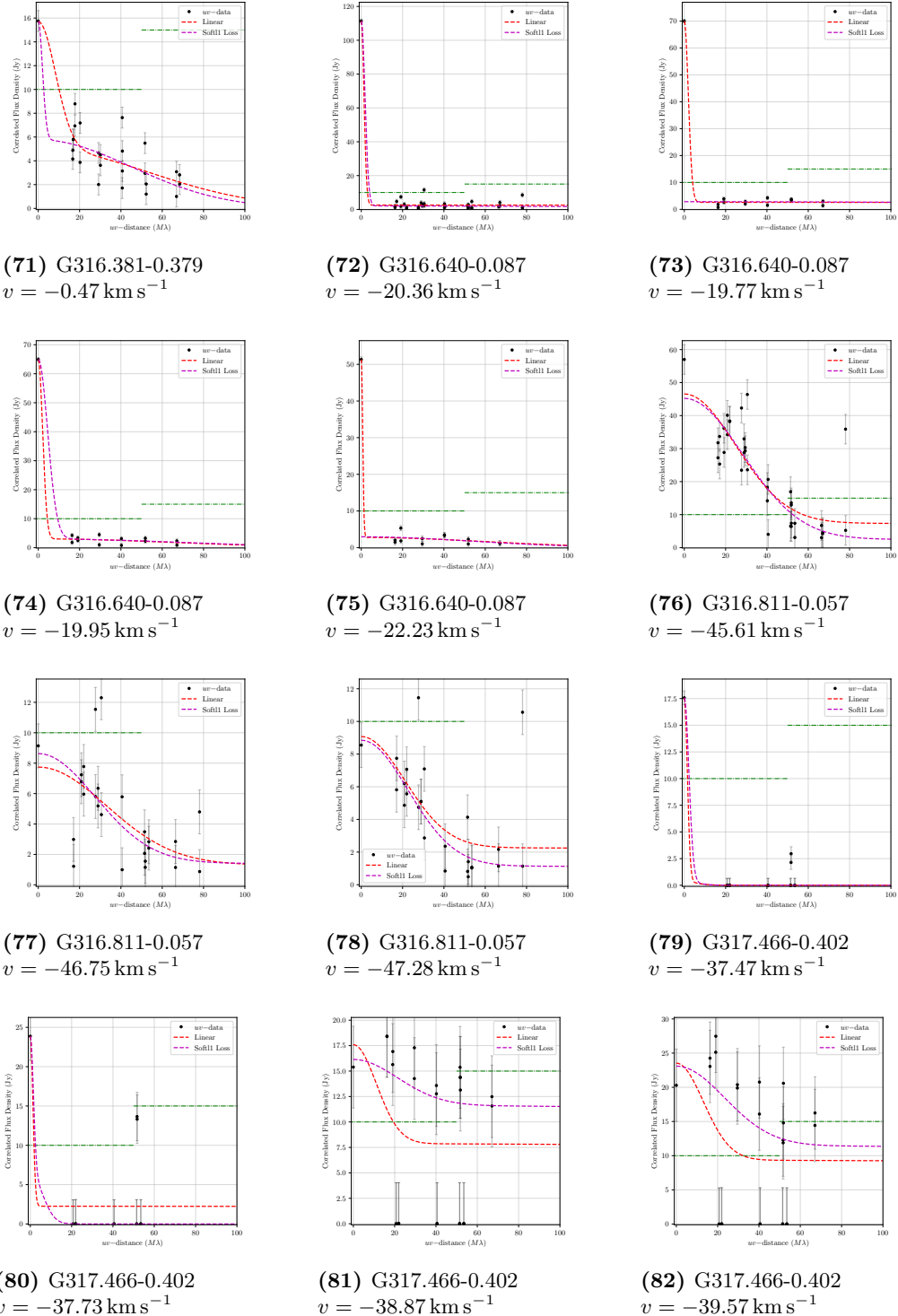


(69) G316.359-0.362  
 $v = 6.01 \text{ km s}^{-1}$

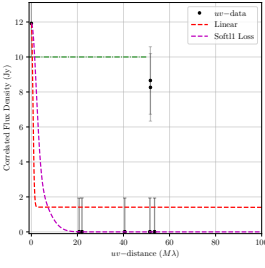


(70) G316.359-0.362  
 $v = 3.38 \text{ km s}^{-1}$

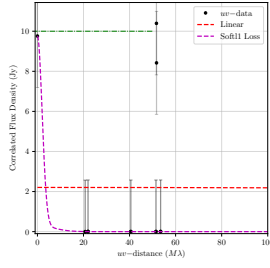
### B.3. ALL MASER SPOT COMPACTNESS



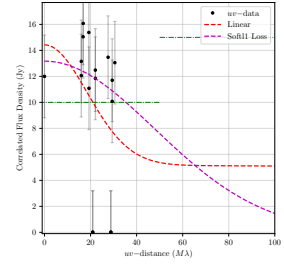
### B.3. ALL MASER SPOT COMPACTNESS



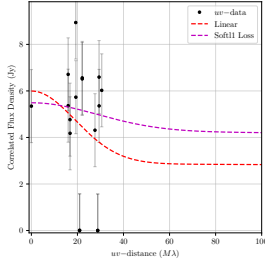
(83) G317.466-0.402  
 $v = -40.98 \text{ km s}^{-1}$



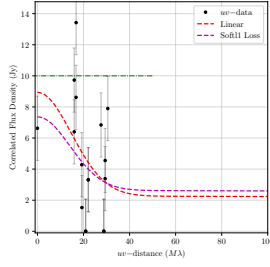
(84) G317.466-0.402  
 $v = -41.86 \text{ km s}^{-1}$



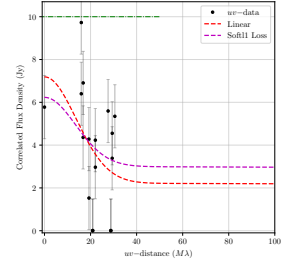
(85) G317.701+0.110  
 $v = -42.15 \text{ km s}^{-1}$



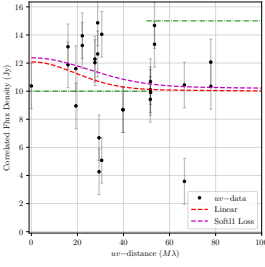
(86) G317.701+0.110  
 $v = -43.55 \text{ km s}^{-1}$



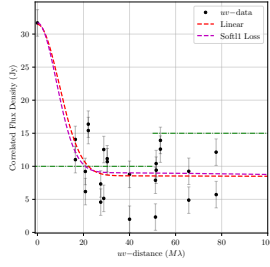
(87) G317.701+0.110  
 $v = -46.01 \text{ km s}^{-1}$



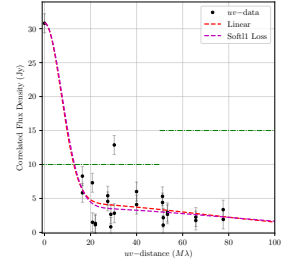
(88) G317.701+0.110  
 $v = -46.19 \text{ km s}^{-1}$



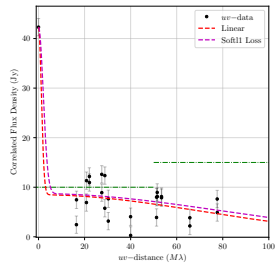
(89) G318.050+0.087  
 $v = -51.47 \text{ km s}^{-1}$



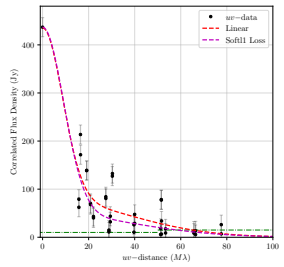
(90) G318.948-0.196  
 $v = -32.09 \text{ km s}^{-1}$



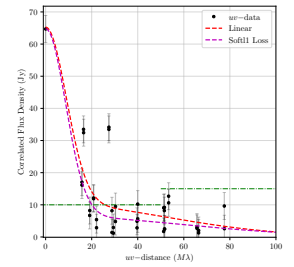
(91) G318.948-0.196  
 $v = -32.88 \text{ km s}^{-1}$



(92) G318.948-0.196  
 $v = -33.58 \text{ km s}^{-1}$

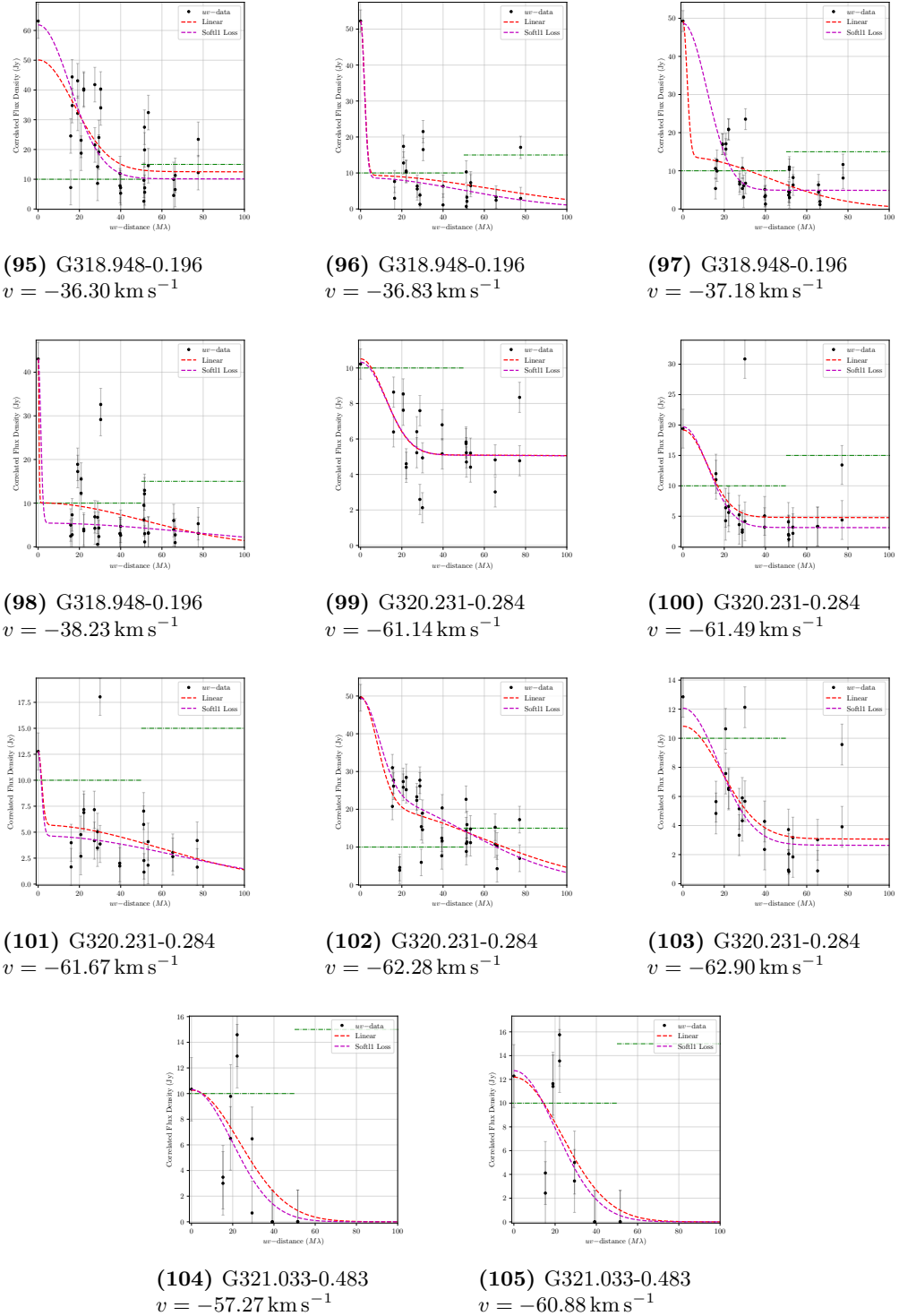


(93) G318.948-0.196  
 $v = -34.63 \text{ km s}^{-1}$

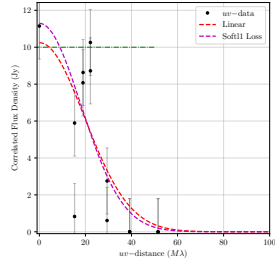


(94) G318.948-0.196  
 $v = -35.34 \text{ km s}^{-1}$

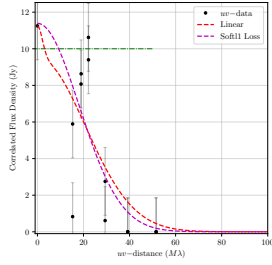
### B.3. ALL MASER SPOT COMPACTNESS



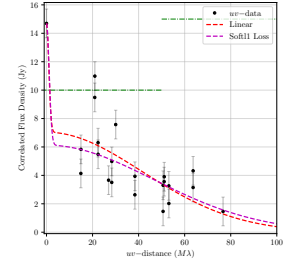
### B.3. ALL MASER SPOT COMPACTNESS



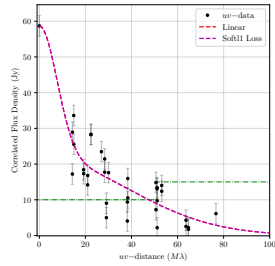
(106) G321.033-0.483  
 $v = -61.23 \text{ km s}^{-1}$



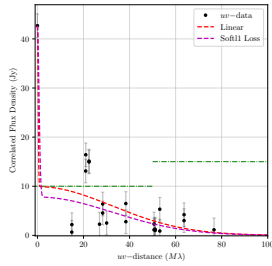
(107) G321.033-0.483  
 $v = -61.40 \text{ km s}^{-1}$



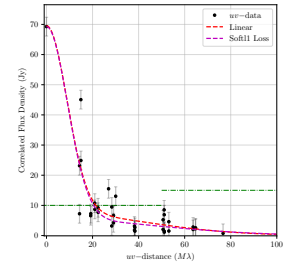
(108) G322.158+0.636  
 $v = -53.54 \text{ km s}^{-1}$



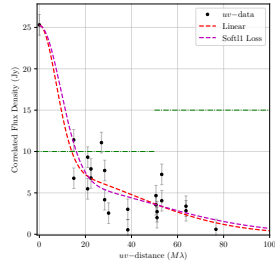
(109) G322.158+0.636  
 $v = -54.51 \text{ km s}^{-1}$



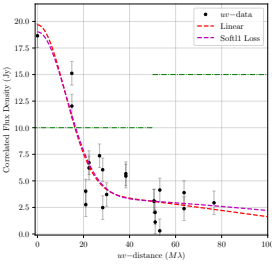
(110) G322.158+0.636  
 $v = -55.03 \text{ km s}^{-1}$



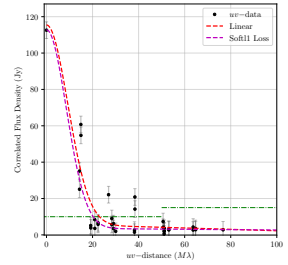
(111) G322.158+0.636  
 $v = -56.09 \text{ km s}^{-1}$



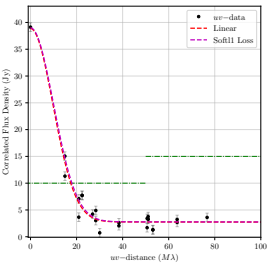
(112) G322.158+0.636  
 $v = -56.88 \text{ km s}^{-1}$



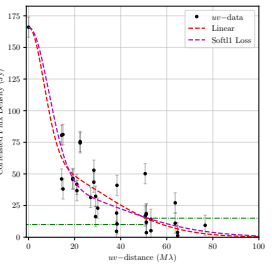
(113) G322.158+0.636  
 $v = -60.04 \text{ km s}^{-1}$



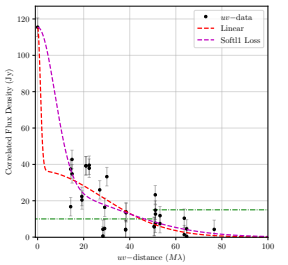
(114) G322.158+0.636  
 $v = -62.06 \text{ km s}^{-1}$



(115) G322.158+0.636  
 $v = -62.50 \text{ km s}^{-1}$

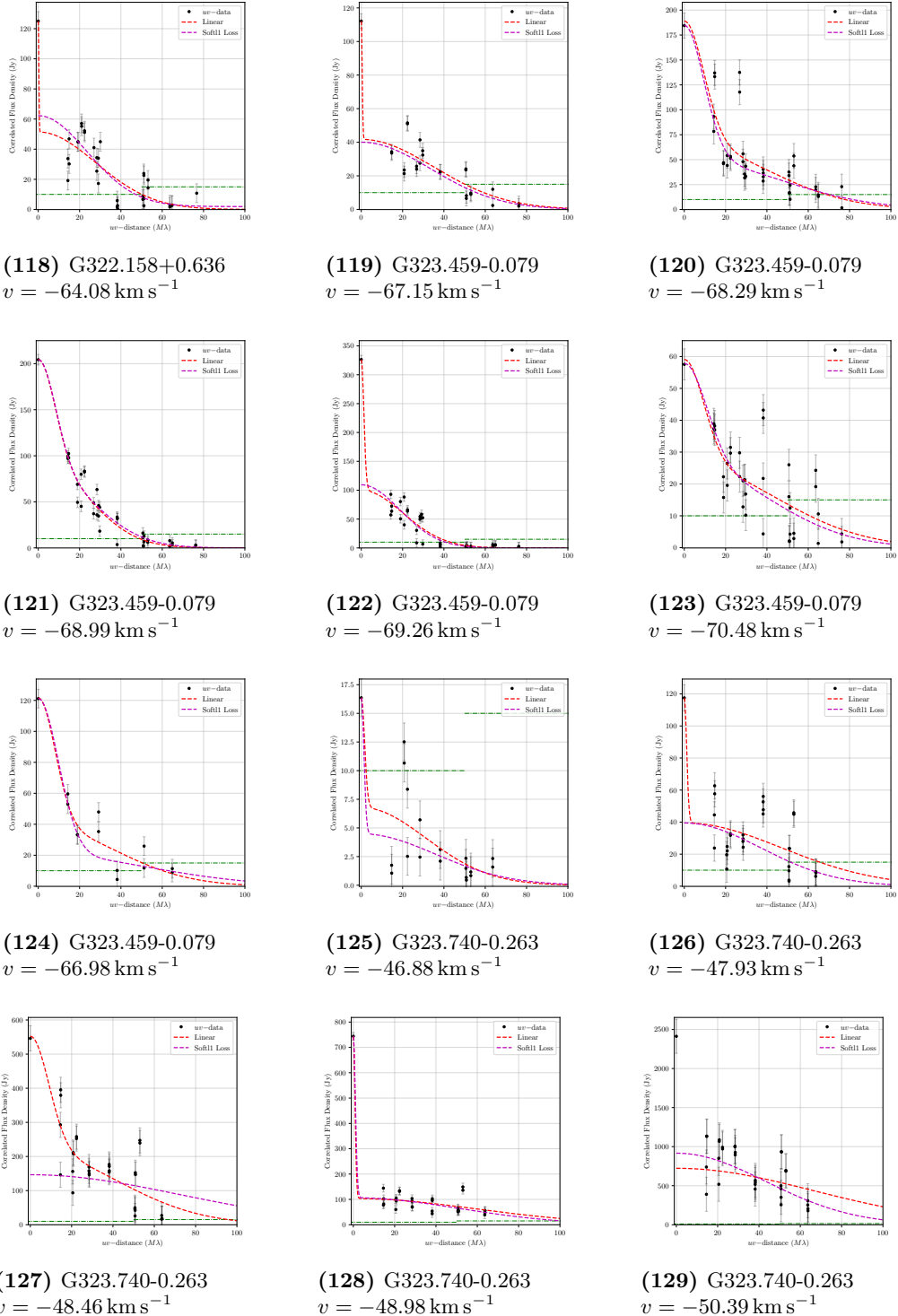


(116) G322.158+0.636  
 $v = -62.94 \text{ km s}^{-1}$

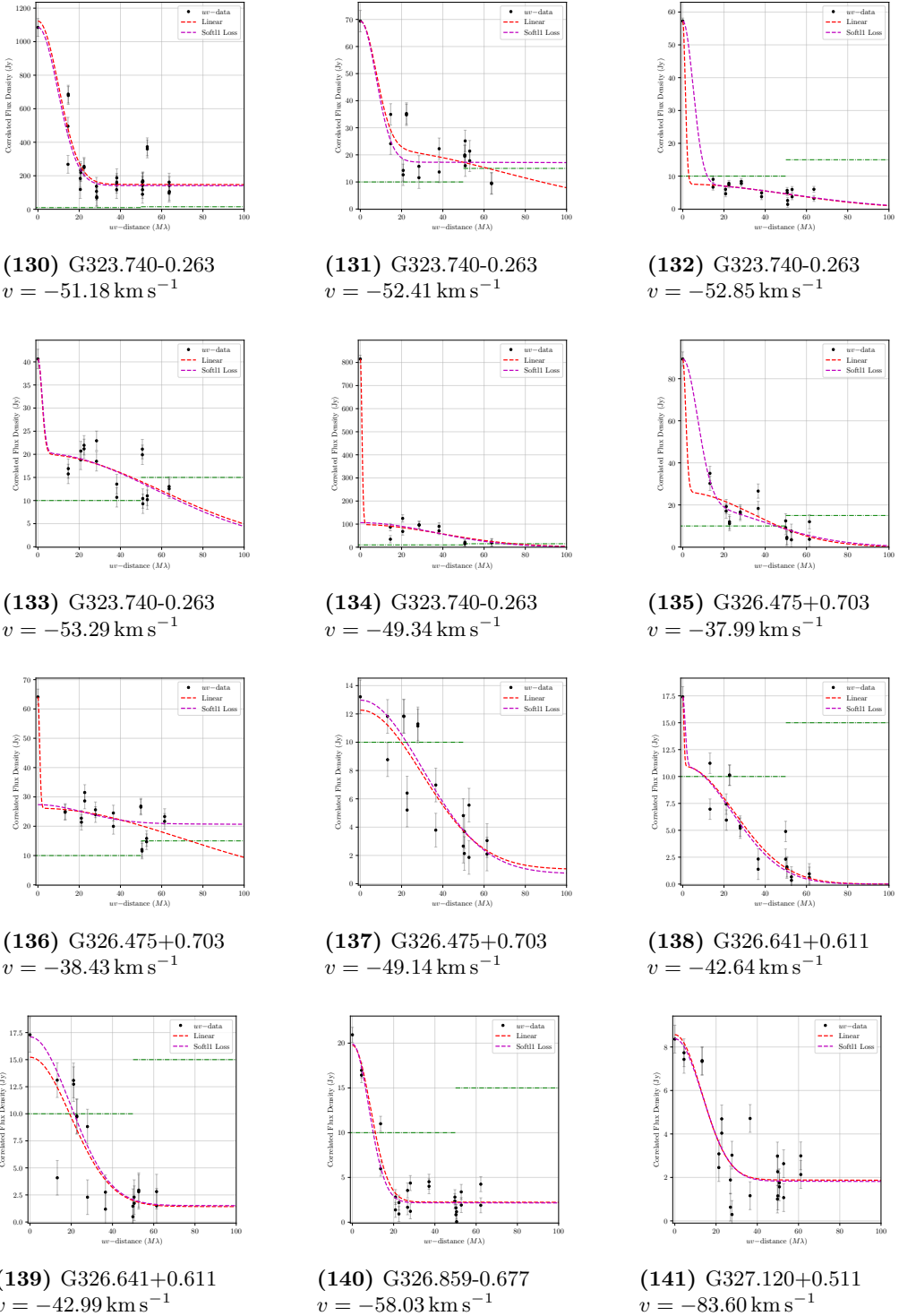


(117) G322.158+0.636  
 $v = -63.29 \text{ km s}^{-1}$

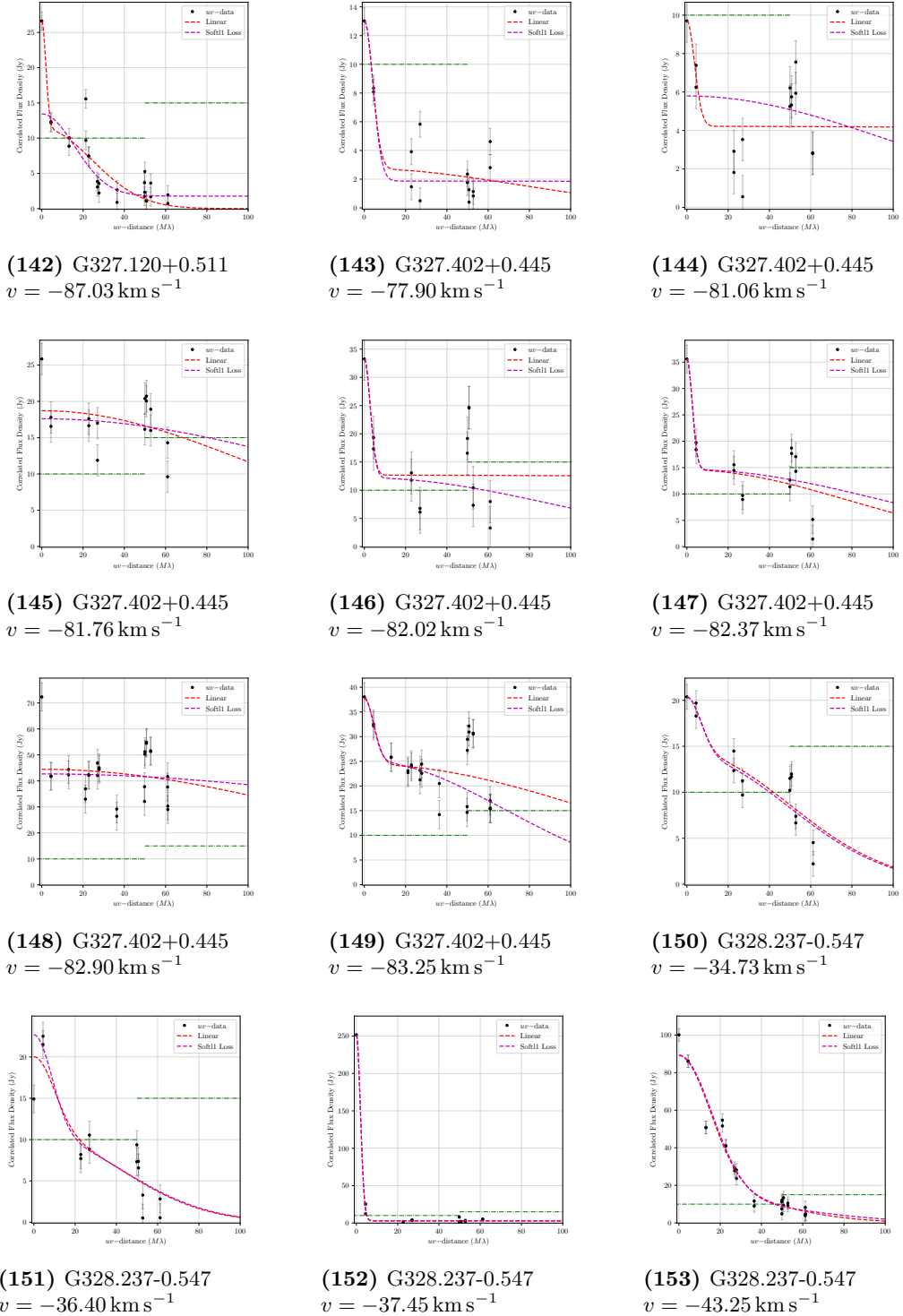
### B.3. ALL MASER SPOT COMPACTNESS



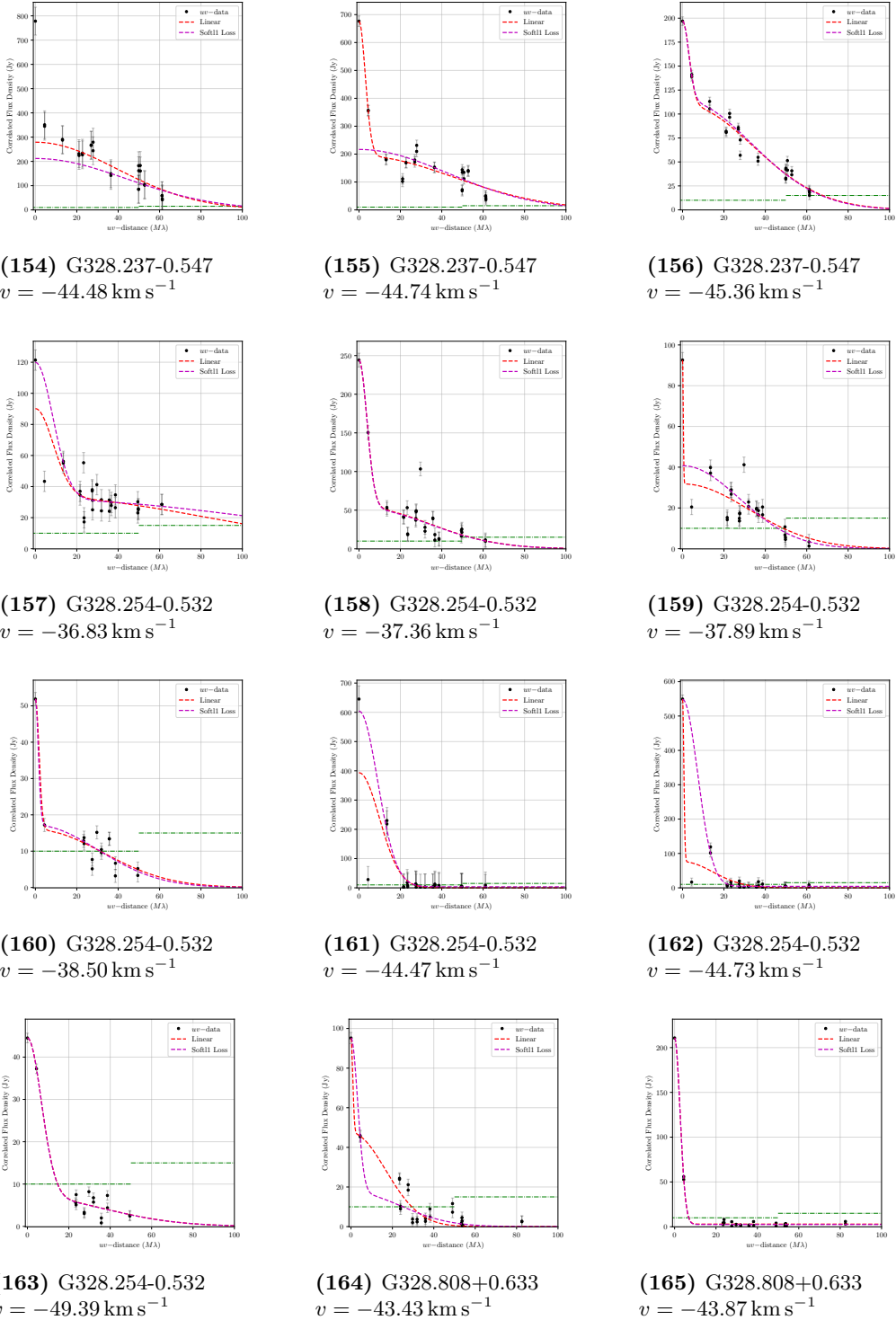
### B.3. ALL MASER SPOT COMPACTNESS



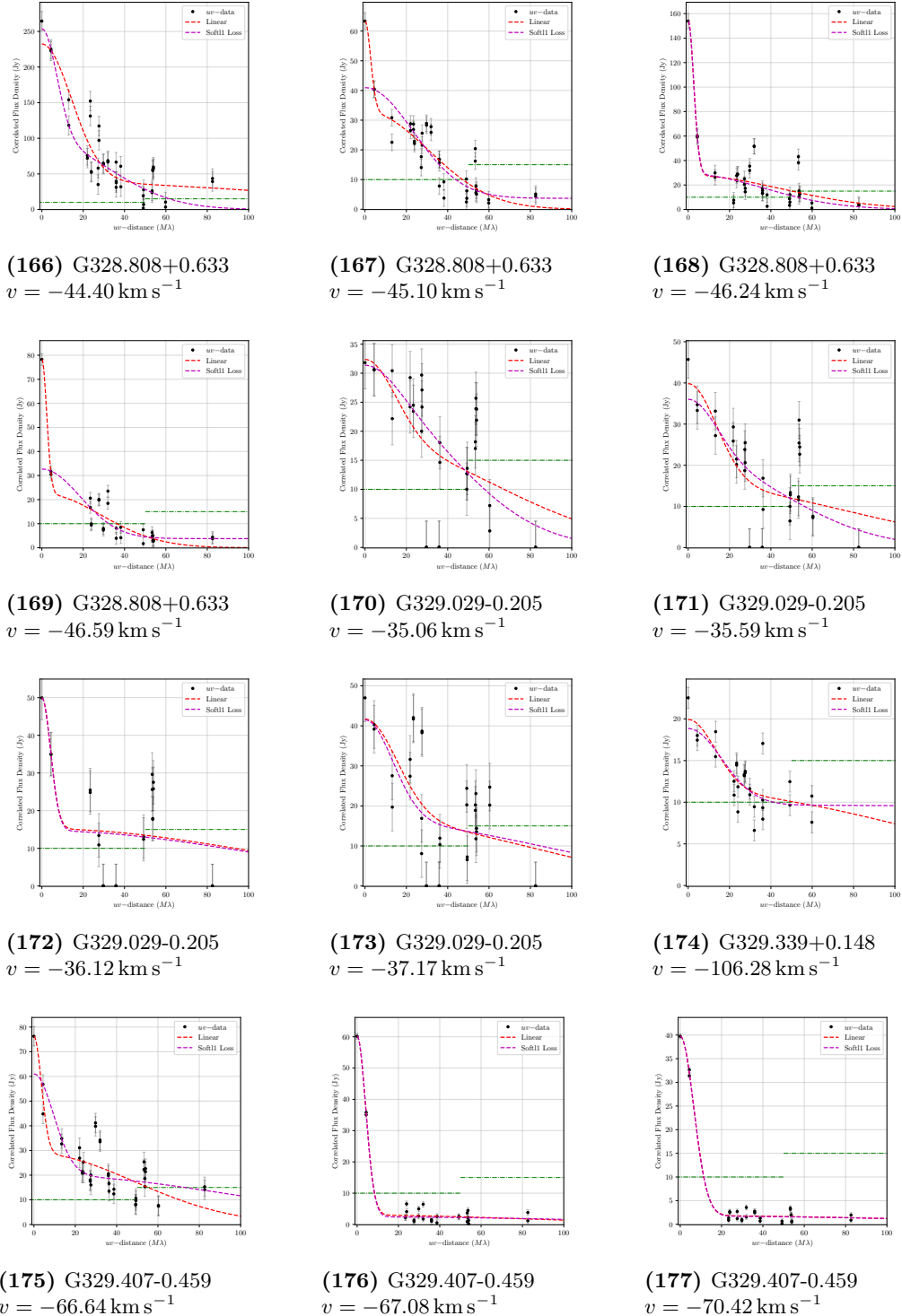
### B.3. ALL MASER SPOT COMPACTNESS



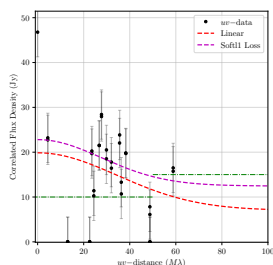
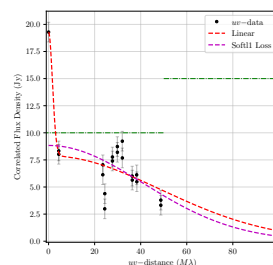
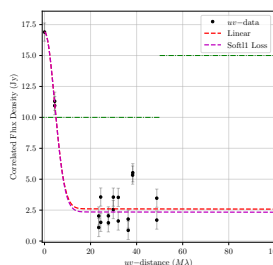
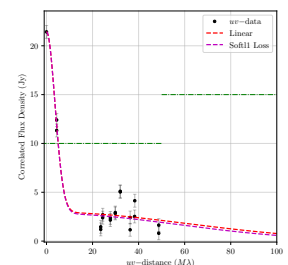
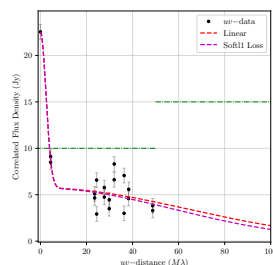
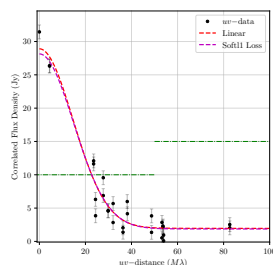
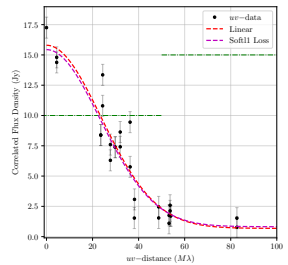
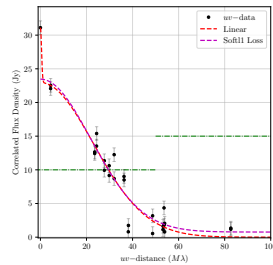
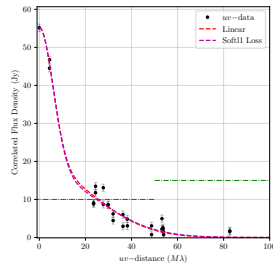
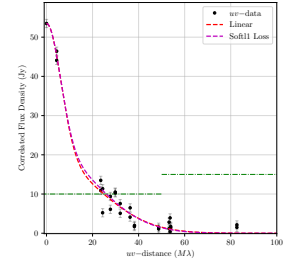
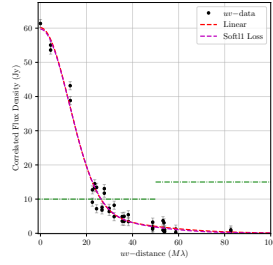
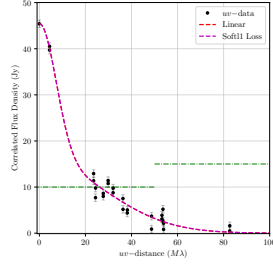
### B.3. ALL MASER SPOT COMPACTNESS



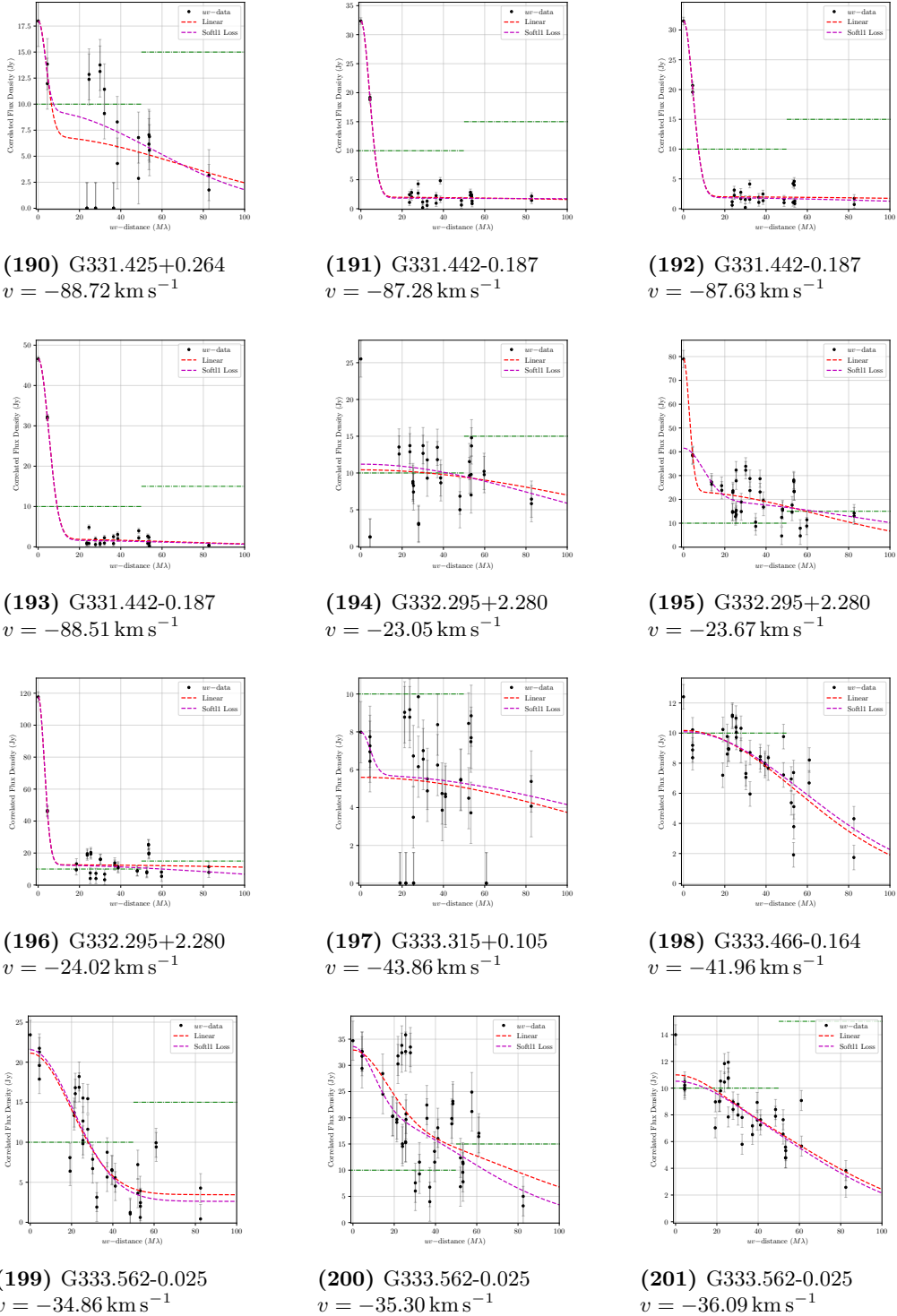
### B.3. ALL MASER SPOT COMPACTNESS



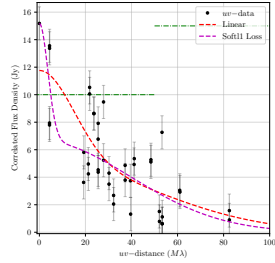
### B.3. ALL MASER SPOT COMPACTNESS



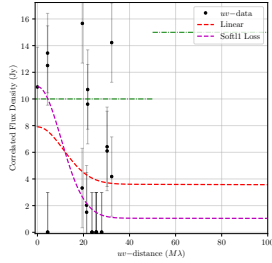
### B.3. ALL MASER SPOT COMPACTNESS



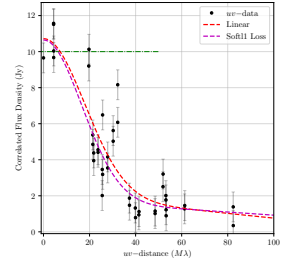
### B.3. ALL MASER SPOT COMPACTNESS



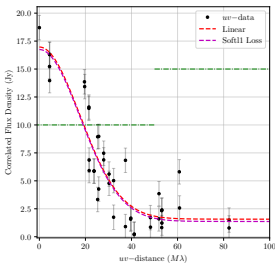
(202) G333.562-0.025  
 $v = -36.44 \text{ km s}^{-1}$



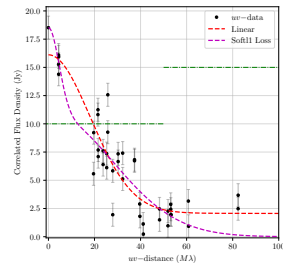
(203) G333.646+0.058  
 $v = -87.39 \text{ km s}^{-1}$



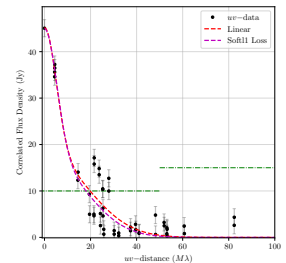
(204) G333.931-0.135  
 $v = -36.94 \text{ km s}^{-1}$



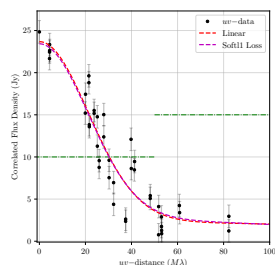
(205) G334.635-0.015  
 $v = -29.13 \text{ km s}^{-1}$



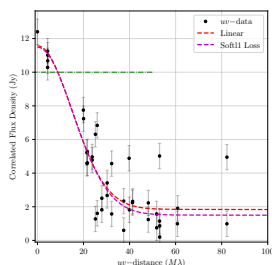
(206) G334.635-0.015  
 $v = -30.18 \text{ km s}^{-1}$



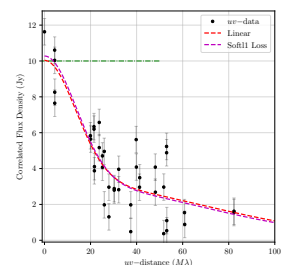
(207) G335.060-0.427  
 $v = -46.93 \text{ km s}^{-1}$



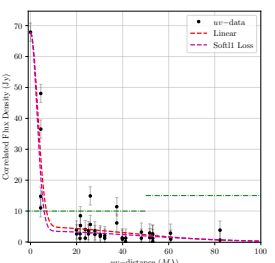
(208) G335.585-0.285  
 $v = -43.88 \text{ km s}^{-1}$



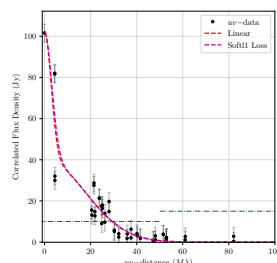
(209) G335.585-0.285  
 $v = -48.19 \text{ km s}^{-1}$



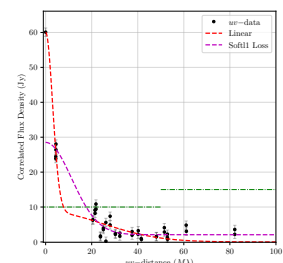
(210) G335.585-0.285  
 $v = -48.62 \text{ km s}^{-1}$



(211) G335.585-0.285  
 $v = -51.43 \text{ km s}^{-1}$

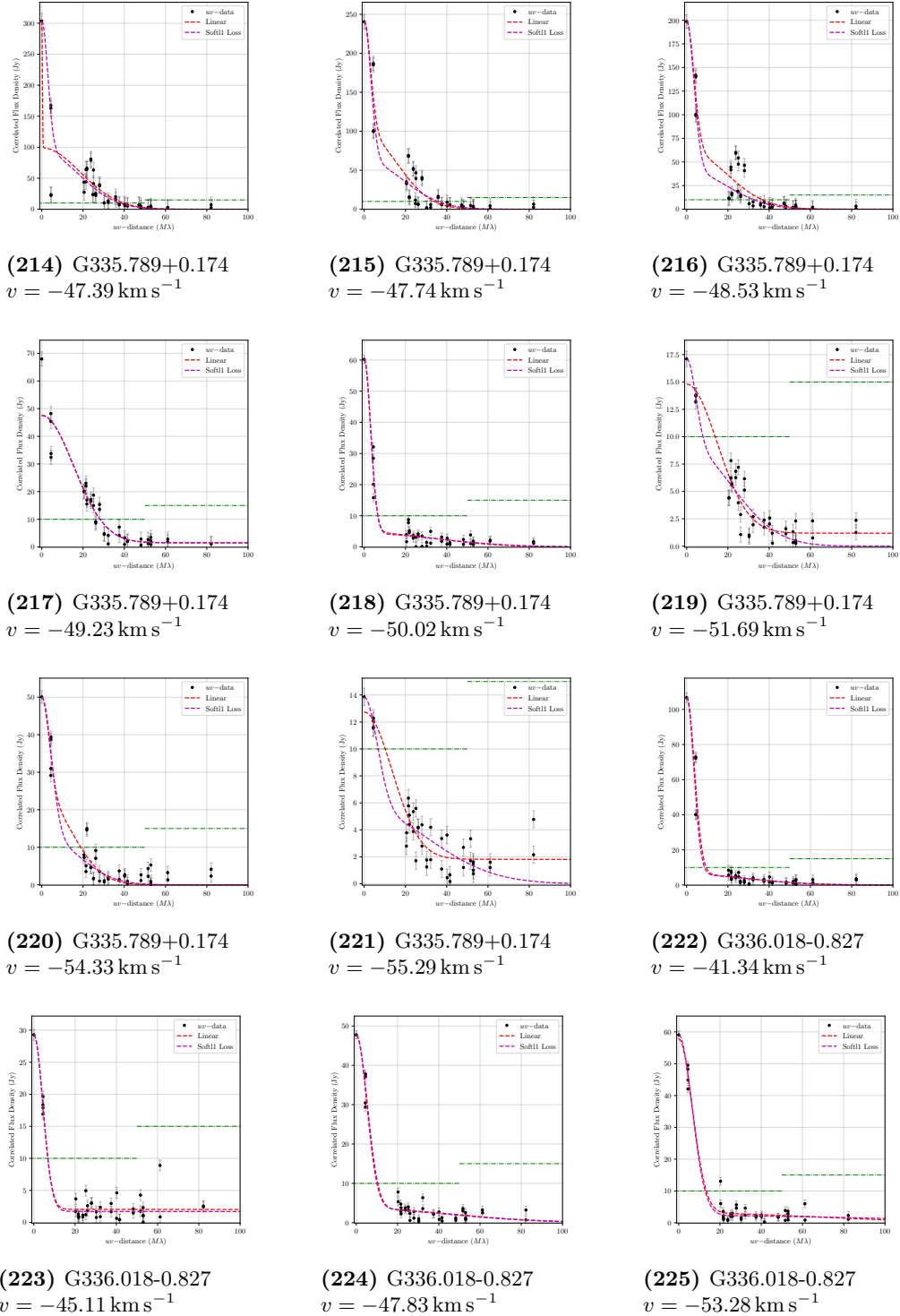


(212) G335.789+0.174  
 $v = -46.16 \text{ km s}^{-1}$

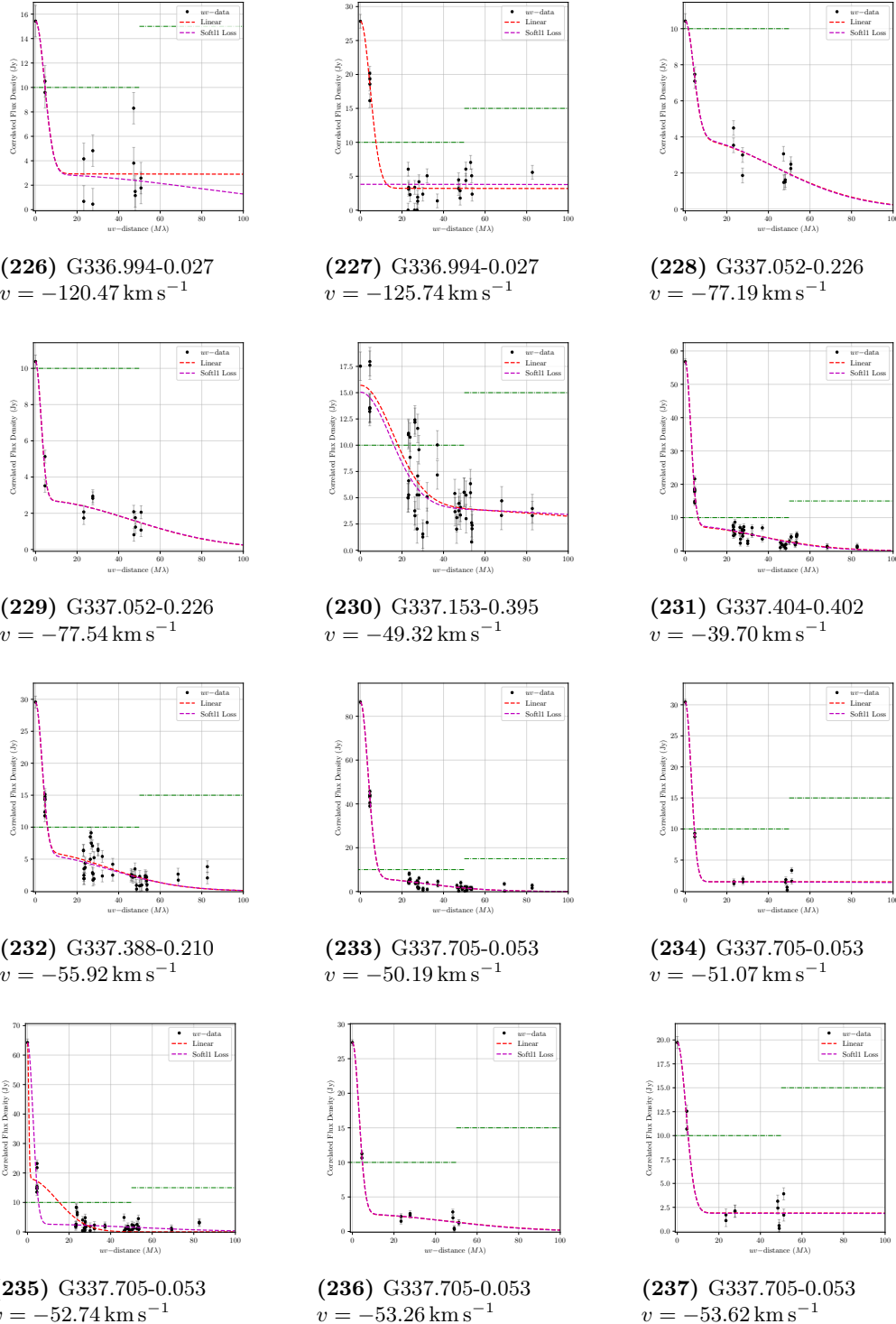


(213) G335.789+0.174  
 $v = -46.60 \text{ km s}^{-1}$

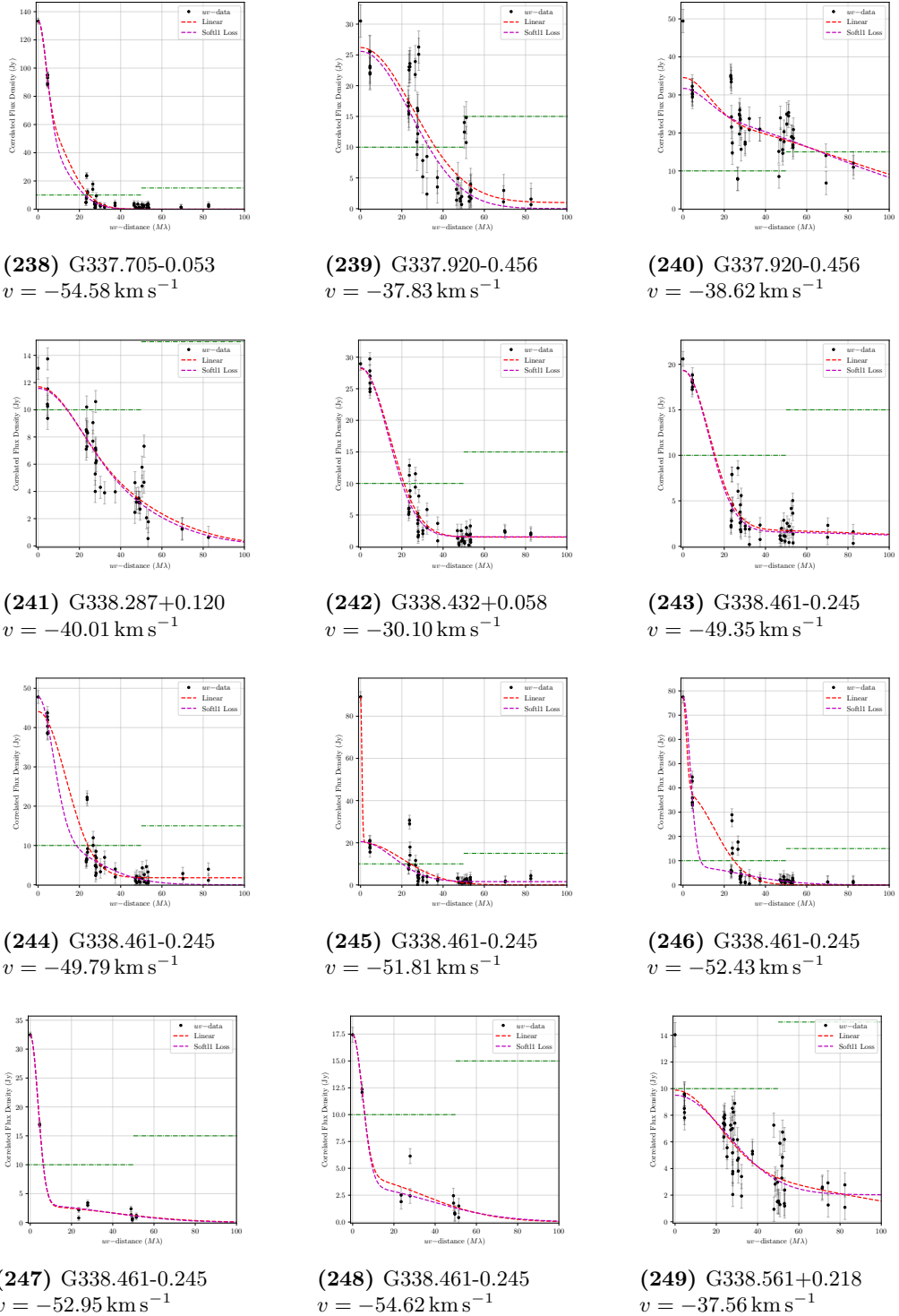
### B.3. ALL MASER SPOT COMPACTNESS



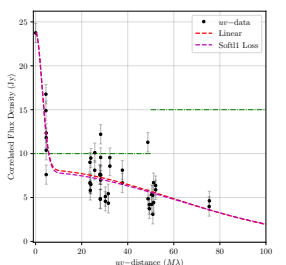
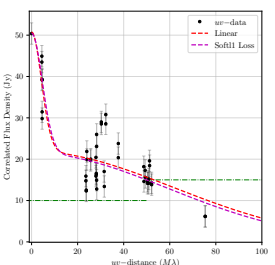
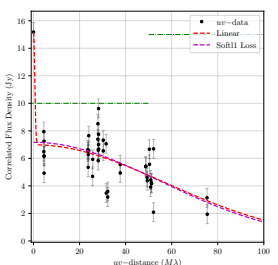
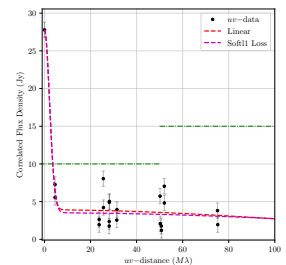
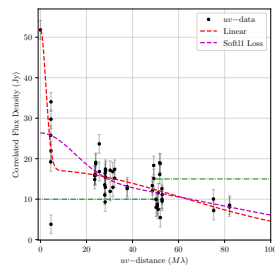
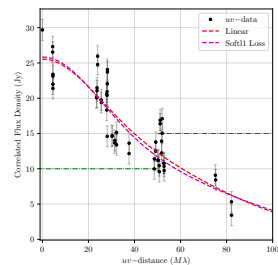
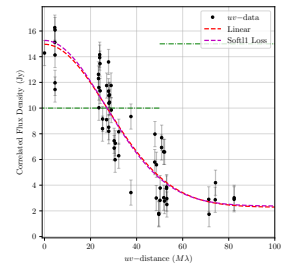
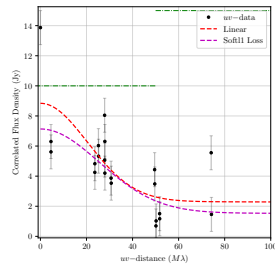
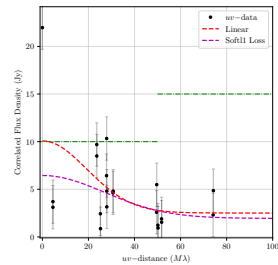
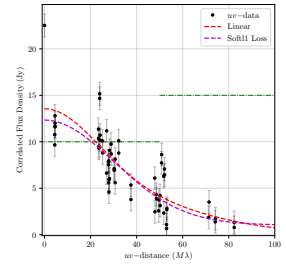
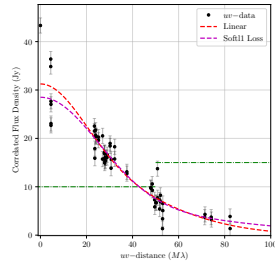
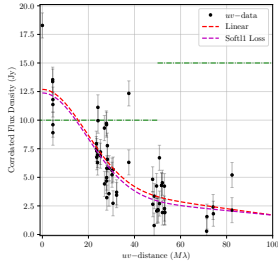
### B.3. ALL MASER SPOT COMPACTNESS



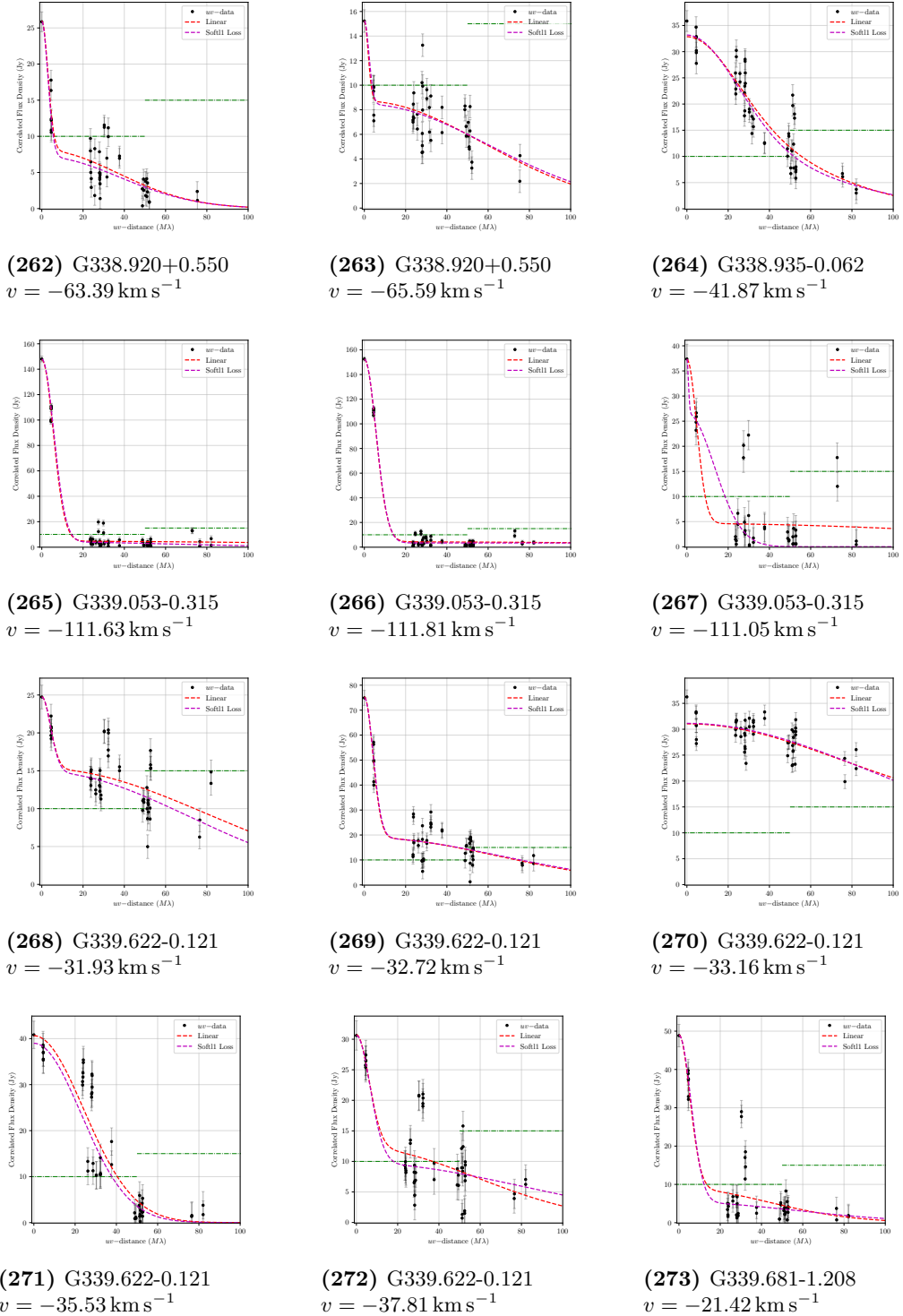
### B.3. ALL MASER SPOT COMPACTNESS



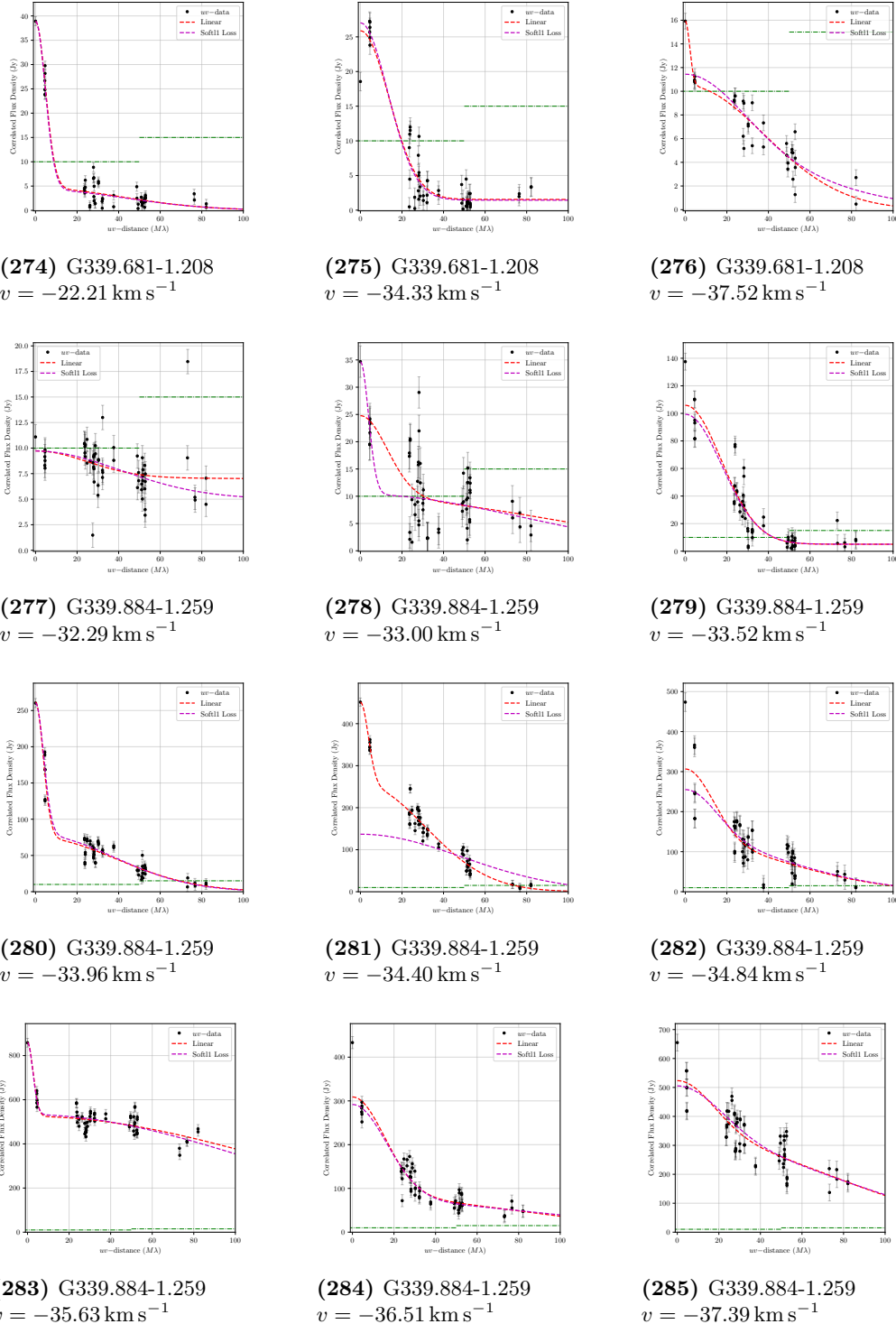
### B.3. ALL MASER SPOT COMPACTNESS



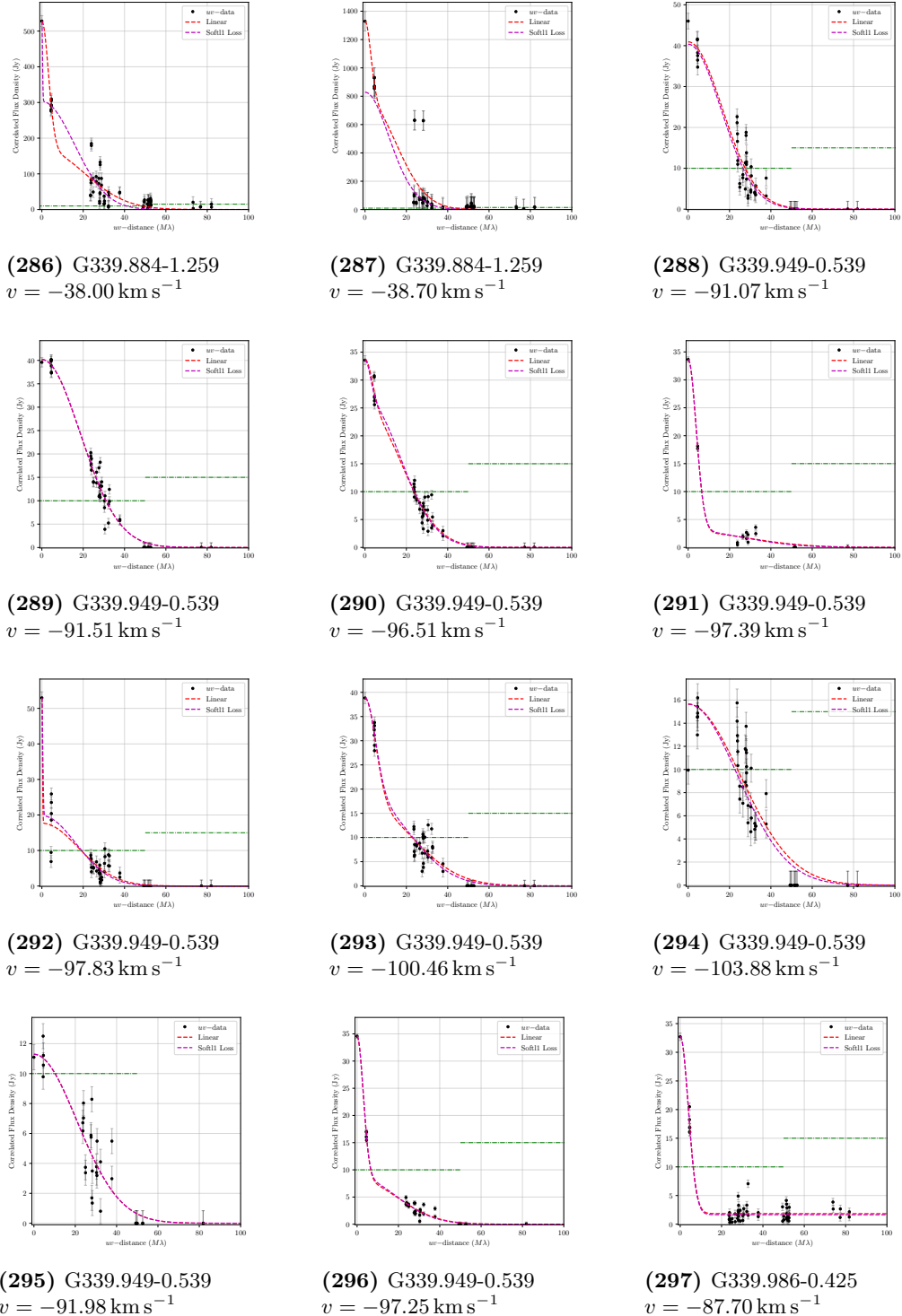
### B.3. ALL MASER SPOT COMPACTNESS



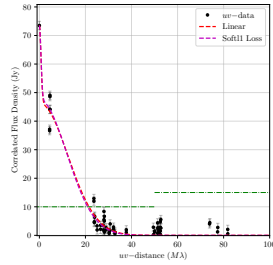
### B.3. ALL MASER SPOT COMPACTNESS



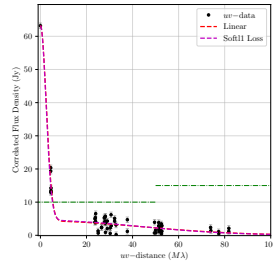
### B.3. ALL MASER SPOT COMPACTNESS



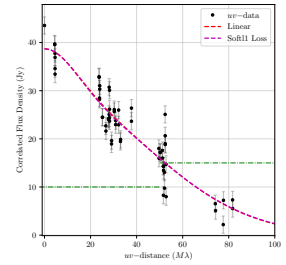
### B.3. ALL MASER SPOT COMPACTNESS



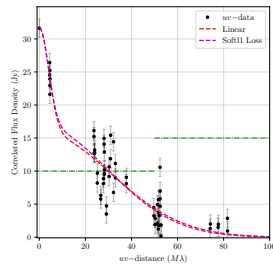
(298) G339.986-0.425  
 $v = -88.49 \text{ km s}^{-1}$



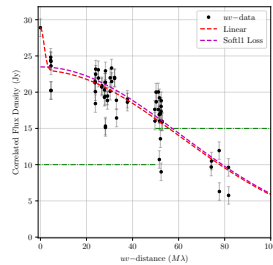
(299) G339.986-0.425  
 $v = -89.19 \text{ km s}^{-1}$



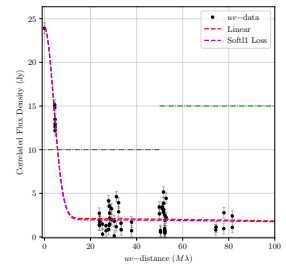
(300) G340.054-0.244  
 $v = -59.36 \text{ km s}^{-1}$



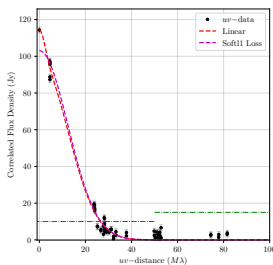
(301) G340.054-0.244  
 $v = -59.72 \text{ km s}^{-1}$



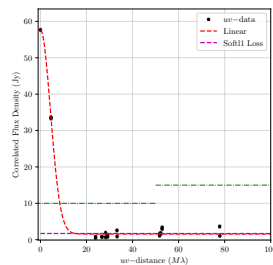
(302) G340.054-0.244  
 $v = -60.86 \text{ km s}^{-1}$



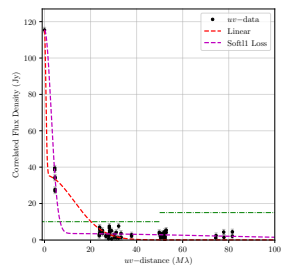
(303) G340.785-0.096  
 $v = -99.07 \text{ km s}^{-1}$



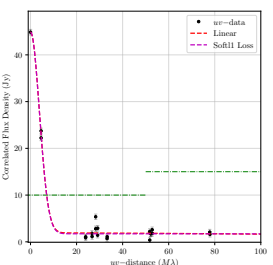
(304) G340.785-0.096  
 $v = -103.72 \text{ km s}^{-1}$



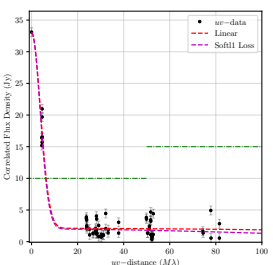
(305) G340.785-0.096  
 $v = -104.69 \text{ km s}^{-1}$



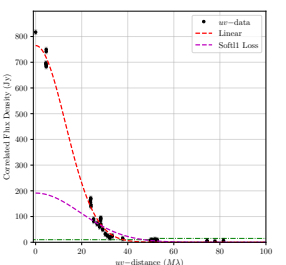
(306) G340.785-0.096  
 $v = -105.13 \text{ km s}^{-1}$



(307) G340.785-0.096  
 $v = -105.48 \text{ km s}^{-1}$

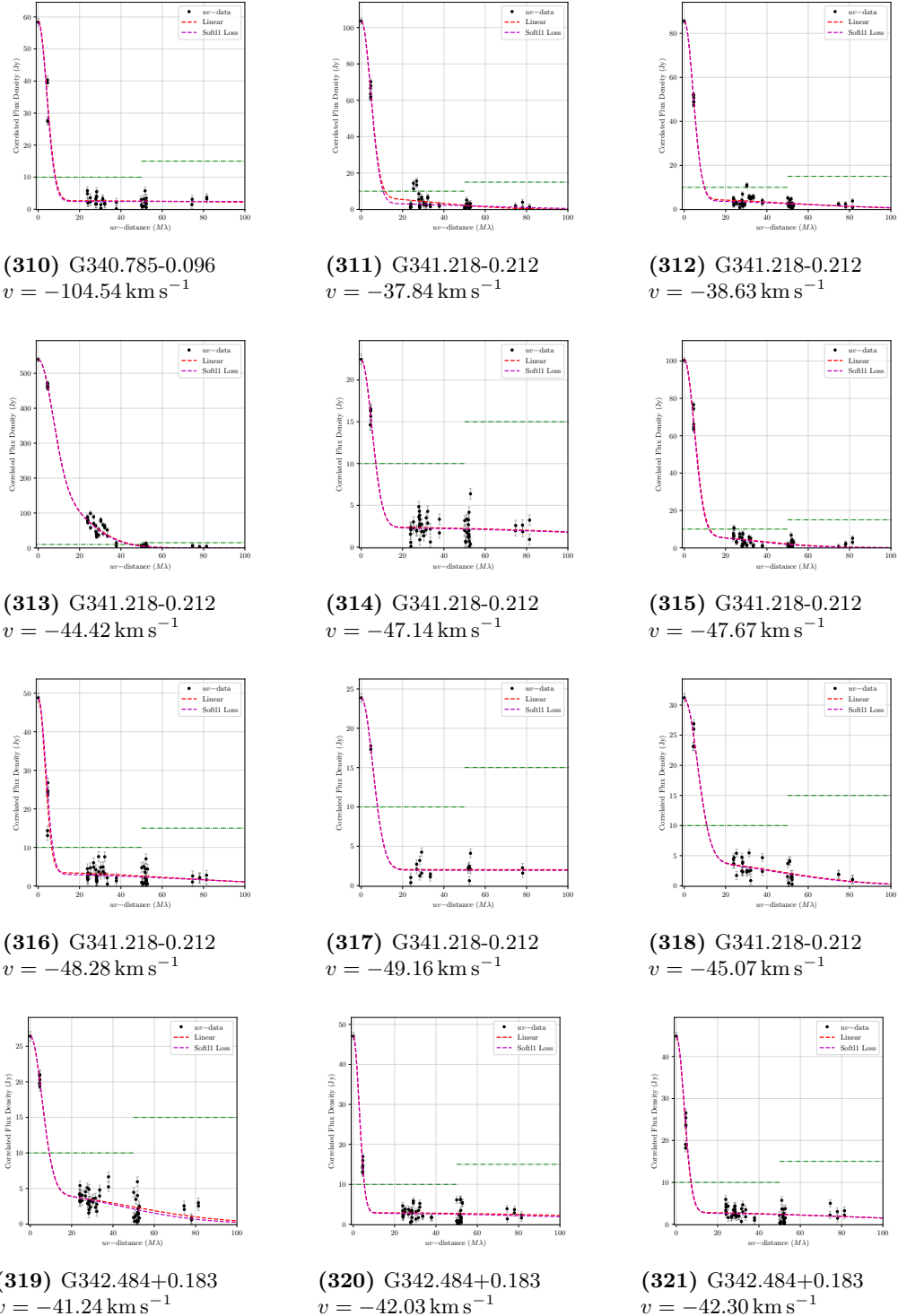


(308) G340.785-0.096  
 $v = -106.00 \text{ km s}^{-1}$

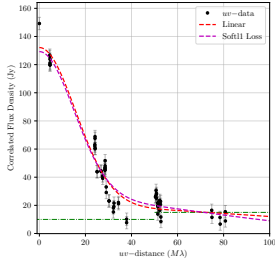


(309) G340.785-0.096  
 $v = -108.02 \text{ km s}^{-1}$

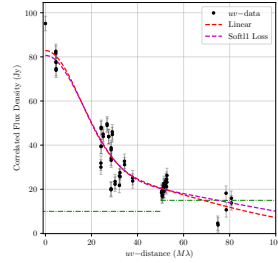
### B.3. ALL MASER SPOT COMPACTNESS



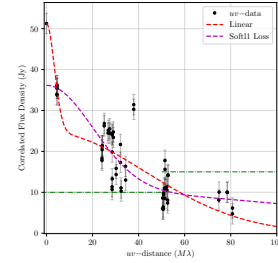
### B.3. ALL MASER SPOT COMPACTNESS



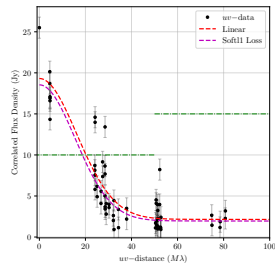
(322) G345.010+1.792  
 $v = -17.02 \text{ km s}^{-1}$



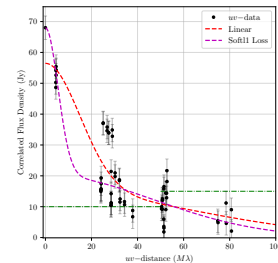
(323) G345.010+1.792  
 $v = -17.46 \text{ km s}^{-1}$



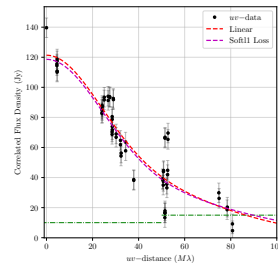
(324) G345.010+1.792  
 $v = -17.90 \text{ km s}^{-1}$



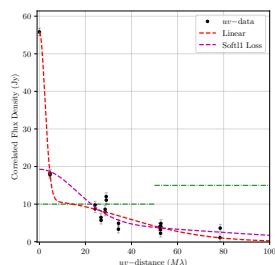
(325) G345.010+1.792  
 $v = -19.30 \text{ km s}^{-1}$



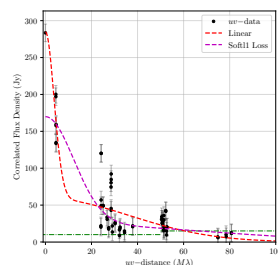
(326) G345.010+1.792  
 $v = -19.83 \text{ km s}^{-1}$



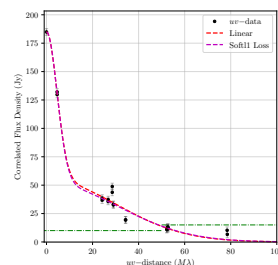
(327) G345.010+1.792  
 $v = -20.18 \text{ km s}^{-1}$



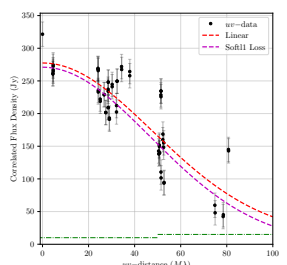
(328) G345.010+1.792  
 $v = -20.62 \text{ km s}^{-1}$



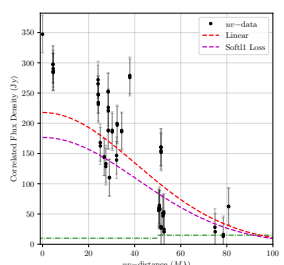
(329) G345.010+1.792  
 $v = -20.97 \text{ km s}^{-1}$



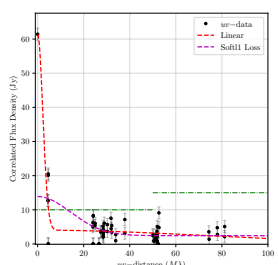
(330) G345.010+1.792  
 $v = -21.24 \text{ km s}^{-1}$



(331) G345.010+1.792  
 $v = -21.76 \text{ km s}^{-1}$

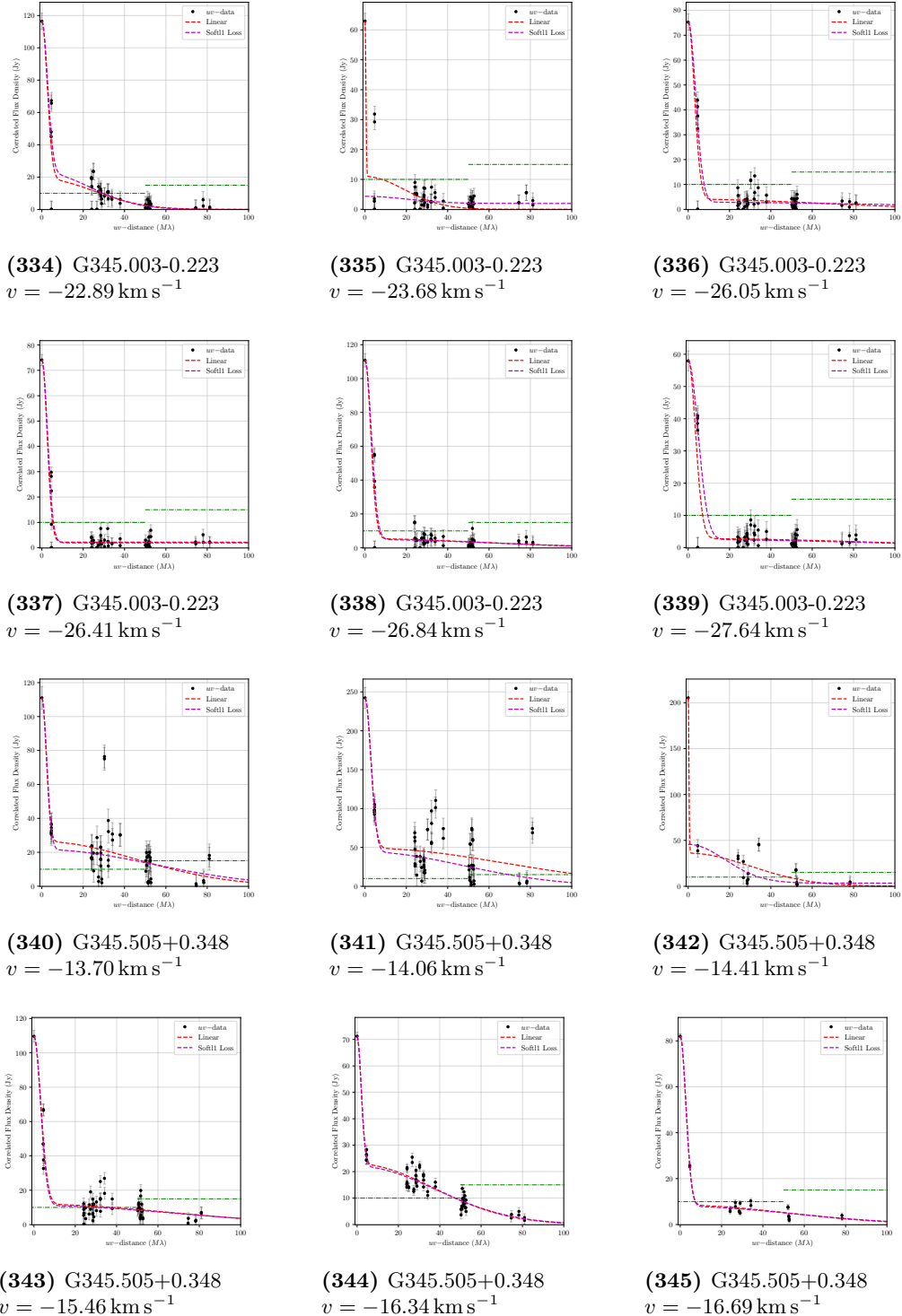


(332) G345.010+1.792  
 $v = -22.03 \text{ km s}^{-1}$

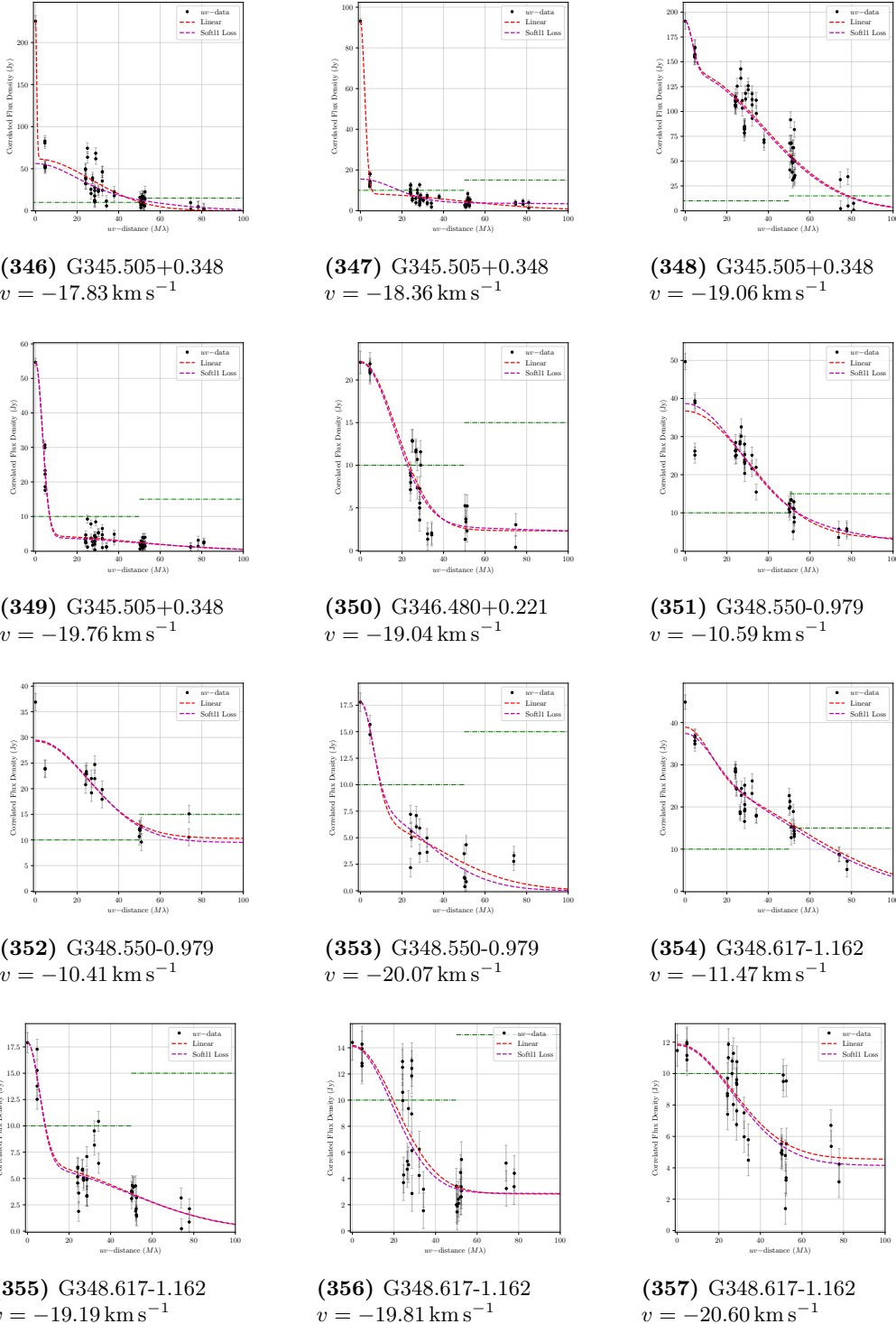


(333) G345.003-0.223  
 $v = -22.37 \text{ km s}^{-1}$

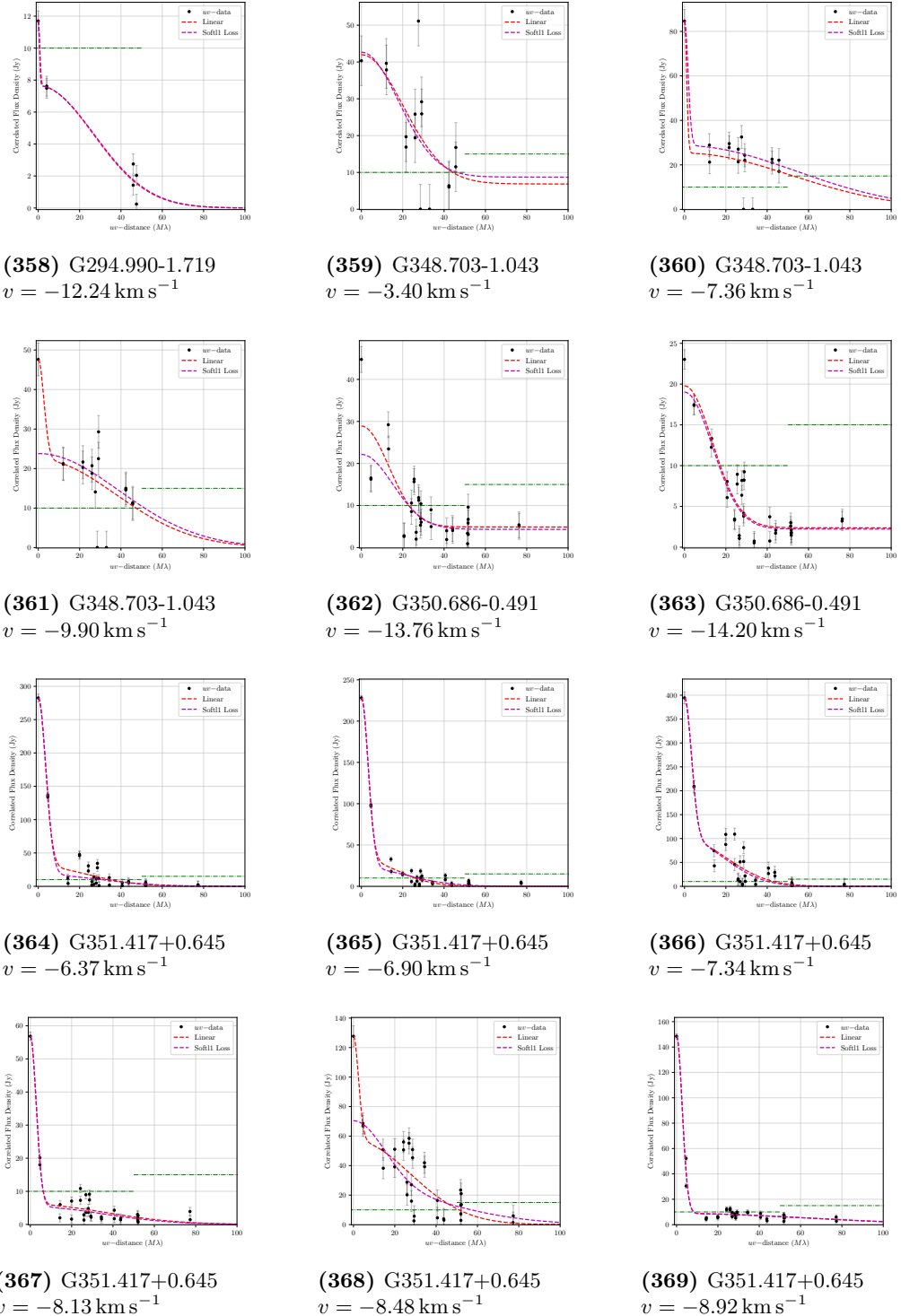
### B.3. ALL MASER SPOT COMPACTNESS



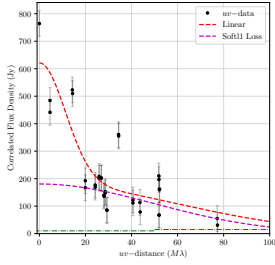
### B.3. ALL MASER SPOT COMPACTNESS



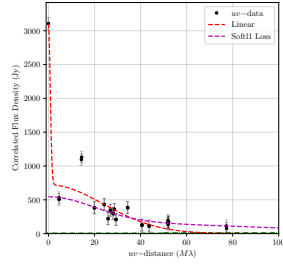
### B.3. ALL MASER SPOT COMPACTNESS



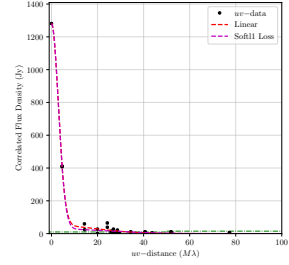
### B.3. ALL MASER SPOT COMPACTNESS



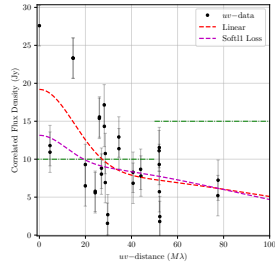
(370) G351.417+0.645  
 $v = -9.71 \text{ km s}^{-1}$



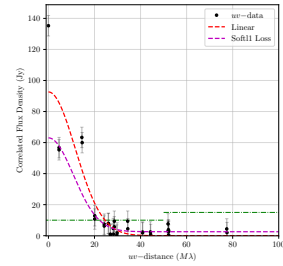
(371) G351.417+0.645  
 $v = -10.32 \text{ km s}^{-1}$



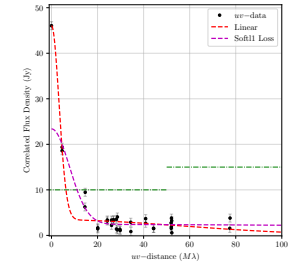
(372) G351.417+0.645  
 $v = -11.11 \text{ km s}^{-1}$



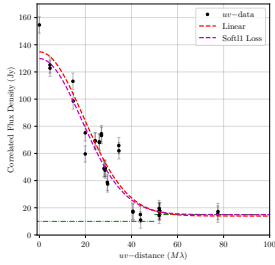
(373) G351.688+0.171  
 $v = -36.07 \text{ km s}^{-1}$



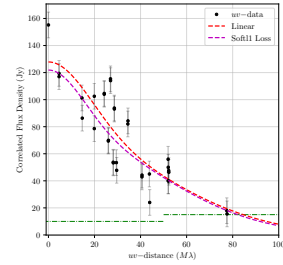
(374) G351.775-0.536  
 $v = 1.80 \text{ km s}^{-1}$



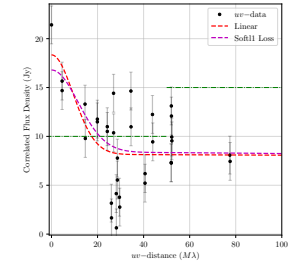
(375) G351.775-0.536  
 $v = 1.27 \text{ km s}^{-1}$



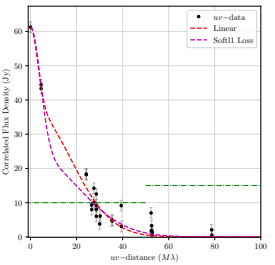
(376) G352.630-1.067  
 $v = -2.91 \text{ km s}^{-1}$



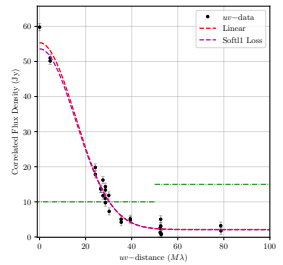
(377) G352.630-1.067  
 $v = -3.27 \text{ km s}^{-1}$



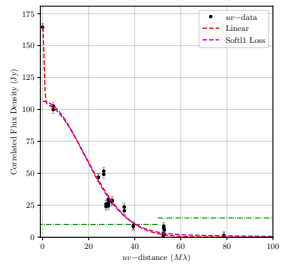
(378) G352.630-1.067  
 $v = -5.28 \text{ km s}^{-1}$



(379) G354.615+0.472  
 $v = -16.48 \text{ km s}^{-1}$

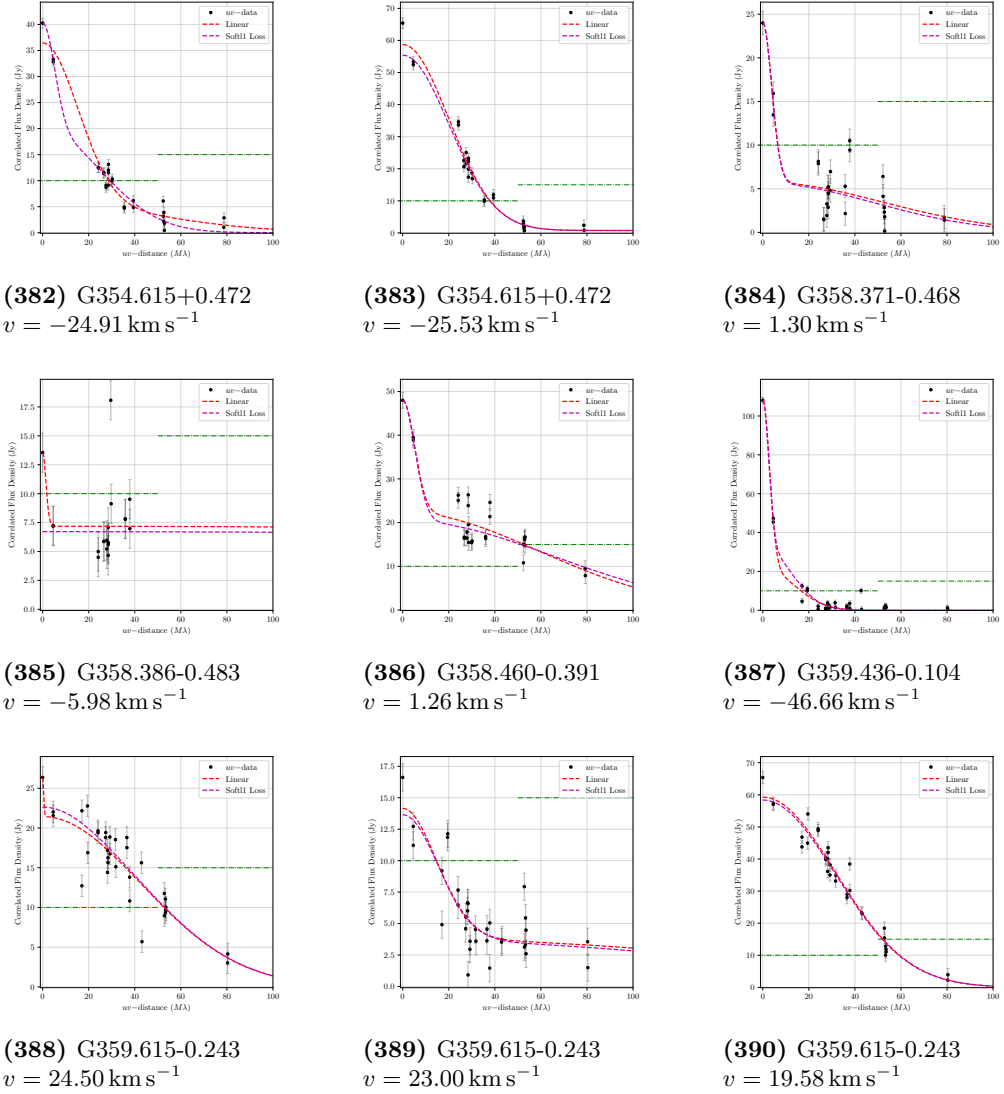


(380) G354.615+0.472  
 $v = -23.16 \text{ km s}^{-1}$



(381) G354.615+0.472  
 $v = -24.21 \text{ km s}^{-1}$

### B.3. ALL MASER SPOT COMPACTNESS







## MULTIVIEW RING CALIBRATION

### C.1 Additional Equations

#### C.1.1 Delay Plane Derivations

In this part of the appendix I want to provide mathematical justification for the planar approximations for baseline, dry tropospheric and source position offset in Section §5.2.

**Baseline Error:** starting from the difference of two LoS geodetic delays caused by a baseline error, I substitute that  $\alpha_1 = \alpha_2 + a$  and  $\delta_1 = \delta_2 + b$ :

$$\begin{aligned} c(\tau_1 - \tau_2) &= \Delta B_x \cos(t - \alpha_1) \cos \delta_1 - \Delta B_y \sin(t - \alpha_1) \cos \delta_1 + \Delta B_z \sin \delta_1 \\ &\quad - \Delta B_x \cos(t - \alpha_2) \cos \delta_2 + \Delta B_y \sin(t - \alpha_2) \cos \delta_2 - \Delta B_z \sin \delta_2 \\ &= \Delta B_x \cos(t - \alpha_2 - a) \cos(\delta_2 + b) - \Delta B_y \sin(t - \alpha_2 - a) \cos(\delta_2 + b) + \Delta B_z \sin(\delta_2 + b) \\ &\quad - \Delta B_x \cos(t - \alpha_2) \cos \delta_2 + \Delta B_y \sin(t - \alpha_2) \cos \delta_2 - \Delta B_z \sin \delta_2 \end{aligned}$$

### C.1. ADDITIONAL EQUATIONS

I can use the double angle formulae to reduce to expression down:

$$\begin{aligned}
\cos(t - \alpha_2 - a) \cos(\delta_2 + b) &= (\cos(t - \alpha_2) \cos a + \sin(t - \alpha_2) \sin a) (\cos \delta_2 \cos b - \sin \delta_2 \sin b) \\
&= \left( \cos(t - \alpha_2) \left( 1 - \frac{a^2}{2} \right) + a \sin(t - \alpha_2) \right) \left( \cos \delta_2 \left( 1 - \frac{b^2}{2} \right) - b \sin \delta_2 \right) \\
&= \cos(t - \alpha_2) \cos \delta_2 \left( 1 - \frac{a^2}{2} - \frac{b^2}{2} \right) - b \cos(t - \alpha_2) \sin \delta_2 - a \sin(t - \alpha_2) \cos \delta_2 \\
&\quad + a b \sin(t - \alpha_2) \sin \delta_2 \\
\\
\sin(t - \alpha_2 - a) \cos(\delta_2 + b) &= (\sin(t - \alpha_2) \cos a - \cos(t - \alpha_2) \sin a) (\cos \delta_2 \cos b - \sin \delta_2 \cos b) \\
&= \sin(t - \alpha_2) \cos \delta_2 \left( 1 - \frac{a^2}{2} - \frac{b^2}{2} \right) + b \sin(t - \alpha_2) \sin \delta_2 + a \cos(t - \alpha_2) \cos \delta_2 \\
&\quad - a b \cos(t - \alpha_2) \sin \delta_2 \\
\\
\sin(\delta_2 + b) &= \sin \delta_2 \cos b + \cos \delta_2 \sin b \\
&= \sin \delta_2 \left( 1 - \frac{b^2}{2} \right) + b \cos \delta_2
\end{aligned}$$

where I have omitted terms with  $O^3$  or greater. All  $O^0$  terms cancel with the second half of the original expression. If I group terms by  $\mathbf{a}$ ,  $\mathbf{b}$ ,  $\mathbf{a}^2$ , ...,  $\mathbf{a} \times \mathbf{b}$  I arrive at:

$$\begin{aligned}
c(\tau_1 - \tau_2) &= \mathbf{a} (-\Delta B_x \sin(t - \alpha_2) \cos \delta_2 + \Delta B_y \cos(t - \alpha_2) \cos \delta_2) \\
&\quad + \mathbf{b} (-\Delta B_x \cos(t - \alpha_2) \sin \delta_2 + \Delta B_y \sin(t - \alpha_2) \sin \delta_2 + \Delta B_z \cos \delta_2) \\
&\quad + \mathbf{a} \mathbf{b} (\Delta B_x \sin(t - \alpha_2) \sin \delta_2 - \Delta B_y \cos(t - \alpha_2) \sin \delta_2) \\
&\quad + \frac{\mathbf{a}^2}{2} (-\Delta B_x \cos(t - \alpha_2) \cos \delta_2 + \Delta B_y \sin(t - \alpha_2) \cos \delta_2) \\
&\quad + \frac{\mathbf{b}^2}{2} (-\Delta B_x \cos(t - \alpha_2) \cos \delta_2 + \Delta B_y \sin(t - \alpha_2) \cos \delta_2 - \Delta B_z \sin \delta_2) \\
&= \mathbf{a} \mathcal{A}_{bl} + \mathbf{b} \mathcal{B}_{bl} + \mathbf{a} \mathbf{b} \mathcal{C}_{bl} + \frac{1}{2} \mathbf{a}^2 \mathcal{D}_{bl} + \frac{1}{2} \mathbf{b}^2 \mathcal{E}_{bl}
\end{aligned} \tag{C.1}$$

If  $\mathbf{a}$ ,  $\mathbf{b}$  are ‘small’ then the  $O^2$  terms are comparatively reduced.

**Dry Tropospheric Error** I have a target (T) and calibrator (C) at respective coordinates  $(\alpha, \delta)$  for a sample telescope at Earth latitude  $\varphi$ . The target and calibrator are (as in the previous derivation) offset from one another  $\mathbf{a}$  radians in RA and  $\mathbf{b}$  radians in DEC.

$$\begin{aligned}
\Delta \tau_{dtr} &= \sigma_{\tau_z} \left( \frac{1}{\cos Z_C} - \frac{1}{\cos Z_T} \right) \\
&= \sigma_{\tau_z} F \\
\therefore F &= (\sin \delta_C \sin \varphi + \cos \delta_C \cos \varphi \cos(t_{lst} - \alpha_C))^{-1} \\
&\quad - (\sin \delta_T \sin \varphi + \cos \delta_T \cos \varphi \cos(t_{lst} - \alpha_T))^{-1} \\
F(\mathbf{a}, \mathbf{b}) &= (\sin(\delta_T + \mathbf{b}) \sin \varphi + \cos(\delta_T + \mathbf{b}) \cos \varphi \cos(t_{lst} - \alpha_T - \mathbf{a}))^{-1} \\
&\quad - (\sin \delta_T \sin \varphi + \cos \delta_T \cos \varphi \cos(t_{lst} - \alpha_T))^{-1}
\end{aligned} \tag{C.2}$$

This function  $F$  is obviously more complex than in the previous example. While it is possible to Taylor expand the sin and cos terms, it is easier to perform a 2D McLaren expansion and determine magnitudes

### C.1. ADDITIONAL EQUATIONS

after:

$$F(\mathbf{a}, \mathbf{b}) = F(0, 0) + F_a(0, 0) \mathbf{a} + F_b(0, 0) \mathbf{b} + F_{aa}(0, 0) \frac{1}{2} \mathbf{a}^2 + F_{ab}(0, 0) \frac{1}{2} \mathbf{a}\mathbf{b} + F_{bb}(0, 0) \frac{1}{2} \mathbf{b}^2 + \sigma_{O^3}$$

where  $F_a = \frac{\partial F}{\partial a}$ ,  $F_{ab} = \frac{\partial^2 F}{\partial a \partial b}$  etc.

I am going to let  $h_T = t_{lst} - \alpha_T$  as the hour angle for the target and

$$\kappa = \sin(\delta_T + \mathbf{b}) \sin \varphi + \cos(\delta_T + \mathbf{b}) \cos \varphi \cos(h_T - \mathbf{a})$$

as it appears frequently. Performing the partial derivatives gives:

$$\begin{aligned} F_a(\mathbf{a}, \mathbf{b}) &= \frac{1}{\kappa^2} (-\cos(\delta_T + \mathbf{b}) \cos \varphi \sin(h_T - \mathbf{a})) \\ F_b(\mathbf{a}, \mathbf{b}) &= \frac{1}{\kappa^2} (\cos \varphi \cos(h_T - \mathbf{a}) \sin(\delta_T + \mathbf{b}) - \sin \varphi \cos(\delta_T + \mathbf{b})) \\ F_{aa}(\mathbf{a}, \mathbf{b}) &= \frac{1}{\kappa^3} (\cos \varphi \cos(\delta_T + \mathbf{b}) (\cos \varphi \cos(\delta_T + \mathbf{b}) (1 + \sin^2(h_T + \mathbf{a})) + \sin \varphi \cos(h_T + \mathbf{a}) \sin(\delta_T + \mathbf{b}))) \\ F_{ab}(\mathbf{a}, \mathbf{b}) &= \frac{1}{\kappa^3} (-\cos \varphi \sin(h_T - \mathbf{a}) (\cos \varphi \cos(h_T + \mathbf{a}) \sin(\delta_T + \mathbf{b}) \cos(\delta_T + \mathbf{b}) - \sin \varphi (\cos^2(\delta_T + \mathbf{b})))) \\ F_{bb}(\mathbf{a}, \mathbf{b}) &= \frac{1}{\kappa} + \frac{2}{\kappa^3} (\cos \varphi \cos(h_T - \mathbf{a}) \sin(\delta_T + \mathbf{b}) - \sin \varphi \cos(\delta_T + \mathbf{b}))^2 \end{aligned}$$

And evaluating them at  $(\mathbf{a}, \mathbf{b}) = (0, 0)$  gives:

$$\begin{aligned} F(0, 0) &= 0 \\ F_a(0, 0) &= \frac{-1}{\cos^2 Z_T} \cos \delta_T \cos \varphi \sin h_T \\ F_b(0, 0) &= \frac{1}{\cos^2 Z_T} (\cos \varphi \cos h_T \sin \delta_T - \sin \varphi \cos \delta_T) \\ F_{aa}(0, 0) &= \frac{1}{\cos^3 Z_T} (\cos \varphi \cos \delta_T (\cos \varphi \cos \delta_T (1 + \sin^2 h_T) + \sin \varphi \cos h_T) \sin \delta_T) \\ F_{ab}(0, 0) &= \frac{-1}{\cos^3 Z_T} \cos \varphi \sin h_T (\cos \varphi \cos h_T \sin \delta_T \cos \delta_T - \sin \varphi (\cos^2 \delta_T + 1)) \\ F_{bb}(0, 0) &= \frac{1}{\cos Z_T} + \frac{2}{\cos^3 Z_T} (\cos \varphi \cos h_T \sin \delta_T - \sin \varphi \cos \delta_T)^2 \end{aligned}$$

And therefore total delay slope is:

$$\begin{aligned} \Delta \tau_{dtr} &= \sigma_{\tau_z} \left( F(0, 0) + F_a(0, 0) \mathbf{a} + F_b(0, 0) \mathbf{b} + F_{aa}(0, 0) \frac{1}{2} \mathbf{a}^2 + F_{ab}(0, 0) \frac{1}{2} \mathbf{a}\mathbf{b} + F_{bb}(0, 0) \frac{1}{2} \mathbf{b}^2 \right) + \sigma_{O^3} \\ &= \mathbf{a} \mathcal{A}_{dtr} + \mathbf{b} \mathcal{B}_{dtr} + \mathbf{a} \mathbf{b} \mathcal{C}_{dtr} + \frac{1}{2} \mathbf{a}^2 \mathcal{D}_{dtr} + \frac{1}{2} \mathbf{b}^2 \mathcal{E}_{dtr} + \sigma_{O^3} \end{aligned}$$

### C.1. ADDITIONAL EQUATIONS

**Source Position Error** starting from the difference of two delays caused by a position errors in the target  $\sigma_C$  and calibrator error  $\sigma_{C'}$ , I substitute that  $\alpha_C = \alpha_T + a$  and  $\delta_C = \delta_T + b$ :

$$\begin{aligned}
c(\tau_{\theta,C} - \tau_{\theta,T}) &= c\Delta\tau_\theta = \sigma_{\alpha,C} \cos \delta_C (B_x \sin(t - \alpha_C) + B_y \cos(t - \alpha_C)) \\
&\quad + \sigma_{\delta,C} (-B_x \cos(t - \alpha_C) \sin \delta_C + B_y \sin(t - \alpha_C) \sin \delta_C + B_z \cos \delta_C) \\
&\quad - \sigma_{\alpha,T} \cos \delta_T (B_x \sin(t - \alpha_T) + B_y \cos(t - \alpha_T)) \\
&\quad - \sigma_{\delta,T} (-B_x \cos(t - \alpha_T) \sin \delta_T + B_y \sin(t - \alpha_T) \sin \delta_T + B_z \cos \delta_T) \\
&= \sigma_{\alpha,C} \cos(\delta_T + b) (B_x \sin(t - \alpha_T - a) + B_y \cos(t - \alpha_T - a)) \\
&\quad + \sigma_{\delta,C} (-B_x \cos(t - \alpha_T - a) \sin(\delta_T + b) + B_y \sin(t - \alpha_T - a) \sin(\delta_T + b) + B_z \cos(\delta_T + b)) \\
&\quad - \sigma_{\alpha,T} \cos \delta_T (B_x \sin(t - \alpha_T) + B_y \cos(t - \alpha_T)) \\
&\quad - \sigma_{\delta,T} (-B_x \cos(t - \alpha_T) \sin \delta_T + B_y \sin(t - \alpha_T) \sin \delta_T + B_z \cos \delta_T)
\end{aligned}$$

where  $\sigma_\alpha$  and  $\sigma_\delta$  are the positional uncertainties in Right Ascension and Declination respectively.

I can use the expansions for  $\cos(t - \alpha_T - a) \cos(\delta_T + b)$ ,  $\sin(t - \alpha_T - a) \cos(\delta_T + b)$  and  $\sin(\delta_T + b)$  shown in Section §C.1.1 as well as the expansions below:

$$\begin{aligned}
\cos(t - \alpha_T - a) \sin(\delta_T + b) &= (\cos(t - \alpha_T) \cos a + \sin(t - \alpha_T) \sin a) (\sin \delta_T \cos b + \cos \delta_T \sin b) \\
&= \left( \cos(t - \alpha_T) \left( 1 - \frac{a^2}{2} \right) + a \sin(t - \alpha_T) \right) \left( \sin \delta_T \left( 1 - \frac{b^2}{2} \right) + b \cos \delta_T \right) \\
&= \cos(t - \alpha_T) \sin \delta_T \left( 1 - \frac{a^2}{2} - \frac{b^2}{2} \right) + a \sin(t - \alpha_T) \sin \delta_T + b \cos(t - \alpha_T) \cos \delta_T \\
&\quad + a b \sin(t - \alpha_T) \cos \delta_T
\end{aligned}$$

$$\begin{aligned}
\sin(t - \alpha_T - a) \sin(\delta_T + b) &= (\sin(t - \alpha_T) \cos a - \cos(t - \alpha_T) \sin a) (\sin \delta_T \cos b + \cos \delta_T \sin b) \\
&= \sin(t - \alpha_T) \sin \delta_T \left( 1 - \frac{a^2}{2} - \frac{b^2}{2} \right) - a \cos(t - \alpha_T) \sin \delta_T + b \sin(t - \alpha_T) \cos \delta_T \\
&\quad - a b \cos(t - \alpha_T) \cos \delta_T
\end{aligned}$$

$$\begin{aligned}
\cos(\delta_T + b) &= \cos \delta_T \cos b - \sin \delta_T \sin b \\
&= \cos \delta_T \left( 1 - \frac{b^2}{2} \right) - b \sin \delta_T
\end{aligned}$$

## C.1. ADDITIONAL EQUATIONS

If I substitute the expansions then collect terms in  $\mathbf{a}$ ,  $\mathbf{b}$ ,  $\mathbf{ab}$ ,  $\mathbf{a}^2$  and  $\mathbf{b}^2$  I am left with:

$$\begin{aligned}
c\Delta\tau_\theta = & [(\sigma_{\alpha,C} - \sigma_{\alpha,T}) \cos \delta_T (B_x \sin(t - \alpha_T) + B_y \cos(t - \alpha_T)) \\
& + (\sigma_{\delta,C} - \sigma_{\delta,T}) (B_x \sin \delta_T \cos(t - \alpha_T) - B_y \sin \delta_T \sin(t - \alpha_T) - B_z \cos \delta_T)] \\
& + \mathbf{a} [-\sigma_{\alpha,C} \cos \delta_T (B_x \cos(t - \alpha_T) + B_y \sin(t - \alpha_T)) \\
& \quad - \sigma_{\delta,C} \sin \delta_T (B_x \sin(t - \alpha_T) + B_y \cos(t - \alpha_T))] \\
& + \mathbf{b} [\sigma_{\alpha,C} \sin \delta_T (B_x \sin(t - \alpha_T) + B_y \cos(t - \alpha_T)) \\
& \quad + \sigma_{\delta,C} (B_x \cos \delta_T \cos(t - \alpha_T) - B_y \cos \delta_T \sin(t - \alpha_T) + B_z \sin \delta_T)] \\
& - \left( \frac{\mathbf{a}^2}{2} + \frac{\mathbf{b}^2}{2} \right) [\sigma_{\alpha,C} \cos \delta_T (B_x \sin(t - \alpha_T) + B_y \cos(t - \alpha_T)) \\
& \quad + \sigma_{\delta,C} (B_x \sin \delta_T \cos(t - \alpha_T) - B_y \sin \delta_T \sin(t - \alpha_T))] \\
& - \frac{\mathbf{b}^2}{2} B_z \cos \delta_T \\
& + \mathbf{ab} [-\sigma_{\alpha,C} B_x \cos(t - \alpha_T) \sin \delta_T + \sigma_{\alpha,C} B_y \sin(t - \alpha_T) \sin \delta_T \\
& \quad - \sigma_{\delta,C} B_x \sin(t - \alpha_T) \cos \delta_T - \sigma_{\delta,C} B_y \cos(t - \alpha_T) \cos \delta_T]
\end{aligned}$$

### C.1.2 Finite Sum of Angles

Here I show justification for an expression given in text:

$$\begin{aligned}
S &= \sum_{i=1}^N R_i^2 \cos^2(\theta_i + \psi) \\
&= \sum_{i=1}^N \frac{R_i^2}{2} (1 + \cos(2\theta_i + 2\psi)) \\
&= N \frac{\bar{R}^2}{2} + \sum_{i=1}^N \frac{R_i^2}{2} (\cos 2\psi \cos 2\theta_i - \sin 2\psi \sin 2\theta_i)
\end{aligned}$$

In the rings we have  $R_i \approx \bar{R}$  and  $\theta_i = \frac{2\pi(i-1)}{N}$  aka. azimuthally well sampled. Continuing:

$$\begin{aligned}
S &= N \frac{\bar{R}^2}{2} + \frac{\bar{R}^2}{2} \left( \cos 2\psi \sum_{i=1}^N \left( \cos \frac{4\pi(i-1)}{N} \right) - \sin 2\psi \sum_{i=1}^N \left( \sin \frac{4\pi(i-1)}{N} \right) \right) \\
&= N \frac{\bar{R}^2}{2} + \frac{\bar{R}^2}{2} \cos 2\psi \left( \cos \left( \frac{4\pi}{N} \right) \sum_{i=1}^N \cos \left( \frac{4\pi}{N} i \right) + \sin \left( \frac{4\pi}{N} \right) \sum_{i=1}^N \sin \left( \frac{4\pi}{N} i \right) \right) \\
&\quad - \frac{\bar{R}^2}{2} \sin 2\psi \left( \cos \left( \frac{4\pi}{N} \right) \sum_{i=1}^N \sin \left( \frac{4\pi}{N} i \right) - \sin \left( \frac{4\pi}{N} \right) \sum_{i=1}^N \cos \left( \frac{4\pi}{N} i \right) \right)
\end{aligned}$$

The trigonometric identities

$$\begin{aligned}
\sum_{n=1}^N \cos(n\theta) &= -\frac{1}{2} + \frac{\sin \theta(N + \frac{1}{2})}{2 \sin \frac{\theta}{2}} \\
\sum_{n=1}^N \sin(n\theta) &= \frac{1}{2} \cot \frac{\theta}{2} - \frac{\cos \theta(N + \frac{1}{2})}{2 \sin \frac{\theta}{2}}
\end{aligned}$$

### C.1. ADDITIONAL EQUATIONS

can be used to simplify the expression. Since  $\theta = \frac{4\pi}{N}$  it should first be noted that:

$$\begin{aligned}\cos \frac{4\pi}{N}(N + \frac{1}{2}) &= \cos(\frac{2\pi}{N}) \\ \sin \frac{4\pi}{N}(N + \frac{1}{2}) &= \sin(\frac{2\pi}{N})\end{aligned}$$

Therefore:

$$\begin{aligned}\sum_{i=1}^N \cos\left(\frac{4\pi}{N}i\right) &= -\frac{1}{2} + \frac{\sin(\frac{2\pi}{N})}{2\sin(\frac{2\pi}{N})} = 0 \\ \sum_{i=1}^N \sin\left(\frac{4\pi}{N}i\right) &= \frac{1}{2} \cot \frac{2\pi}{N} - \frac{\cos(\frac{2\pi}{N})}{2\sin(\frac{2\pi}{N})} = 0 \\ \therefore \sum_{i=1}^N (R_i \cos(\theta_i + \psi))^2 &= \frac{\overline{R^2}}{2} N = \frac{\overline{R^2} + \sigma_R^2}{2} N\end{aligned}$$

where  $\overline{R^2}$  is the square of the mean,  $\overline{R^2}$  is the mean squared and  $\sigma_R^2$  is the variance of  $R$ .

### C.1. ADDITIONAL EQUATIONS

## C.2 Additional Figures

### C.2.1 Raw Phases

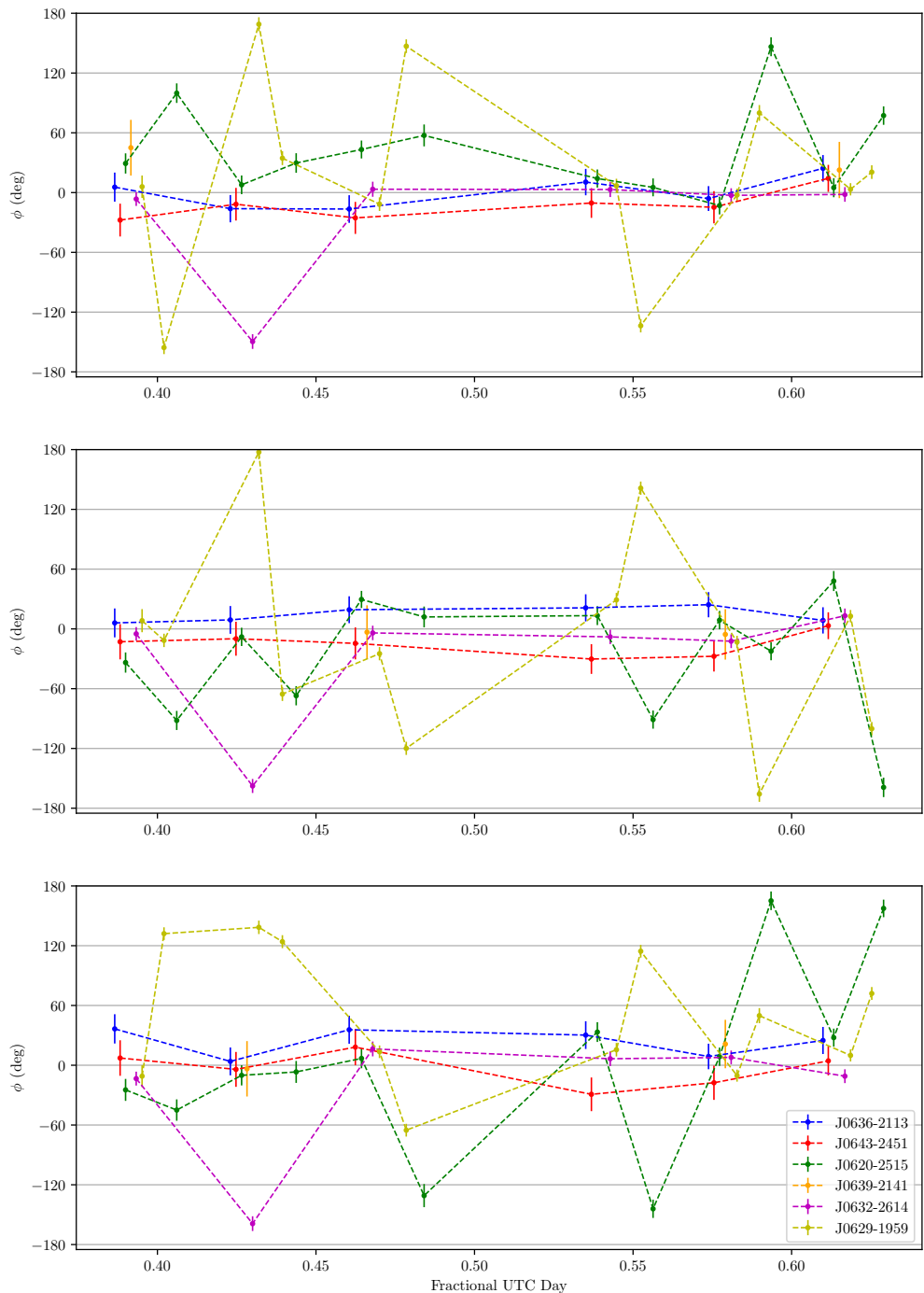


**Figure C.1:** G0634-2335  $\bar{R} = 3$  deg Ring, MV025

## C.2. ADDITIONAL FIGURES

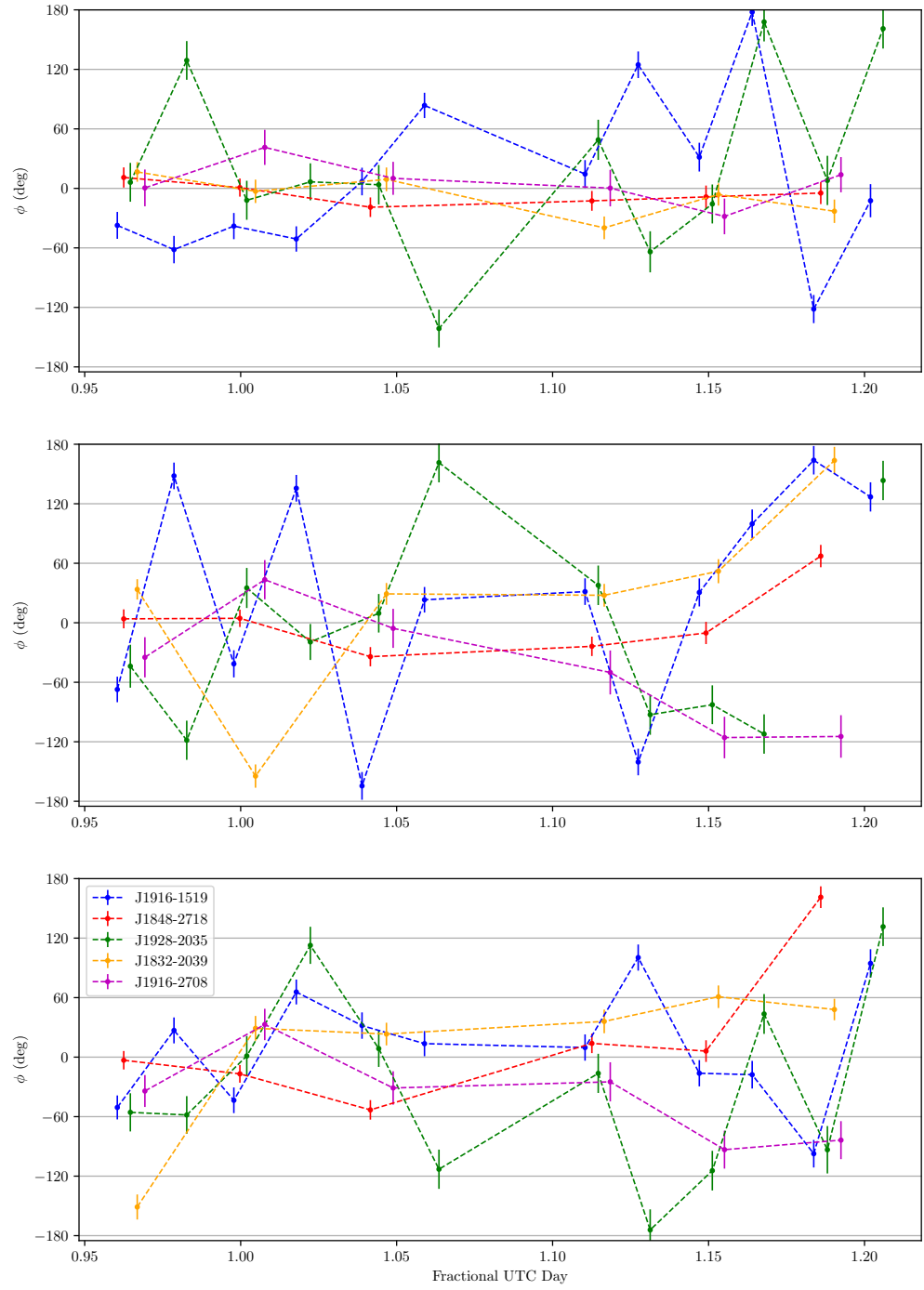


**Figure C.2:** G1901–2112  $\bar{R} = 6.5$  deg Ring, MV025

## C.2. ADDITIONAL FIGURES

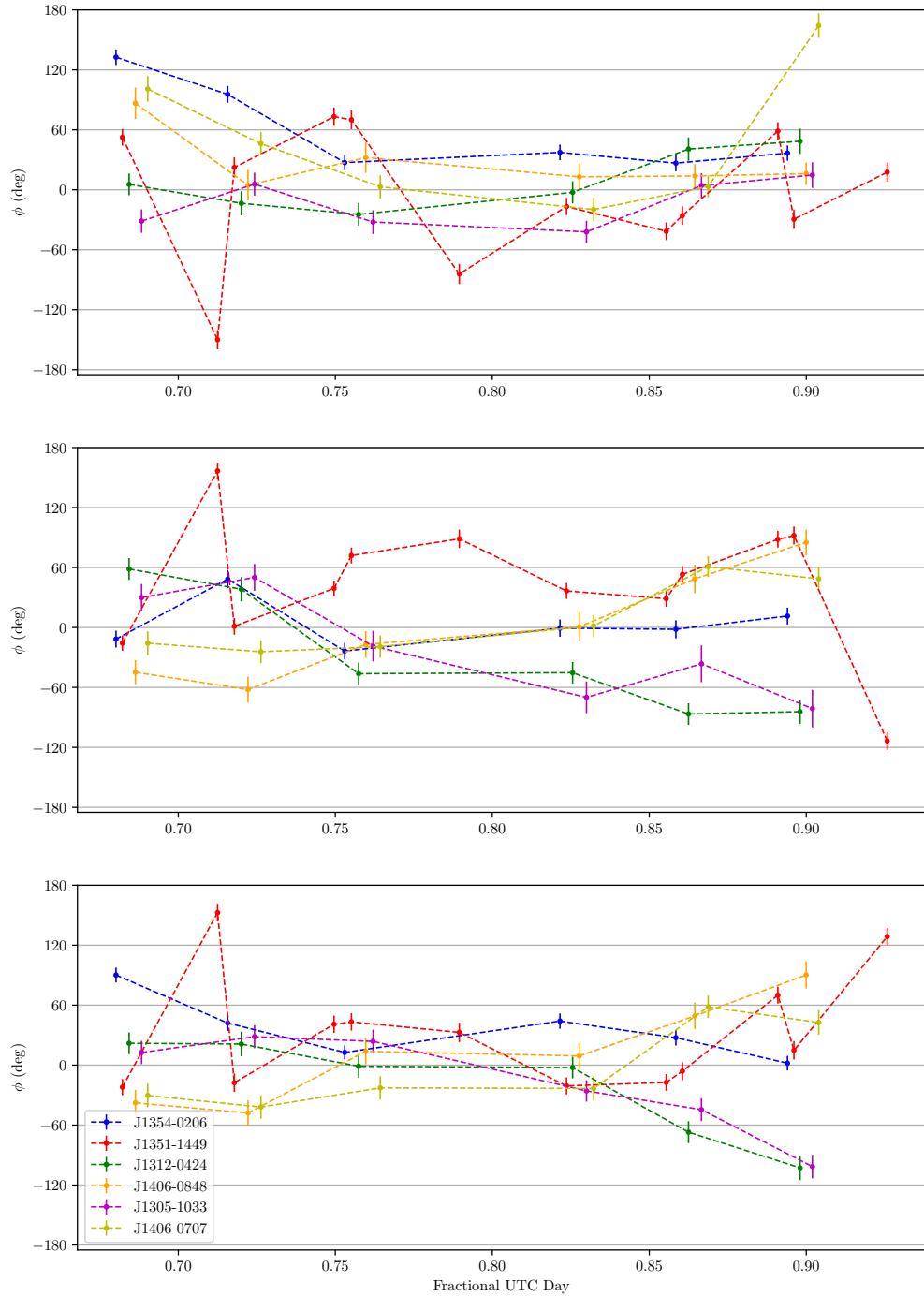


**Figure C.3:** G1336-0829  $\bar{R} = 7.5$  deg Ring, MV025

## C.2. ADDITIONAL FIGURES

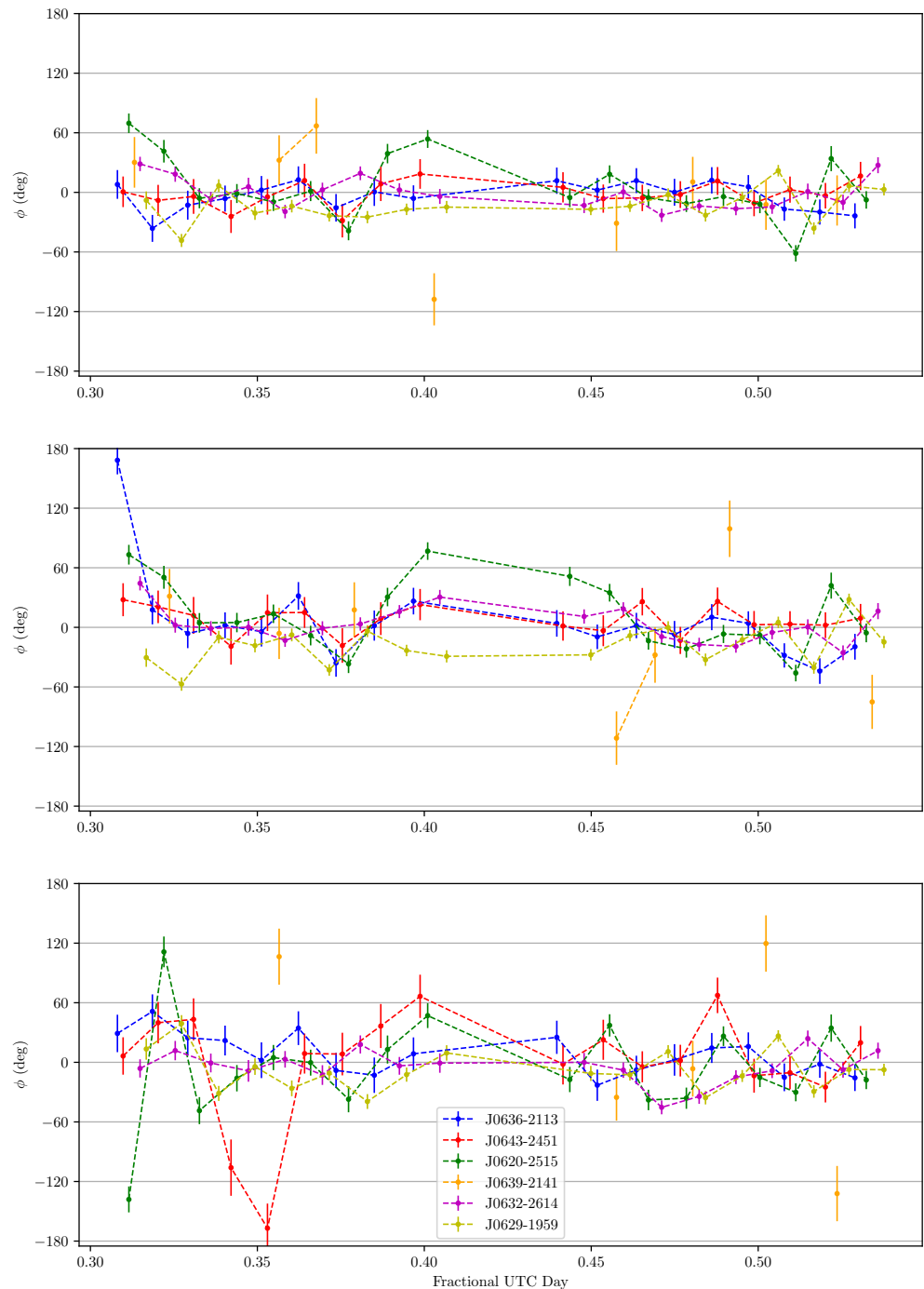


**Figure C.4:** G0634-2335  $\bar{R} = 3$  deg Ring, MV026

## C.2. ADDITIONAL FIGURES

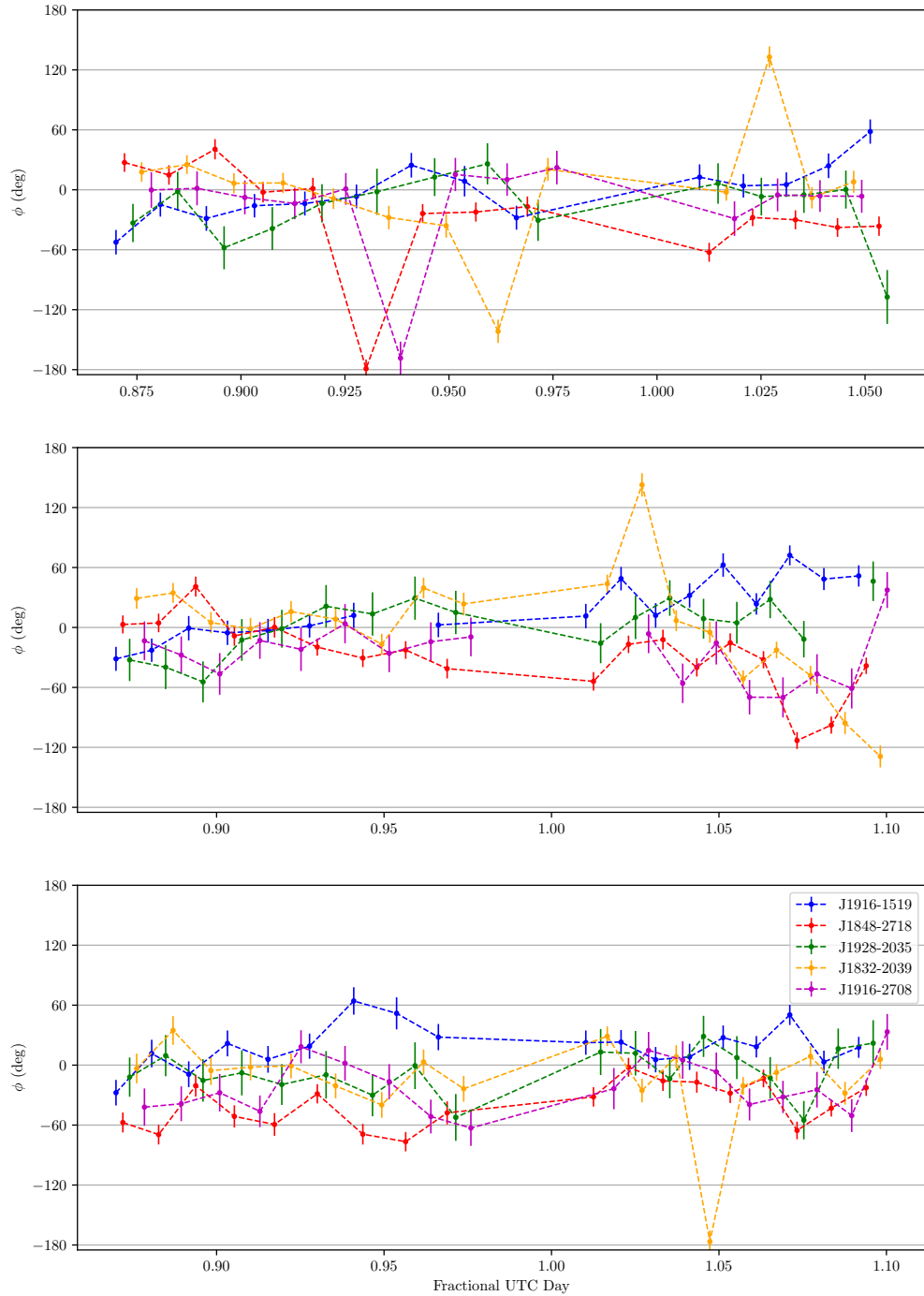


**Figure C.5:** G1901–2112  $\bar{R} = 6.5$  deg Ring, MV026

## C.2. ADDITIONAL FIGURES

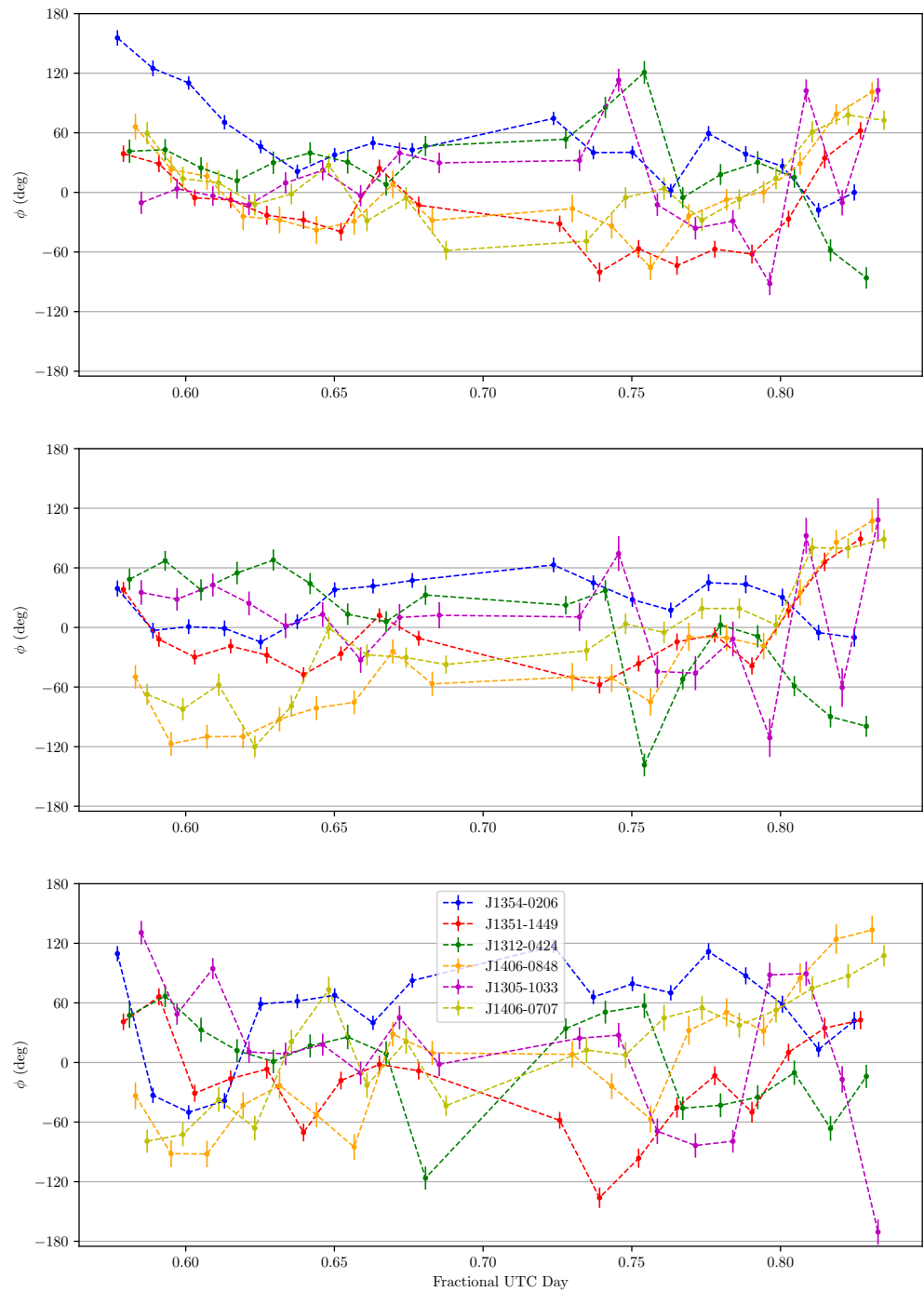


**Figure C.6:** G1336-0829  $\bar{R} = 7.5$  deg Ring, MV026

## C.2. ADDITIONAL FIGURES

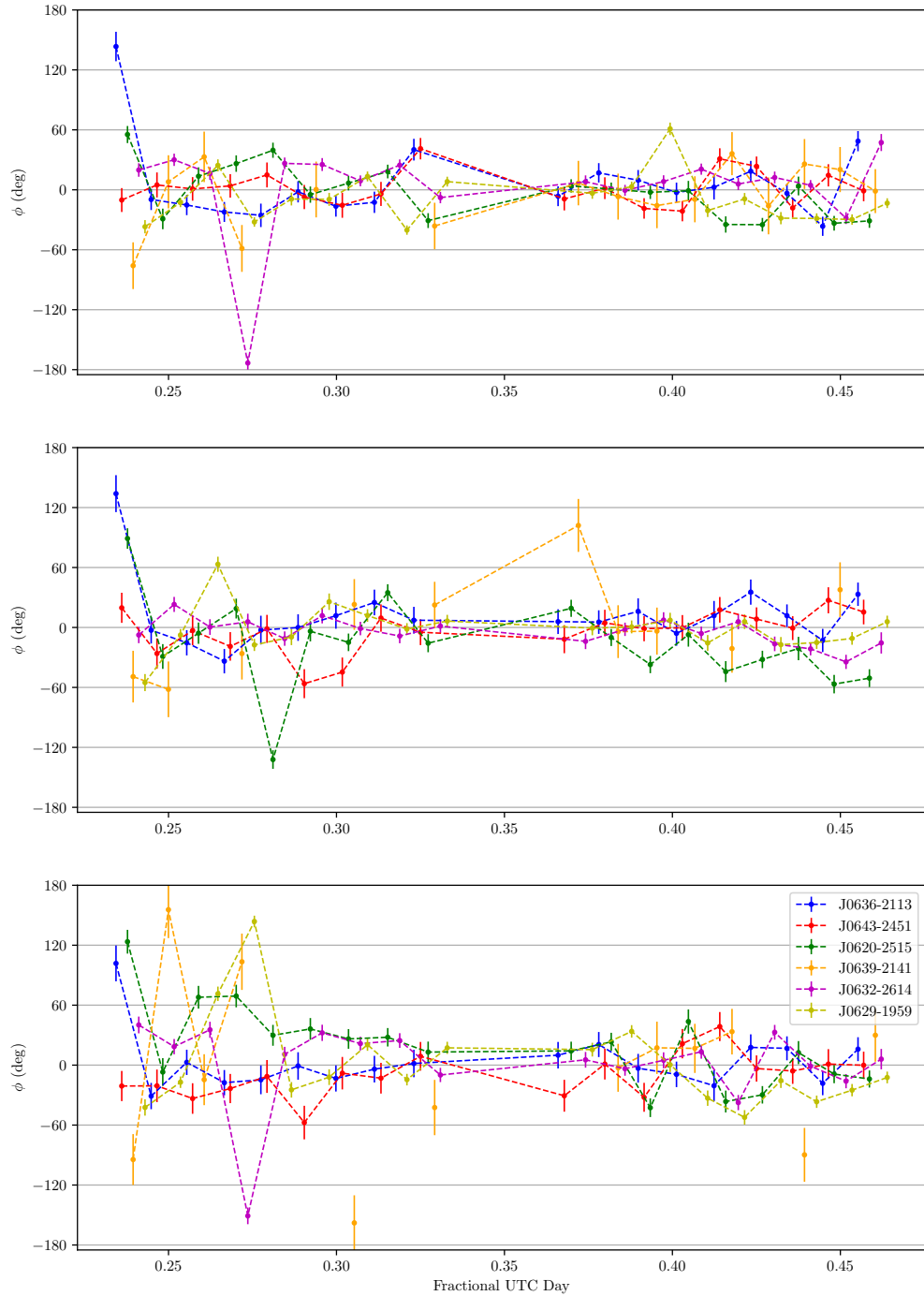


**Figure C.7:** G0634–2335  $\bar{R} = 3$  deg Ring, MV027

## C.2. ADDITIONAL FIGURES

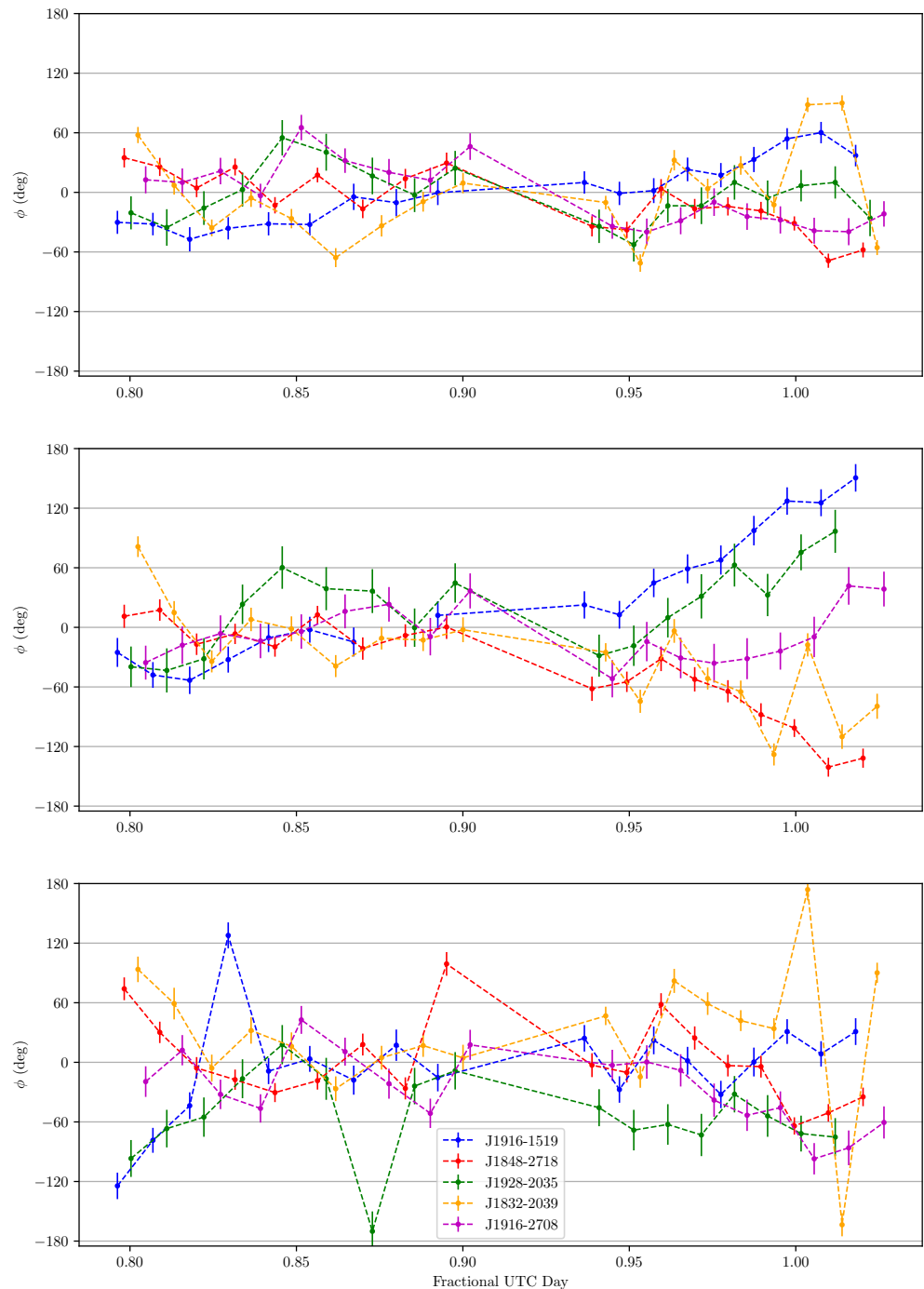


**Figure C.8:** G1901–2112  $\bar{R} = 6.5$  deg Ring, MV027

## C.2. ADDITIONAL FIGURES

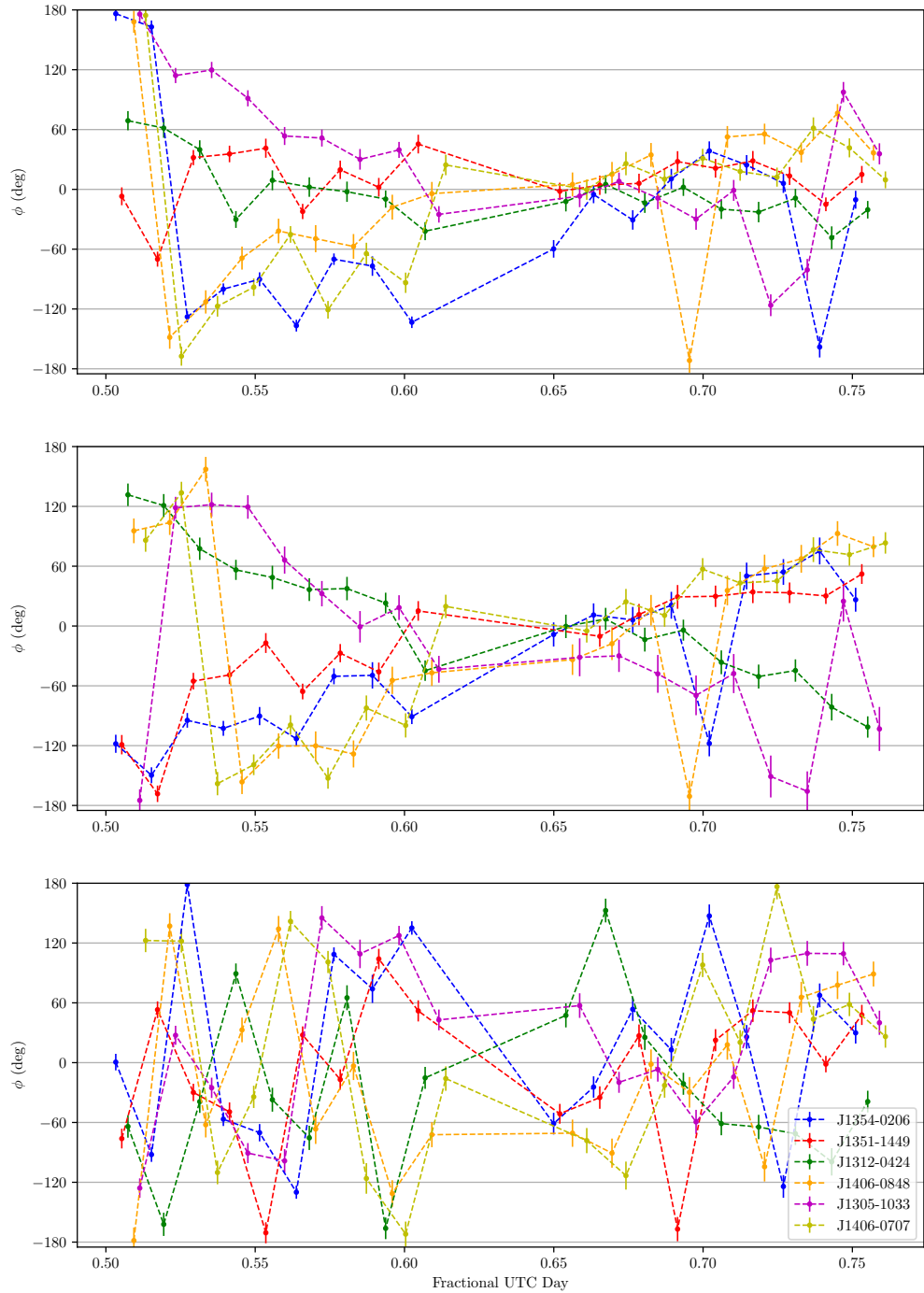


**Figure C.9:** G1336-0829  $\bar{R} = 7.5$  deg Ring, MV027

## C.2. ADDITIONAL FIGURES

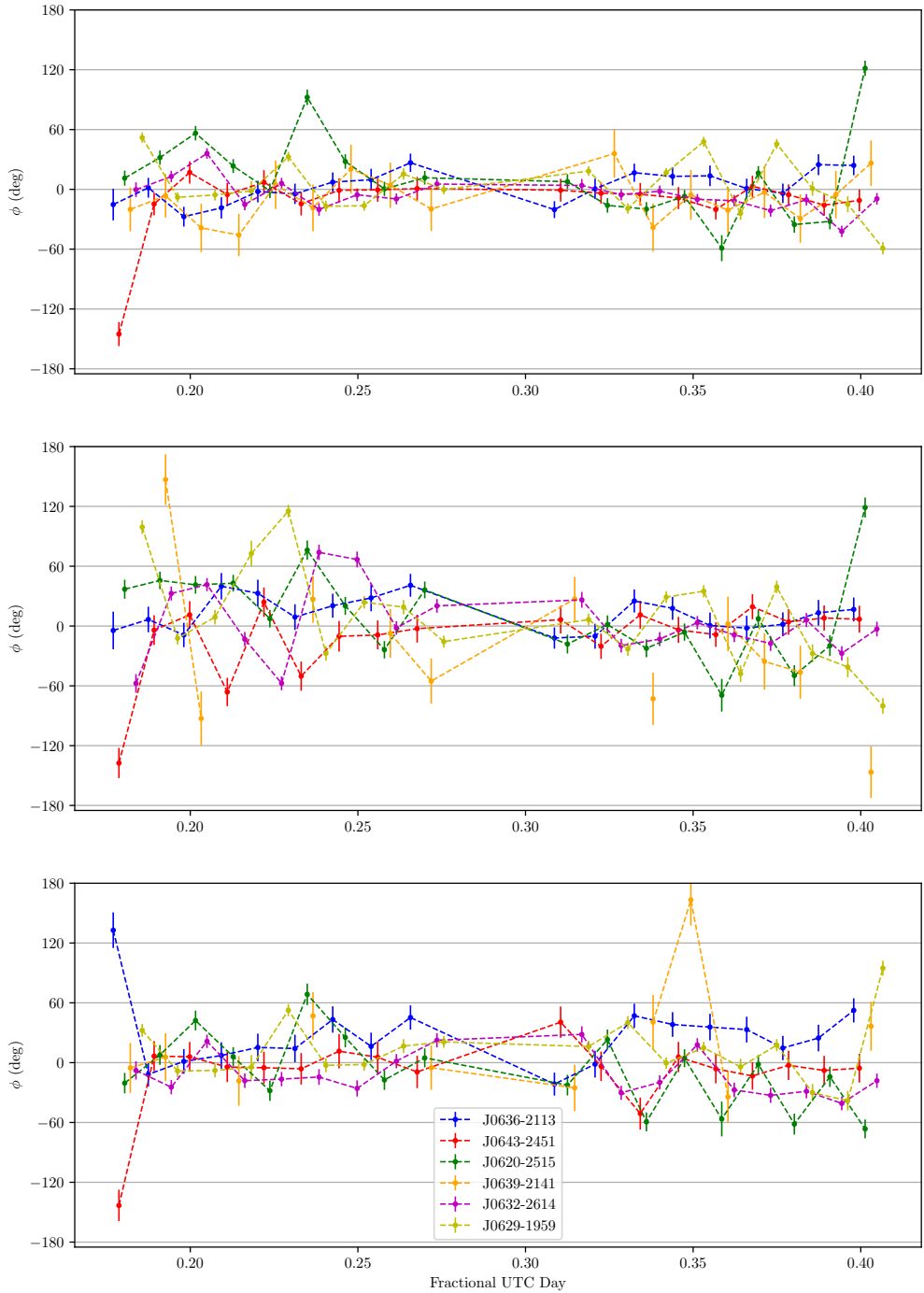


**Figure C.10:** G0634–2335  $\bar{R} = 3$  deg Ring, MV028

## C.2. ADDITIONAL FIGURES

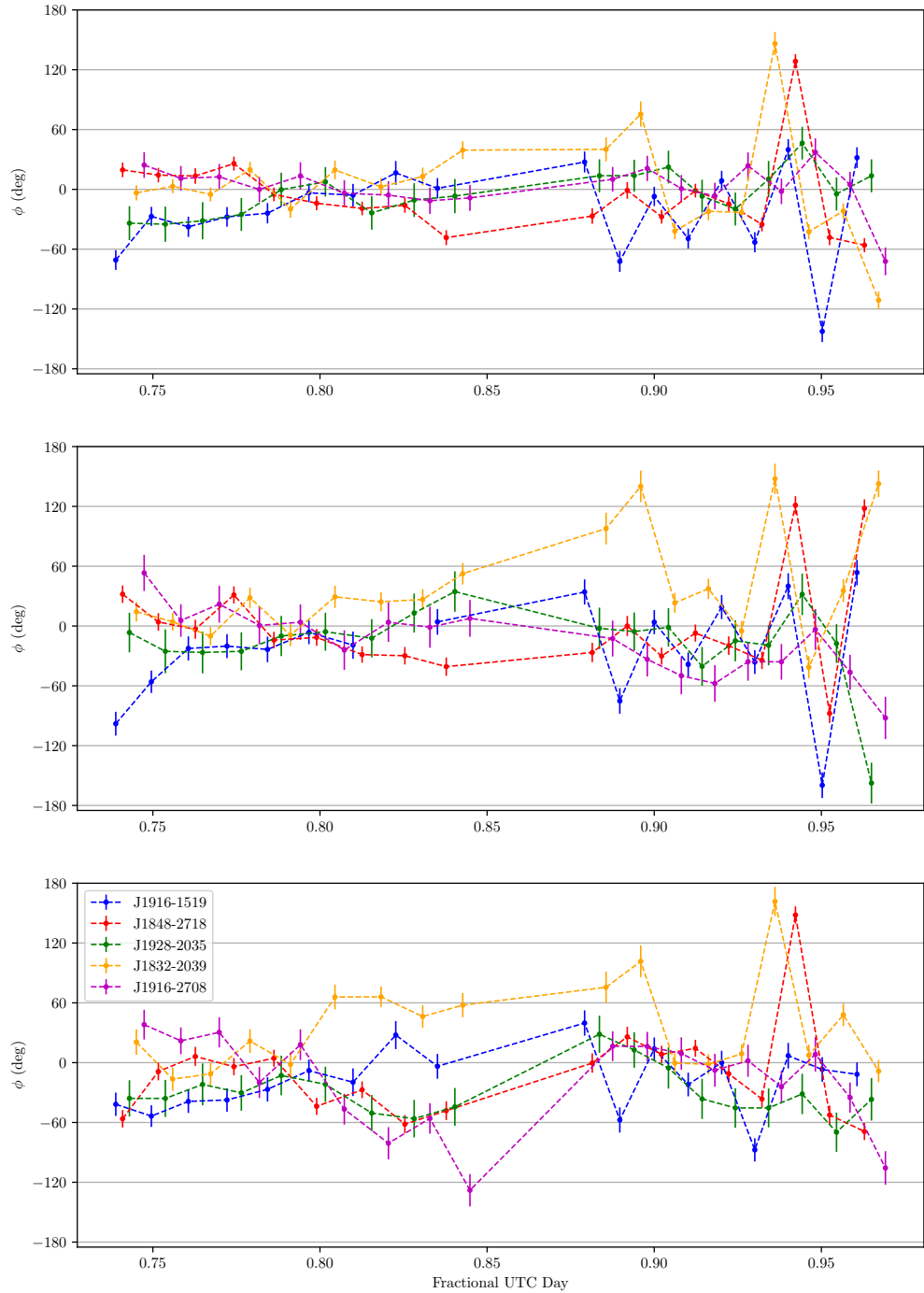


**Figure C.11:** G1901–2112  $\bar{R} = 6.5$  deg Ring, MV028

## C.2. ADDITIONAL FIGURES

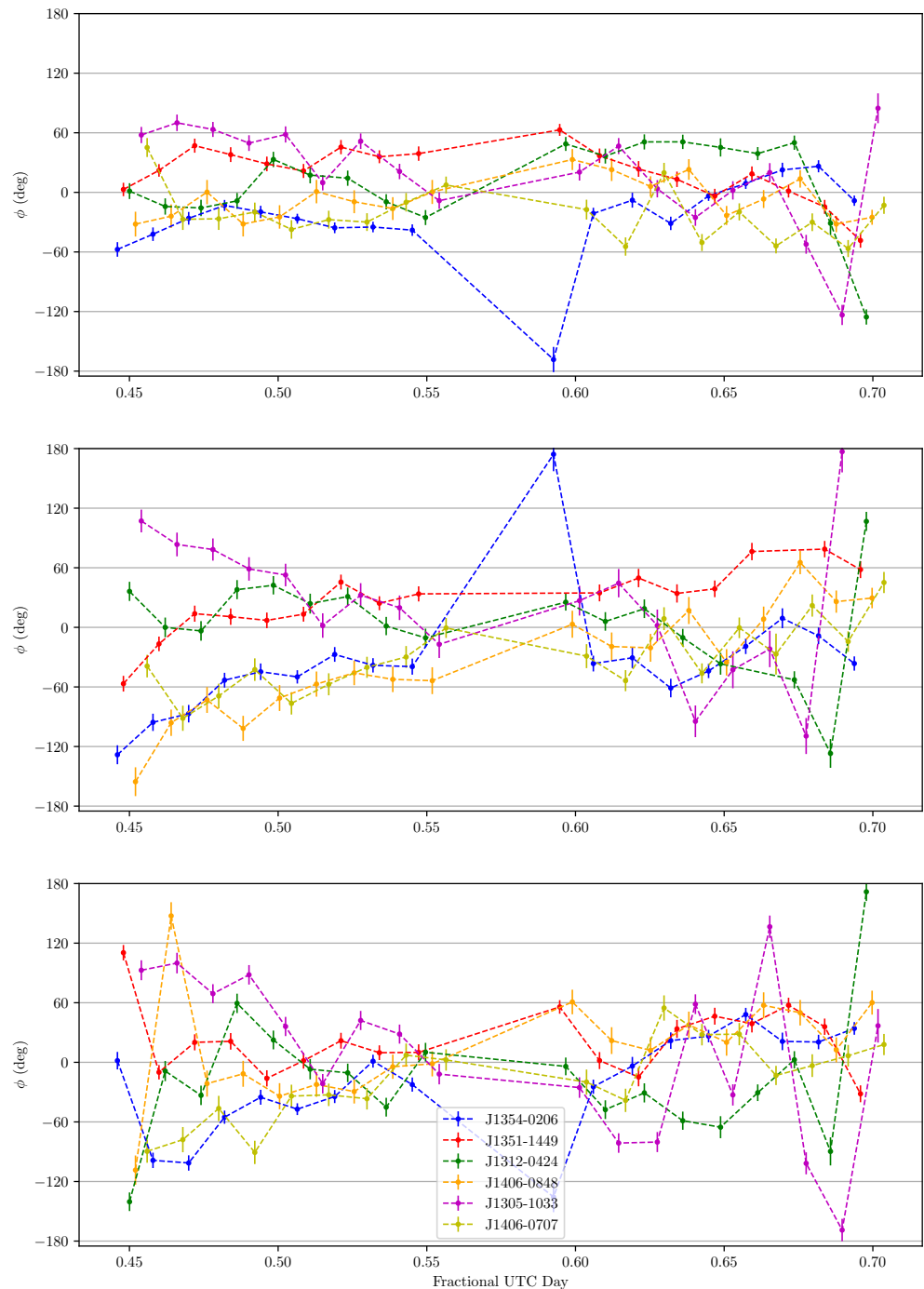


**Figure C.12:** G1336-0829  $\bar{R} = 7.5$  deg Ring, MV028

## C.2. ADDITIONAL FIGURES

### C.2.2 Phase and Phase Slopes measured by MultiView

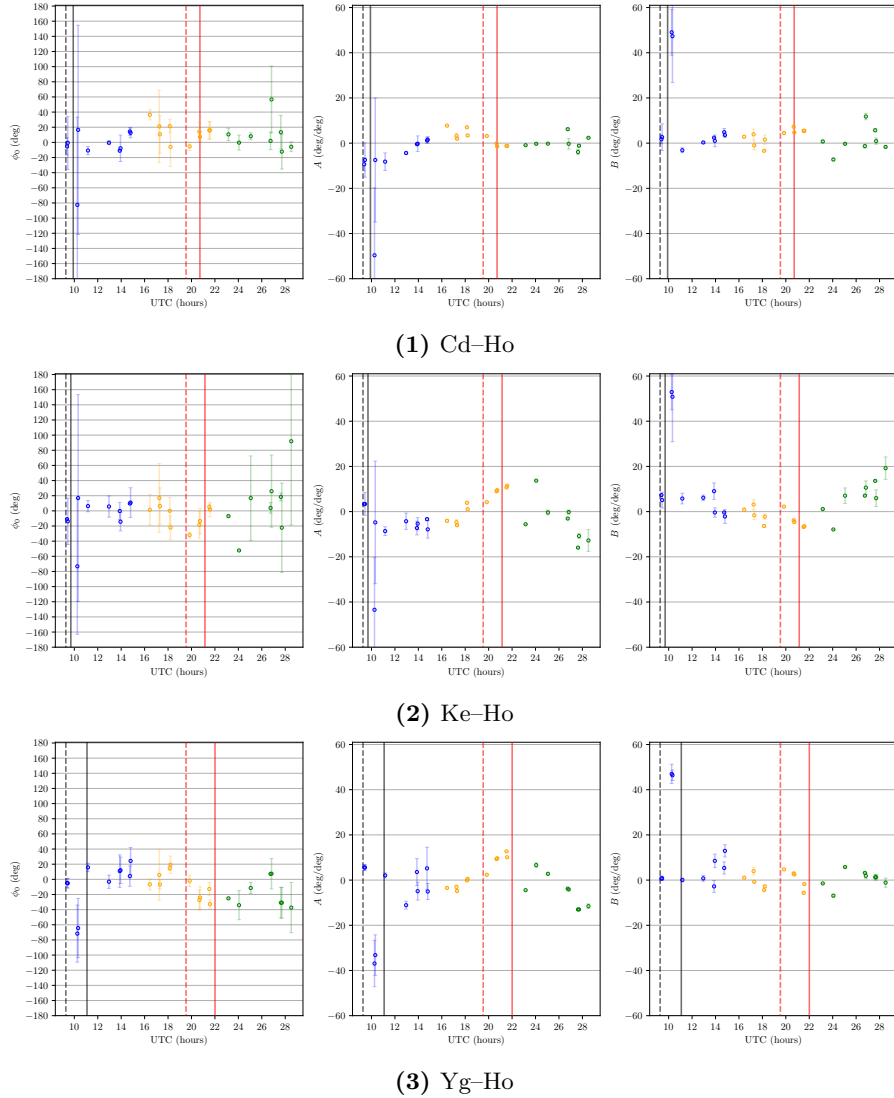


**Figure C.13:** MV025

## C.2. ADDITIONAL FIGURES

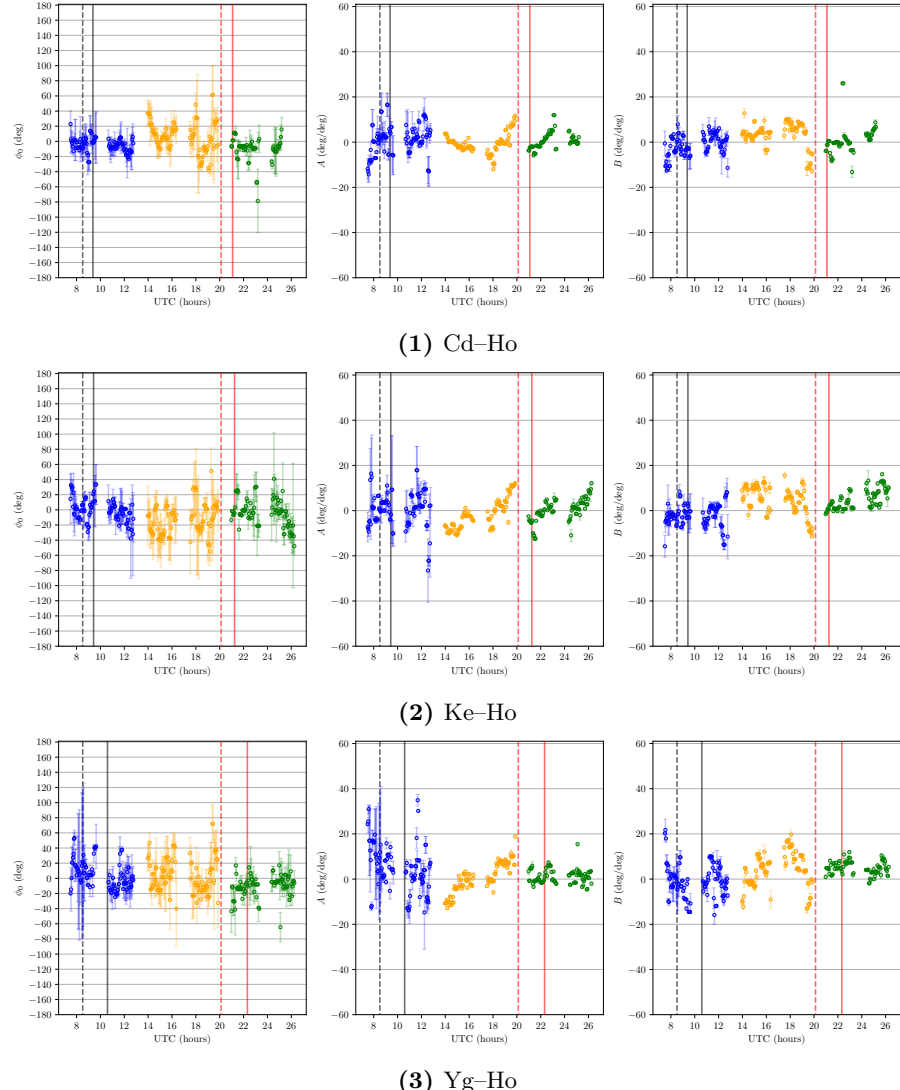


**Figure C.14:** MV026

## C.2. ADDITIONAL FIGURES

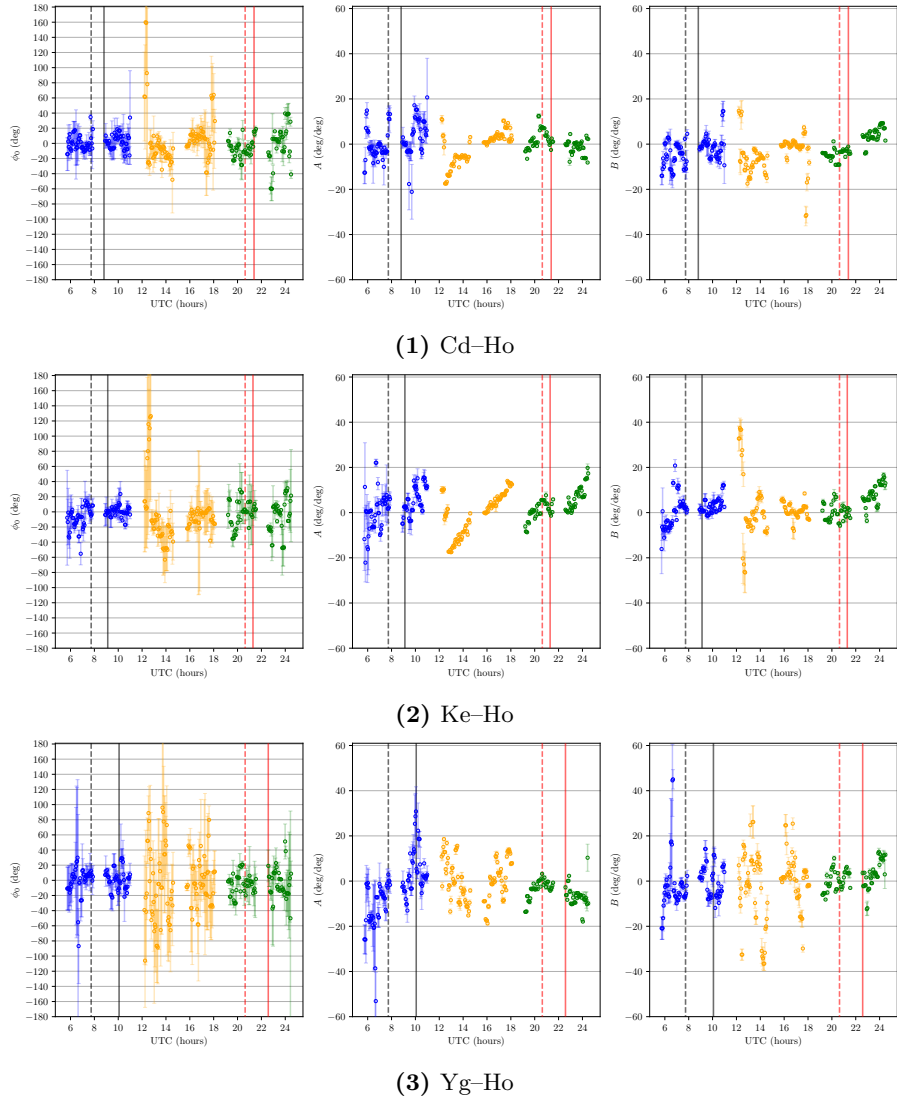


**Figure C.15:** MV027

## C.2. ADDITIONAL FIGURES

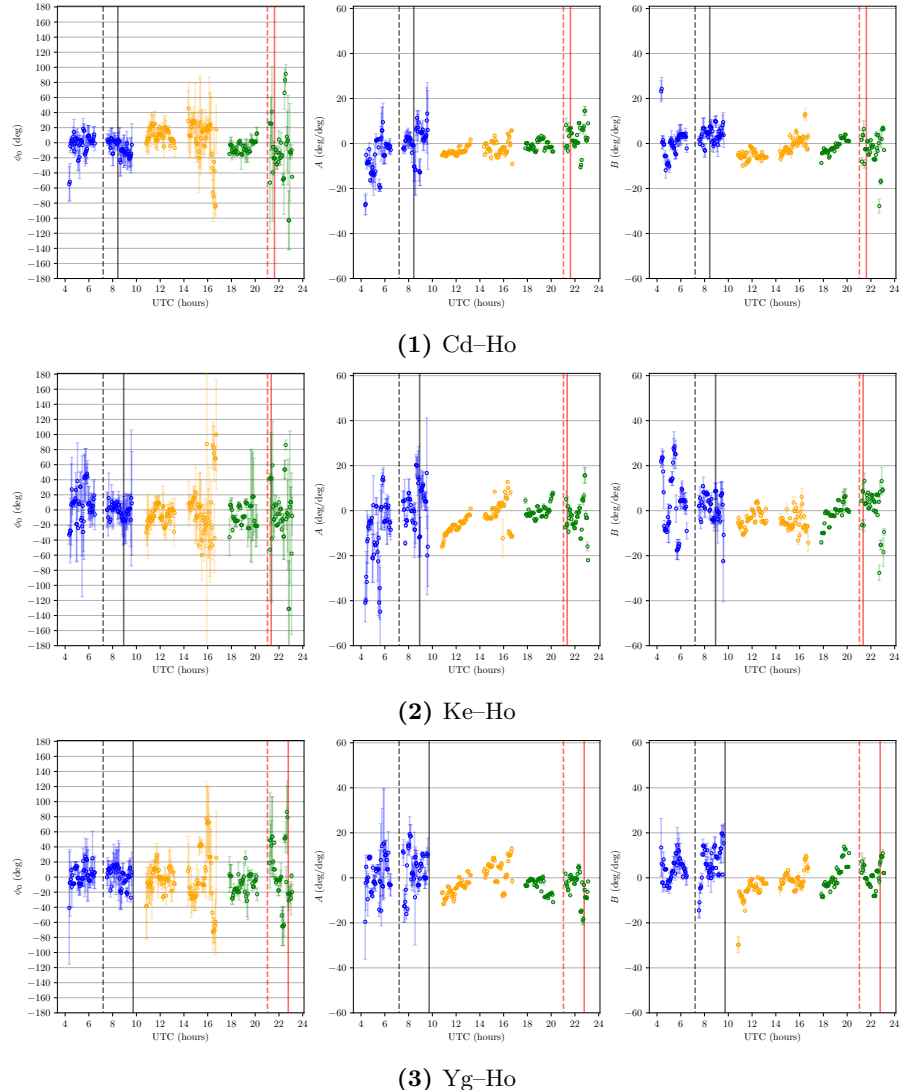


**Figure C.16:** MV028

### C.3. ADDITIONAL TABLES

## C.3 Additional Tables

### C.3.1 Inverse Phase Referencing Astrometry

Epoch	Source	$S$ (mJy)	$\sigma_S$ (mJy)	$\Delta\alpha$ (mas)	$\sigma_{\Delta\alpha}$ (mas)	$\Delta\delta$ (mas)	$\sigma_{\Delta\delta}$ (mas)
MV025	G0634–2335	1407.0	4.00	-0.002	0.002	0.001	0.002
	J0636–2113	230.75	1.02	-0.163	0.004	0.018	0.003
	J0643–2451	176.24	0.98	-0.062	0.005	-0.102	0.004
	J0620–2515	99.67	6.03	0.219	0.049	0.113	0.035
	J0639–2141	37.52	1.15	0.032	0.024	0.076	0.022
	J0632–2614	497.08	3.24	0.013	0.005	-0.038	0.005
	J0629–1959	219.00	19.60	-0.296	0.073	-0.038	0.058
MV026	G0634–2335	910.99	0.74	0.001	0.001	0.001	0.001
	J0636–2113	134.82	1.22	-0.106	0.008	-0.048	0.006
	J0643–2451	114.56	0.67	-0.119	0.006	0.027	0.004
	J0620–2515	211.28	2.61	0.033	0.011	0.059	0.008
	J0639–2141	27.11	0.41	0.041	0.014	0.022	0.010
	J0632–2614	462.77	2.51	0.048	0.005	0.027	0.004
	J0629–1959	658.78	3.04	0.024	0.004	-0.096	0.003
MV027	G0634–2335	1136.0	1.00	-0.002	0.001	-0.001	0.001
	J0636–2113	190.00	1.77	0.079	0.008	0.073	0.007
	J0643–2451	170.11	0.87	0.124	0.005	0.053	0.004
	J0620–2515	315.82	3.59	-0.314	0.010	-0.203	0.008
	J0639–2141	33.82	0.40	0.201	0.010	0.143	0.008
	J0632–2614	568.78	3.99	-0.134	0.006	-0.100	0.005
	J0629–1959	811.42	6.37	0.052	0.007	-0.019	0.005
MV028	G0634–2335	947.04	1.06	-0.004	0.001	0.000	0.001
	J0636–2113	146.42	1.56	-0.122	0.009	0.049	0.008
	J0643–2451	130.05	0.74	0.040	0.006	0.000	0.004
	J0620–2515	211.60	3.15	0.034	0.013	0.028	0.010
	J0639–2141	29.40	0.34	-0.059	0.010	-0.127	0.008
	J0632–2614	442.38	4.12	0.063	0.008	0.005	0.006
	J0629–1959	606.29	7.91	-0.113	0.012	0.028	0.009

### C.3. ADDITIONAL TABLES

Epoch	Source	$S$ (mJy)	$\sigma_S$ (mJy)	$\Delta\alpha$ (mas)	$\sigma_{\Delta\alpha}$ (mas)	$\Delta\delta$ (mas)	$\sigma_{\Delta\delta}$ (mas)
MV025	G1336–0829	743.35	0.94	-0.023	0.001	-0.076	0.001
	J1354–0206	292.82	6.32	-0.229	0.020	-0.110	0.018
	J1351–1449	322.14	8.45	0.111	0.022	0.363	0.018
	J1312–0424	46.39	2.38	0.031	0.055	-0.054	0.046
	J1406–0848	74.33	3.25	-0.216	0.046	0.198	0.030
	J1305–1033	139.79	2.87	0.114	0.018	-0.068	0.014
	J1406–0707	132.32	3.37	0.199	0.022	0.105	0.019
MV026	G1336–0829	415.98	0.77	-0.036	0.002	-0.067	0.002
	J1354–0206	282.82	4.80	-0.462	0.016	-0.012	0.013
	J1351–1449	242.44	3.41	0.153	0.012	0.008	0.011
	J1312–0424	74.49	1.72	-0.351	0.021	-0.120	0.016
	J1406–0848	43.62	2.27	-0.175	0.042	-0.350	0.037
	J1305–1033	47.61	2.12	-0.202	0.041	-0.073	0.031
	J1406–0707	9.86	2.06	-0.019	0.167	-0.003	0.163
MV027	G1336–0829	571.82	1.14	-0.025	0.002	-0.019	0.002
	J1354–0206	21.86	8.21	-1.577	0.513	-1.182	0.425
	J1351–1449	175.39	5.10	0.155	0.025	0.107	0.024
	J1312–0424	48.62	3.30	-0.460	0.071	-0.275	0.049
	J1406–0848	-39.05	3.81	1.089	0.100	-1.581	0.088
	J1305–1033	14.80	3.60	-0.490	0.243	-0.288	0.238
	J1406–0707	44.40	2.45	-0.461	0.048	0.267	0.040
MV028	G1336–0829	476.14	0.77	-0.023	0.002	-0.028	0.001
	J1354–0206	201.55	4.17	-0.081	0.020	-0.281	0.017
	J1351–1449	287.88	5.78	-0.025	0.017	0.209	0.015
	J1312–0424	43.01	2.55	0.154	0.055	0.045	0.039
	J1406–0848	95.91	1.96	-0.243	0.020	-0.177	0.017
	J1305–1033	59.97	2.91	-0.139	0.046	0.144	0.039
	J1406–0707	88.94	1.54	0.175	0.016	-0.102	0.014

### C.3. ADDITIONAL TABLES

Epoch	Source	$S$ (mJy)	$\sigma_S$ (mJy)	$\Delta\alpha$ (mas)	$\sigma_{\Delta\alpha}$ (mas)	$\Delta\delta$ (mas)	$\sigma_{\Delta\delta}$ (mas)
MV025	G1901–2112	191.052	0.820	-0.031	0.004	-0.006	0.003
	J1916–1519	61.031	3.805	0.247	0.052	0.333	0.043
	J1848–2718	274.016	1.606	0.106	0.005	-0.009	0.004
	J1928–2035	15.209	1.641	-1.743	0.055	-2.446	0.206
	J1832–2039	125.929	4.012	-0.223	0.033	0.342	0.019
	J1916–2708	81.726	1.116	0.060	0.012	-0.278	0.008
MV026	G1901–2112	119.279	0.233	-0.005	0.002	-0.005	0.001
	J1916–1519	122.695	1.164	-0.014	0.008	0.132	0.006
	J1848–2718	171.466	1.901	0.161	0.010	-0.162	0.006
	J1928–2035	46.523	0.417	0.092	0.008	0.024	0.005
	J1832–2039	132.461	2.469	-0.080	0.018	0.028	0.011
	J1916–2708	59.731	0.670	0.111	0.010	-0.147	0.007
MV027	G1901–2112	140.980	0.208	-0.004	0.001	-0.002	0.001
	J1916–1519	89.282	1.358	0.477	0.014	0.371	0.011
	J1848–2718	228.981	2.463	-0.502	0.011	-0.367	0.007
	J1928–2035	40.462	0.718	0.631	0.016	0.225	0.012
	J1832–2039	108.851	3.585	-0.454	0.033	-0.105	0.021
	J1916–2708	61.593	1.076	0.226	0.014	-0.041	0.011
MV028	G1901–2112	137.140	0.246	-0.001	0.002	-0.001	0.001
	J1916–1519	113.679	1.646	0.157	0.014	-0.049	0.010
	J1848–2718	176.485	2.970	0.069	0.017	-0.102	0.010
	J1928–2035	46.149	0.524	0.256	0.010	0.009	0.008
	J1832–2039	161.779	2.108	-0.202	0.013	0.163	0.008
	J1916–2708	58.530	0.826	-0.031	0.013	-0.137	0.010

### C.3. ADDITIONAL TABLES

#### C.3.2 Inverse MultiView Astrometry

Epoch	Source	$S$ (mJy)	$\sigma_S$ (mJy)	$\Delta\alpha$ (mas)	$\sigma_{\Delta\alpha}$ (mas)	$\Delta\delta$ (mas)	$\sigma_{\Delta\delta}$ (mas)
MV025	G0634–2335	1256.0	7.0	0.069	0.005	0.026	0.000
	J0636–2113	244.2	0.9	-0.112	0.003	-0.035	0.000
	J0643–2451	152.8	1.8	-0.079	0.011	-0.065	0.000
	J0620–2515	211.5	6.4	0.172	0.027	0.037	0.020
	J0639–2141	39.9	0.7	0.087	0.016	0.033	0.010
	J0632–2614	503.1	6.1	0.075	0.010	0.020	0.000
	J0629–1959	380.3	6.7	-0.082	0.039	-0.164	0.030
MV026	G0634–2335	869.9	1.7	0.042	0.002	0.029	0.000
	J0636–2113	145.0	1.0	-0.024	0.006	0.026	0.000
	J0643–2451	116.2	0.5	0.014	0.004	0.044	0.000
	J0620–2515	250.9	2.1	-0.081	0.008	0.035	0.000
	J0639–2141	27.1	0.4	0.192	0.016	0.067	0.010
	J0632–2614	481.6	1.7	0.050	0.003	0.024	0.000
	J0629–1959	636.9	3.3	0.007	0.005	-0.037	0.000
MV027	G0634–2335	1114.0	2.0	0.016	0.002	0.026	0.000
	J0636–2113	191.3	1.7	0.059	0.008	0.048	0.000
	J0643–2451	175.2	0.9	0.061	0.005	-0.004	0.000
	J0620–2515	355.5	2.8	-0.028	0.007	0.000	0.000
	J0639–2141	35.8	0.3	0.091	0.009	0.062	0.000
	J0632–2614	608.0	3.7	0.011	0.005	0.016	0.000
	J0629–1959	998.6	5.3	-0.075	0.005	-0.031	0.000
MV028	G0634–2335	919.0	1.4	0.018	0.001	-0.014	0.000
	J0636–2113	151.1	1.3	-0.040	0.008	0.032	0.000
	J0643–2451	139.1	0.7	0.064	0.005	0.020	0.000
	J0620–2515	282.1	3.0	-0.088	0.010	-0.069	0.000
	J0639–2141	29.8	0.3	0.084	0.010	-0.120	0.000
	J0632–2614	515.9	2.2	0.001	0.004	0.032	0.000
	J0629–1959	697.5	6.4	-0.008	0.008	-0.061	0.000

### C.3. ADDITIONAL TABLES

#### C.3.3 Self-Calibration Astrometry

Epoch	Source	$S$ (mJy)	$\sigma_S$ (mJy)	$\Delta\alpha$ (mas)	$\sigma_{\Delta\alpha}$ (mas)	$\Delta\delta$ (mas)	$\sigma_{\Delta\delta}$ (mas)
MV025	G0634–2335	1419.0	3.0	-0.003	0.002	0.001	0.001
	J0636–2113	256.1	0.8	-0.002	0.003	-0.009	0.002
	J0643–2451	201.0	0.7	-0.005	0.003	-0.011	0.002
	J0620–2515	495.7	1.1	0.000	0.002	0.003	0.001
	J0639–2141	54.0	0.6	0.035	0.010	-0.026	0.008
	J0632–2614	762.9	1.0	-0.013	0.001	-0.004	0.001
	J0629–1959	1.1	0.0	-0.008	0.001	0.021	0.001
MV026	G0634–2335	917.3	0.5	0.002	0.001	0.001	0.000
	J0636–2113	168.3	0.4	0.022	0.002	0.013	0.002
	J0643–2451	129.2	0.4	0.005	0.004	0.019	0.002
	J0620–2515	316.6	0.4	-0.026	0.001	-0.008	0.001
	J0639–2141	33.9	0.3	0.057	0.009	0.008	0.008
	J0632–2614	518.3	0.5	0.003	0.001	0.000	0.001
	J0629–1959	752.8	0.6	0.010	0.001	0.022	0.001
MV027	G0634–2335	1142.0	1.0	-0.001	0.001	0.000	0.001
	J0636–2113	227.0	0.6	-0.001	0.002	0.004	0.002
	J0643–2451	190.0	0.4	-0.009	0.002	0.001	0.002
	J0620–2515	431.7	0.6	-0.004	0.001	-0.004	0.001
	J0639–2141	40.2	0.3	0.074	0.007	0.049	0.006
	J0632–2614	678.6	0.8	0.000	0.001	-0.001	0.001
	J0629–1959	1.0	0.0	0.001	0.001	0.008	0.001
MV028	G0634–2335	961.4	0.8	-0.003	0.001	-0.002	0.001
	J0636–2113	185.2	0.4	0.009	0.002	0.006	0.002
	J0643–2451	152.1	0.3	0.006	0.002	0.008	0.002
	J0620–2515	343.3	0.4	-0.008	0.001	-0.003	0.001
	J0639–2141	35.7	0.3	0.028	0.007	0.006	0.006
	J0632–2614	555.8	0.5	-0.003	0.001	0.000	0.001
	J0629–1959	913.4	0.6	0.009	0.001	0.011	0.001



